Safety in Mines Research Advisory Committee

Final Report

Experimental investigation of fundamental processes in mining induced fracturing and rock instability

J.A.L. Napier, K. Drescher, M.W. Hildyard,

M.O. Kataka, D.F. Malan, E.J. Sellers

Research Agency	**:**	**CSIR Miningtek**
Project No	**:**	**GAP 601b**
Date	**:**	**March 2002**
Report No	**:**	**2002-0106**

Executive summary

The main themes of the project GAP601b have been experimental investigations of creep effects, further underground observations of time-dependent behaviour, investigation of scale effects and rock mass stability and studies of the interaction of seismic waves with underground excavations.

Previous work reported in SIMRAC project GAP332 highlighted the importance of understanding time-dependent stope closure in deep level hard rock mining. Additional efforts have been made to extend this knowledge to quantify creep behaviour in the uniaxial compression of lava and quartzite samples. Additional laboratory testing of joint creep and the role of joint infilling has been carried out. This has shown that the size distribution of the gouge material affects the creep response rate indicating differences between the response of natural joints and mining induced fractures. The overall behaviour of the joint creep tests can be explained by postulating a simple non-linear constitutive model for the slip resistance. Satisfactory agreement with experimental observations can be obtained by assuming that the creep rate is proportional to the difference between the applied shear stress and the shear resistance. Tests have also been carried out to study the relaxation behaviour, under confined loading, of quartzite and lava samples in the post-peak regime. This has shown that the extent of stress relaxation in the quartzite is larger in a given time period than in the lava.

A number of significant advances have been made in acoustic emission (AE) monitoring studies of rock samples that are subjected to compressive loading. These studies have required the development of techniques to enable small-scale AE sensors to be used as velocity transducers. This has allowed test results from small-scale samples to be interpreted with currently available moment tensor inversion methods and to deduce micro-event source sizes and mechanisms. These studies have yielded evidence that the laboratory scale frequency-magnitude statistics are compatible with mine and even earthquake scale observations and motivate the relevance of small scale testing to the understanding of stope scale damage processes. This work has been complemented by a number of laboratory tests of three-dimensional fracture formation in cubic-shaped, triaxially loaded samples. Planar, slot-shaped openings are introduced in these samples to study the formation of fractures near “kinked” edge outlines that are analogous to the lead-lag geometries of deep level longwall layouts. The analysis of the fracture patterns that are formed has been carried out by means of x-ray scans of the rock samples to reconstruct the detailed shapes of the induced fracture surfaces. It is found that the fracture surface forms initially at the stressed edge of the slot outline and

progressively changes shape away from the plane of the opening to follow the average orientation of the stressed edge.

A number of numerical developments have been pursued to enable three-dimensional modelling of these lead-lag fracture processes. Most of these efforts have been only partially successful. Specific numerical methods that were employed include finite element analysis (ELFEN), discrete particle assembly simulations (PFC^{3D}) and boundary element displacement discontinuity simulations (3DIGS). These difficulties have prompted the development of a completely new approach to problems of three-dimensional fracture propagation and dynamic fault slip simulation that is based on a mesh-free formulation of the boundary element displacement discontinuity method. Initial trials of this method have been very encouraging but were limited to the simulation of tensile fracturing of planar cracks.

Further underground measurements have indicated that, in the Vaal reef, hangingwall-parallel stress relaxation can be significant following the advance of the mining face. This emphasises that the choice of the mining rate can be used to control the effective clamping stress in the hangingwall. Underground observations were used to construct descriptive functional relationships linking time-dependent closure rates to the mining rate and the distance to the stope face. These relationships provide a practical quantification of the closure rate behaviour that can be used in the evaluation and design of stope support units. A document describing guidelines for measuring and analysing continuous stope closure behaviour in deep tabular excavations has been produced.

Some effort has been made to assess the feasibility of predicting the time to failure of rock samples in uniaxial loading. This is a prototype problem that stands as a surrogate for the more difficult task of predicting seismic events or rockbursts. In this work it has been demonstrated that the DIGS computer code, with random mesh tessellations that contain an initial population of flaws (mesh elements having no cohesion), can be used to provide realistic simulations of laboratory-scale uniaxial compression tests. It does not appear to be possible to use the simulated time series of fracture energy release increments to predict, in any reliable manner, the time of sample failure. It was, however, possible to study the evolution of the distribution of damage cluster sizes that are formed in the random mesh assembly. This shows that before, or just at, the point of failure, one dominant cluster of connected mesh elements emerges in the sample. (This is similar to the manifestation of a so-called “percolation” threshold that is observed in studies of ideal lattice failure). This suggests that any prediction of the failure time requires not only a record of seismic activity but, also, additional information relating to the evolutionary formation of internal damage clustering. In the numerical simulations it appears that the temporal separation between the formation of the percolating cluster and the final time of

failure increases as the deadweight loading on the sample is reduced. Special techniques would have to be developed to monitor the formation of such structures near deep level stopes.

Considerable efforts have been made to quantify size effects and to develop representations of these effects in numerical models. A survey of the size effect literature was completed to assist this study. From this it seems that a straightforward means of representing size effect behaviour is by the inclusion of slip and tension weakening effects on explicit discontinuities in a numerical model. Modifications were made to the DIGS code to allow cohesion and tensile strength values to be reduced as linear or non-linear functions of discontinuity slip and opening movements. Some confirmation of the validity of this approach was obtained by the analysis of available laboratory scale size effect experiments. Additional laboratory tests were also carried out to confirm these results but it was found that the range of sample sizes tested was too small to exhibit overall size effect trends. The implications of the slip weakening behaviour in relation to the analysis of rock stability and seismic behaviour have also been studied. The stability behaviour of an assembly of interacting slip elements can be analysed by standard matrix eigenvalue methods. Additional modifications were made to the DIGS code to allow unified modelling of slip and tension weakening effects as well as time-dependent slip behaviour. This has been applied to the simulation of mining induced seismic activity in a random mesh model where active slip structures evolve in sporadic steps analogous to actual seismic activity.

The implications of size effect and slip weakening behaviour were considered in the evaluation of a simple stabilising pillar layout problem. In this case, it was found that the relative stability of self-similar layout configurations could be evaluated by determining the critical value of the slip weakening parameter that would cause foundation failure in each layout. This suggests that the critical value of the weakening parameter may be used as a novel layout evaluation criterion. The feasibility of this proposal remains to be tested.

A simplified method for the simulation of blast-induced fracture growth was introduced in the DIGS code. In this approach, the blast pressure is distributed along the blast-induced fractures in each growth step. The results of this approach provide a basic tool for the determination of the extent of blast-induced fractures in a non-uniform stress field. These results have to be extended to three dimensions to provide useful design insights.

A major output of the GAP601b project has been an extensive study of the interaction of seismic waves with underground openings and the analysis of wave propagation through fractured rock. A number of fundamental results have been established. These include the development of methods to quantify dispersion behaviour in numerical models and quantitative demonstrations that the computer code WAVE can, in fact, be used to reproduce measured

wave attenuation effects near the surface of an underground tunnel. A number of studies were carried out to identify mechanisms that can lead to ground motion amplification and to identify regions of likely damage due to seismic events. It was shown that the presence of stress free stope surfaces can lead to an increase in particle velocities of at least six times the values that would be estimated from standard far-field asymptotic analyses. These studies have shown, as well, that wave-surface interactions can lead to the generation of significant tensile stresses suggesting that an exclusive focus on peak particle velocities as a support design criterion is inappropriate. The study has further shown how wave dispersion and locked in stress on fractures can affect ground motions when explicit models of hangingwall fracturing are constructed. In addition, it has been demonstrated that hangingwall block loosening can be promoted by the interaction of surface waves with such blocks.

The complexity of underground boundary conditions can prevent the quantitative interpretation of detailed wave propagation effects. At the same time, the WAVE code provides a unique tool for the simulation of dynamic effects associated with mine seismic activity. In particular, it has been shown that, for the analysis of dynamic wave propagation problems, WAVE is at least one to two orders of magnitude more efficient in both computer memory and run time efficiency than other general-purpose finite element or finite difference computer codes. WAVE is currently the only special purpose computer code that can be used to carry out mine scale modelling of wave propagation around deep level excavations and is a unique resource to the South African mining industry.

Acknowledgements

The authors gratefully acknowledge the support received for this research from SIMRAC. We would also like to thank Prof. Andre Vervoort for assistance with the x-ray scanning of experimental samples. We wish to thank Prof. R. Paul Young for the support and supervision of investigations into wave propagation effects and for the provision of experimental data.

Table of Contents

Executive summary **2**

Acknowledgements **5**

Table of Contents **6**

List of Figures **8**

List of Tables **21**

List of contracted Enabling Outputs **20**

1.0 Introduction and methodology **21**

2.0 Experiments and modelling of time-dependent damage mechanisms in rock and near mine openings **24**

2.1 Laboratory experiments of time-dependent rock discontinuity and rock mass behaviour 24

2.1.1 Mechanisms of time dependent deformation in hard rocks 24

2.1.2 Acoustic emission testing 36

2.1.3 Cube sample tests and X-ray scanning 44

2.1.4 Underground observations and the effect of mining rate on support design 49

2.2 Formulation of descriptive mechanisms of time-dependent damage and stope face stability. 60

2.2.1 Friction mobilisation model 60

2.2.2 Stope face stiffness and stability analysis 62

2.3 Statistical uncertainty in time to failure and the stope stress environment 65

2.3.1 Simulation of time to failure and prediction of time of failure – model formulation and numerical experiments and implications 65

2.3.2 Statistical determination of variability in rocks relevant to the mining industry 73

2.3.3 Point kernel approach for considering statistical uncertainty in rock mass properties 80

3.0 Effect of scale in the assessment of rock deformation mechanisms **84**

3.1 Understanding the size effect in rock masses 84

3.1.1 Review of theories of size effect 84

3.1.2 Experimental data on the size effect in rock 91

3.2 Computational methods to represent the mechanisms of failure at different size scales. 98

3.2.1 Slip and tension-weakening models 98
3.2.2 Implications of time-dependent behaviour 101
3.2.3 Implications for foundation failure and preconditioning 109
4.0 Seismic wave transmission through fractured rock and two and three dimensional fracture propagation 115
4.1 Seismic wave interaction with underground openings 115
4.1.1 Review of previous modelling 115
4.1.2 Modelling an underground experiment at Kopanang 118
4.1.3 Modelling an underground Experiment at the URL, Canada 123
4.1.4 The influence of excavation free surface on the distribution and amplitudes of ground motion 129
4.2 Interaction of seismic waves with fracture assemblies 136
4.2.1 Overview of previous research on wave propagation through fracturing 137
4.2.2 Laboratory measurements of seismic waves in quartzite 138
4.2.3 Models of laboratory experiments with fractures 143
4.2.4 Models of *in-situ* experiments with fractures 146
4.2.5 Wave behaviour through random fracture assemblies 151
4.2.6 The effect of fracturing on amplitude and distribution of motion in stopes 157
4.3 Numerical methods for three-dimensional fracture propagation and assessment of dynamic effects. 165
4.3.1 Numerical issues relating to dynamics 165
4.3.2 Attenuation of a seismic wave in WAVE 173
4.3.3 Lead-lag geometry modelling 180
4.3.4 Mesh-free method for fracture propagation 193
4.4 Modelling of blast-induced fracture propagation. 195
4.4.1 DIGS model with simplified pressure distribution 195
5.0 Conclusions 205
6.0 References 213
7.0 Supplementary document list 228
8.0 List of papers written within the scope of GAP 601b. 229

List of Figures

Safety in Mines Research Advisory Committee 1

Figure 2.1.1.1 Application of the tests results to the stope fracture model 26

Figure 2.1.1.2 Close-up view of the testing configuration for uniaxial creep tests 27

Figure 2.1.1.3 Creep rate vs normalised axial stress 28

Figure 2.1.1.4 Creep rate vs axial stress 29

Figure 2.1.1.5 Testing configuration for direct shear 30

Figure 2.1.1.6 A measured displacement-time curve showing the change in shear and normal displacement during the different loading steps 31

Figure 2.1.1.7 A detail of the measured shear displacement-time curve showing all three phases of creep 32

Figure 2.1.1.8 The change of friction angle with shear displacement showing the effect of the different loading steps 32

Figure 2.1.1.9 Shear stress – normal stress results for the three types of infilling 34

Figure 2.1.1.10 Stress/Strength-time curves for quartzite and lava 35

Figure 2.1.2.1 Number of acoustic emissions versus time when these events are generated. Circles represent non-double couple event (implying tensile failure) and diamond shapes represent double couples (implying shear failure). 38

Figure 2.1.2.2. Plot of Log (Energy) versus log (Moment) for AE (represented by diamond) and mining induced events (represented by crosses), from McGarr, 1984 and Natural earthquakes, (represented by squares), from Kanamori, et. al., 1993. Dotted lines are lines of constant apparent stress. 39

Figure 2.1.2.3. Frequency magnitude relationship plot for acoustic emission and mine data from McGarr (1993). 40

Figure 2.1.2.4 Peak ground velocity versus moment. Filled squares represent AE, triangles represent mine events and circles represent natural earthquakes (mine and earthquake data from McGarr (1993)). 40

Figure 2.1.2.5 Test of sample 201 showing creep strain and acoustic emission counts 41

Figure 2.1.2.6 Test data for sample 115 showing creep strain and acoustic emission counts 42

Figure 2.1.2.7 a) Test set up and b) typical stress – strain curves for post failure test with acoustic emission monitoring 43

Figure 2.1.2.8 Test data showing stress, AE count and AE energy with time 44

Figure 2.1.3.1. Three-dimensional reconstruction of the fracture pattern in an Elsburg quartzite block with a lead-lag of 20mm. The superimposed white lines denote the lead-lag panel layout. 47

Figure 2.1.3.2. Three-dimensional reconstruction of the fracture pattern in an Elsburg quartzite block with a lead-lag of 10mm. The superimposed white lines denote the lead-lag panel layout. 47

Figure 2.1.3.3. Three-dimensional reconstruction of the fracture pattern in a Marble Bar quartzite block with no lag. 48

Figure 2.1.4.1. Strain cells installed in the stope hangingwall at Moab Khotsong Mine. 50

Figure 2.1.4.2. Closure measurements in the 70-47-E10 panel at Great Noligwa Mine. 51

Figure 2.1.4.3. Measuring the hangingwall roughness. 51

Figure 2.1.4.4. Measurement of hangingwall roughness at Moab Khotsong Mine. The profile was taken along dip, parallel to the face, with the origin of the graph in the upper part of the panel. The areas encircled indicated where some minor block got dislocated in the hangingwall. 52

Figure 2.1.4.5. Example to illustrate the effect of mining rate on rate of closure. 53

Figure 2.1.4.7. Closure measured in a VCR (hard lava) panel when there was no mining activity for a period of four days. The time periods in brackets indicate the intervals used to calculate the steady-state closure rates. Two closure instruments at different distances to the face were used to collect the data. 55

Figure 2.1.4.8. Measured and simulated values of steady-state closure for the VCR (hard lava) panel. 55

Figure 2.1.4.9. Effect of distance to face on the rate of steady-state closure. Although there is some scatter present in the data with a resulting poor fit to the given function, it will be used as a useful approximation of the trend 56

Figure 2.1.4.10. The effect of mining rate on the total amount of steady-state closure at a particular point in the stope. This is for a VCR (hard lava) panel. 57

Figure 2.1.4.11. Measured and simulated values of steady-state closure for a VCR panel with a soft lava hangingwall..... 59

Figure 2.1.4.12. Effect of distance to face on the rate of steady-state closure for the VCR with a soft lava hangingwall..... 59

Figure 2.1.4.13. The effect of mining rate on the total amount of steady-state closure at a particular point in the stope. This is for a VCR (soft lava) stope..... 59

Figure 2.2.1.1 Comparison of slip evolution as a function of time for incremental loads applied to a sliding block with two values of the critical slip distance, Yc. 61

Figure 2.2.1.2 Comparison of the fraction of the slip surface exceeding the critical slip limit as a function of time for two values of the critical slip parameter Yc. 61

Figure 2.2.1.3 Comparison of the average slip resistance as a function of the cumulative slip for two values of the critical slip parameter Yc. 62

Figure 2.2.2.1 Comparison of stope face stiffness as a function of panel span when mining through a fault and when the fracture zone is explicitly simulated..... 63

Figure 2.2.2.2 Comparison of the average stress ahead of a simulated parallel-sided panel when mining through (i) perfectly elastic ground, (ii) elastic ground and a single vertical fault and (iii) a single vertical fault and a model of the off-reef fracture zone around the stope. 64

Figure 2.2.2.3 Comparison of average stope closure, adjacent to the stope face, as a function of the stope span. 64

Figure 2.3.1.1b Static fatigue test cumulative viscous fracture length for different loads (Delaunay mesh/ Material 1)..... 67

Figure 2.3.1.2 Static fatigue test fraction viscous length for different loads (Delaunay mesh/ Material 1). 67

Figure 2.3.1.3a Static fatigue test cumulative fracture length for different loads (Delaunay mesh Material 2). 68

Figure 2.3.1.3b Static fatigue test cumulative viscous fracture length for different loads (Delaunay mesh/Material 2). 68

Figure 2.3.1.4 Static fatigue test fraction viscous length for different loads (Delaunay mesh Material 2). 69

Figure 2.3.1.5 Static fatigue test cumulative fracture length for different loads (Voronoi mesh / Material 1). 69

Figure 2.3.1.6 Static fatigue simulations of the time to failure for deadweight loading of a rectangular sample with different internal strength and mesh parameters. 71

Figure 2.3.1.7 Number of clusters plotted as a function of time for different deadweight loads (Delaunay mesh/Material 1). 71

Figure 2.3.1.8 Progressive evolution of the cluster size distribution for the 50 MPa loading of the Delaunay/ Material 1 sample. (Note the change to bimodality at time 95). 72

Figure 2.3.1.9 Cumulative energy release curves for different loads on the Delaunay/ Material 1 sample, including the times at which the cluster size distribution becomes bimodal, marked by vertical lines. 72

Figure 2.3.2.1 Averages and standard deviations of shore hardness for four rock types 75

Figure 2.3.2.2 Observed and predicted Weibull cumulative distribution functions of shore hardness for four rock types 76

Figure 2.3.2.3 Relationship between Shore Hardness and unconfined strength and Young's modulus. 77

Figure 2.3.2.4 Change in average rebound number with number of hits for four rock types 78

Figure 2.3.2.5 Change in average rebound number with number of hits for four rock types 78

Figure 2.3.2.6 Weibull plot of plasticity index to determine Weibull parameters 79

Figure 2.3.3.1 Schematic of a virtual element at point Q transmitting influence to point P. 81

Figure 2.3.3.2 (a) Model of ledging stope mining through a zone containing two faults (b) Seismicity projected onto reef plane for random cohesion and radii. The area of the bubbles is scaled to event magnitude. 82

Figure 2.3.3.3 (a) Comparison of frequency-magnitude distributions to demonstrate the influence of uniform or exponential distributions property distributions. (b) closure of the central raize. 82

Figure 3.1.1.1 a: Structure used to develop size effect law (after Bazant and Chen,1997). b: Schematic diagram of size effect laws 85

Figure 3.1.1.2 a) Example of experimental results showing the decrease in strength with size from Bieniawski and van Heerden (1977) and b) after Hoek and Brown (1980) and c) equation from Hoek and Brown extrapolated to 80m diameter 87

Figure 3.1.1.3 The effect of sample size and shape on strength and post failure response (after Hudson et al. 1971). 88

Figure 3.1.1.4 Effect of sample size on joint shear behaviour. a: Consistent strength decrease and deformation increase with size from Barton et al. 1991. b: Variable response from Hencher et al. 1993. 89

Figure 3.1.2.1 a) Photograph of the beam bending testing and b) schematic showing the dimensions of the beam. 93

Figure 3.1.2.2 Strength change with beam size for Elsburg quartzite. 94

Figure 3.1.2.4 Photograph of failing beam showing the visible crack and the process zone. 94

Figure 3.1.2.4 Typical load displacement curve from beam tests 95

Figure 3.1.2.5 a) Load deformation curves for different size beams and b) the post failure energy related to beam size. 95

Figure 3.1.2.6 Variation in strength with diameter for Elsburg quartzite in unconfined compression. 96

Figure 3.1.2.7 Variation in tensile strength (Brazilian test) with diameter for Elsburg quartzite. 97

Figure 3.1.2.8 Variation in strength with diameter for Middle Elsburg conglomerate reef from unconfined compression of samples with 1:1 diameter to height ratios. 98

Figure 3.2.1.1 Simulation of size effect in primary crack formation, using a tension weakening model, from the crown of a circular hole in a uniaxially loaded rock sample. (Experimental data points from Carter, 1992) 99

Figure 3.2.1.2 Load vs strain across a representative averaging length above the crown of a circular hole showing the effect of additional fracturing from sites in a tessellation mesh and the effect of suddenly increasing the slope of the tension weakening law (hole radius = 3mm). 100

Figure 3.2.1.3 Comparison of linear and power law tension weakening laws applied to a 3 mm borehole in a square specimen. 101

Figure 3.2.2.1 Qualitative response of a crack to slip weakening. 104

Figure 3.2.2.2. Time response of a single crack uniformly loaded in shear with different slip weakening parameter values. 107

Table 3.2.2.2. Material properties for fault slip scaling tests. 108

Figure 3.2.2.3. Effect of scale on the response of two faults separated by a strong asperity. (Time units unspecified). 109

Figure 3.2.3.1 Sample loading test with different tessellation mesh densities. 111

Figure 3.2.3.2 Schematic pillar layout showing two of four failure planes forming a potential wedge-shaped foundation failure mechanism. 111

Figure 3.2.3.3 Simulated stope closure profiles following four successive mining steps of a parallel-sided panel in two geological environments in which parting plane weaknesses are present and are absent in the hangingwall region. 113

Figure 3.2.3.4 Effect of simulated preconditioning blast magnitude on the closure response in a stope with weak footwall parting plane but having no weak parting planes in the hangingwall. 114

Figure 3.2.3.5 Effect of simulated preconditioning blast strength on the stress induced in the stope hangingwall behind an advancing stope face. 114

Figure 4.1.1.1 Comparison of displacement waveforms for two geophone positions (from Handley et al., 1996). 118

Figure 4.1.2.1 Plan view of the tunnel-site for the rockburst experiment, showing the excavation and positions of the main blast, calibration blast, accelerometers ACT and ACM, geophones mounted on the side-wall C5, C6, C4, C8 and A8, and geophone A6, sited 5 m into the solid rock. (Geophone names in brackets indicate a different name for the calibration blast). 119

Figure 4.1.2.2 Test blast in solid rock: Comparison of the recorded (solid line) and modelled (dotted line) velocity seismograms at distances of 0.6 m, 1.2 m and 1.8 m from the blast. 120

Figure 4.1.2.3 Comparison of velocity seismograms for the calibration blast at varying distances along the tunnel near wall. Motion is normal to the tunnel surface. Approximate P-wave arrivals and the position of the S wave, are identified. 120

Figure 4.1.2.4 Recorded (solid line) and modelled (dotted line) velocity waveforms for the calibration blast, compared for geophones A4, A5 and A2 which were a triaxial set mounted on the tunnel wall 1.7 m ahead of the calibration blast. 121

Figure 4.1.2.5 Recorded (solid line) and modelled (dotted line) velocity waveforms for the calibration blast, compared for geophones A6, A7 and A8 which were a triaxial set mounted 5 m into the tunnel wall in solid rock, 1.5 m ahead of the calibration blast. 121

Figure 4.1.2.6 Comparison of the recorded (solid line) and modelled (dotted line) velocity seismograms for the main blast, at ACT, ACM, C5, C6, C4 and C8. (Time windows are 15 ms, and modelled waveforms were time shifted by up to 0.5ms for the first arrivals to coincide). 122

Figure 4.1.2.7 Comparison of the recorded (solid line) and modelled (dotted line) velocity seismograms for the triaxial geophones A6, A4 and A7. These were mounted 30 metres ahead of the blast and 5 metres into the tunnel wall. A6, A4 and A7 are respectively the tunnel-normal, vertical, and tunnel-parallel components. (All time windows are 15ms, and modelled waveforms were time shifted by 0.3ms for the first arrivals to coincide). 122

Figure 4.1.3.1 Acoustic emission array showing positions of boreholes AE1-AE4, sensors 1-20, and the orientation of the far-field principal stress tensor. (a) End on view of the Mine-by tunnel (looking from the face back into the tunnel). (b) View from the tunnel surface looking down the boreholes into the solid. 124

Figure 4.1.3.2 P-wave velocity. (a) Ellipsoidal model with three orthogonal directions of wave-speed calculated for different face positions (b) Variation of C_p with distance from the tunnel wall for paths approximately parallel to the tunnel surface - horizontal paths (AE4-AE2) and vertical paths (AE1-AE3). (From Carlson and Young, 1992). 125

Figure 4.1.3.3 S-wave velocity. Variation of C_s with distance from the tunnel wall for paths approximately parallel to the tunnel surface (a) paths downwards towards left (AE1-AE4 and AE2-AE3) (b) paths downwards towards right (AE1-AE2 and AE4-AE3). (From Carlson and Young, 1992). 125

Figure 4.1.3.4 Crack density variation with distance from the tunnel wall, calculated from the measured values of C_p and C_s (From Carlson and Young, 1992). 126

Figure 4.1.3.5 Sketch of the model of the acoustic array. The full array consisted of 4 boreholes each with 5 sensors spaced at 0.2 m starting at 0.2 m from the tunnel surface. The model used a reduced 8x8 array and the positions of the sensors used are shown. For the model, the boreholes were rotated into a diamond pattern as shown. The block indicates the model boundaries. 126

Figure 4.1.3.6 Elastic model (red line) compared to velocity scan AT01 (black line) for source at sensor 3 - sensors 3, 5, 7, 10, 13, 15, 18, 20. Model scaled such that peak P-wave amplitude of sensor 18 matches the data. 128

Figure 4.1.4.1 Maximum induced tensile stress (in MPa) for σ_{zz}. Plan sections are shown for two distances below the excavation, and indicate that horizontal tensile stress of up to 2 MPa is induced close to the surface, and that this falls off rapidly with distance from the surface. 131

Figure 4.1.4.2 Decay of velocity and stress with depth into the hanging-wall. The peak frequency was 330 Hz, with a wavelength of approximately 10 m. (a) Decay of the peak horizontal velocity (xvel), peak vertical velocity (yvel), and peak total velocity (vabs). (b) Decay of the peak horizontal tensile stress (sxx), peak vertical tensile stress (syy), and peak tensile stress (sg2). The results shown are normalised to the maximum velocity and tensile stress, which were 0.1 m/s and 1.8 MPa respectively. 132

Figure 4.1.4.3 Decay rate of velocity and maximum tensile stress for different frequencies. (a) Peak frequency of 330 Hz ($\lambda \approx 10$ m) (b) Peak frequency of 120 Hz ($\lambda \approx 27$ m) 133

Figure 4.1.4.4 Relationship of stress-drop and source distance to velocities in the stope. Results are based on a vertical slip source with a square area of 32 m side-length, initiating at the centre and propagating up to the stope plane. Resulting magnitudes range from 1.83 to 1.76, 1.71 to 1.64 and 1.51 to 1.44, for stress drops of 30 MPa, 20 MPa and 10 MPa respectively. The maximum velocities are valid for any source

size (L), where the distance of the source to the stope is expressed in terms of L. In this case (b) indicates the velocity at a distance of 6.25 L. 134

Figure 4.1.4.5 Velocities for three modelled events superimposed on a graph (from Jager and Ryder, 1999) of far-field and projected near-field velocities for different magnitude events. 'X' is for the 30 MPa daylighting event of Figure 4.1.4.4; 'O' is for the M=1.3 event of Figure 4.1.4.1a; 'o' is the same event as 'O' without the influence of the stope. The presence of the stope, and cases with a high stress-drop, lead to in-stope velocities associated with much larger magnitude events in current guidelines. 135

Figure 4.2.2.1 Waveforms from solid rock samples of 20 mm and 117 mm lengths. 140

Figure 4.2.2.2 Waveforms for a 93 mm long rock sample containing 3 cracks. 140

Figure 4.2.2.3 Plot of Log amplitude verse Log distance from the source for a solid and cracked samples. 141

Figure 4.2.2.4 The linear-linear plot of amplitude spectra for waveforms from steel of 120 mm length, 119 mm of length full rock, 93 mm of length full rock and 93 mm of length for cracked rock sample. Notice that the high frequencies are strongly attenuated for the cracked rock sample and the rock is more attenuated than steel. 142

Figure 4.2.3.1 Shear-wave comparisons for experimental and modelled waveforms, for the different fracture orientations. Waveforms from the experiment recorded voltage (Volts), while the model records stress (MPa). 144

Figure 4.2.4.1 URL model with the addition of open cracks with an average crack density of 0.1. (a) 38 40x40 element cracks (196.5 mm x 196.5 mm) (b) 6061 8x8 element cracks (36.5 mm x 36.5 mm). 148

Figure 4.2.4.2 Comparison of wave-forms for different crack models with sizes ranging from 196 mm down to 26 mm. All crack models have an average crack density of 0.1. Source amplitudes are scaled such that all models match the P-wave amplitude of the data for path 3 to 18. Red and blue lines indicate the P-arrival in the data and elastic model respectively. 149

Figure 4.2.5.1 Model geometry to calculate phase velocity and attenuation for 11.3 mm cracks with a central crack density of 0.1. The crack volume consists of 288 mm by 39 mm by 288 mm, and contains 1182 cracks. (a) Three-dimensional view (b) Two-dimensional cross sections at different positions along the z-axis. 154

Figure 4.2.5.2 Stages for calculating phase velocity and attenuation (a) Produce the time domain waveforms for the crack models (b) Calculate the difference between the Fourier phase spectrum of the emerging waveform and the input waveform (c) Calculate the Fourier amplitude spectrum. Results are shown for models with two different crack lengths and with central crack densities of 0.025 (red), 0.050 (blue), 0.075 (green) and 0.1 (cyan), and are compared to an uncracked (c.d.= model (black). (i) L.H.S. Models with 3.3 mm cracks with 13366 and 26732 cracks respectively (ii) R.H.S. Models with 11.3 mm cracks with 296, 591, 887 and 1182 cracks respectively. Equations 4.2.5.1 and 4.2.5.2 are then applied giving the results in Figure 4.2.5.3. 155

Figure 4.2.5.3 Velocity and attenuation spectra for a distribution of 4 element (3.3 mm) open cracks with a crack density of 0.025 and 0.05. 156

Figure 4.2.5.4 Velocity and attenuation spectra for a distribution of 12 element (11.3 mm) open cracks with a crack density of 0.025, 0.05, 0.075 and 0.1. 156

Figure 4.2.6.1 Stope model with vertical fractures in the foot-wall of the stope. The fractures are rectangular with edge-lengths between 4 m and 14 m, and are in a band between 4 m and 18 m below the stope. (a) Fracture density of 0.01 (b) Fracture density of 0.1 157

Figure 4.2.6.2 Effect of fracturing on the vertical velocity seismograms 200 m along the stope. (a) Horizontal fractures parallel to the stope free surface, with a low linear fracture stiffness (Table 5.3-E3). (b) Pre-stressed random vertical fractures with a capacity for failure. Each case is compared with that of an unfractured stope. 161

Figure 4.2.6.3 The influence of vertical fracturing. Contours indicate the maximum velocity (in m/s) induced by event #1 (magnitude 1.3) in a plane 2 m below the excavation. (a) Random vertical fractures with a normal and shear fracture stiffness of $1*10^{10}$ Pa/m and $5*10^{9}$ Pa/m respectively (Table 5.3-G3). (b) Random vertical fractures which are pre-stressed and allowed to fail due to induced stresses. The '*' indicates examples of further energy release on fractures. 161

Figure 4.2.6.4 Comparison of the motion of the block versus the intact hangingwall, for Rayleigh wave propagation induced by three types of loading. Waveforms on the L.H.S. are velocity, and those on the R.H.S., displacements. Comparisons are for a point in the centre of the block and for the same position in an intact hangingwall.

There is a nett displacement, and for cyclical loading (as in (c)), the block “ratchets” downwards. 163

Figure 4.2.6.5 Comparison of vertical motion and Horizontal stress for Rayleigh wave propagation in an intact hangingwall. Horizontal tension for both senses of slip event tends to occur during reverse or upward motion. As a result a block will tend to slip during upward motion of the hangingwall. 164

Figure 4.3.1.1 Waveforms from which the phase and group velocities are calculated. (a) Spatial waveforms at two different times used in the first method for calculating dispersion (b) Time waveforms at two different positions used in the second method for calculating dispersion. Waveforms are shown for both a 2^{nd} order and 4^{th} order staggered grid. 166

Figure 4.3.1.2 Group velocity calculated from spatial waveforms for the 2^{nd} order (w-2), 4^{th} order (w-4) and 8^{th} order (w-8) staggered mesh. The graph (w-4s) is for a 4^{th} order mesh with half the resolution in each dimension as the other meshes. 168

Figure 4.3.1.3 Phase velocities for different codes and grid schemes, with the dotted line indicating the accurate frequency range normally assumed for the 2^{nd} order staggered grid. Results are based on a 1 m grid spacing for WAVE and FLAC (i.e. an area of 1 m^2 per zone). Two different ELFEN and UDEC results are shown, one for an element area of approximately 1.2 m^2 the other for an element area of approximately 0.6 m^2. 170

Figure 4.3.1.4 Example mapping, showing position of a crack in the two coordinate systems. ‘ ’ indicates position of velocity u1, while ‘ ’ indicates position of velocity u2. Note that u1 is dual-valued on the crack. Stress positions are not shown. 172

Figure 4.3.2.1. Log amplitude of the first pulse versus log distance for a) waveforms from 0 to 110 m away from the source and b) waveforms from 120 to 296 m away from the source 175

Figure 4.3.2.2. The Fourier spectral amplitudes for waveforms at stations 106m, 196m, 256m and 396m away from the source. Notice that the high frequencies are strongly attenuated for events further away from the source. 176

Figure 4.3.2.3 The waveforms used for location for event 2. The event is located at (121, 72, 44) with an error of 7 m. This event is supposed to be at (116, 76, 40). .. 177

Figure 4.3.2.4. Wave models showing a) a 3-D view and b) a 2-D section of the model for a typical configuration of event, stope and sensors. 177

Figure 4.3.2.5. Spectral amplitude fit for event 1 on the log-log scale. Channel 2 is above the stope and the event. Channels 3 and 4 are between the stope and the event. Notice that the lower frequencies are affected by the stope (see arrow). 178

Figure 4.3.2.6 Moment tensor solution from WAVE for an event a) sheared in the vertical direction and b) sheared in the horizontal (X) direction. 179

Figure 4.3.2.7 Moment tensor solution from WAVE for an event with a stope 7 m west of the event a) sheared in the vertical direction and b) sheared in the horizontal (X) direction. 179

Figure 4.3.1.1 Example of numerical prediction of the fracture pattern in the experimental samples using the two-dimensional boundary element program DIGS. 181

Figure 4.3.1.2. a) Schematic of block test sample and b) actual loading data 182

Figure 4.3.1.3. a) Coarse mesh and damage pattern at 100 MPa vertical load and b) observed fractures. 183

Figure 4.3.1.4. a) modelled fracture pattern with coarse mesh and b) observed fracture pattern reconstructed from x-ray tomography 184

Figure 4.3.1.5 Cut-away views of the refined mesh model showing damage contours. a) at the slot level b) near the sample surface 184

Figure 4.3.1.6 a) Photograph of test sample with 30mm lead lag layout indicating the fracturing along the edges of the stress raiser and with annotation indication the position of the fracture that cuts through the leading panel. b) a section view of the ELFEN model of the sample, which produced damage contours that indicate a similar fracture pattern. 185

Figure 4.3.1.7. Section view through the block model indicating a) the located acoustic emission and b) the acoustic emission predicted by the PFC3D model. 187

Figure 4.3.1.8. Perspective view of the PFC model indicating the cluster size and position at two stages in the model analysis. a) At about half the applied load and b) at the maximum applied load. 187

Figure 4.3.1.9. Comparison of the variation in the a) observed and b) predicted incremental energy release rates with time (steps in the model are equivalent to a time increment). Also shown is the applied stress increase with time. 188

Figure 4.3.1.10 Orthographic view of fractures developed from a horizontal stope plane. 190

Figure 4.3.1.11 Cumulative fracture growth following an extension of one half of the stope face by 1m. 191

Figure 4.3.1.12 High angle view of incremental fracture growth following a 1m mining step. The mining increment is at the top right hand edge of the stope. 192

Figure 4.3.4.1 Illustration of fracture propagation under tension from an initially re-entrant crack. 194

Figure 4.3.4.2 Fracture propagation past an asperity illustrating the progressive crack front evolution. 194

Figure 4.4.1.1 Flow chart of DIGS code with semi coupled gas flow calculations 198

Figure 4.4.1.2 Generic pressure – relative volume curves for two explosive types. 199

Figure 4.4.1.3 Pressure time curve for DIGS model with borehole pressure calculated from empirical data 200

Figure 4.4.1.4 Fracture formation around a production blast for a) 1000 MPa blast pressure and b) 40 MPa initial blast pressure 201

Figure 4.4.1.5 Effect of blast pressure and shothole position on fracturing due to preconditioning blast with a) 1000 MPa at 300m from the hangingwall, b) 100 MPa at 300mm from the hangingwall and c) 1000 MPa at 1.5m from the hangingwall .. 203

Figure 4.4.1.6 Effect of blast pressure and gas flow model parameters on the slip on the hangingwall parting. All boreholes 300mm away from the hangingwall. 203

Figure 4.4.1.7 Three dimensional fracture pattern obtained from 3DIGS model. 204

List of Tables

Table 2.1.1.1 Summary of compression creep test results 29

Table 2.1.1.2 Summary of creep shear test results 33

Table 2.1.1.3 Summary of triaxial post-failure relaxation test results 36

Table 2.1.4.1. Changes in stress measured at Moab Khotsong Mine. 50

Table 3.1.2.1 Dimensions of beam tests on Elsburg Quartzite. 93

Table 3.2.2.1 – Parameter estimation of Bieniawski's sandstone loading experiments, using a simple analytical model. 105

Table 3.2.3.1 Critical stability of different pillar layouts. 110

Table 4.2.4.1 Relative P-wave and S-wave amplitudes for path 3 to 18 for varying crack-sizes. Amplitudes are relative to the elastic model which was chosen to match the P-wave amplitude of the data. 148

Table 4.2.6.1 Maximum in-stope velocity and induced tensile stress at 40 m and 200 m from the event, for different models of the fracture zone. All models use the same event. Values are given as a ratio to that of an unfractured model. (B) is the unfractured model. (E) Horizontal fractures parallel to the stope and extending across the same area as the stope. (F) Smaller, random horizontal fractures. (G) Random vertical fractures (H) A reduced modulus in a zone around the stope. 158

Table 4.3.1.1 Comparison between different codes and grid schemes, for memory and run-times required to obtain the equivalent dispersion accuracy as shown in Figure 4.3.1.1. Values are relative to that of a 4^{th} order staggered mesh with 2 metre grid-spacing. 170

List of contracted Enabling Outputs

No	Enabling Output	Pages
1	**Devise and perform experiments to study the time-dependent response and associated damage mechanisms in rock.**	1
1.1	A compilation of experimental data of time dependent damage using acoustic emission monitoring techniques.	1
1.2	Formulation of theories and mechanisms of time dependent damage and their application to mining rate strategies using underground and experimental observations.	1
1.3	Quantification of statistical uncertainty in time to failure and the stope stress environment.	1
2	**Assess existing size effect theories and formulate computational methods to represent the mechanisms of failure at different size scales in two and three dimensions.**	1
2.1	A review of theories of size effect.	1
2.2	Experimental data to understand size effects in computational methods.	1
3	**Quantify the mechanisms of seismic wave transmission through fractured rock by numerical and physical experiments.**	1
3.1	An understanding of the mechanisms of seismic wave interaction with underground openings.	1
3.2	Experimental techniques for the study of the interaction of seismic waves with fracture assemblies.	1
3.3	Numerical tools for investigating seismic wave interactions with openings and for assessing the formulation of design strategies under uncertain loading and material response.	1
3.4	Computational models for representing dynamic blast induced fracture propagation.	1

1.0 Introduction and methodology

This section provides a brief introduction and outline of the methodology used to carry out project GAP601b. Descriptions of the work performed and the main results are discussed in detail in sections 2 to 4 of this report.

Investigations into fundamental aspects of rock mass behaviour have been supported through the successive SIMRAC research projects GAP029, GAP332 and GAP601b. The primary motivation for this research effort has been to establish guidance for the effective design of layout sequences, assistance in support design and the evaluation of different mining strategies through improved understanding of the mechanics of the rock mass surrounding deep level excavations. In order to carry out this programme considerable use has been made of laboratory experimentation, underground observations and the development of numerical tools to assist the interpretation of observations and to enable quantitative projections of expected behaviour.

Projects GAP029 and GAP332, carried out mainly over the period of six years from 1993 to 1998, provided detailed information relating to the formation of the stope fracture zone, fundamentals of elastodynamic wave behaviour and, most importantly, the quantification of time dependent stope closure effects. Explicit simulations of the progressive formation of the stope fracture zone have demonstrated how slip and undulations on parting planes influence fracturing ahead of the stope face and how these mechanisms enhance closure in the back area. In addition, the influence of the regional stress field orientation on fracture orientations has been modelled and confirmed qualitatively in underground field observations. Extensive underground observations have revealed the utility of employing continuous measurements of stope closure to quantify the characteristic response of different geotechnical environments and to explore possible changes in stope face stability as mining proceeds. This work is directly relevant in quantifying the understanding of the effects of changing the stope face advance rate, the introduction of continuous mining compared to drill and blast operations and the consequences of stope face preconditioning.

Motivated by the practical importance of these applications, laboratory studies of time dependent rock behaviour have been continued in Project GAP601b by performing extensive additional experiments to quantify the time to failure response of different rock samples subjected to compressive loads. Other experiments have been performed to examine the stress relaxation rate for confined samples subjected to load controlled displacements in the post-

failure state. Further experiments have also been carried out to quantify the time dependent shear behaviour of natural and gouge-filled rock joints.

At the same time it has become increasingly apparent that a purely deterministic description of stope-scale rock mass behaviour is, in many respects, inappropriate in the formulation of excavation design and mining strategies. The most pressing problems confronting underground workers and rock engineering practitioners are the occurrence of unexpected seismic activity, face bursting and rock falls. The development of random mesh discontinuity models (tessellation models) together with the implementation of time dependent discontinuity creep behaviour, has provided a means of simulating this behaviour. The modelling of time to failure is a basic requirement in assessing the potential for violent rock failure and for discovering if any precursory measures can be used for predicting incipient failure. Some effort is made in Project GAP601b to investigate the circumstances in which precursory effects can be used effectively and situations in which future behaviour is inherently unpredictable. The interpretation of the face region “stiffness” and quantification of the fracture zone structural stability are examined briefly.

Linked to the question of time to failure and stability is the effect of scale in determining the behaviour of quasi-brittle materials such as rock. At present no clear rules exist to extrapolate laboratory scale effects to the field scale. In the present work, acoustic emission signals observed in a laboratory scale loading experiment are compared to larger scale mine seismic activity and earthquake observations to assess whether standard seismological measures and frequency-magnitude scaling can be uniformly applied. In addition, considerable effort has been made to extend the DIGS/IDA code to include slip weakening and tension weakening behaviour to enable scale dependent effects to be represented and evaluated and to reduce artificial dependence of the numerical results on the choice of the model grid size.

Most computer tools that are used for studies of rock failure assume that this behaviour occurs in plane strain. Some attention has been given to develop an initial capability to analyse problems of three-dimensional failure, relating to lead-lag panel fracturing. Calibration of these computer codes is difficult and a number of three-dimensional laboratory experiments are described in the report to study the formation of fractures near representative “stope face” lead-lag and “pillar” stress-raising configurations. X-ray techniques are used to map internal fracture positions in these experiments.

A key component to the assessment and evaluation of rock mass behaviour near deep level openings is the ability to be able to model wave propagation effects. Extensive photo-elastic laboratory experiments have been carried out previously in projects GAP029 and GAP332 and

have revealed important interaction mechanisms between stress waves and slot-shaped openings. These studies demonstrated wave trapping due to parting plane layers as well as surface wave effects. Project GAP601b has sought to extend this work by analysing observations from a field scale experiment of a simulated rock burst as well as detailed wave propagation studies carried out near the surface of an experimental tunnel. Particular emphasis is given to quantifying the effects of excavation surfaces and fracture assemblies on the amplification of rock velocities at the surfaces of underground openings. Limitations of current tools that are available for the simulation of wave propagation effects are discussed. This work forms a major output of Project GAP601b.

2.0 Experiments and modelling of time-dependent damage mechanisms in rock and near mine openings

2.1 Laboratory experiments of time-dependent rock discontinuity and rock mass behaviour

2.1.1 Mechanisms of time dependent deformation in hard rocks

Closure measurements in South African mines show definite time-dependant behaviour (Malan, 1998). Time dependant deformation in hard rocks consists of at least three components: (1) compression creep of the intact rock, (2) shear creep on discontinuities and (3) post-failure relaxation of rock material (Malan and Drescher, 2000). Understanding the mechanisms of time-dependant behaviour of hard rocks is of great importance when describing the response of the stope face fracture zone and the consequent implications of changes to the mining rate and mining method.

Mining induced seismic events (e.g. rock burst) are linked to rheological processes in the rock mass and do not always occur immediately after the blast. Malan (1998) has shown that closure in stopes continues to take place long after the blast. It appears that time dependent closure is related to both time dependent failure in the rock and to “creep” on joints and discontinuities in the stope fracture zone. The testing undertaken in this study is intended to help quantify the various time-dependant deformation processes around typical deep level hard rock tabular excavations. Quantification of the time-dependent deformations provides essential information for the development of numerical models of the behaviour of the stope face.

Several uniaxial compression creep experiments appear in the literature, such as those described by Price (1964) or Singh (1975). However, most of these studies were carried out using material that can be regarded as relatively weak and soft compared to the rocks in deep South African gold mines. For example, rocks such as shale (with a strength of < 50 MPa), sandstone (with a UCS of 50-100 MPa) and even marble (UCS ranges from 100-150 MPa) are relatively soft compared to the Witwatersrand quartzite (100 to 250 MPa) or the Ventersdorp lava (400 to 600 MPa), which are encountered in the deep mines. Most of the studies on uniaxial compression creep report only the strain-time data for the axial deformation and do not mention the lateral deformation.

In terms of creep testing on discontinuities very little information is found in the literature. Cylindrical tests specimens containing a discontinuity were tested in triaxial compression by Wawersik (1974). In these tests, conducted on Westerly granite, the discontinuity was inclined at 30° relative to the direction of the principal stress. Amadei (1979) proposed that the shear creep of a joint would be governed by the ratio of applied shear stress to peak shear strength. Schwartz and Kolluru (1984) studied the behaviour of synthetic rock material (consisting of a gypsum plaster mix) to test the hypothesis of Amadei. Bowden and Curran (1984) also carried out tests on artificial discontinuities prepared from shale. Malan (1998) and Malan, Drescher and Vogler (1998) preformed more elaborate testing to investigate the shear creep of discontinuities, which are commonly encountered in typical South-African deep mines. Shear creep experiments were performed on natural joints with natural gouge and artificial joints with artificial gouge (crushed rock).

As far as the relaxation of failed rock is concerned, studies are limited to the relaxation of failed rock under uniaxial compression. Hudson and Brown (1973) investigated the load relaxation of failed rock when the axial deformation was kept constant after the failure of a specimen. Apart from Malan and Drescher (2000) it appears as if relaxation measurements during post-failure triaxial compressive strength tests have not been attempted previously.

A conceptual model of the stope fracture zone has been developed and a version, after Gay and Jager (1986) is shown in Figure 2.1.1.1. The time-dependant response of a stope at great depth can therefore be understood by performing three different types of test.

- The time-dependent deformation of the intact rock ahead of the face can be approximated by the results of uniaxial compression creep tests.
- Triaxial post failure testing provides insight into the stress-relaxation behaviour of the failed rock just ahead of the face. The mining rate can play an important role here: If the mining rate is faster than the relaxation of the failed rock the stress just ahead of the face increases. During the triaxial post failure relaxation tests, it was noted that the specimens appear to be very unstable in the post-failure region if the post failure stress level is close to the failure strength. If the mining rate is such that the stress ahead of the face moves into the unstable post-failure stress region, there is a good possibility that a rock burst can occur.
- The time dependent, shear displacement on discontinuities surrounding the stope can be studied using shear creep tests on discontinuities. The effect of moisture content on creep rate was also investigated, but other important factors such as the frequency of the discontinuities and their orientation could not be studied in the available test configurations.

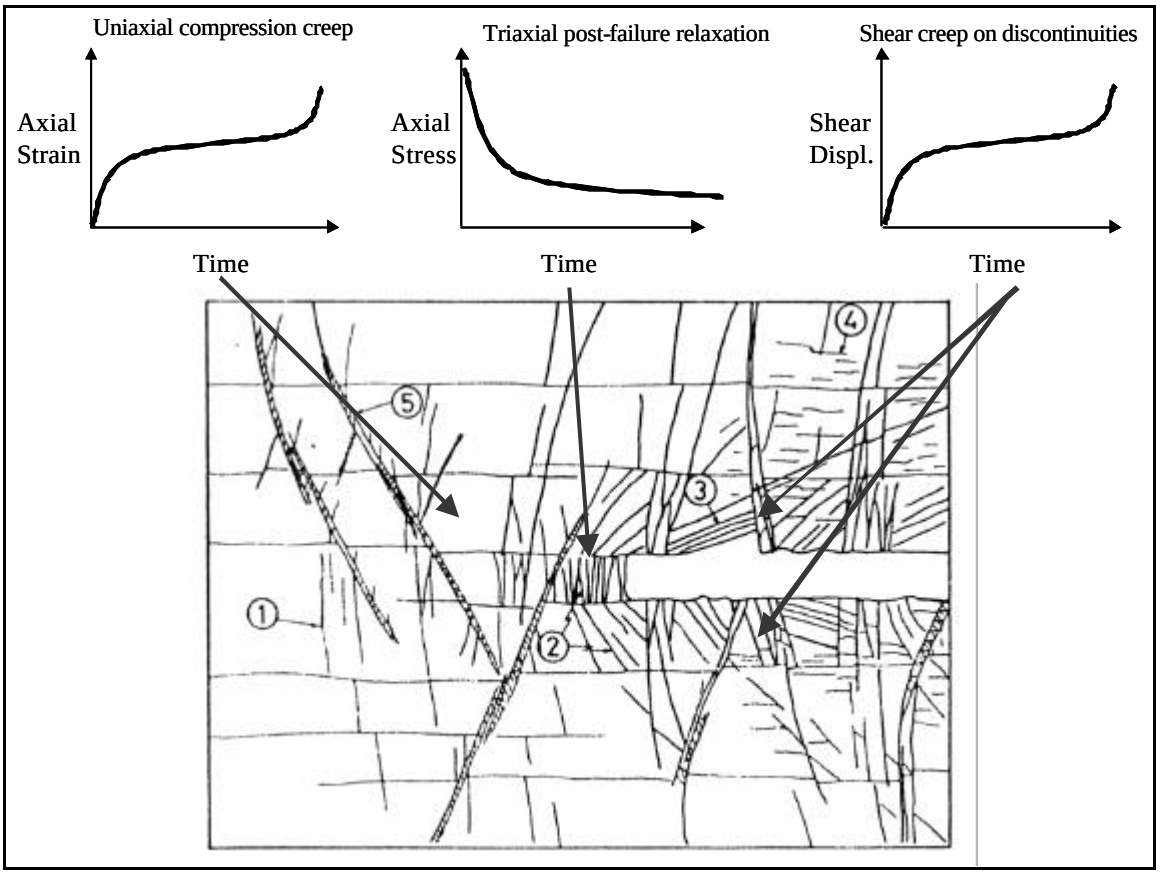

Figure 2.1.1.1 Application of the tests results to the stope fracture model

The first objective of this study was to obtain more strain-time data (axial and lateral strain) under uniaxial compression for Elsburg quartzite and Ventersdorp lava (typical South African hard rocks). The second objective was to gain insight into how the geological environment altered the time-dependant behaviour of discontinuities. This was achieved by performing direct shear creep tests using crushed Elsburg quartzite and Ventersdorp lava as well as natural gouge as infilling. The crushed rock simulates the infilling on recent, mining induced fractures for comparison with the natural gouge that would have formed and been altered over geological time scales. The third objective was to studying the axial stress relaxation of failed rock under triaxial compression and to try to gain further understanding of the response of the stope fracture zone, ahead of the excavation. All these processes have been quantified by the tests described, which have provided the first data available for energy change calculations in fractured rock masses. The tests and results have been described in more detail by Drescher (2002)

The static uniaxial creep tests were performed using the CSIR creep-testing machine, originally used by Bieniawski (1967). The data acquisition system has been modified to include a computerized data logger. The system is fitted with an uninterruptible power supply unit. The machine is housed in a special climate controlled laboratory, where the temperature is kept constant at 20±0.5°C and the relative humidity is maintained at 50±2%. This is done to eliminate any effect temperature and moisture fluctuation might have on either the specimen or the equipment. A photograph of the testing machine is shown in Figure 2.1.1.2. Specimens are loaded mechanically by weights and the load is enhanced by a system of two cantilever beams each with a 7:1 loading ratio, which gives an overall loading ratio of 49:1. The specimen set-up is as shown in Figure 2.1.1.2. LVDT's (Linear Voltage Differential Transformer) are used alongside the axial strain gauges to measure axial strain. This is done to confirm that the axial strain (especially creep strain) measured by the strain gauges is in fact the deformation of the rock and not the time dependant behaviour of the strain gauges. The strain gauge readings are usually more accurate than the LVDT readings, and are thus used for evaluation. The LVDT's are also used as a trigger for the data logging. Data points are typically taken every 2 hours during the secondary creep phase. The data logger will be triggered (by the LVDT's, in 20 microstrain increments) to take readings more often if the strain rate accelerates suddenly. Hence tertiary creep can also be captured by the system just before the specimen fails.

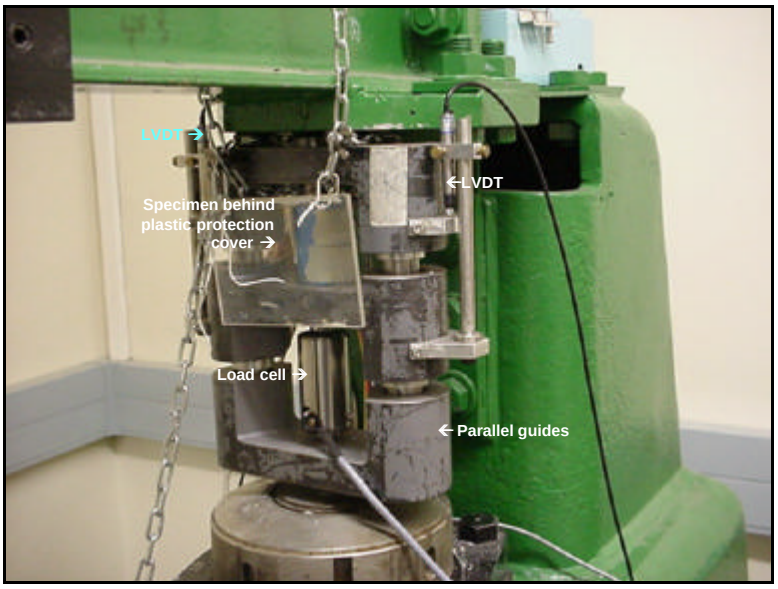

Figure 2.1.1.2 Close-up view of the testing configuration for uniaxial creep tests

Creep parameters suitable for use in numerical investigations have been determined for hard rocks from the South African gold mines. It has been shown that if hard rocks are subjected to sufficient uniaxial compressive stress they do exhibit well-defined time-dependent behaviour. Significantly, quartzite and lava show similar axial and lateral creep rates when the stress is

normailsed with respect to the unconfined compression stress (i.e. at similar σ/σ_C ratios). Thus, the ratio of the applied stress to the ultimate strength determines the creep rate. As shown in Figure 2.1.1.3, the creep rate remains negligible until the stress exceeds 60% of the compression strength. When the stress exceeds 85% of the compression strength, the creep rate increases considerably.

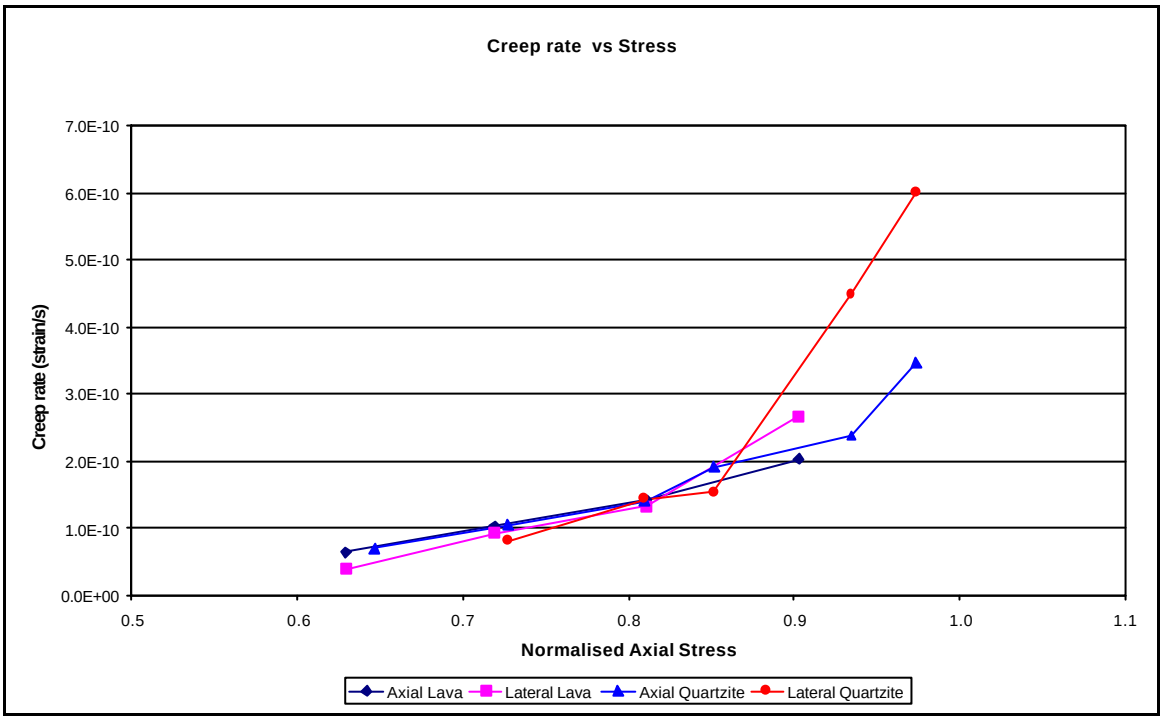

Figure 2.1.1.3 Creep rate vs normalised axial stress

However, for tabular excavations at depths of 3000m to 4000m, the stress levels will be close to the peak stress of quartzite, but will be relatively low to the strength of the lava. As shown in Figure 2.1.1.4, the axial and lateral creep rates at stress levels near the failure strength of the quartzite will be orders of magnitude greater than the axial and lateral creep rates of the lava, at the equivalent stress level.

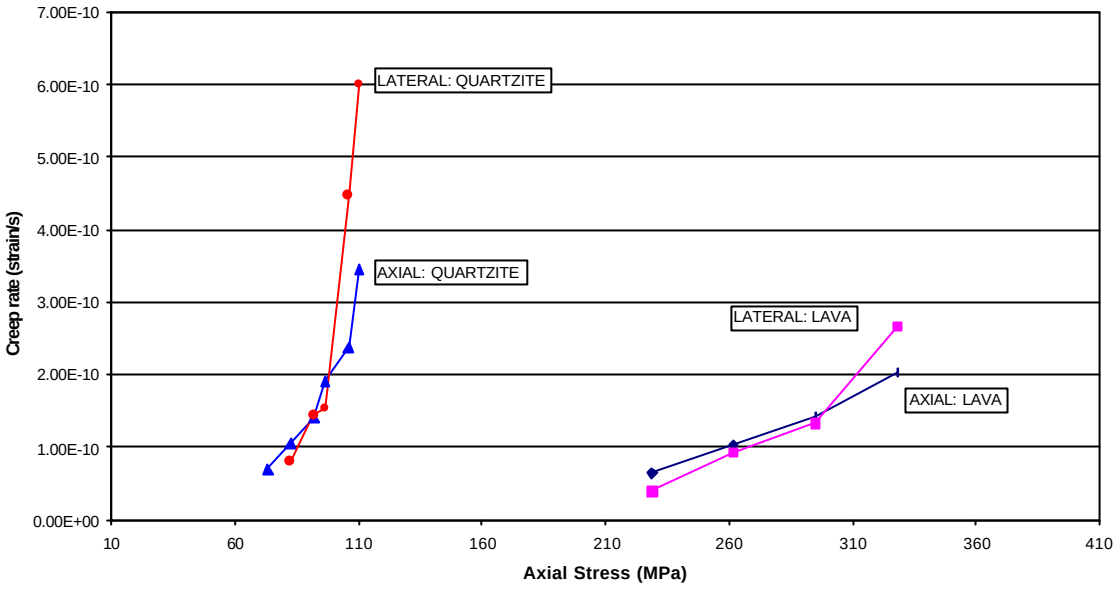

Figure 2.1.1.4 Creep rate vs axial stress

It is furthermore noteworthy that although the strength of lava is more than twice as high as that of the quartzite, the strain at failure of the lava is more than that of the quartzite. It is also evident from the results that the onset of unstable fracture propagation for lava occurs at a higher σ/σ_c ratio than for the quartzite.

Energy calculations show that the percentage energy dissipation for the quartzite is significantly more than for the lava and this is a consequence of damage. This also shows that in lava there is more energy available for violent failure than in quartzite. Hence, a rockburst in lava in perceived to be more violent than a rockburst in quartzite.

Table 2.1.1.1 Summary of compression creep test results

Spec No	Creep Strength (MPa)	% Strength	Axial Creep rate (strain/s)	Lateral Creep rate (strain/s)	Energy Dissipation (kJ/m^3)	Total Energy at % Strength (kJ/m^3)	Percentage Energy Dissipation
Lava							
1640-23	364	90	2.03E-10	2.67E-10	64.0	671.3	9.5
1640-53	435	91	3.14E-10	3.33E-10	91.8	922.7	10.0
1640-55	399	91	1.06E-10	1.44E-10	48.5	728.8	6.7
1640-63	402	91	3.36E-10	4.83E-10	102.3	799.8	12.8
Quartzite							
2056-116	118	89	1.83E-10	2.75E-10	23.4	137.1	17.1
2056-117	114	93	2.39E-10	4.47E-10	27.1	147.8	18.4
2056-118	113	91	2.72E-10	3.53E-10	26.0	143.3	18.1
2056-121	135	93	4.69E-10	9.83E-10	29.0	163.9	17.7

The shear testing equipment is described in detail by Vogler, Malan & Drescher (1998). The tests are performed in the climatically controlled laboratory with a temperature of 20±0.5°C and a relative humidity of 50±2%. The control system was modified to allow automatic adjustment of the normal and shear loads after a given time interval. Figure 2.1.1.5 shows a close-up picture of a specimen, which is set-up for testing. An identical set of LVDT's is installed on each side of the specimen. The average readings of both sets of LVDT's are used during evaluation. The shear surfaces of the quartzite blocks are cleaned with Acetone before any given test. The infilling is placed on the lower shear surface and levelled to a given thickness (for this study 0.5, 1 or 2 mm). The upper block is then placed on the infilling. The arms and weight hanger are placed on top, giving a slight normal preload. The LVDT's are brought to the starting positions and the data acquisition is started. Finally, the weights are slowly lowered and the initial normal compression of the infilling is measured. The computerized control system then controls the remainder of the test.

For the purpose of this study, tests were conducted at 50% ± 2% humidity, referred to as dry tests and water saturated (relative humidity of 100%, referred to as wet). The time interval between the different air pressure (shear stress) levels is set at 48 hours. The shear stress levels of approximately 70%, 80%, 85%, 90%, 95% and 100% of the anticipated failure strength are then applied sequentially.

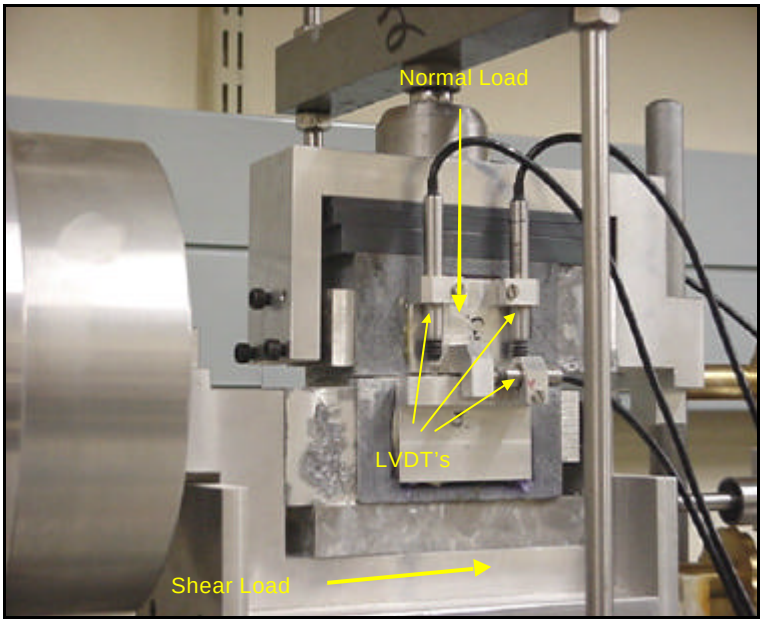

Figure 2.1.1.5 Testing configuration for direct shear

For a discontinuity that contains an infilling and is subjected to a normal stress, the application of a constant shear stress will lead to shear deformations that exhibit primary, secondary and tertiary creep phases. It proved to be rather difficult to obtain a curve showing all three creep phases. Figure 2.1.1.6 shows the increase in displacement with each load increments and demonstrates that that only primary and secondary creep phases occur for low values of the ratio of applied shear stress to peak shear stress ratio (τ/τ_s). Once the specimen approaches the point of failure, the creep curve consists of a secondary creep phase followed by the tertiary creep phase as in the test shown in Figure 2.1.1.7.

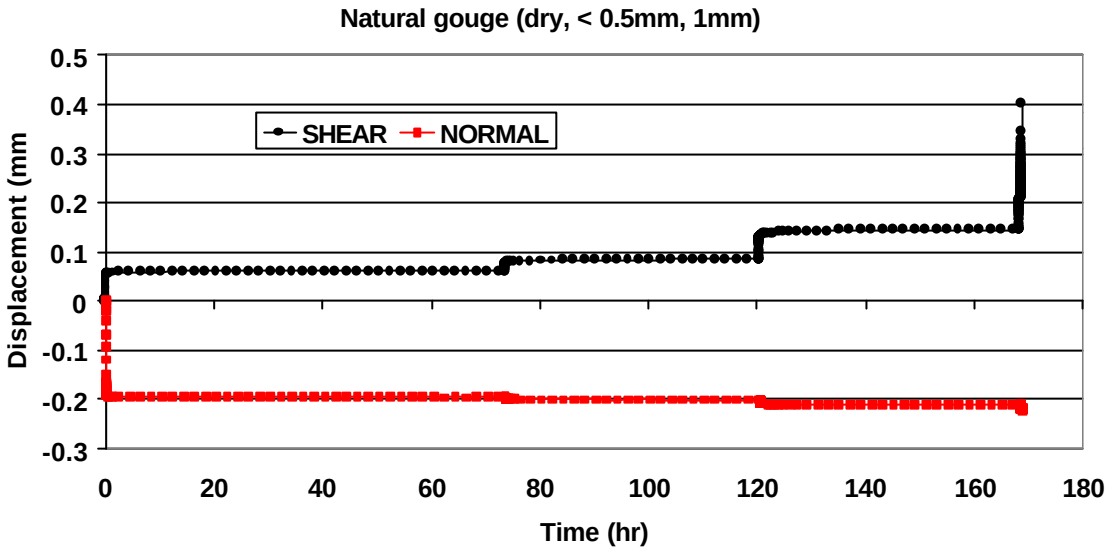

Figure 2.1.1.6 A measured displacement-time curve showing the change in shear and normal displacement during the different loading steps

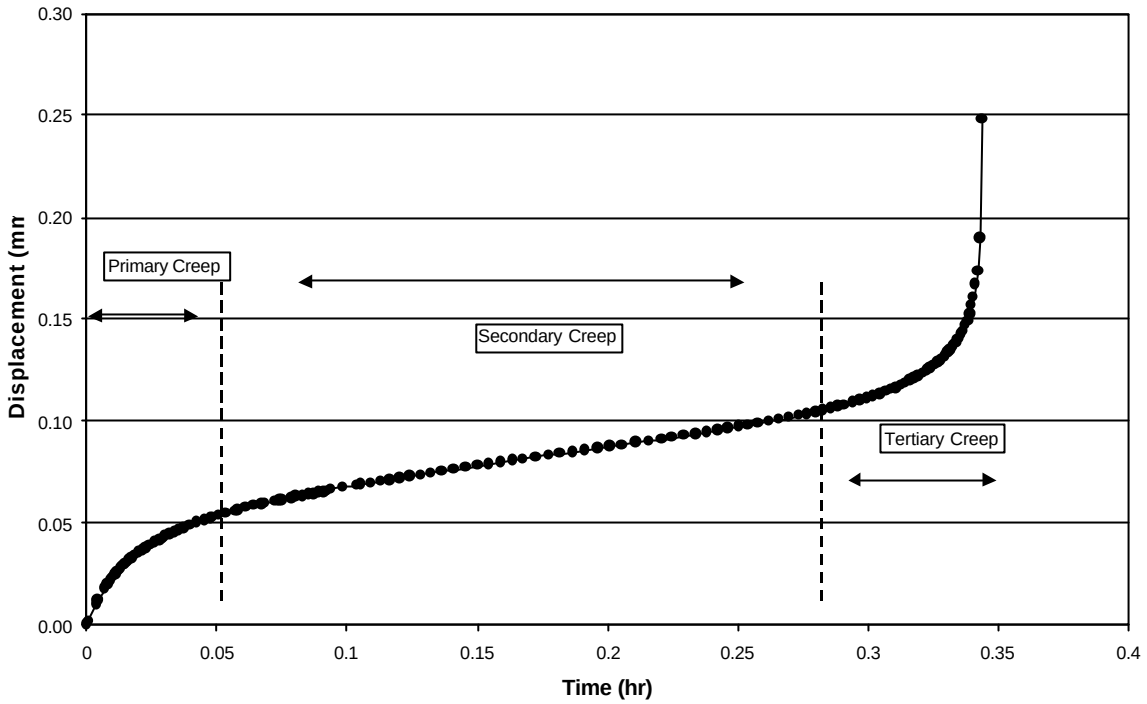

Figure 2.1.1.7 A detail of the measured shear displacement-time curve showing all three phases of creep

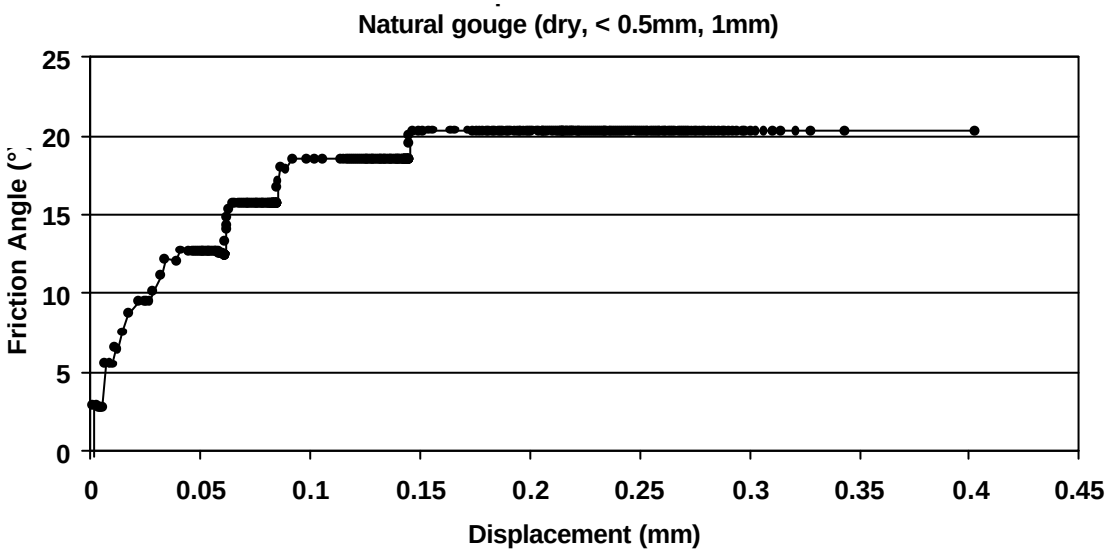

Figure 2.1.1.8 The change of friction angle with shear displacement showing the effect of the different loading steps

Figure 2.1.1.8 shows that the effective friction angle increases with each loading increment. As shown in Table 2.1.1.2 it was also determined that higher ratios of shear stress to the ultimate shear resistance lead to higher shear creep rates. There appears to be a tendency that the thicker infillings lead to higher creep rates. A numerical model that provides qualitative description of this behaviour is described in section 2.2.1.The experimental results show that

the peak shear strength of the natural gouge is significantly less than that of the crushed quartzite and crushed lava.

Table 2.1.1.2 Summary of creep shear test results

Spec. No 2056-	Thickness (mm)	t/t_s (%)	Humidity (%)	Peak Friction angle (°)	Shear Creep rate (mm/hr)	Shear Energy Dissipation (kJ/m^2)	Total Shear Energy (kJ/m^2)	Percentage Shear Energy Dissipation
Crushed Elsburg Quartzite								
CPS-143	0.5	92	50	19.5	1.53E-04	0.0036	0.0076	47.4
CPS-144	1	90	50	29.6	1.50E-04	0.018	0.025	71.7
CPS-145	2	91	50	28.2	1.60E-04	0.016	0.041	37.7
CPS-146	1	89	100	28.5	4.42E-04	0.034	0.043	81.1
Crushed Ventersdorp Lava								
CPS-162	0.5	92	50	23.1	1.21E-04	0.019	0.049	37.9
CPS-148	1	90	50	30.5	6.15E-05	0.019	0.038	55.2
CPS-149	2	89	50	30.7	4.60E-05	0.016	0.029	55.2
CPS-150	1	90	100	31.9	2.86E-04	0.033	0.050	66.6
Natural Gouge								
CPS-239	0.5	94	50	17.5	2.41E-05	0.0028	0.0056	50.0
CPS-238	1	91	50	20.3	5.69E-05	0.0086	0.016	54.6
CPS-240	2	89	50	20.8	5.81E-05	0.014	0.021	67.5
CPS-241	1	89	100	18.5	8.75E-05	0.014	0.019	72.8

Furthermore, from Table 2.1.1.2, it is evident that for all three joint infill materials, the moisture content has an influence on the amount of time-dependent shear displacement as well as the shear creep rate. More experiments are required to completely characterize this effect. The test results show that the shear creep mechanism is governed by the ratio between the thickness of the infilling and the grain size distribution of the infilling. Figure 2.1.1.9 shows that the ultimate frictional resistance of the natural gouge is much lower than the infillling manufactured from crushed quartzite or lava.

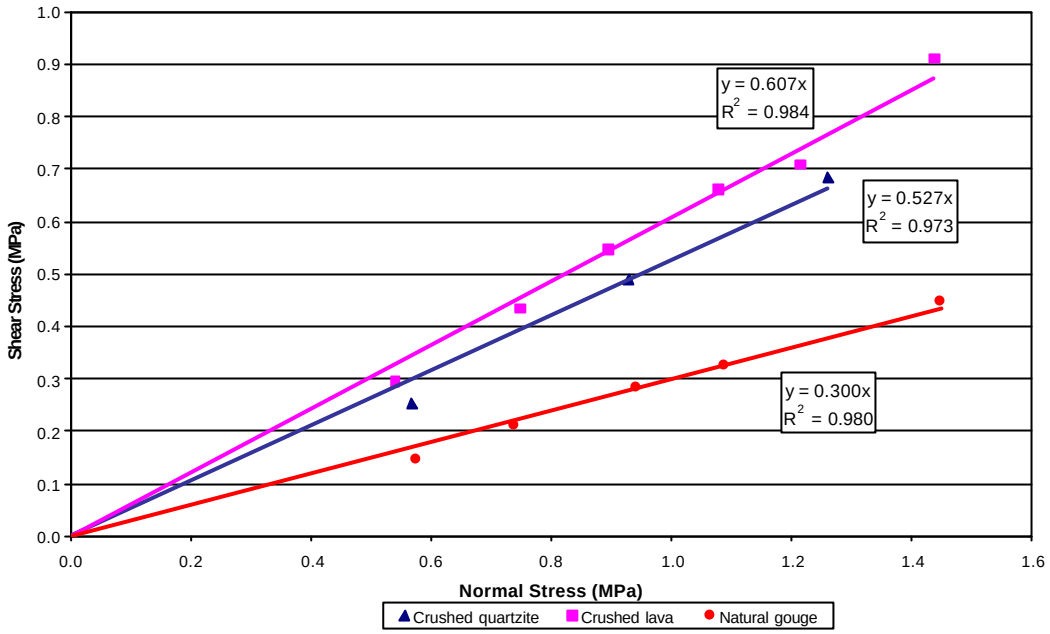

Figure 2.1.1.9 Shear stress – normal stress results for the three types of infilling

The post failure relaxation tests were performed in a MTS, Model 850 uniaxial and triaxial rock-testing machine. For this study, the confining pressure was chosen to be 40 MPa as an approximate representation of the confining stress ahead of the stope face. At the start of the test, the axial and confining stresses are increased simultaneously, in true hydrostatic conditions. When the confinement level of 40 MPa is reached, the confinement is kept constant and the axial loading switches over to circumferential strain control with a circumferential strain rate of 0.01mm/min.

When the pre-determined post-failure load-level is reached, the machine is switched to the "relaxation" control mode, during which the axial ram position as well as the confinement are kept constant (within 0.02%) for a period of 24 hours. The load, time and circumferential strain data is logged during the test. For some later tests, this testing method was extended to perform multiple relaxation steps in a single test, in which the aim was to obtain up to three post failure relaxation steps. Each of these tests took four days to complete.

The first conclusion is that the post failure relaxation time periods for hard rocks under a high confinement are orders of magnitude greater than the relaxation periods for softer rocks under uniaxial compression conditions. For mines, operating at great depth (more than 2000m) the implication is that the rock material might relax much more slowly than might have been assumed and this means that after failure the rock mass continues to store large amounts of strain energy.

Comparing the behaviour of quartzite and lava, the test results show that during the initial relaxation period of 24 hours the total stress relaxation for the failed quartzite is approximately twice that of the failed lava. The relaxation rate after the initial 24 hour period is more than three times higher for the quartizte than for the lava.

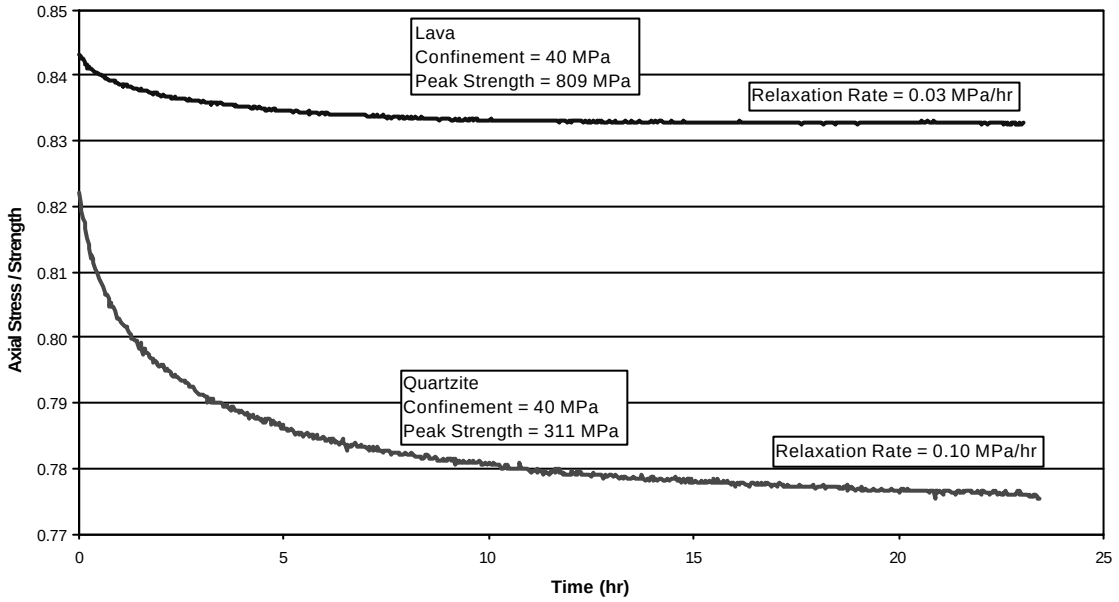

Figure 2.1.1.10 Stress/Strength-time curves for quartzite and lava

Due to the scatter of results and the time consuming nature of the tests, insufficient data has been collected to conclusively relate the relaxation rate to the ratio of stress to ultimate strength. The results are summarised in Table 2.1.1.3.The relaxation rates appear to be related to the amount of fracturing in the samples. After the tests, the quartzite shows a well-developed fracture pattern while the lava shows only a few cracks, i.e. the damage in the lava specimen is significantly more localised than the damage in the quartzite specimen.

The circumferential strain measurements associated with the post-failure relaxation show that the amount of circumferential strain for quartzite is more than for the lava (larger immediate response) while the strain rate during the 10 to 24 hr period is higher for lava than for quartzite. These trends are compatible with the observations of the axial stress relaxation.

Energy calculations show that for similar ratios of the initial stress level to the ultimate strength, (σ/σ_C post-failure) the percentage energy dissipation is significantly more for the quartzite than for the lava.

Table 2.1.1.3 Summary of triaxial post-failure relaxation test results

Specimen No	Peak Strength (MPa)	s/s_c starting point	Relaxation Rate (MPa/hr)	Energy dissipation (kJ/m^3)	Energy at start of relaxation (kJ/m^3)	Percentage Energy dissipation
Elsburg Quartzite						
2056-157-1	311	0.82	0.10	15.2	1704	0.89
2056-157-2	311	0.72	0.09	13.1	1689	0.77
2056-157-3	311	0.62	0.05	3.9	1676	0.23
Ventersdorp Lava						
2056-123	809	0.84	0.03	12.8	3834	0.33

In order to proceed further, it is necessary to develop numerical models that can represent the entire range of rock mass response as presented in the conceptual model mentioned above. Several aspects of this development are presented in the following sections.

Although this study increased the knowledge of the time-dependent behaviour of discontinuities, it is recommended that further tests on other natural infillings would be of interest. A limiting factor during this study was the normal loading capacity of the shear creep apparatus. It is also important to investigate shear creep behaviour of discontinuities at higher normal stresses. As far as triaxial post-failure testing is concerned, further post-failure relaxation tests on different materials are required to quantify a fundamental understanding of the relaxation processes. Additional tests at different confinements should also be considered.

2.1.2 Acoustic emission testing

The prediction and control of mine seismicity can be assisted significantly by the effective application of numerical analysis [e.g. *Napier, 1998, Sellers et al, 1998, Spottiswoode, 1999*]. Confidence in the application of these codes can only be established if it can be demonstrated that predicted behaviour corresponds to real rock fracture processes. The first stage in such a

verification program entails the reproduction of laboratory test behaviour with controlled loading and boundary conditions. However, for the verification process to be relevant, it must also be shown that the rock response in the laboratory test relates to the behaviour at the larger scales relevant to underground excavations. This study was undertaken to investigate the scaling of rock fracturing from small laboratory samples up to the dimensions of a mine, and even a continental plate boundary, by considering the acoustic emissions generated during the failure process to be a form of microseismicity.

Acoustic emissions are transient elastic waves resulting from crack formation in brittle materials. Valuable information, such as the location and mechanisms of microfractures that generate the waves can be extracted from these waveforms. In rock mechanics, acoustic emission (AE) has often been used as a non-destructive method to follow damage and failure [see*, e.g., Mogi, 1968; Scholz, 1968a,b; Lockner, et al., 1991; Cox and Meredith, 1993; Shah & Labuz, 1995]*. Since AE is a natural by product of brittle fracturing and microcrack growth, analysis of AE signals is well suited to studying these processes.

In order to understand the scaling of rock fracture processes, a series of uniaxial compression tests were performed on cylindrical quartzite samples having a diameter of 96mm and a length of 242 mm. Nine piezoelectric sensors were used to monitor the acoustic emissions resulting from the microcracking within the samples as the applied load was increased. In contrast to previous AE studies, the sensors were calibrated as velocity transducers. By calibrating the standard piezo-sensors, it has been possible to investigate the scaling of the fracture processes in terms of well-known seismological parameters developed to quantify mining induced seismicity and natural earthquakes.

Moment tensor solutions of eight clusters of events were obtained using a relative moment tensor method (Andersen and Spottiswoode, 2001) enabling the study of the change in fracture mechanisms throughout the test duration. The relative method removes the influence of unknown sensor coupling coefficients and path effects. As shown in Figure 2.1.2.1, it was found that early microcracking was tensile in nature and the events were distributed across the entire sample. Once the acoustic emission rate accelerated prior to failure, all events analysed were found to have double couple components, indicating that shearing was occurring.

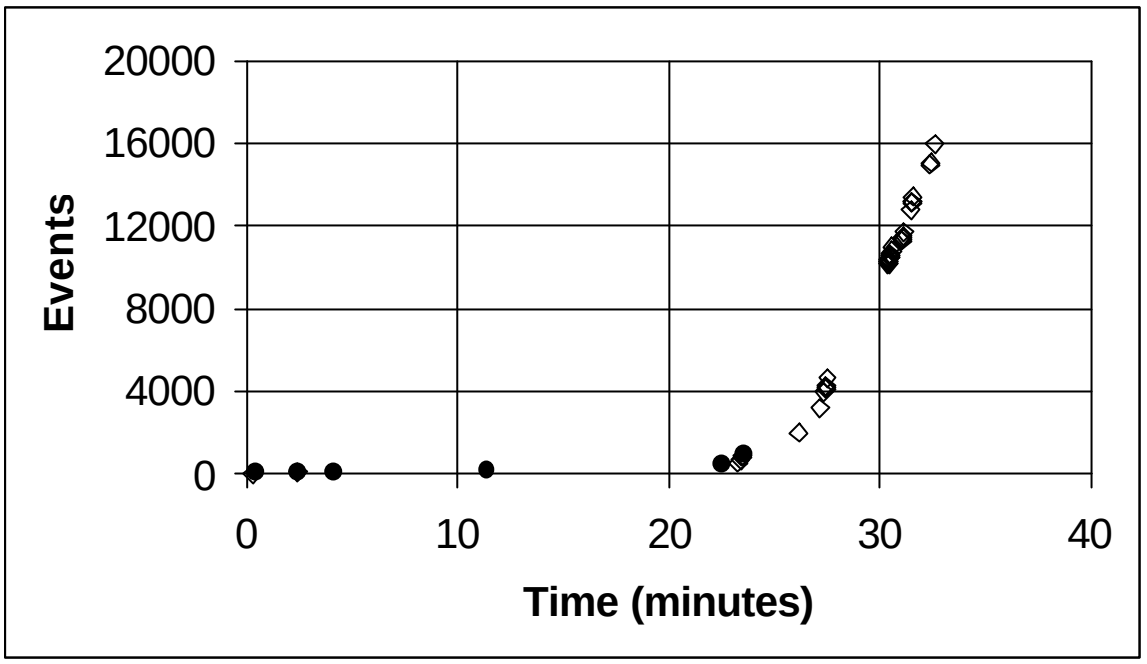

Figure 2.1.2.1 Number of acoustic emissions versus time when these events are generated. Circles represent non-double couple event (implying tensile failure) and diamond shapes represent double couples (implying shear failure).

A calibration process was followed that indicated that the spectral response of the piezoelectric AE sensors corresponded to that of a velocity transducer. The selection of a calibration factor independent of frequency enabled the velocity response of the AE sensors to be determined. The waveforms were converted into a seismic processing system that enabled the calculation of standard seismological parameters.

It was found that the magnitudes calculated using either moment or energy were similar. The apparent stress was limited to a range of between 0.01 MPa and 1 MPa observed for mine seismicity and natural earthquakes over a wide range of length scales. In addition, the stress drop was essentially independent of moment, indicating self- similarity of the fracture response.

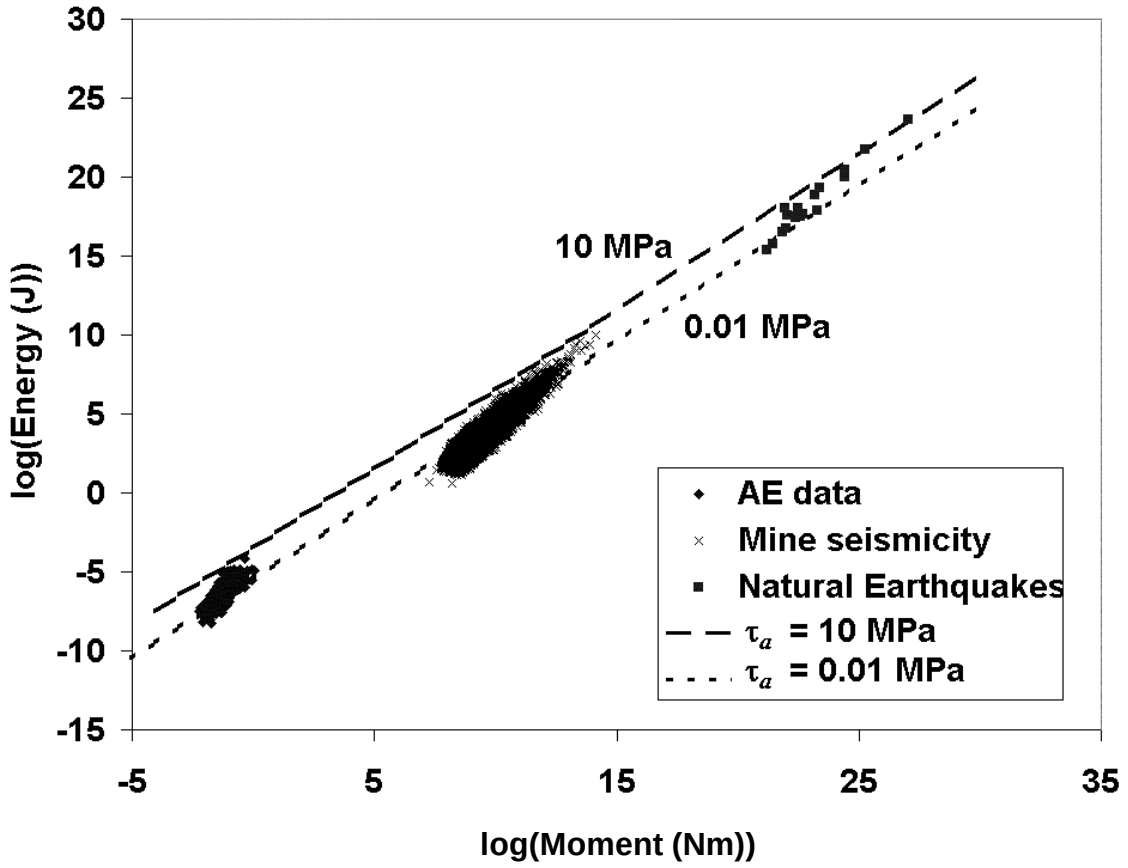

Figure 2.1.2.2. Plot of Log (Energy) versus log (Moment) for AE (represented by diamond) and mining induced events (represented by crosses), from McGarr, 1984 and Natural earthquakes, (represented by squares), from Kanamori, et. al., 1993. Dotted lines are lines of constant apparent stress.

This conclusion was confirmed by the frequency – magnitude plot (Figure 2.1.2.3) which indicated a slope of unity, corresponding well to observed mining induced seismicity from an ultra deep longwall. If the seismicity has a b-value of 1, the fractal dimension of the source should be equal to 2 implying that the events lie on a plane (Turcotte, 1992). This agrees with failure on a localized shear plane as observed in the tests. The peak velocity (Figure 2.1.2.4) and ground motion parameters also indicated self-similar scaling with the observations from larger scales.

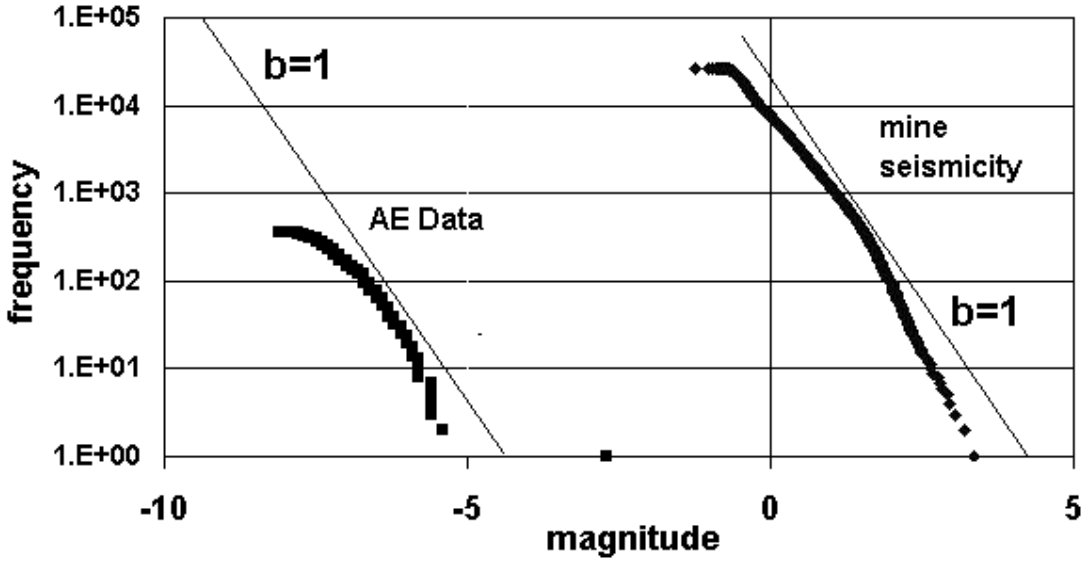

Figure 2.1.2.3. Frequency magnitude relationship plot for acoustic emission and mine data from McGarr (1993).

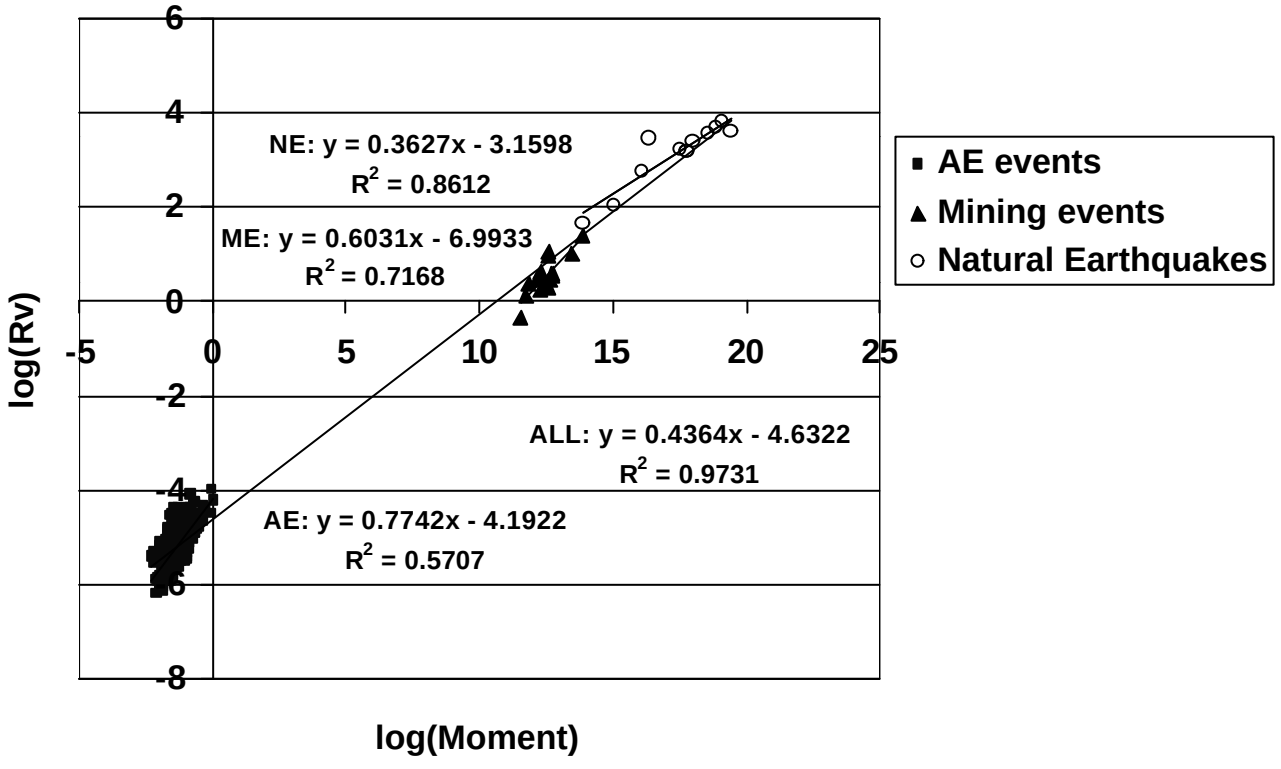

Figure 2.1.2.4 Peak ground velocity versus moment. Filled squares represent AE, triangles represent mine events and circles represent natural earthquakes (mine and earthquake data from McGarr (1993)).

Acoustic emission in tests on rock samples have been previously recognised to have amplitude -frequency characteristics similar to those of earthquakes. In this study, it has been observed that a frequency magnitude relationship holds with a b-value close to unity. These results are similar to those observed from mining induced events and provide objective evidence that rock fracture processes observed in the laboratory are relevant to the understanding of mining induced fracturing and seismicity. Further research should concentrate on samples that contain slots to simulate mine excavations. Some authors have suggested that earthquake self-similarity can break down at very small magnitudes. This study seems to suggest that self-similarity still holds for very small magnitudes and that the AE processes on a localised fracture plane scale in a similar way to mining induced earthquakes and natural earthquakes.

The monitoring of acoustic emission can provide considerable information regarding the micro failure processes occurring during testing. Acoustic events are emitted during the process of crack development and monitoring the number of events during a test can help to link the observed stress – strain response with the development of damage in the material. Some of the uniaxial compression creep tests on Elsburg Quartzite, described in section 2.1.1, were monitored using two acoustic emission transducers. A sample of quartzite 19mm in diameter and 38mm long was placed into the creep test rig and loaded. The load was increased in stages every 24 or 48 hours. The acoustic emissions were monitored with two piezoelectric sensors glued to the sample with cyano-acrylate gel glue. The sensors had a frequency range from 100 kHz to 1000kHz. Calculations using the Brune (1970) model for seismic sources suggest that cracks of radii between 0.1mm and 10mm were recorded.

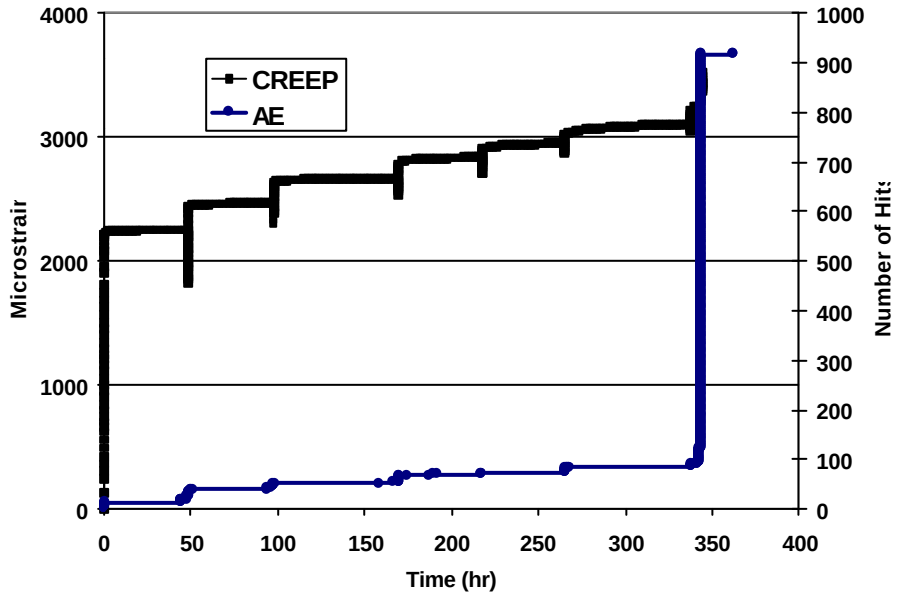

Figure 2.1.2.5 Test of sample 201 showing creep strain and acoustic emission counts

The test shown in Figure 2.1.2.5 exhibits increased acoustic emission activity as successive load increments are imposed on the sample. Very little creep deformation occurs in the first four loading stages, but the creep rate increases closer to failure. Even at high load levels, very little acoustic emission is evident during the creep phase between load increments. The ultimate failure is accompanied by a significant increase in acoustic emission. Another test, also using Elsburg quartzite, is shown in Figure 2.1.2.6 and indicated more acoustic emission activity during the earlier creep phases. This suggests that the creep of intact rock is not completely aseismic and that the creep deformation is associated with the formation of additional microcracks or with sporadic mobilization of asperities on slip interfaces. These results can be compared to numerical simulations of time to failure described in section 2.3.1. It is of interest to note that the numerical simulations display qualitatively similar behaviour to the AE hit rate (see for example Figure 2.3.1.1a).

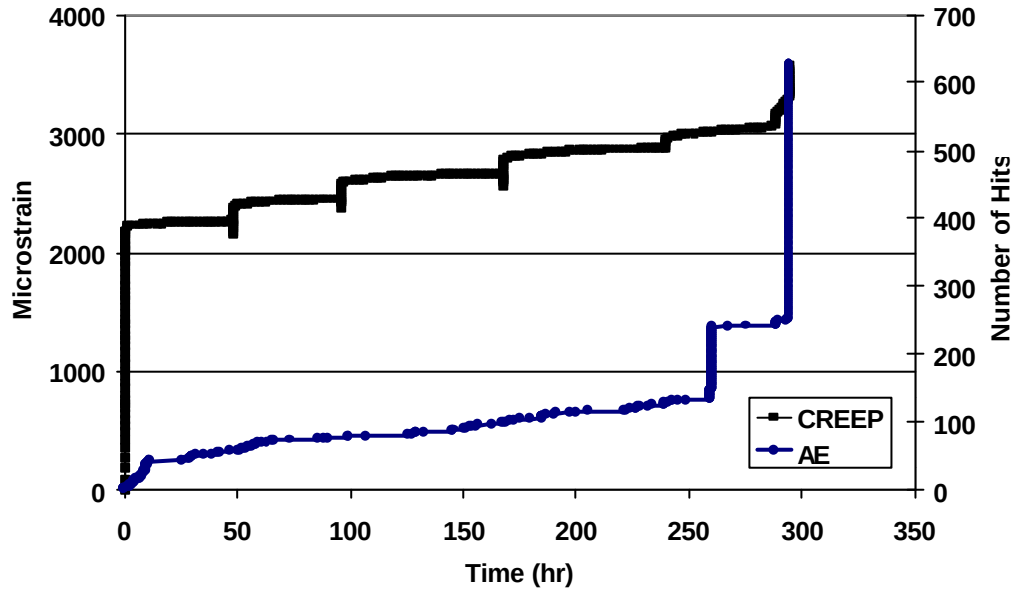

Figure 2.1.2.6 Test data for sample 115 showing creep strain and acoustic emission counts

A series of tests were conducted in the MTS testing machine at the University of the Witwatersrand to determine the relationship between acoustic emissions and the post failure response of rock under triaxial conditions. Most acoustic emission testing is carried out in uniaxial compression due to the relative ease of applying the sensors to the samples. In triaxial testing, the confinement is applied using oil in a confining pressure chamber. Special sensors that can withstand the oil pressure of 40 MPa and are unaffected by the oil of the confining medium were employed in these tests. The sensor wires were modified so that the signals could be brought through the waterproof electrical connections in the base of the cell. Prior to testing two sensors were glued to the Teflon jacket surrounding the sample using cyano-acrylate glue.

Sensors could not be placed directly onto the sample, as the jacket material could not stretch sufficiently. As shown in Figure 2.1.2.7a, the axial stress, axial deformation and radial deformation were monitored and the MTS data acquisition system was linked to the MISTRAS acoustic emission data acquisition unit so that the AE could be correlated with the stress-strain response.

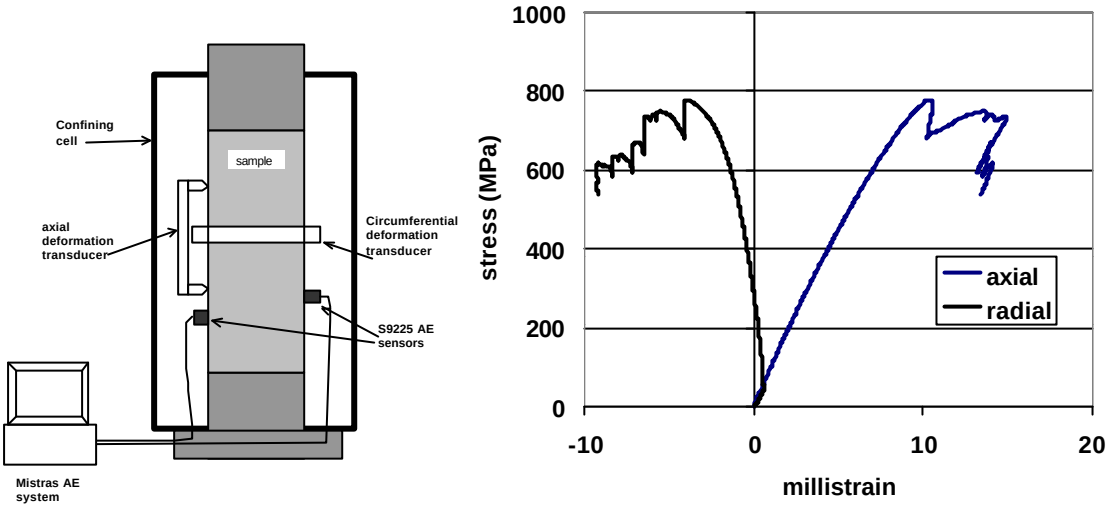

Figure 2.1.2.7 a) Test set up and b) typical stress – strain curves for post failure test with acoustic emission monitoring

The stress strain response of the Elsburg quartzite is shown in Figure 2.1.2.7b. The loading rate was controlled by adjusting the radial strain to emulate a stiff loading system. The ultimate strength of the sample, at a confinement of 40 MPa, was 780 MPa. The axial stress dropped by about 50MPa immediately after the ultimate stress was attained. This was followed by a complex series of load increases and decreases until the point of final failure.

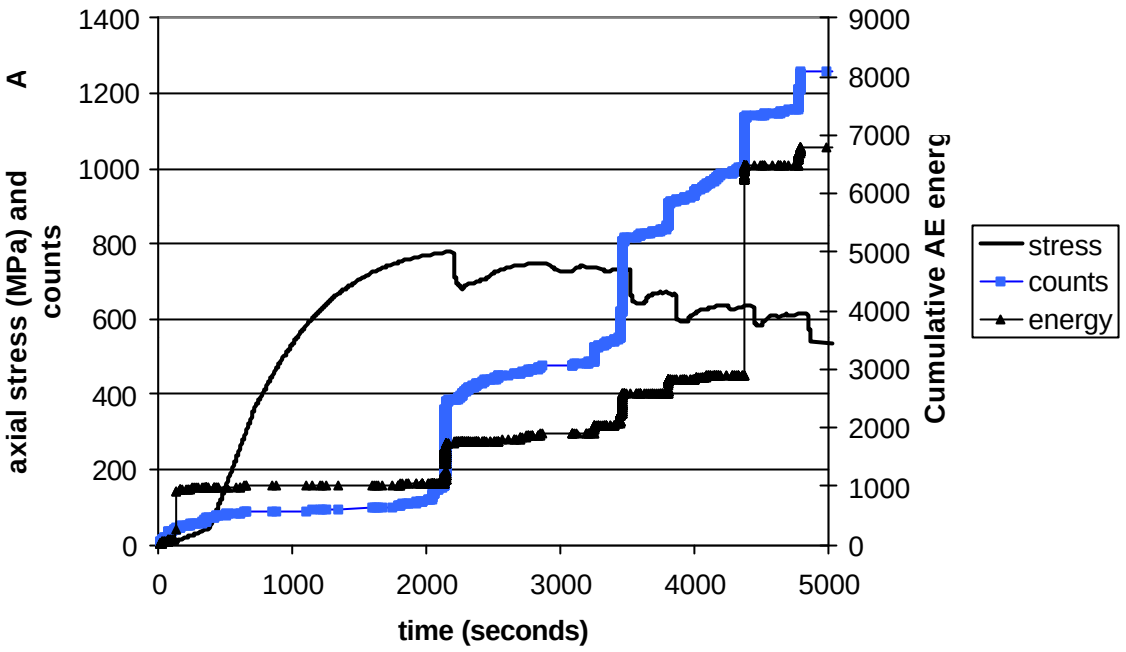

Figure 2.1.2.8 Test data showing stress, AE count and AE energy with time

The stress – time curve is shown in Figure 2.1.2.8 along with the cumulative number of AE counts and the cumulative AE energy. Each stress drop is accompanied by an increase in the number of AE events and the AE energy. It appears that an increase in the cumulative number of events occurs prior to the initial stress drop, but the possibility of small differences in timing between the load and the AE measurement systems means that this cannot be conclusively determined. The number of AE emissions and the AE energy are fairly well correlated. There does not seem to be a well-defined relationship between the magnitude of the stress drop and the AE counts or energy.

2.1.3 Cube sample tests and X-ray scanning

Understanding of three-dimensional fracture processes around deep level gold mines is important in order to be able to predict the rock mass response to planned excavation shapes and to quantify the implications of layout sequencing in the formation of stabilising pillars and the effects of panel lead-lag distances. One of the challenges in this regard is the development of numerical models for representing rock failure phenomena so that the future stability of a mine excavation can be accurately predicted. Selection of the correct models and verification of the material parameters can best be done by comparison with specific experiments conducted under controlled conditions. X-ray computerized tomography has proved to be an ideal method

for obtaining a view into rock test samples and to provide a digital reconstruction of the fracture pattern formed in response to loads applied to the samples.

A set of experiments were performed to create stress induced fractures that could serve as verification examples for three-dimensional numerical models that are being developed to analyse the fracture processes around mine excavations. The aim of the experimental program was to design tests that would be relevant for learning more about the fracturing around the mine layouts to be studied. The experimental configuration consisted of cubic samples that were tested under poly-axial stress states. Slots cut into the samples simulate the tabular characteristics of mine openings in deep gold mines. By creating configurations that have some similarity with mining layouts, the study of the experimental results also provided an additional understanding of mining induced rock fracture processes.

The experiments proved to be very successful for creating 3D fracture patterns, however, it was obvious that there were significant variations of the fracture surfaces within the sample that could not be determined from visual study of the block surfaces. The fracture traces on the sample provide an indication of the paths of the fracture planes, but cannot provide detailed information about the shape and extent of fracturing within the sample. The conventional method for obtaining three dimensional views is to section the sample at regular intervals, but this method is destructive, time consuming and still does not give a complete picture of the fracturing. Medical x-ray computerised tomography was successfully applied to reconstruct a digital representation of the three-dimensional fracture. The details of the theory of CT x-ray scanning and applications to geo-materials are presented elsewhere (e.g. Verhelst et al, 1995, Keller, 1998, Van Geet, 2001) and are not repeated here. Visualisation software was written based on standard visualisation techniques (Schroeder et al., 1997). The scanned images were imported into specially developed software that provides an interactive graphical method for studying the scan in three orthogonal planes, simultaneously. Further software developments were implemented to contour a particular density threshold and so to produce a three-dimensional image of the fracture surface. Some artefacts in the reconstruction of the image (Verhelst, 1995, Van Geet, 2001) lead to the limitation that only fractures within the central (60 %) region of the block can be automatically processed. A manual digitising method was developed to add other fractures to the automatically generated planes.

The three dimensional fracture images shown in Figures 2.1.3.1 to 2.1.2.3 demonstrate the insight that can be obtained when viewing a digital reconstruction of the entire fracture pattern. A series of samples were prepared to investigate the three dimensional nature of fracturing around the lead-lag layout of tabular stopes. The blocks were cut in half and the lower surface was ground down to simulate the tabular excavation. The shape of the excavation in plan is

equivalent to two mining panels, with one panel lagging behind the other by a distance that was varied between samples. Figure 2.1.3.1 shows the fracture pattern observed in the sample with a lag of 20mm. The figure shows that the fracture surface follows the edge of the slot in the centre of the sample. Further into the “hangingwall” and “footwall”, the surface becomes s-shaped. Similarly, for the sample with a 10mm lag (Figure 2.1.3.2), the sharp edge of the slot initiates the fracture, which gradually transforms into a curved surface. Figure 2.1.3.2 also illustrates how the fracture curves below the leading panel, especially in the region adjacent to the other panel. In the underground situation, this would represent a great hazard. Due to the relatively low dip of the fracture at this point, the process of fracture formation and any subsequent slip displacement in this region would transmit seismic waves directly upwards at the edge of the panel and the gully with a consequent risk of injury or loss of life**.**

Figure 2.1.3.3 shows the more regular of the fractures when there is no lag between the panels. The fractures are reconstructed especially well in the Marble Bar quartzite. The slot in the sample does not close in this very stiff rock and the fractures form above and below the excavation. Tensile fractures form behind the curved fracture surface. These are related to the finite boundaries of the experimental set up. The “hangingwall” and “footwall” form cantilevers that bend towards the open slot, inducing tensile stresses at top and bottom surfaces of the block and driving the fractures towards the centre of the block. The automatic algorithm used to analyse the x-ray scan data identified only one of the two observed tensile fractures. Studies of the various threshold values for the CT number indicated that attenuation artefacts due to beam hardening are present within the sample. These have been recognised previously (Verhelst, 1995, Van Geet, 2001). Algorithms have been developed to remove these artefacts, but have not yet been implemented.

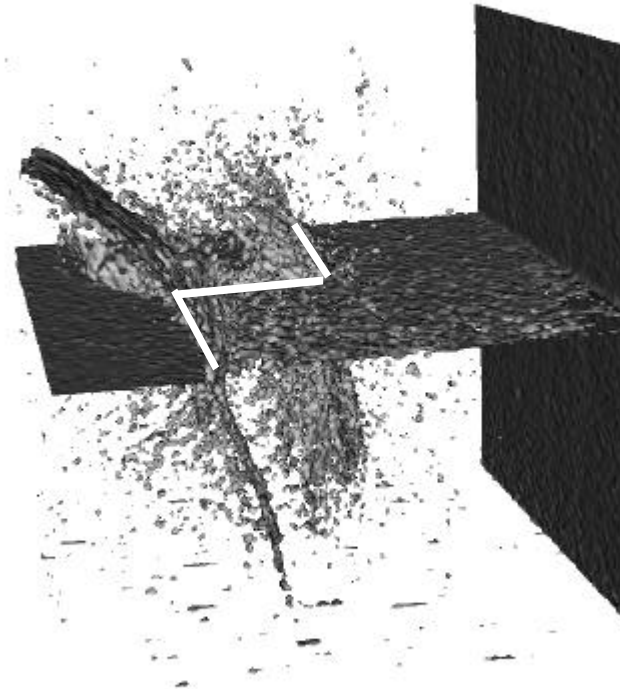

Figure 2.1.3.1. Three-dimensional reconstruction of the fracture pattern in an Elsburg quartzite block with a lead-lag of 20mm. The superimposed white lines denote the lead-lag panel layout.

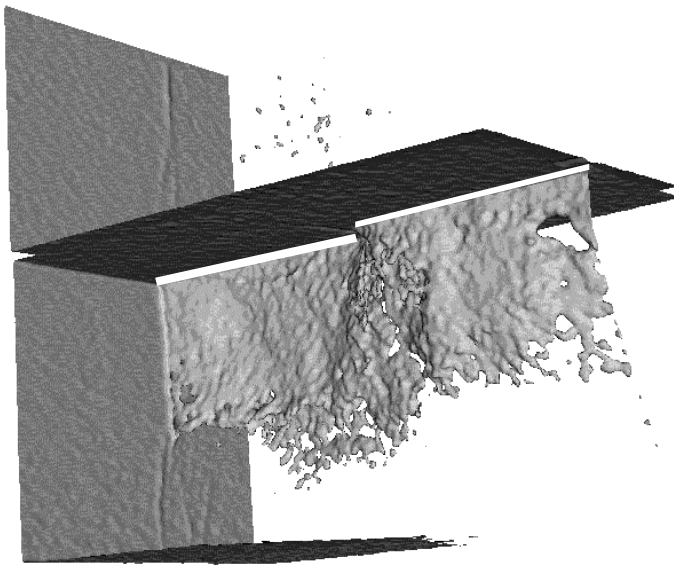

Figure 2.1.3.2. Three-dimensional reconstruction of the fracture pattern in an Elsburg quartzite block with a lead-lag of 10mm. The superimposed white lines denote the lead-lag panel layout.

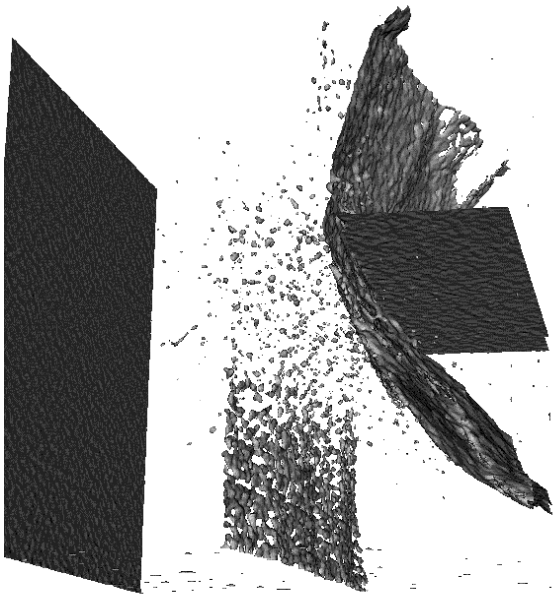

Figure 2.1.3.3. Three-dimensional reconstruction of the fracture pattern in a Marble Bar quartzite block with no lag.

An alternative method of determining the fracture traces was developed. The interactive viewer was modified to be able to plot both the automatic reconstruction and the planes obtained from manual delineation. Combining both methods provides additional possibilities for representing the entire fracture surface, or for adding features such as other heterogeneities that can be observed in the scan, but not included in the isosurface contour.

The reconstructed image can be viewed from many angles and can be compared visually with fracture patterns predicted by numerical models or acoustic emission event locations. Analysis of the images has suggested that the lag between the faces results in considerable distortions in the fracture surface between two panels. This information is valuable for focussing underground studies that can be used to confirm the effect of mining geometry on fracture formation.

2.1.4 Underground observations and the effect of mining rate on support design

As falls of ground are the cause of more than half the rock-related fatalities underground, it is vital that the mechanisms of these falls are investigated in more detail. Of particular interest here is the time-dependent unravelling of the hangingwall and the effect of mining rate on the occurrence of falls of ground. These particular topics have not been addressed in earlier research projects, even though some authors like Arnold (1995) noted that “increased rates of face advance, brought about by concentrated mining methods, which were being introduced at the time, decreased the time- dependent loosening or unravelling of the hangingwall blocks”. The mechanism of unravelling is not well understood and the rate of unravelling has never been quantified. It is therefore not known for a particular area what the minimum rate of mining should be to reduce the incidence of falls of ground. A significant development in this study was the improved understanding of the effect of mining rate on the rate of closure. From the underground observations, a technique was developed to estimate the amount of closure that will act on support units for different mining rates This work will lead to more effective stope support design.

A literature survey on the mechanisms of falls of ground indicated that apart from Arnold’s reference to time-dependent unravelling, very little on this topic can be found. It is nevertheless well known in the industry that it is bad practice to leave faces standing as this leads to deteriorating hangingwall conditions. One possible reason for this time-dependent unravelling is a gradual loss of horizontal clamping stress in the hangingwall if no mining takes place. Squelch (1990) measured horizontal clamping stresses in the hangingwall in the order of 3 to 10 MPa in unfilled panels. Arnold (1995) hypothesised that continuous face advance is necessary to regenerate and maintain clamping stresses in the hangingwall.

Experimental work was conducted at Great Noligwa Mine to investigate the time-dependent unravelling of the hangingwall and the effect of mining rate on the occurrence of falls of ground. An experimental site was established in the 70-47-E10 panel of the mine. Strain measurements were made in the hangingwall and simultaneous measurements were made of the time-dependent closure of the stope and the roughness profiles of the hangingwall. The strain measurements were conducted to measure any possible relaxation of horizontal clamping stresses in the hangingwall, which could lead to time-dependent falls of ground. For the strain measurements, a CSIRO cell and two doorstoppers were installed in the hangingwall of the stope. These cells were installed above one of the gullies as this was the only area where horizontal holes could easily be drilled. Even then, installation using the standard method of drilling the hole with diamond core drills proved impractical. A new technique had to be developed for installing the cells. A rockdrill bit was modified so that the holes could be drilled

using percussion equipment available in the stope. The doorstopper cells require that the end of the hole should be smoothed off prior to glueing the cell to the end of the hole. An attachment was developed for a hand held pneumatic drill consisting of a thin tube about 1m long, with a smoothing bit welded to the end, that could be inserted into the hole to smooth off the end. Figure 2.1.4.1 shows the area where the cells were installed.

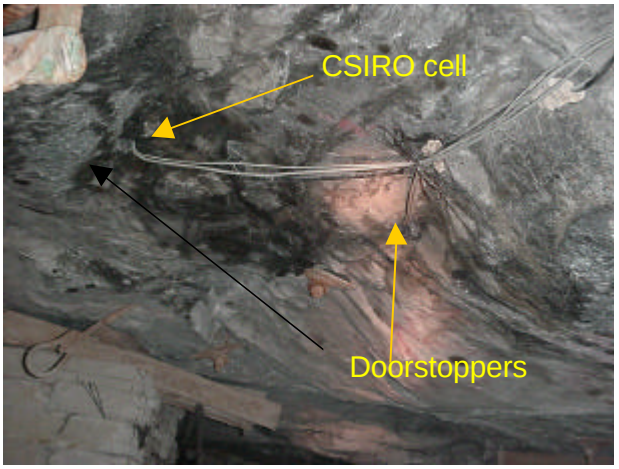

Figure 2.1.4.1. Strain cells installed in the stope hangingwall at Moab Khotsong Mine.

Table 2.1.4.1. Changes in stress measured at Moab Khotsong Mine.

Date	***Decrease in horizontal stress Strike direction***	***Decrease in horizontal stress Dip direction***
4/9/2000 – 7/9/2000	6.58 MPa	7.14 MPa
7/9/2000 – 12/9/2000	3.14 MPa	12.18 MPa
12/9/2000 – 18/9/2000		

The readings taken on various days following the installation indicated decreasing strains. Assuming that the Young's modulus of the rock is 70 GPa and the Poisson's ratio is 0.15, the stress changes suggested by the CSIRO cell readings are given in Table 2.1.4.1. Even though a decrease is indicated, the absolute values look suspiciously high. The stress measurements using the percussion holes were found to be too inaccurate to perform further readings.

The closure data collected in this particular area (see Figure 2.1.4.2) indicated relatively high rates of steady-state closure as can be expected for the Vaal Reef. The daily closure at a distance to face of 10 m is approximately 12 mm/day when the faces are advanced.

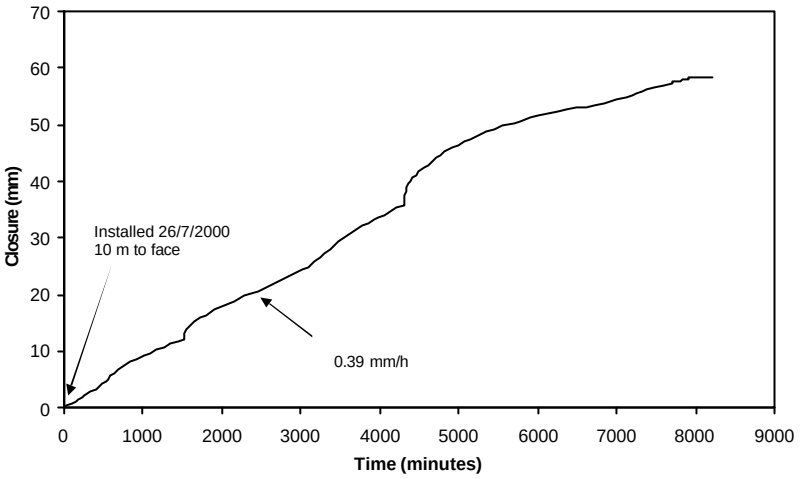

Figure 2.1.4.2. Closure measurements in the 70-47-E10 panel at Great Noligwa Mine.

To supplement the closure data, roughness measurements of the hangingwall were made to see if any time-dependent unravelling was noticeable. The methodology was to string a length of piano wire tightly between two elongates to serve as a reference level as shown in Figure 2.1.4.3. At 100 mm intervals, the distance between the piano wire and the hangingwall was measured. Figure 2.1.4.4 illustrates the roughness profiles measured during a two week period at the same measurement position. Suprisingly there was not a significant change in roughness, indicating that the hangingwall remains relatively intact in spite of the moderately high rate of closure.

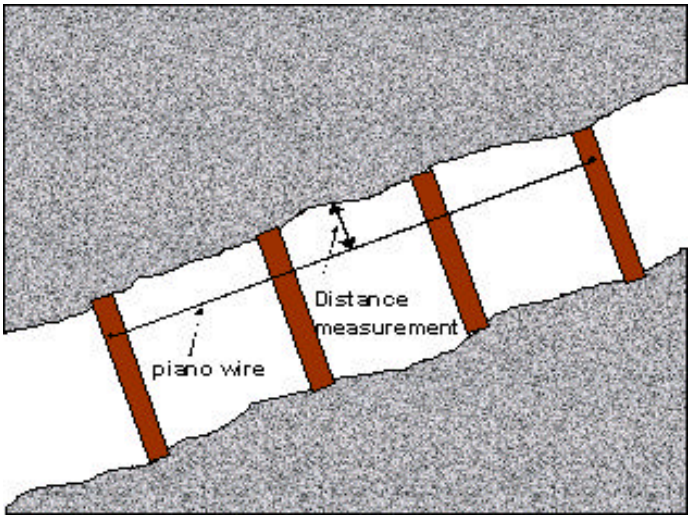

Figure 2.1.4.3. Measuring the hangingwall roughness.

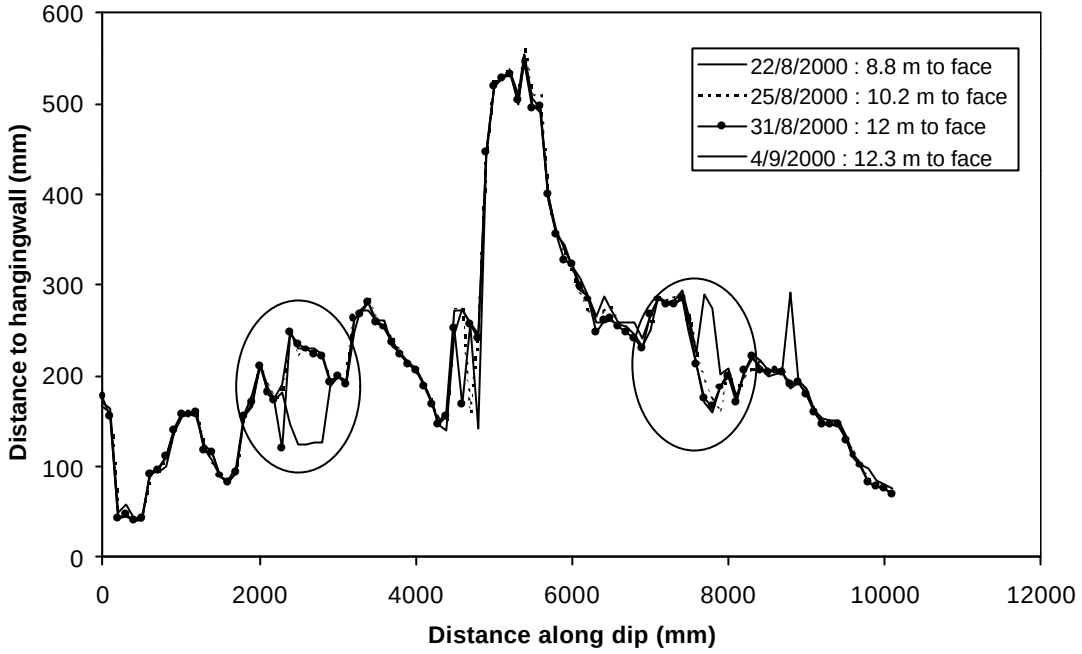

Figure 2.1.4.4. Measurement of hangingwall roughness at Moab Khotsong Mine. The profile was taken along dip, parallel to the face, with the origin of the graph in the upper part of the panel. The areas encircled indicated where some minor block got dislocated in the hangingwall.

Further underground measurements focused on developing a technique to estimate the effect of mining rate on the total closure acting on support units. This information is necessary to understand how safety in stopes might be affected by slow mining rates. If the deformation of the rock mass was purely elastic (no time-dependent deformation), the effect of mining rate would not play any role. From Figure 2.1.4.2 it is, however, clear that time-dependent closure behaviour is very prominent in some areas of the mining industry. Mining rate will therefore play a significant role on the amount of closure acting on support units as explained below.

For support design purposes, it is important to quantify the amount of closure that will act on a support unit from the time of installation until it is a certain distance behind the face. This is illustrated in Figure 2.1.4.5. In this particular example, the support unit is installed 3 m from the face on a specific day. After a period of time, the face has been advanced by 5 m, and the support unit is now at distance of 8 m from the face. As the rate of closure contains a time-dependent component, which persists even if there is no mining activity, the total closure acting on this support unit will be dependent on the mining rate.

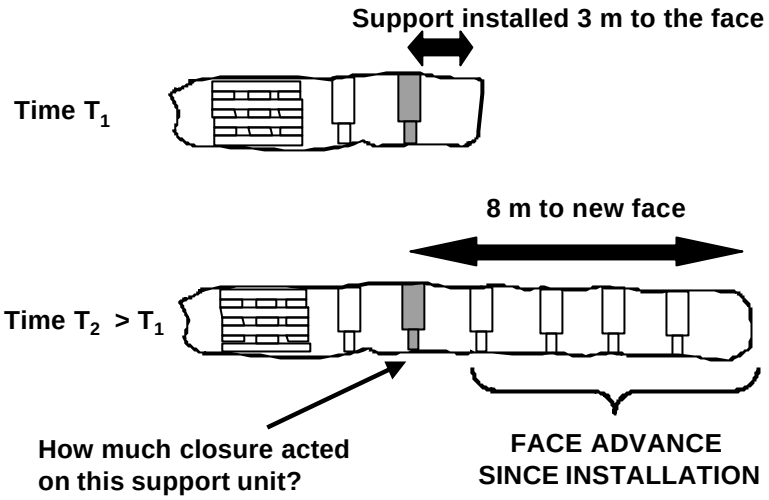

Figure 2.1.4.5. Example to illustrate the effect of mining rate on rate of closure.

The total daily closure, S^i_{daily}, acting on a support unit on a particular day i (where i = 1,2,3… to denote successive days) can be given by the equation

$$S^i_{daily} = S^i_I + S^i_P + S^i_{SS} \qquad (2.1.4.1)$$

where S^i_I is the instantaneous closure, S^i_P is the primary closure phase and S^i_{ss} is the total steady-state closure for the particular day (see Figure 2.1.4.6).

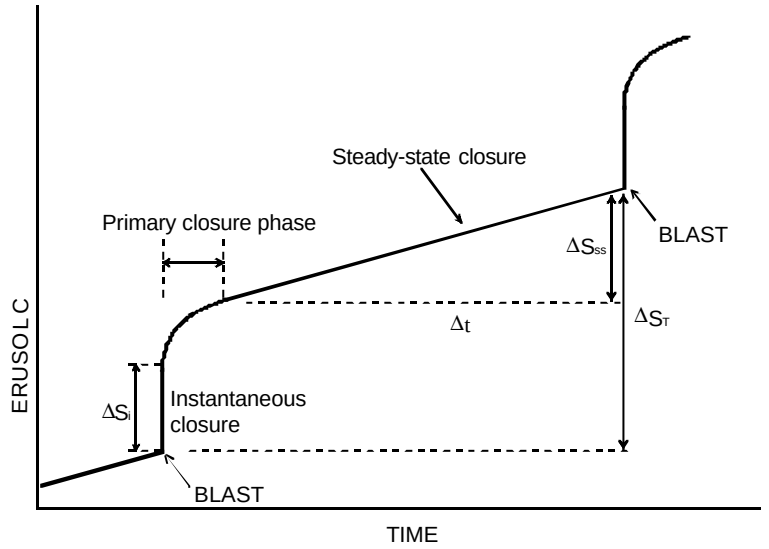

Figure 2.1.4.6. Typical continuous stope closure after blasting and the definition of closure terms.

If there is no blasting (or large seismic events), the instantaneous and primary closure components are zero and equation (2.1.4.1) reduces to

$$S^i_{daily} = S^i_{SS} \qquad (2.1.4.2)$$

For the example in Figure 2.1.4.5, the total closure can now be calculated for different mining rates. If blasting occurs every day (5 days to advance 5 m) the total closure acting on the support unit is

$$S_{TOTAL} = \sum_{i=1}^{5} S^{i}_{daily} = \sum_{j=1}^{5} \left(S^{j}_{I} + S^{j}_{P} \right) + \sum_{i=1}^{5} S^{i}_{SS} \qquad (2.1.4.3)$$

where j denotes each successive mining increment. The first term in equation 2.1.4.3 denotes the sum of the instantaneous and primary closure following each blast (assumed to be independent of mining rate) while the second term is the sum of all the time-dependent closure. If blasting, however, only occurs every second day (10 days to advance 5 m) the total closure acting on the support unit will be

$$S_{TOTAL} = \sum_{i=1}^{10} S^{i}_{daily} = \sum_{j=1}^{5} \left(S^{j}_{I} + S^{j}_{P} \right) + \sum_{i=1}^{10} S^{i}_{SS} \qquad (2.1.4.4)$$

When comparing equations (2.1.4.3) and (2.1.4.4), it can be seen that the total closure acting on the support unit will be larger for the slower mining rate, even though the total face advance is 5 m in both cases. The difference in closure magnitude acting on the support unit for various mining rates will depend on the rate of steady-state closure. The larger the rate of steady-state closure, the bigger the effect of the mining rate. To quantify this effect, the following technique was developed from the underground observations.

The rate of steady-state closure appears to be constant in the short term but it gradually decreases when there is no blasting or seismic activity. This is illustrated in Figure 2.1.4.7. This particular data set was obtained in a VCR (hard lava) up-dip panel (87-49 area) at Mponeng Mine. The measurements were obtained over a long weekend when there was no mining activity for several days. The steady-state closure is best approximated by a function of the form

$$\Delta S_{SS} = a\left(1 - e^{-bt}\right) \qquad (2.1.4.5)$$

where a and b are parameters and t is time. The steady-state closure for Station No. 2 in Figure 2.1.4.7 after the seismic event was plotted in Figure 2.1.4.8 together with the model given in equation (2.1.4.5). The parameters used to obtain this fit were a = 3.85 mm and b = 0.015 h^{-1}. Note that these values are only applicable to this particular stope.

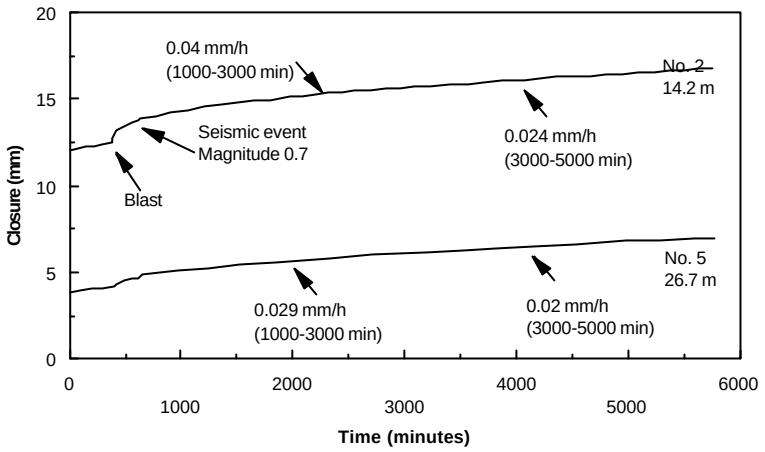

Figure 2.1.4.7. Closure measured in a VCR (hard lava) panel when there was no mining activity for a period of four days. The time periods in brackets indicate the intervals used to calculate the steady-state closure rates. Two closure instruments at different distances to the face were used to collect the data.

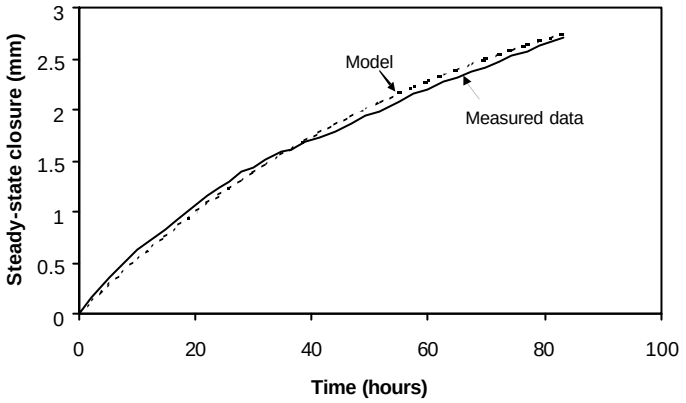

Figure 2.1.4.8. Measured and simulated values of steady-state closure for the VCR (hard lava) panel.

From equation (2.1.4.5), the rate of steady-state closure is given by

$$\frac{dS_{SS}}{dt} = ce^{-bt} \tag{2.1.4.6}$$

where c =ab. From equation (2.1.4.6), the rate of steady-state closure at t = 0 is given by c. For convenience, equation (2.1.4.5) will be written as

$$\Delta S_{SS} = \frac{c}{b}\left(1 - e^{-bt}\right) \tag{2.1.4.7}$$

Continuous closure measurements indicated that the rate of steady-state closure is also a function of measurement position in the panel. This is indicated in Figure 2.1.4.9 where the rate of steady-state closure appears to decrease as the distance to face increases. The parameter c

in equation (2.1.4.7) is therefore a function of the distance to face. As the rate of steady-state closure is also a function of the face advance distance on a particular day and the position in the panel along strike, there is some scatter present in the data as illustrated in Figure 2.1.4.9. From studies described in Malan (1998), where three closure meters were installed at increasing distance to the face, it is clear that after any particular blast, the rate of steady-state closure decreases into the back area. The parameter c will therefore be approximated by the following function

$$c = \alpha e^{-\beta d} \tag{2.1.4.8}$$

where d is the distance to the face. From the fit in Figure 2.1.4.9, calibrated values for α and β are 0.1195 mm/h and 0.0454 m^{-1}, respectively. Inserting equation (2.1.4.8) in (2.1.4.7) gives

$$\Delta S_{SS} = \frac{\alpha e^{-\beta d}}{b}\left(1 - e^{-bt}\right) \tag{2.1.4.9}$$

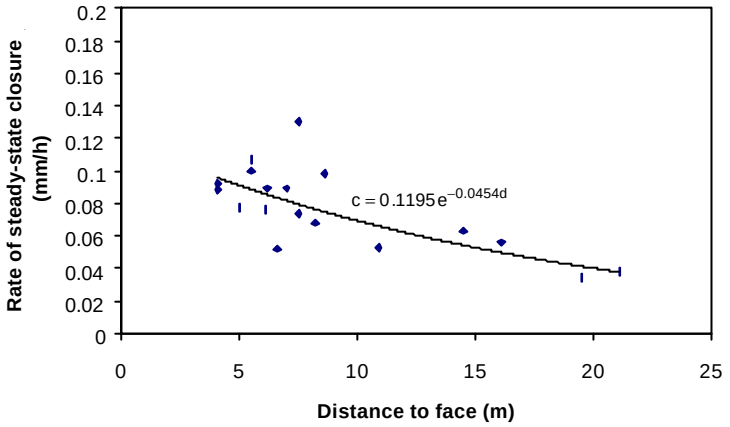

Figure 2.1.4.9. Effect of distance to face on the rate of steady-state closure. Although there is some scatter present in the data with a resulting poor fit to the given function, it will be used as a useful approximation of the trend.

As the decrease in rate of steady-state closure illustrated in Figure 2.1.4.8 is repeated after every blast, equation (2.1.4.9) should be further modified to allow for the incremental enlargement of the stope. If a closure meter is installed at a fixed position in the stope and a number of increments are mined, the total amount of steady-state closure measured at that position will be given by

$$S_{SS}{}^{T} = \sum_{k=1}^{n} \frac{\alpha e^{-\beta(k\Delta\ell + f)}}{b}\left[1 - e^{-b(\tau_k - \tau_{k-1})}\right] \tag{2.1.4.10}$$

where n is the number of mining increments and τ_k is the time when the k^{th} increment is mined. The distance to face is given by

$$d = k\Delta\ell + f \qquad (2.1.4.11)$$

where $\Delta\ell$ is the size of each mining increment and f is the original distance to face. Equation (2.1.4.10) was used to simulate the effect of different mining rates (for a total face advance of 20 m) on the steady-state closure at a measuring point 5 m behind the original face. The size of each mining increment was assumed to be 1 m. The calibrated values for α, β and b obtained from Figures 2.1.4.8 and 2.1.4.9 were used. The results are illustrated in Figure 2.1.4.10. t is assumed that the parameters α and β are not functions of the mining rate.

The effect of different mining rates is clearly visible in Figure 2.1.4.10. It should be emphasised that the closure plotted in Figure 2.1.4.10 is only the steady-state closure and does not include the instantaneous or primary closure components. If long period closure measurements are available for a particular panel at a known mining rate, equation (2.1.4.10) can be used to estimate how a wide range of mining rates will affect the rate of closure. Limited continuous closure measurements in the panel will be required to calibrate the parameters α, β and b in equation (2.1.4.10).

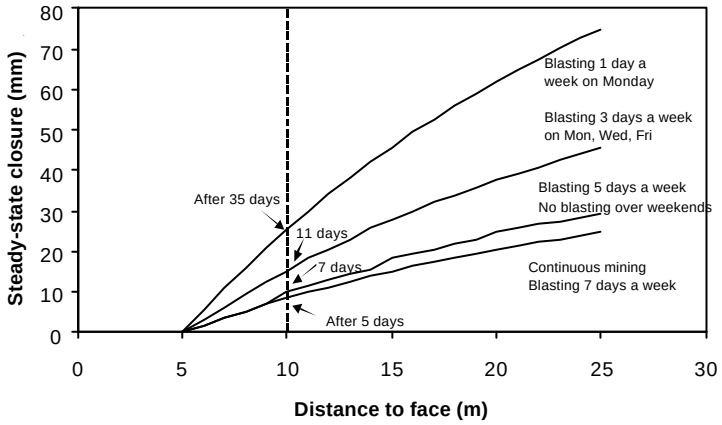

Figure 2.1.4.10. The effect of mining rate on the total amount of steady-state closure at a particular point in the stope. This is for a VCR (hard lava) panel.

From Figure 2.1.4.10, note that at a distance of 10 m from the face (for support originally installed 5 m from the face), the cumulative steady-state closure is 8.4 mm for continuous mining operations. This gives a steady-state closure rate of 1.7 mm/m. If there is only one blast a week, the steady-state closure at the same distance to face will be 25.5 mm. The corresponding rate of closure is 5.1 mm/m which is an increase of 3.4 mm/m. Imagine then that the stope is mined using continuous operations (blasting every day). Long period closure

measurements during this period (for a closure station installed 5 m from the face) might indicate that the rate of total stope closure for a face advance of 5 m is some value, say x mm/m. If it is decided to decrease the mining rate to just one blast a week, the new rate of closure that can be expected is (x +3.4) mm/m. The current support design should then be tested using this new rate to establish if any changes are required.

The analysis above was conducted for the VCR with a hard lava hangingwall. These areas are typically characterised by low rates of steady-state closure and it appears that mining rate does not have a major effect on the rate of closure. For the VCR with a soft lava hangingwall and in some areas of the Vaal Reef, however, the rate of steady-state closure is very high and changes in mining rate are expected to have a significant effect on the volume of stope closure per area mined. This is illustrated below using closure data collected in the VCR with a soft lava hangingwall at Kloof Mine (31-34 area).

Figure 2.1.4.11 illustrates a typical rate of steady-state closure and a decrease in this rate in the absence of mining activity. The model in equation (2.1.4.5) is fitted to this data to give calibrated values of a = 57 mm and b = 0.009 h^{-1}. The rate of steady-state closure also decreases into the back area as illustrated in Figure 2.1.4.12. Calibrated values for the model in equation (2.1.4.8) is α = 1.9246 mm/h and β = 0.1259 m^{-1}.

The values calibrated above were used in equation (2.1.4.10) to investigate the effect of mining rate. This is illustrated in Figure 2.4.1.10. Note that the cumulative amount of steady-state closure at a fixed measuring position after a certain amount of face advance is much more than that illustrated in Figure 2.1.4.13. For continuous mining, the steady-state closure at 10 m from the face is 72 mm or 14.4 mm/m. For blasting once a week, this increases to 218.9 mm or 43.8 mm/m. The difference in the rate of steady-state closure is therefore 29.4 mm/m. This is significantly higher than the 3.4 mm/m calculated for the VCR with a hard lava hangingwall. In areas with a high rate of steady-state closure, it is therefore important not to mine at very slow rates.

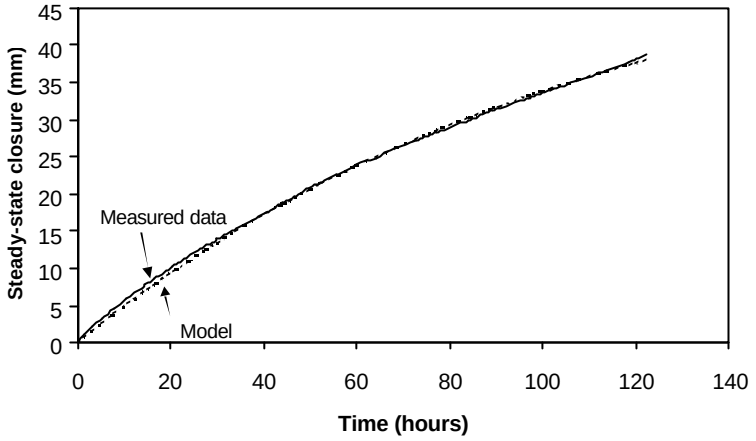

Figure 2.1.4.11. Measured and simulated values of steady-state closure for a VCR panel with a soft lava hangingwall.

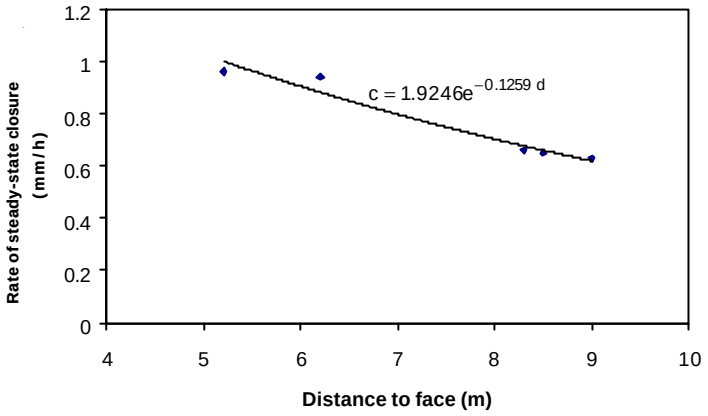

Figure 2.1.4.12. Effect of distance to face on the rate of steady-state closure for the VCR with a soft lava hangingwall.

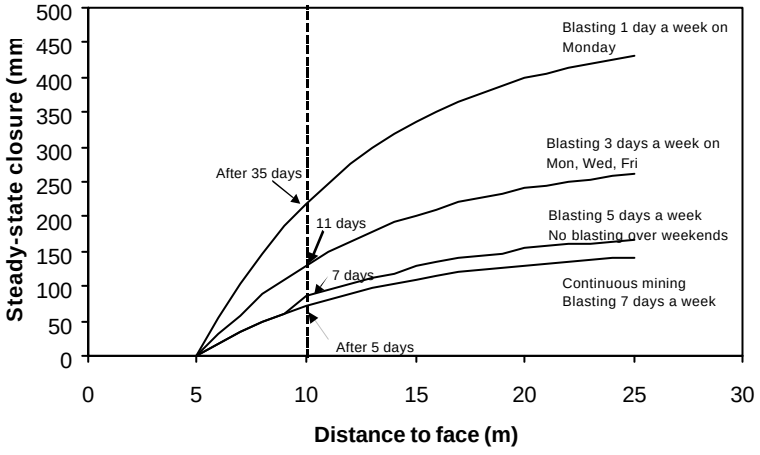

Figure 2.1.4.13. The effect of mining rate on the total amount of steady-state closure at a particular point in the stope. This is for a VCR (soft lava) stope.

2.2 Formulation of descriptive mechanisms of time-dependent damage and stope face stability.

2.2.1 Friction mobilisation model

Extensive experimental work, reported in section 2.1.1, has been carried out to determine the response of laboratory scale rock samples with “manufactured” and natural gouge on a discontinuity interface within each sample. In a number of these experiments, incremental shear loads are applied to each sample and the time dependent slip response is observed. It is important to develop a quantitative representation of this response for use in computer models of time dependent stope deformation. An initial model has been proposed in which the slip resistance of the discontinuity surface is assumed to increase as the slip increases. The slip resistance is assumed to be a function of the difference between a maximum critical slip, Yc, and the current slip, y. As y increases, the effective frictional slip resistance increases and is fully “mobilised” when y = Yc. It is also assumed that the slip rate is proportional to the difference between the applied shear stress and the slip resistance. This model has been implemented in the DIGS code. A qualitative test of the behaviour of the model is shown in Figure 2.2.1.1 where successive shear load increments are applied to a material block sliding on a surface. The slip response of the block, as a function of time, is given in Figure 2.2.1.1 for two different values of the critical slip distance, Yc. It can be seen that the response follows a “stepped” increase in the slip as the load is increased and that the slip decay rate depends strongly on the critical slip distance parameter. In the case of the small critical slip distance (Yc = 1mm), the friction becomes fully mobilised beyond time step 84 and slip is unbounded.

The general appearance of the response curves in Figure 2.2.1.1 is encouragingly very similar to the laboratory observations, shown in Figure 2.1.1.6. It must be emphasised though that, in this case, no attempt has been made to link the size of the load increments or the scale of the numerical model to the actual loads and size of the laboratory tests. The numerical model is, in fact, applied to a large block 20 m long by 5 m high and parts of the discontinuity surface are found to slip differentially. Figure 2.2.1.2 shows the fraction of the slip surface where the critical slip distance is exceeded and where the frictional resistance is fully mobilized. This can be seen to increase more steeply (and in more abrupt jumps) for the test with the smaller critical slip parameter. It is also of interest to plot the frictional resistance as a function of the cumulative slip. This is shown in Figure 2.2.1.3 and is again qualitatively very similar to the results reported in section 2.1.1 (see Figure 2.1.1.7). The results presented here show very encouraging

agreement to the laboratory observations. However, further investigations into the implications of this behaviour at the stope scale have not been pursued in the current project.

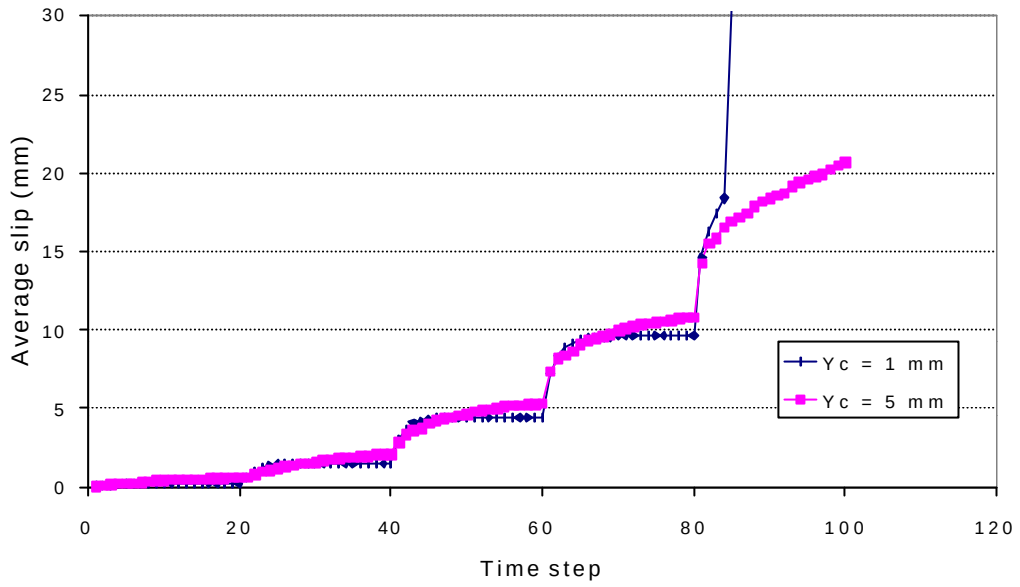

Figure 2.2.1.1 Comparison of slip evolution as a function of time for incremental loads applied to a sliding block with two values of the critical slip distance, Yc.

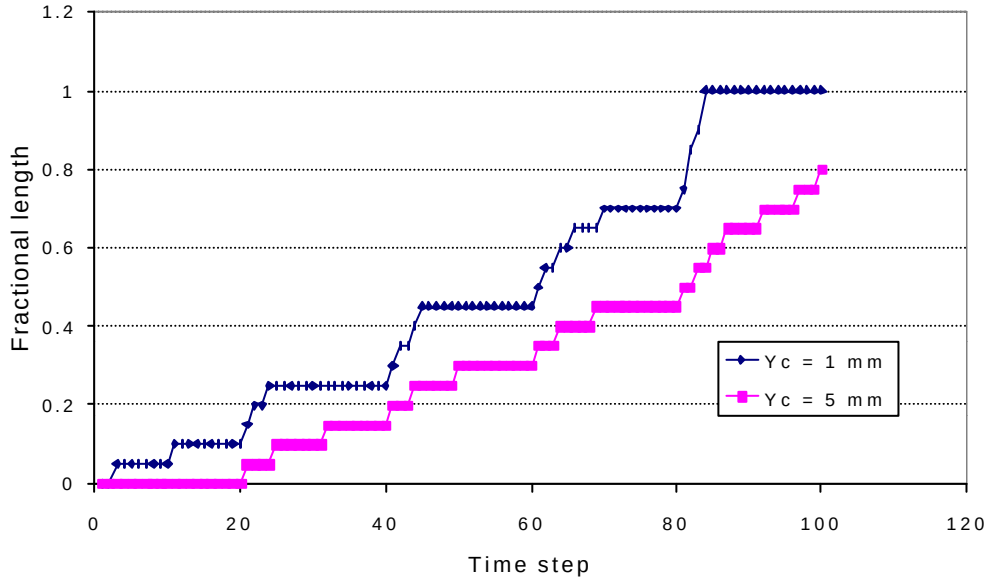

Figure 2.2.1.2 Comparison of the fraction of the slip surface exceeding the critical slip limit as a function of time for two values of the critical slip parameter Yc.

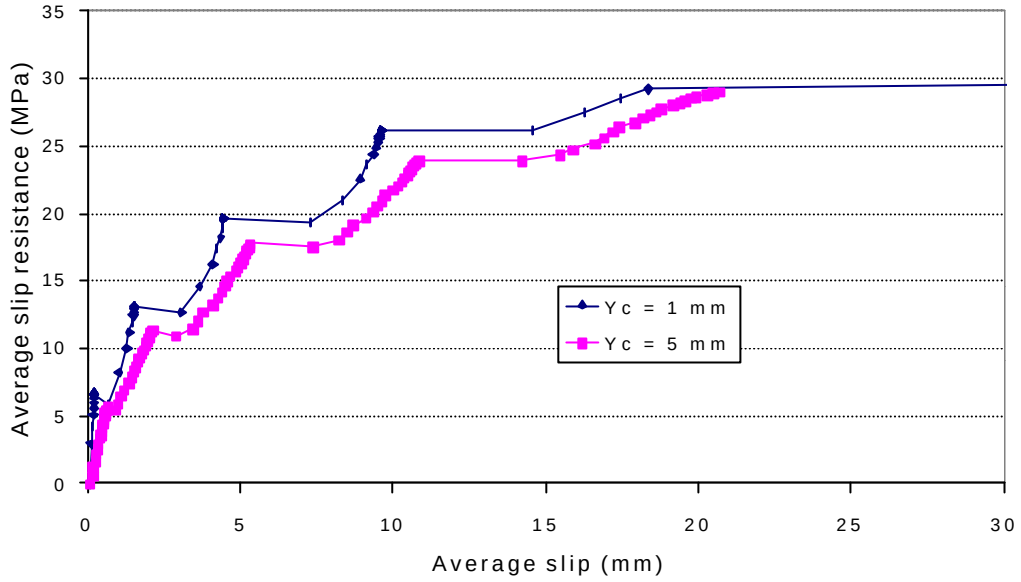

Figure 2.2.1.3 Comparison of the average slip resistance as a function of the cumulative slip for two values of the critical slip parameter Yc.

2.2.2 Stope face stiffness and stability analysis

In order to assess general mechanisms of stope face instability (and the consequent questions of uncertainty in the rock behaviour) it is useful to consider the possible role of the face loading stiffness as a measure of stability. In addition to this, it is important to assess how the interaction of the stope with geological features, such as faults, affects the face stiffness and stability. An initial analysis has been performed in which a stope is modelled as a parallel-sided slit that is widened on one side in incremental mining steps of one metre. The face stiffness, *k*, is defined as the ratio of the average stress, *S*, over a distance of one metre ahead of the face, divided by the average closure, *D*, that arises in this interval when the face is advanced by one metre (i.e. $k = S / D$. It may be noted that the energy release rate (ERR) is given approximately by $ERR = ½ S D$). Figure 2.2.2.1 shows a plot of the face stiffness as a function of the mining span for three different cases. These are, respectively, mining with no off-reef fracturing, mining through a vertical hangingwall fault, located at a span of 50 m, and mining through this fault with a simulated random mesh fracture zone above the stope. In the case of no fracture zone and no fault the face stiffness remains nearly constant at approximately 28 MPa/mm. When the fault is introduced, but no fracture zone is present, the face stiffness is seen to start decreasing when the stope span exceeds 46 m and falls dramatically to a low value of approximately 7 MPa/mm when the fault is intersected at a span of 50 m. If the explicit fracture zone is modelled as well as the fault, the face stiffness is lower and is also seen to fall to about 7 MPa/mm when the fault is intersected and then to increase when mining advances past the fault intersection. Figure

2.2.2.2 shows the average vertical stress in the first metre ahead of the stope face. In the case of no fault and no fracturing (elastic solution) this shows a steady increase as the stope span increases. In the presence of the fault, the vertical stress is seen to peak above the elastic trend prior to intersection with the fault due to partial slip along the fault. At the point of intersection ("daylighting") the average vertical stress ahead of the face drops significantly and then builds up slowly as the mining span is increased. The drop in stiffness prior to and at the point of intersection with the fault, shown in Figure 2.2.2.1, obviously has important implications with respect to the potential for face damage and possible "face bursting". The procedure outlined here provides a means to explore the consequences of a decrease in stiffness when the full stope face width is modelled. This suggests that future work should be directed to investigate whether a general face stability measure can be devised that will be more suitable for the prediction and assessment of unstable face conditions. In order to "sense" the proximity of the fault to the mining face it is useful to monitor trends in the stope closure. However, from Figure 2.2.2.3, it appears that the change in the rate of closure prior to the intersection of the stope with the fault is not very clear-cut. If some means of assessing the stress ahead of the stope face is available, it may be possible to track trends in the face "stiffness", as shown in Figure 2.2.2.1, for the case where the fracture zone is simulated explicitly.

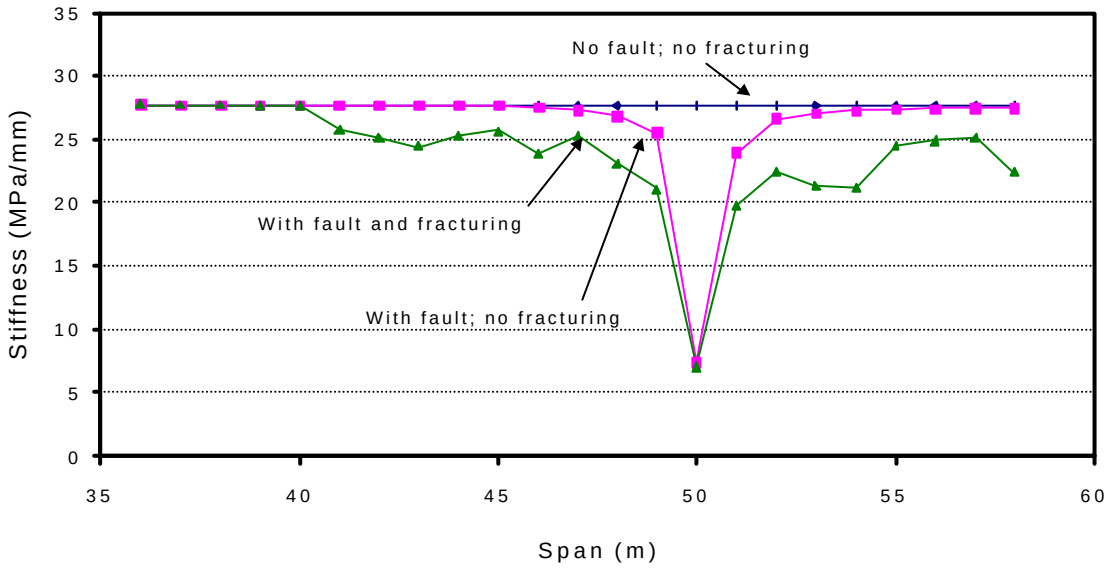

Figure 2.2.2.1 Comparison of stope face stiffness as a function of panel span when mining through a fault and when the fracture zone is explicitly simulated.

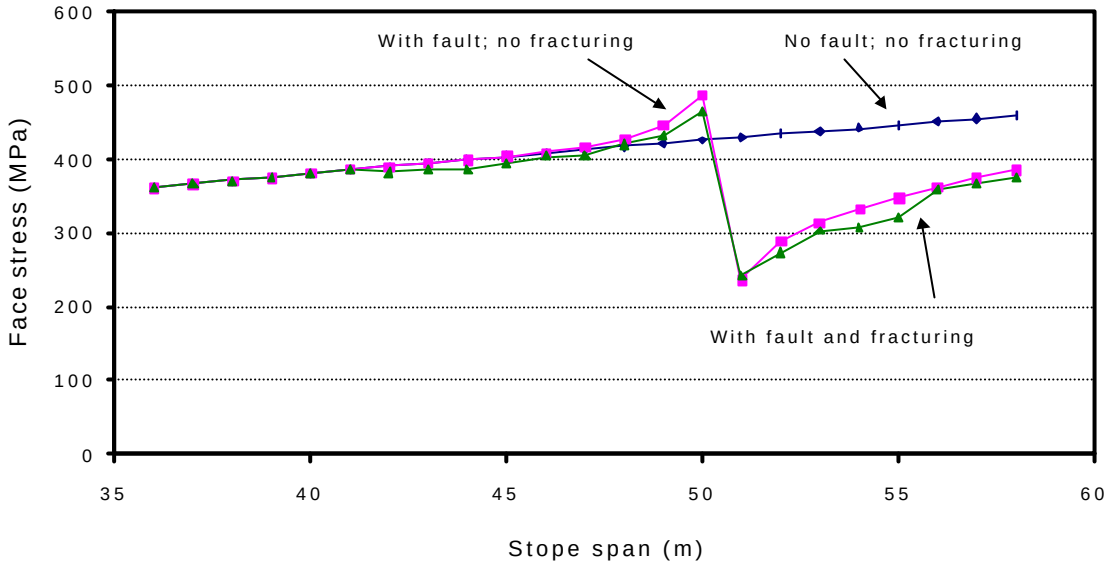

Figure 2.2.2.2 Comparison of the average stress ahead of a simulated parallel-sided panel when mining through (i) perfectly elastic ground, (ii) elastic ground and a single vertical fault and (iii) a single vertical fault and a model of the off-reef fracture zone around the stope.

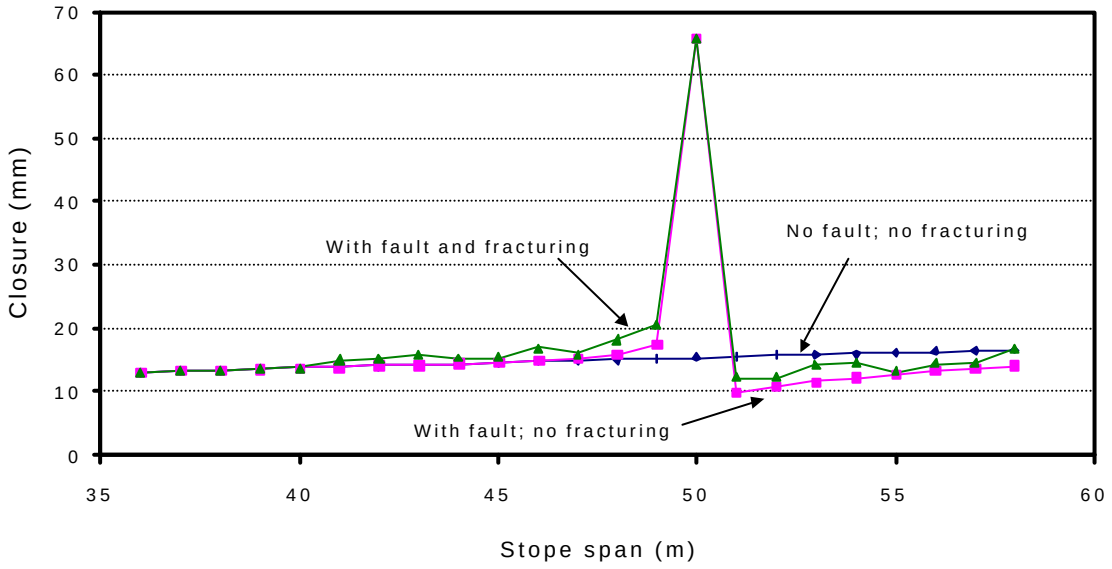

Figure 2.2.2.3 Comparison of average stope closure, adjacent to the stope face, as a function of the stope span.

2.3 Statistical uncertainty in time to failure and the stope stress environment

2.3.1 Simulation of time to failure and prediction of time of failure – model formulation and numerical experiments and implications

A series of numerical experiments have been carried out to investigate the question of time to failure in relation to static fatigue loading tests. In these experiments, a rectangular shaped sample is loaded uniformly on one surface perpendicular to the major axis of the sample and supported on a rigid frictionless base at the opposite end of the sample. In order to formulate an appropriate theory of material failure (Napier and Malan, 1997) it is important to assess whether the viscoplastic crack slip model incorporated previously in the DIGS code is able to reproduce the qualitative behaviour observed in such tests. Particular attention must be given to the question of whether the implementation of the creep model needs to be modified to accomplish these aims. All further modelling of time dependent stope closure and seismic recurrence will hinge on these assumptions. Three primary controls of the material behaviour are the crack surface “fluidity”, the material strength prior to slip and the random mesh structure used in the tessellation model. It should be recognized that the use of the random mesh introduces a degree of statistical uncertainty into the results that also has to be quantified. In the first series of tests, a Delaunay triangular mesh is used in which friction and cohesion loss occur after failure is initiated and each crack is allowed to creep at a rate proportional to the local net excess shear stress (Material 1).

The total mobilised fracture length and the total length of the subset of viscous sliding elements at each time step is presented in Figures 2.3.1.1a and 2.3.1.1b. Figure 2.3.1.1a shows clearly the points in time at which uncontrolled deformation (failure) initiates. These times are related to the applied load and show a characteristic behaviour commonly observed in deadweight loading tests. Figure 2.3.1.2 is a plot of the ratio of the viscous length to the total mobilised length derived from Figures 2.3.1.1a and 2.3.1.1b. It is of particular interest to note the dramatic change in this ratio at the times when rapid failure commences. A further series of tests was carried out using the same tessellation mesh but with a different material behaviour. In this case the material properties were defined to be such that failure was initiated when the shear stress on a mesh segment reached a critical cohesion irrespective of the normal stress level. After failure initiation, the cohesion was reduced to zero and the friction angle increased to a nominal level of 30 degrees. These properties are designated as Material 2. Figures 2.3.1.3a and 2.3.1.3b show the total mobilised length of fractures and the total subset length of viscoplastic sliding cracks at each point in time. The ratio of the total viscous length to the total mobilised

length is shown in Figure 2.3.1.4 and can be contrasted to Figure 2.3.1.2. The material behaviour is clearly controlled strongly by the extreme cohesion weakening behaviour and the viscous length fraction is seen to be more strongly dependent on the level of loading than in the case of Material 1.

A run in which the Material 1 properties were used but the tessellation mesh was changed to a Voronoi structure with internal triangles is shown in Figure 2.3.1.5. Although this mesh is essentially a triangulation, it is apparent that the response differs markedly from the Delaunay triangle mesh results shown in Figure 2.3.1.1a, with a longer time to failure at a given load. Further testing is required to establish the statistical bounds on these results. It is apparent that a wide range of time to failure response characteristics can be observed in these random mesh analyses. There is no clear evidence that precursory information can be deduced from these analyses to predict the onset of rapid deformation. The availability of experimental time to failure data should assist in determining an appropriate choice of both material parameters and mesh structure to represent the statistical response of a given material. This should provide an important initial step in describing the material behaviour of large scale regions. It must be emphasised that the appropriate choice of material description is, at present, a question that is not resolved in any currently available numerical tool for the analysis of inelastic rock behaviour.

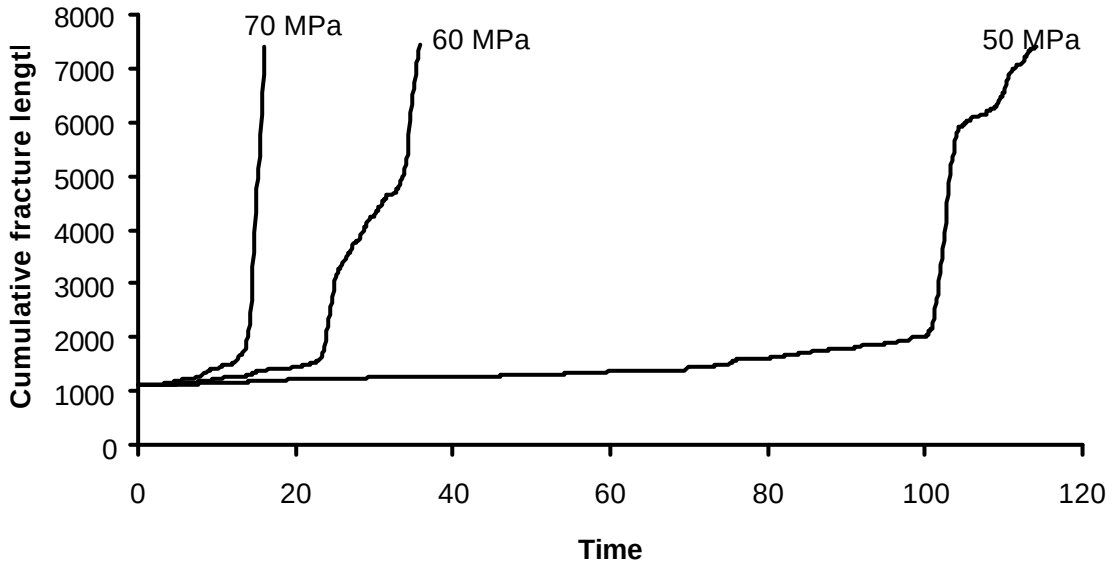

Figure 2.3.1.1a. Static fatigue test cumulative fracture length for different loads (Delaunay mesh/Material 1).

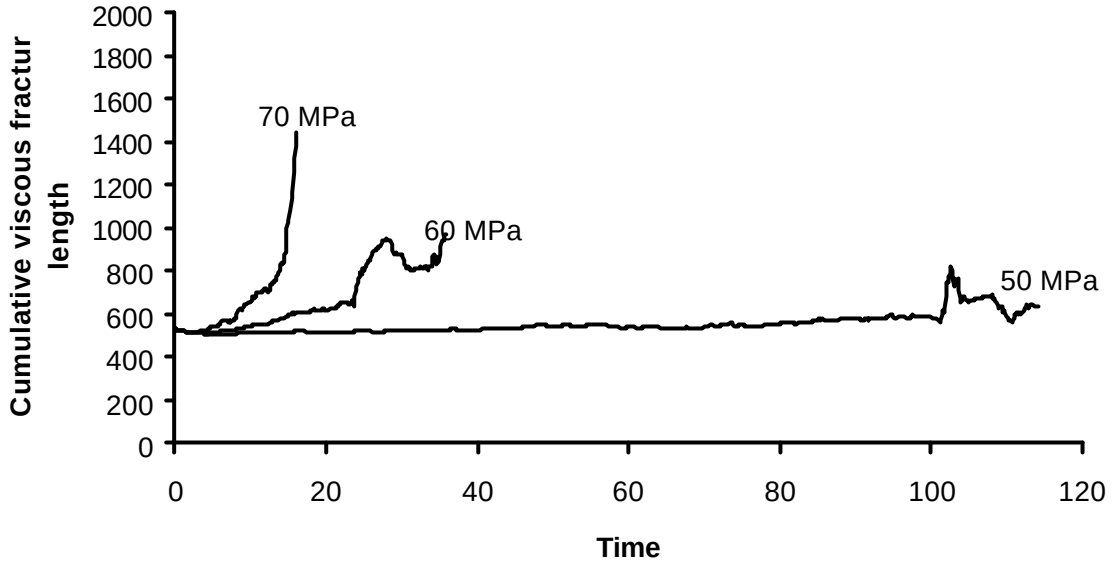

Figure 2.3.1.1b Static fatigue test cumulative viscous fracture length for different loads (Delaunay mesh/ Material 1).

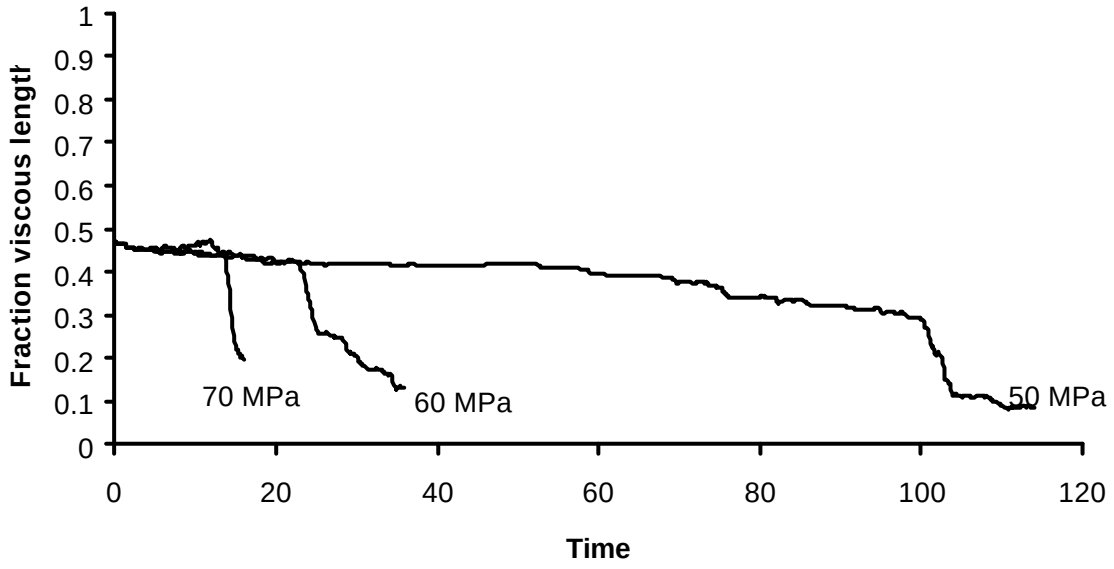

Figure 2.3.1.2 Static fatigue test fraction viscous length for different loads (Delaunay mesh/ Material 1).

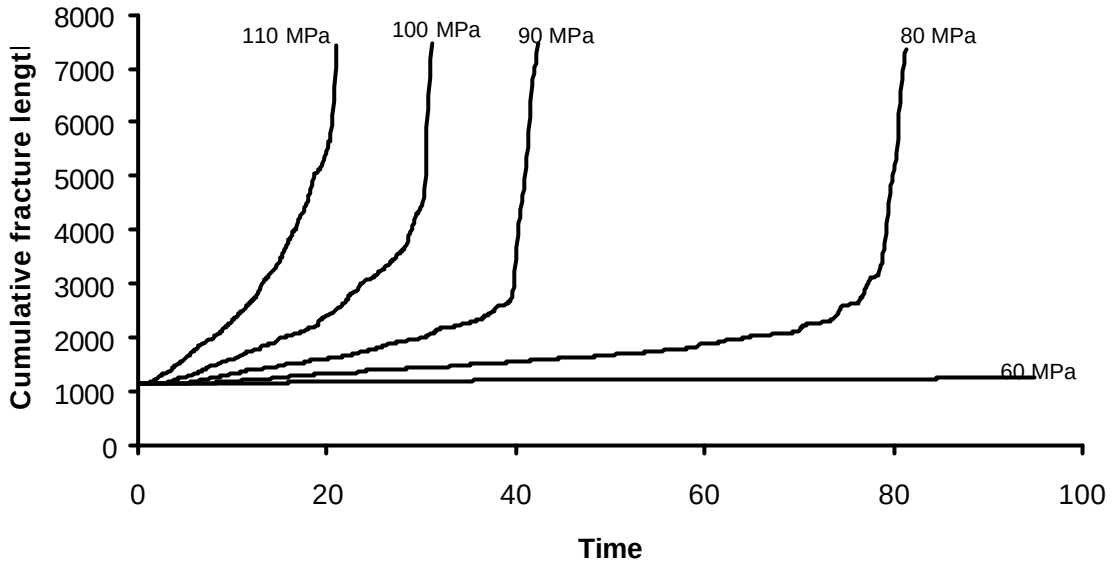

Figure 2.3.1.3a Static fatigue test cumulative fracture length for different loads (Delaunay mesh Material 2).

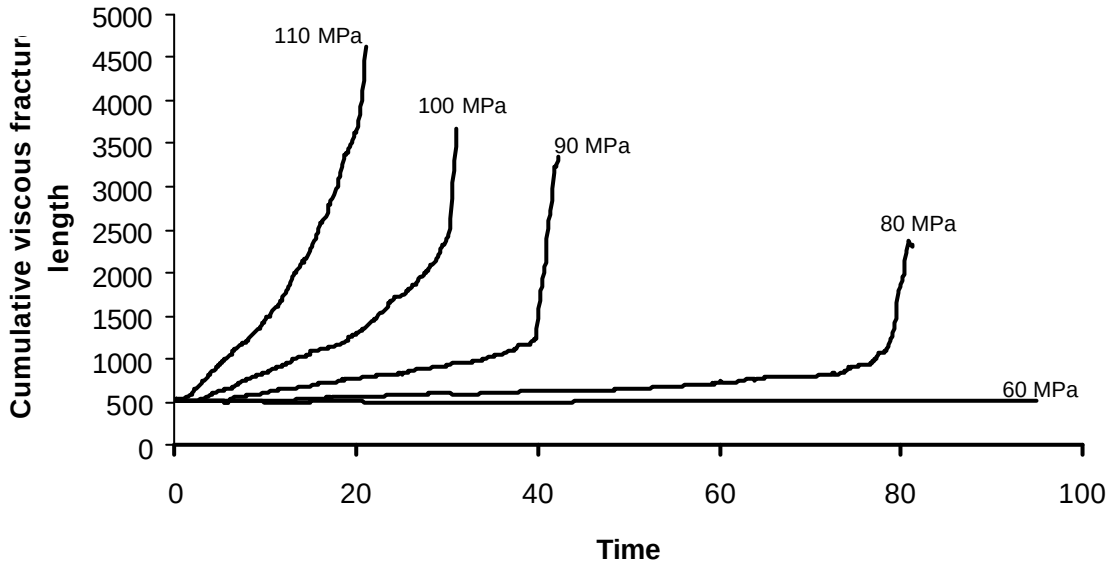

Figure 2.3.1.3b Static fatigue test cumulative viscous fracture length for different loads (Delaunay mesh/Material 2).

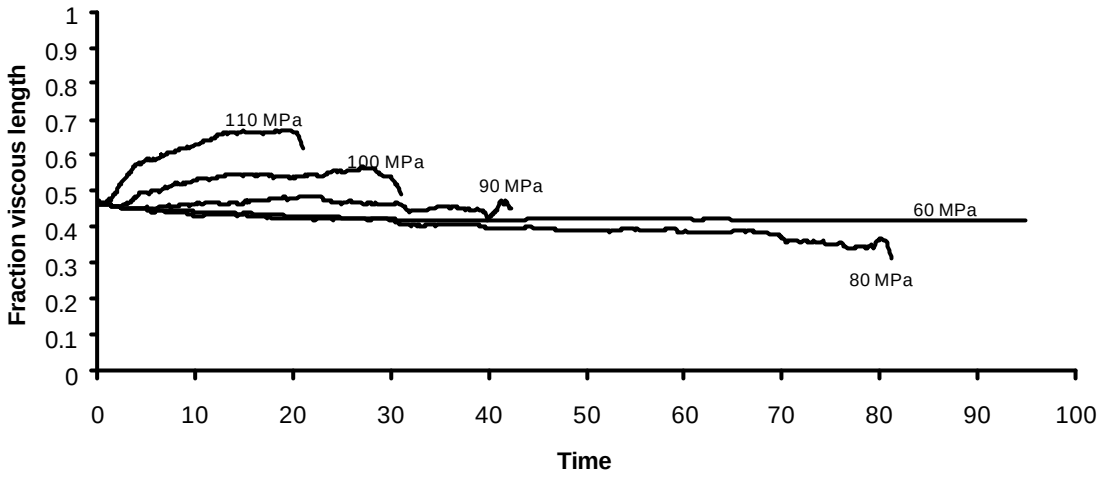

Figure 2.3.1.4 Static fatigue test fraction viscous length for different loads (Delaunay mesh Material 2).

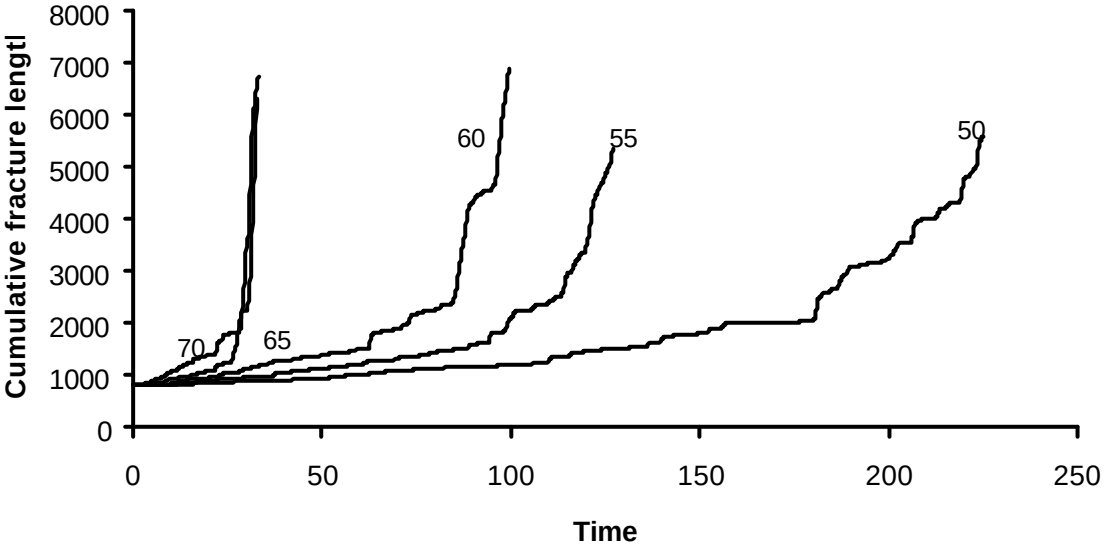

Figure 2.3.1.5 Static fatigue test cumulative fracture length for different loads (Voronoi mesh / Material 1).

Further analysis of numerical experiments that simulate the deadweight loading of rectangular shaped samples was carried out. As noted previously, two sets of material failure parameters were used in the numerical experiments together with two types of random mesh tessellation. When different loads are applied to each sample it is observed that the time to failure decreases as the load on the sample is increased. A summary of this behaviour is shown in Figure 2.3.1.6,

for the different material/ mesh combinations that have been studied. (Only one realization of each load/ mesh combination has been obtained in this study). The time to failure trends are in good qualitative agreement with experiments carried out on laboratory scale samples. However, it is clear that different mesh schemes and internal mesh point failure characteristics can have unpredictable effects on the overall behaviour. Furthermore, no clear-cut precursory patterns arise in the cumulative histories of the energy release time series prior to the actual time of failure.

In order to analyse the evolution of damage in the samples, a computer program was written to calculate the number and size of mobilised crack clusters at any specified time. In this procedure, all mobilized tessellation elements are examined at each specified time step and are checked for mutual connectivity. A cluster is defined to be a set of connected crack elements and the cluster size is defined to be the sum of the lengths of the elements in the cluster. Starting from the initially specified flaw population, elements creep in response to the applied load causing adjacent elements to fail. This leads eventually to long-range coalescence and failure. Figure 2.3.1.7 shows the time evolution of the number of clusters for the “Delaunay mesh/ Material 1” sample. (This will be designated as D/M1). The number of clusters is seen to decrease with time as adjacent fractures coalesce. The rate of decrease appears to increase as the sample load is increased. (This trend was observed to be more erratic for a different mesh scheme involving a Voronoi tessellation with internal triangulation).

It is particularly interesting to track the cluster size distribution as a function of time. This is shown for the 50 MPa loading of the D/M1 sample in Figure 2.3.1.8. In this figure, the size distribution evolution is displayed at different times and the limits of the cluster size classes are chosen at logarithmic intervals of exp(n+1) for n=1 to 9 (i.e. 7.4, 20, 55 148, 403, 1097, 2981, 8103, 22026 length units respectively). It can be seen from Figure 2.3.1.8 that as time advances, the “tail” of the size distribution extends. More striking is the observation that at some critical time, the cluster size distribution becomes bimodal. In Figure 2.3.1.8 this occurs at about time 95. This suggests that at some critical time one dominant cluster emerges that presumably represents the final region of fracture localisation in the sample. The cluster size analysis was carried out for other load experiments performed on the D/M1 sample. It was also observed that the cluster size distribution became bimodal close to the time of failure. The transition to bimodality is shown by the vertical lines in Figure 2.3.1.9 at times of 95, 25 and 13 for the three loads of 50, 60 and 70 MPa respectively. The cumulative energy release, corresponding to each load, is plotted in Figure 2.3.1.9 to indicate the time of failure. It appears that the transition to bimodality becomes closer to the time of failure as the load is increased.

The main conclusion from these experiments is that the observed energy release (seismic) signals may not yield clear-cut patterns preceding the failure time. A more detailed knowledge of the distribution of damage in the material is required. One measure of this damage is the distribution of cluster sizes and possibly the spatial distribution of seismic activity near the stope face. The hypothesis that has to be tested is whether the spatial clustering of events becomes more concentrated just prior to the time of occurrence of a major event. Further investigation of the cluster size concept would seem to be warranted in relation to incipient failure near the stope face.

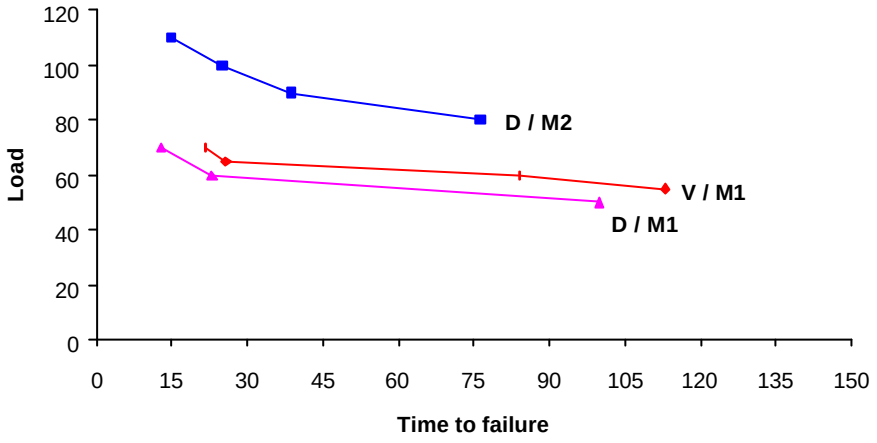

Figure 2.3.1.6 Static fatigue simulations of the time to failure for deadweight loading of a rectangular sample with different internal strength and mesh parameters.

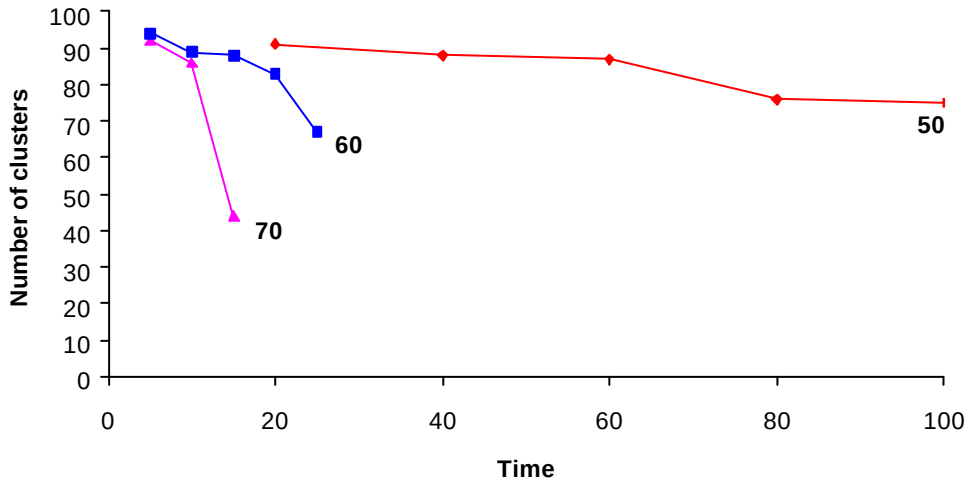

Figure 2.3.1.7 Number of clusters plotted as a function of time for different deadweight loads (Delaunay mesh/Material 1).

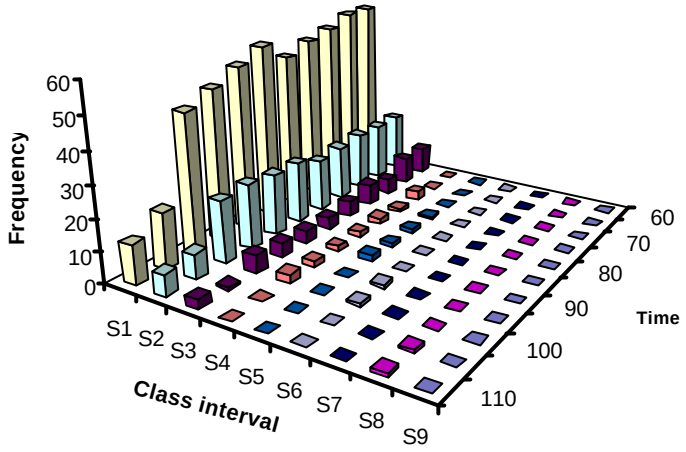

Figure 2.3.1.8 Progressive evolution of the cluster size distribution for the 50 MPa loading of the Delaunay/ Material 1 sample. (Note the change to bimodality at time 95).

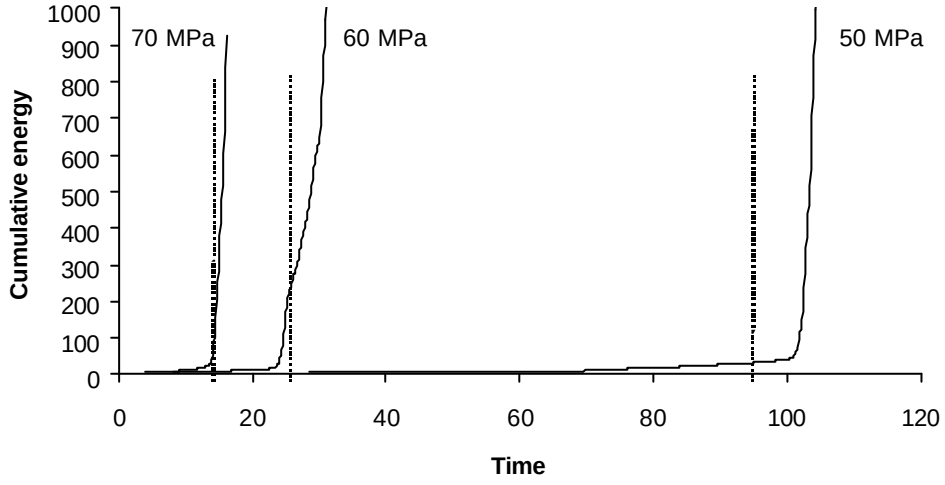

Figure 2.3.1.9 Cumulative energy release curves for different loads on the Delaunay/ Material 1 sample, including the times at which the cluster size distribution becomes bimodal, marked by vertical lines.

2.3.2 Statistical determination of variability in rocks relevant to the mining industry

The variation of the properties of different rock is well known, but has not often been quantified. Variability exists within a rock mass on all scales. Rocks consist of crystals or grains that have different sizes and are cemented together by various rock forming minerals. At larger scales, the rock has been affected by millions of years of tectonic activity that have introduced faults, joints, bedding, veins and many other structural features (Johnson and Schweitzer, 1996). These structural features are distributed throughout the rock mass and result in a variation of rock engineering properties, such as strength and moduli, at all scales.

Previously, the focus of numerical model development was to develop models that consider the rock mass as a solid continuum. Discontinuities could be included as flaws, but were seldom considered to have a statistical distribution of properties. Research work for this and other SIMRAC projects (Napier et al, 1995, Napier et al, 1999) over the past few years have identified the need to consider spatial variations in the material parameters, as being fundamental in creating the conditions that cause the failure processes to occur simultaneously on all scales. For example, displacement discontinuity studies of uniaxial and triaxial compression and extension tests (Sellers and Napier, 1997) showed that the presence of flaws was a necessity for imprinting the final localized failure plane. The density and distribution of flaws is just as important as the small scale material properties for determining the ultimate stress-strain response of the sample.

Other researchers (e.g. Tang and Kaizer, 1998) have also highlighted how the prediction of the fracture processes occurring in rockbursts is dependent on the specification of statistical variations of material properties within the sample. The work of Tang et al. (2000) suggests that rocks, on the laboratory scale can be modelled using Weibull distributions of the elastic moduli and compression strengths. The statistics of many structural features have been described in the geological literature. Dykes, joint spacing, and faults have all been assigned statistical properties in many case studies. The determination of any particular distribution and parameters must be carried out within each specific geotechnical area.

The testing of numerical modelling predictions against laboratory test results requires that the variation of material properties should be determined at the laboratory scale. The elastic moduli and fracture mechanics properties of many rock-forming minerals have been calculated independently (e.g. Atkinson and Avdis, 1980), however, finding a method of quantifying the variation in rock properties on the spatial scale of a rock test specimen has been difficult. The Shore Schleroscope measures the rebound height of an impactor that is dropped onto a sample

(ISRM,) and provides a means of estimating the elastic properties of the material at the point of impact. The results have been calibrated to estimate other properties such as the rock strength. For this project, the spatial variation in Shore hardness has been applied to compare the statistical variation of rock properties for four rock types. The rock types considered were Elsburg quartzite, Ventersdorp Contact Reef, Merensky Reef and Marble Bar quartzite and are all relevant to the gold or platinum mines.

Elsburg quartzite is a metamorphosed quartz-wacke, associated with the footwall of the Vendersdorp contact reef and is a light green rock that contains fine to medium sized grains (0.24mm - 1.52mm) set in a light beige matrix, consisting mostly of mica. The quartz content is about 84 % and the rock texture is weakly schistose and stylolitic. The unconfined compression strength ranges from 120 MPa to 180 MPa and the Young's modulus varies between 55 GPa and 65 GPa. The Poisson's ratio is 0.2. The Marble Bar quartzite is a light-grey rock forming part of the Witwatersrand supergroup, but does not occur near gold reefs. The rock is a fine grained (0.072mm - 0.56mm) metamorphosed quartz-arenite with a quartz content of 95%. Small clots of muscovite are coarsely distributed throughout the rock. The rock has a Young's modulus of about 85 GPa and a Poisson ratio equal to 0.15. The unconfined compression strength is about 350 MPa. The Merensky Reef is a coarse grained pegmatoidal pyroxenite with subhedreal grains of orthopyroxene, clino pyroxene, and plagioclase, and minor supphides. These grains are about 10mm in diameter.

The Ventersdorp Contact Reef(VCR) is a middle Elsburg formation that is a green-grey medium grained conglomerate. The rock consists of medium grained, subrounded white vein quarzite pebbles up to 3cm in diameter and medium to fine grained sub angular grey quartz pebbles in a khaki green matrix with dessiminated pyrite.

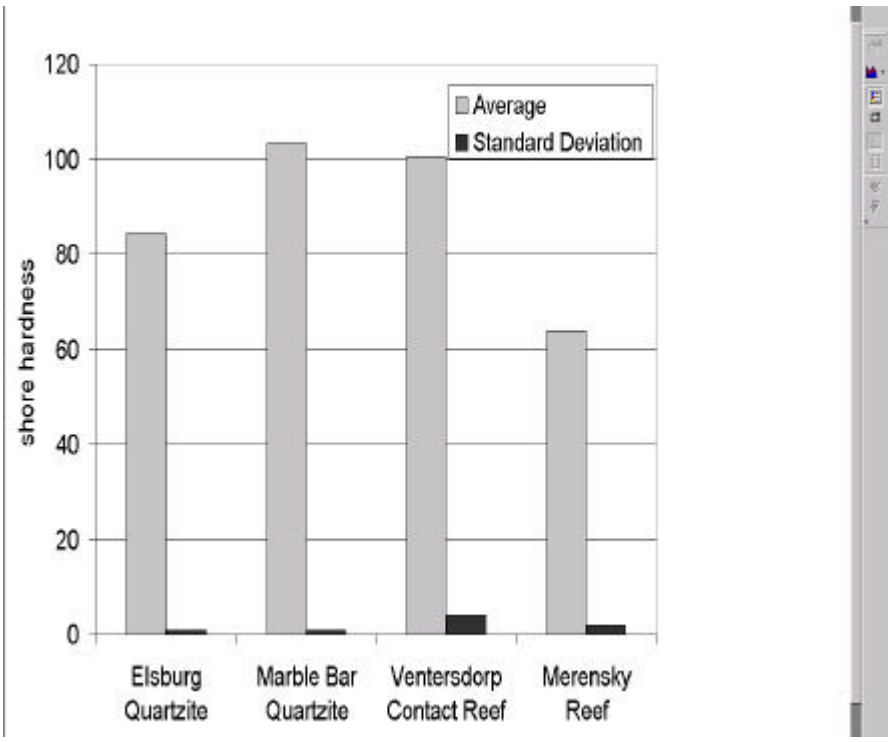

Figure 2.3.2.1 Averages and standard deviations of shore hardness for four rock types

To investigate the spatial variability, a matrix of 7 rows and 7 columns was drawn onto the surface of a sample with each block having a side length of 10mm. To remove the effects of surface roughness, and cutting marks, the surfaces were ground according to the ISRM specifications for compressive strength tests (ISRM, 1978). Thirty Shore rebound hardness tests were performed in each block of the matrix. This is slightly different to the ISRM specifications that state that 5mm should separate each impact, but was required due to the relatively small amount of sample available and to facilitate the testing. The plasticity index tests were then performed at the approximate center of each block. The same point was impacted thirty times.

The Shore hardness of each block was calculated in the standard manner, by removing the highest and lowest 5 points, and then calculating the average of the others. The average and standard deviation of the shore hardness for each of the four rock types are given in Figure 2.3.2.1. The 1470 rebound tests for each rock type were then ordered and plotted against their position in the sequence as shown in Figure 2.3.2.2. The plots are equivalent to the cumulative probability distribution function F(r) of the rebound number r for each rock type.

The numerical models presented by Tang et al () apply a Weibull distribution as a measure of the statistical variability of the sample. The Weibull cumulative probability density function is given by

$$F(x) = 1 - e^{-(x/b)a}$$

where α determines the shape of the curve and β is a characteristic value of x that scales the distribution. In oder to provide data and compare with the models by Tang et al. (2000), a Weibull distribution was fitted to each curve. The method involves plotting ln(Ln(1/(1-F(r)))) against ln(r) and fitting a straight line to the result. The parameter α is equal to the slope m of the straight line and β= exp(c/α), where c is the y intercept. This is one of many ways of fitting the Weibull distribution (e.g. Statsoft, 2002). The predicted distributions are shown in Figure 2.3.2.2. The distributions fit the more homogeneous rock types e.g. the two quartzites and the Merensky reef better. The value of the parameter α is high for these rock types, as suggested for uniform rock types by Tang (). The fit is poor for the Venterdorp Contact reef. The plot of ln(Ln(1/(1-F(r)))) against ln(r) is bilinear, indicating that two Weibull distributions are required to fit the data. This can be interpreted to mean that there is considerable variation in Shore hardness in the Matrix and grain boundaries, but that there is relative homogeneity between the quartz grains. The distribution would change significantly for other similar size samples, and may only stabilize once there was enough spatial variation in the test positions.

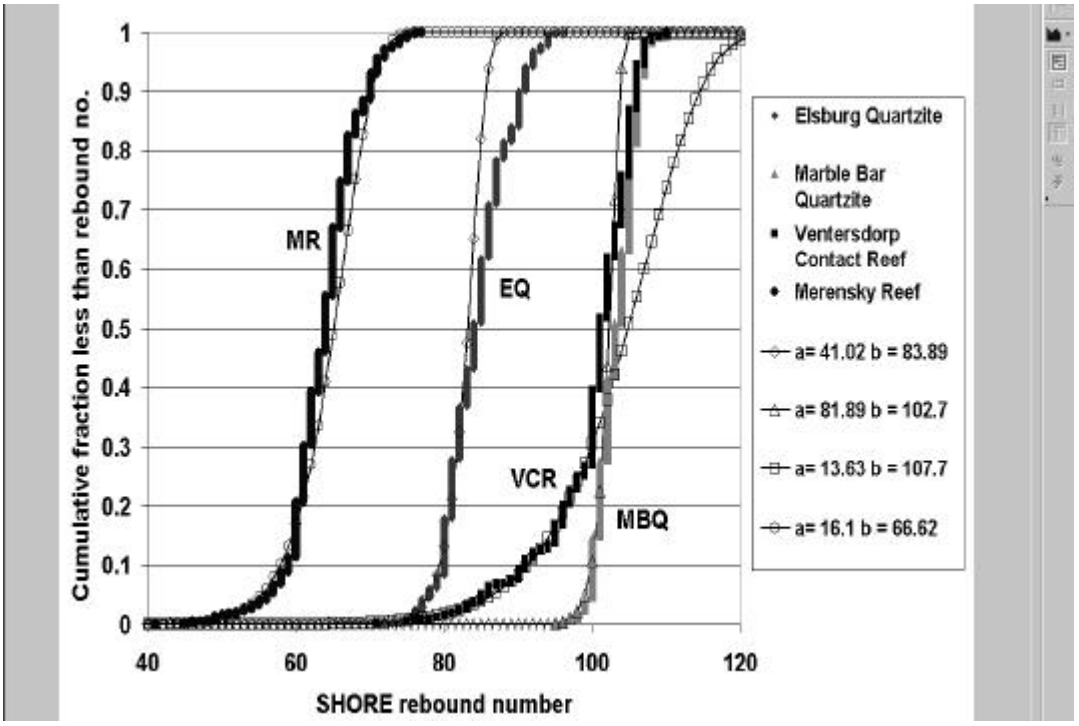

Figure 2.3.2.2 Observed and predicted Weibull cumulative distribution functions of shore hardness for four rock types

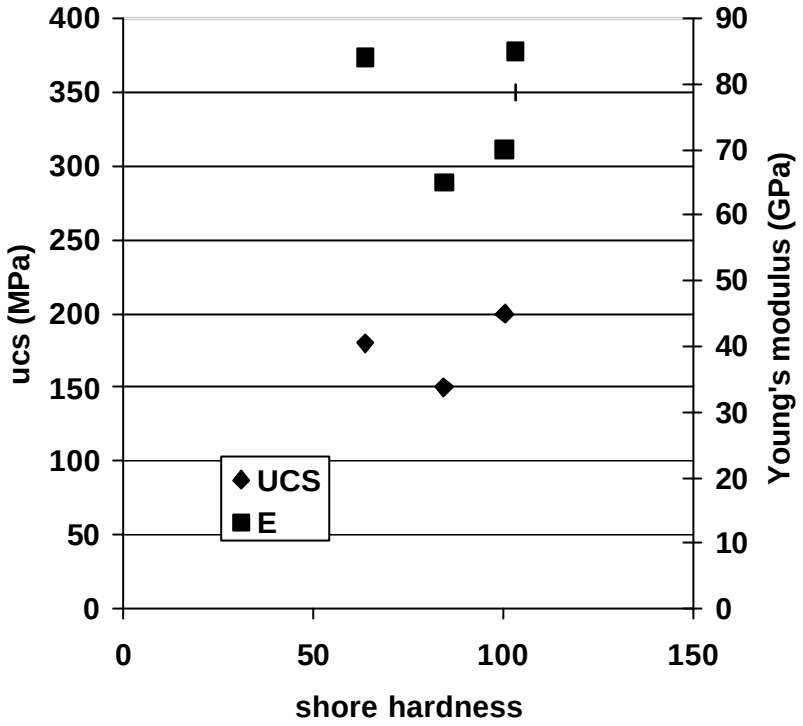

Figure 2.3.2.3 Relationship between Shore Hardness and unconfined strength and Young's modulus.

The Shore plasticity index was determined for each rock type by impacting the center of each block 30 times. The change in the Shore rebound number with the number of hits is shown in Figure 2.3.2.4. Histograms of the percentage change between the maximum and minimum hardness values for each block are shown in Figure 2.3.2.5. The fine-grained rocks with little matrix material show very low changes in the rebound number. The chances of hitting matrix material being very small. The coarser grained Merensky reef has values of rebound number that are more evenly distributed. The VCR has values which range from the lowest to the highest, but the small number of high values is due to the low percentage of matrix in this particular sample.

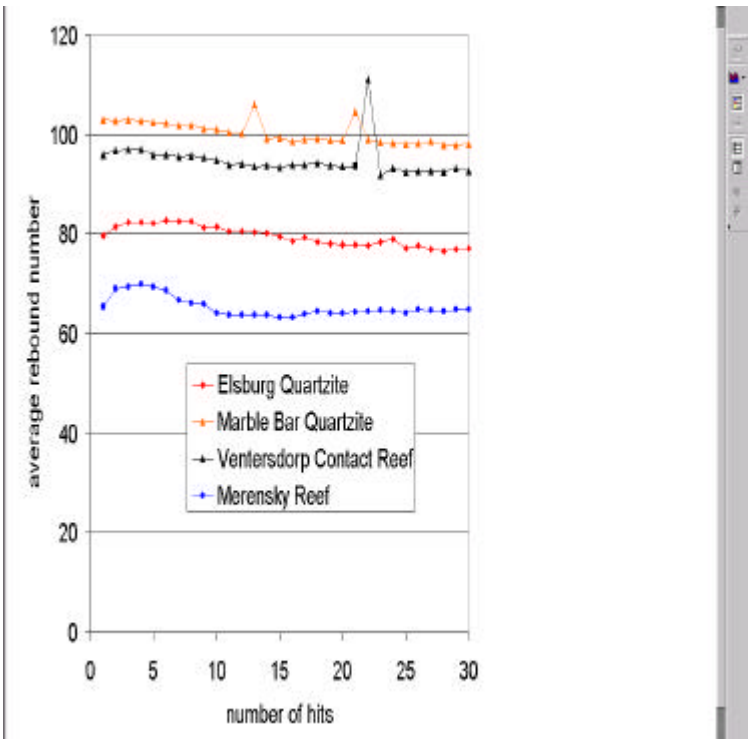

Figure 2.3.2.4 Change in average rebound number with number of hits for four rock types

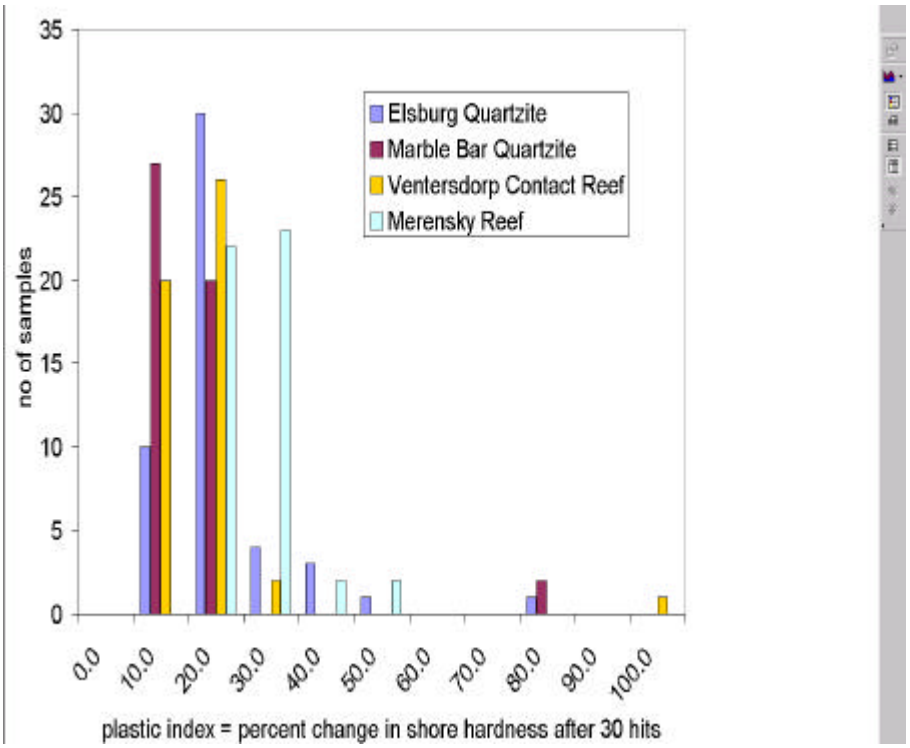

Figure 2.3.2.5 Change in average rebound number with number of hits for four rock types

The Weibull plot of ln(Ln(1/(1-F(pi)))) against ln(pi) for the plasticity index data is shown in Figure 2.3.2.6 and indicates the futility of fitting a Weibull distribution to this data using a linear regression. More elaborate tests from geostatisics to study correllations of the length scales are required to be able to interpret the grain size from the hardness results.

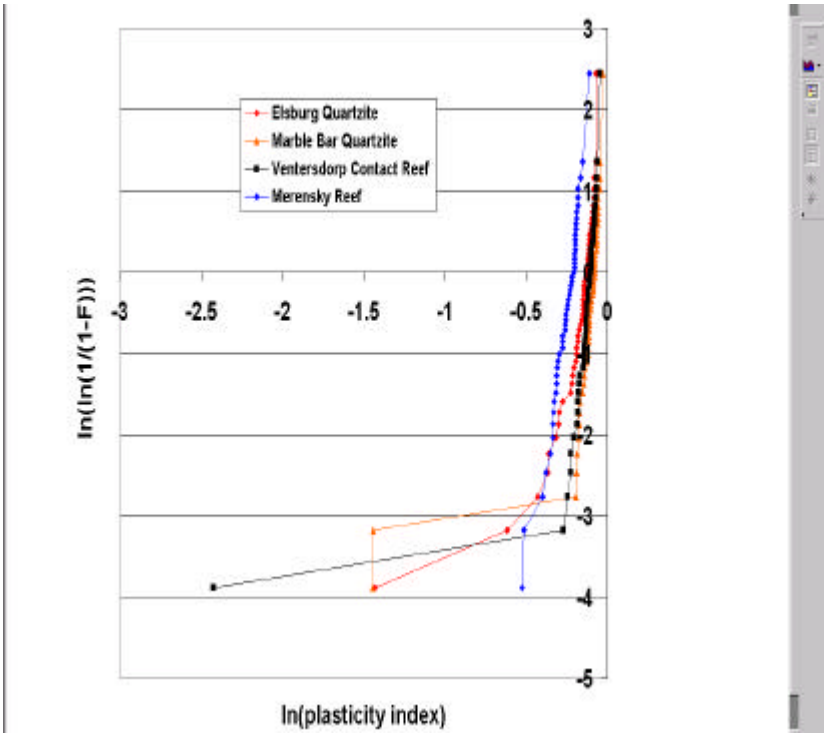

Figure 2.3.2.6 Weibull plot of plasticity index to determine Weibull parameters

The results of these tests illustrate that the inherent variability in different rock types can be quantified and should be accommodated in numerical models. The variability is dependent on the relationship of the sample size to the grain size distribution. The implication of these studies is that the rock behaviour is controlled by variability that occurs on a relatively small scale. Numerical models of the large scale rock mass must consider these small scale variation, as well as the variations such as veins, joints and faults that exist on intermediate scales.

2.3.3 Point kernel approach for considering statistical uncertainty in rock mass properties

The analysis of the state of stress and potential for damaging rockbursts on a mine-wide scale in South African gold mines presents an extremely difficult problem due to the large area of the workings and the very narrow seam widths. Early workers have considered elastic analytical solutions that were then extended to become the early boundary element analysis codes such MINSIM. However, rockburst and seismic events are nonlinear, dynamic events that introduce permanent deformations into the rock mass, through the creation of new fault surfaces or by slip on pre-existing weaknesses. The addition of nonlinear fracturing processes has been considered using a number of approaches such as the explicit crack growth and tessellation boundary element models included in DIGS, but require special numerical techniques for large scale problems. Consideration of the seismic response confirms the structural observations that faulting, fracturing and rock bursting happen regularly and on a number of different scales of length and time.

The analyses of these multiple scales of geological features in full three-dimensional models has been successful for limited problem sizes and for models that limit the nonlinearities to the plane of the excavation. However, capabilities for predicting or reproducing possible event size and time distributions, stope closures and dynamic damage due to the self-organizing fracture coalescence processes on many scales remains a significant challenge. Seismic events occur on all scales and will result from slip on planes of weakness or, when the stress is sufficiently high, will create fresh discontinuities. The dominance of these planar features in controlling the rock mass behaviour suggests the application of boundary element techniques. However, the multitude of different scales places great demands on computational resources. A move to meshless methodologies has been taken in computational fluid dynamics – another field where the consideration of nonlinearities on multiple scales is required.

A combined meshed/meshless methodology that builds on the successes of the mine-wide boundary programs such as MINSIM and incorporates the fracturing processes in a meshless representation is based on the point kernel approximation of displacement discontinuity influences. The proposed methodology combines a meshless representation of slip on multiple interacting discontinuities with standard boundary element based mine planning software. The meshless component consists of “virtual elements” that are not included in the solution, but transmit the influence of slip displacements from a single point in the model using the point kernel representation of the displacement discontinuity (Figure 2.3.3.1). This is able to

approximate element based models, but significantly reduces the computational overheads that are required to treat explicit crack discretisation and intersections. Directional slip information gained from observed seismic events is transmitted directly by “passive virtual elements”. A set of “active virtual elements” can also be included at random or on predefined planes to extend the integration concept to permit forward modelling to predict future seismic activity. Active points are assigned rheological properties and can slip when their assigned strength is exceeded.

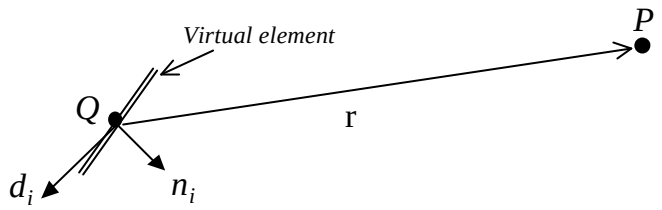

Figure 2.3.3.1 Schematic of a virtual element at point Q transmitting influence to point P.

Example applications have been used to demonstrate how the passive and active methods are able to mimic time dependent stope closure profiles, as observed underground. Forward modelling of the rock mass response and predicted seismic activity was shown to depend strongly on the choice of statistical distributions of the material and geometric properties of the active virtual elements.

A model of two faults passing through a ledging stope was used as an example (Figure 2.3.3.2a). A series of runs with different distributions of cohesion and source sizes were used to investigate the effect on the predicted seismic activity of randomly selecting the material properties. Figure 2.3.3.2b shows the slip distribution, projected onto the reef plane, when the cohesion is selected to range between 0 MPa and 2 MPa and the source size varies between 0m and 12m. The Gutenberg-Richter law considers that natural seismicity has a cumulative frequency – magnitude distribution that has a slope of b=1. Variations from the ideal power law behaviour provide some insight into the loading and underlying structure of the region producing the seismicity. The frequency-magnitude plot provides a useful means of comparing analyses. A number of analyses were run with the “active virtual element” model of Figure 2.3.3.2 to establish the effect of uniform or exponential distributions of radii and cohesion. The frequency magnitude distributions are shown in Figure 2.3.3.3a for a range of the exponential distribution parameter b.

Stopes underground are known to exhibit time dependent closure and this has been attributed to time dependent slip on discontinuities. The closure of the centre point of the raise is plotted as a function of model time in Figure 2.3.3.3b. The profiles demonstrate that both the closure and ride are affected by the slip on the discontinuities. The effect of each event is small and decreases rapidly with distance from the stope and the cumulative effect of large numbers of events are needed to produce observed closure profiles. In addition, the cumulative effect of repeated dynamic stress waves passing through the fractured rock mass should be considered. The rapid reduction in the influence of the displacement discontinuity implies that significant numbers of slip planes must be added to the model to reproduce observed behavior. In addition, the cumulative effect of repeated dynamic stress waves passing through the fractured rock mass should also be considered.

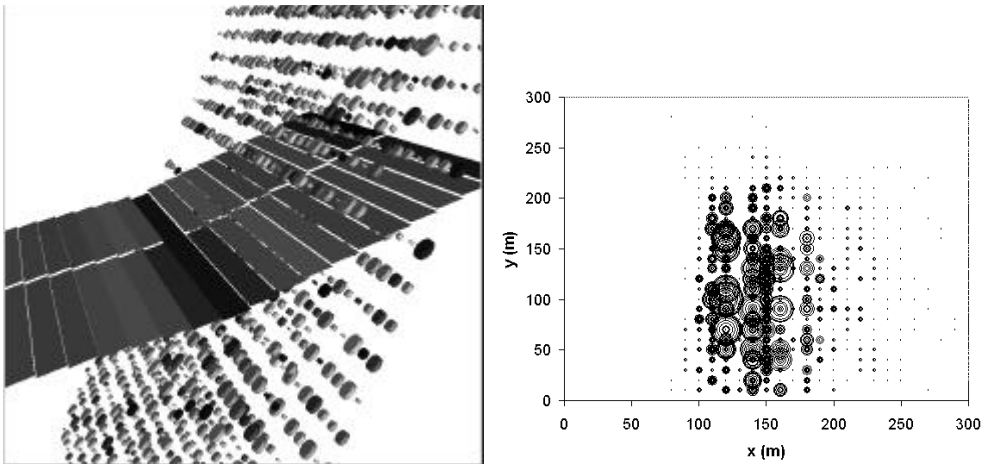

Figure 2.3.3.2 (a) Model of ledging stope mining through a zone containing two faults (b) Seismicity projected onto reef plane for random cohesion and radii. The area of the bubbles is scaled to event magnitude.

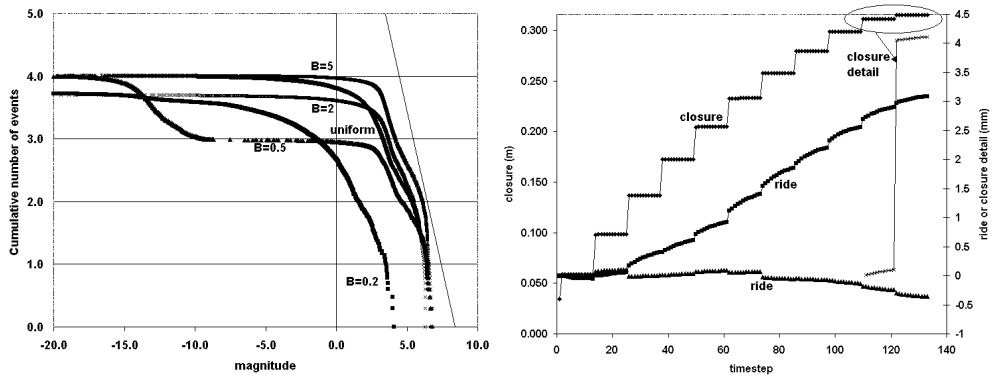

Figure 2.3.3.3 (a) Comparison of frequency-magnitude distributions to demonstrate the influence of uniform or exponential distributions property distributions. (b) closure of the central raize.

The point kernel approach has shown that large numbers of faults and discontinuities can be considered in a single analysis. However, case is required in positioning of the elements as the stress singularities induced by the point or constant elements may results in overestimates of the extent of failure. The ability to input a statistical distribution of input data for the position and properties of geological discontinuities implies that the point kernel method could provide a good starting point for the application of reliability based procedures (e.g. Harr, 1987, Lilly and Li, 2000) in the design of tabular openings at depth and for calculating the risk related to seismic events.

3.0 Effect of scale in the assessment of rock deformation mechanisms

3.1 Understanding the size effect in rock masses

3.1.1 Review of theories of size effect

Size effects have been of considerable practical interest in rock mechanics for a number of years, because they impact directly on the application of material parameters determined in the laboratory to the design of excavations and structures in the field. In order to design pillars, tunnels and other underground excavations, the rock engineer must be able to estimate the in situ rock strength. The most convenient way of determining the strength is to drill core samples from the rock mass and test these in the laboratory. The laboratory strength must then be related to the in situ strength. However, even in the laboratory, the strength appears to depend on the sample size. Thus, methods must be developed for extrapolation to the strength underground. Numerical model parameters are determined from laboratory tests and so it is important to understand how the models respond to changes in the size of the structure being analysed.

The considerable literature on size effects was reviewed in an interim report (Sellers, 1999) that is submitted as a supplementary document. The review focused on the theories of size effect, experimental evidence and the implementation in numerical modelling procedures. The main issues to be investigated are

- How should material descriptions be formulated to reflect size effects?
- Is there a way of predicting *in situ* response from laboratory testing?
- Are there size effects in both, pre- and post-failure behaviour and how do they differ?
- Can the material model incorporate the size effect without the need to specify different parameters for any given size of the structure being analysed?
- Can standard model formulations be modified and how?

A size effect is manifested when the failure strength is affected by the representative volume of material under consideration. The selection of the way in which certain material parameters e.g. energy release, and crack lengths change with the size of the representative volume, or

structure volume determines the size effect. Bazant's size effect law (e.g. Bazant and Chen, 1997) requires that the process zone width is independent of the structure size. As shown in Figure 3.1.1.1a, a crack in a quasi–brittle material such as rock is surrounded by a process zone that will relieve the stress in a region surrounding the crack. For large structures of dimension D, the process zone is small relative to the structure and the structural response can be predicted from the linear fracture mechanics theory as shown in the size effect curves of Figure 3.1.1.1b. For small structures, the stress relief zones will be negligible relative to the thickness of the process zone and there is no size effect. This is consistent with the strength theories, such as the theory of plasticity, that have no characteristic dimension.

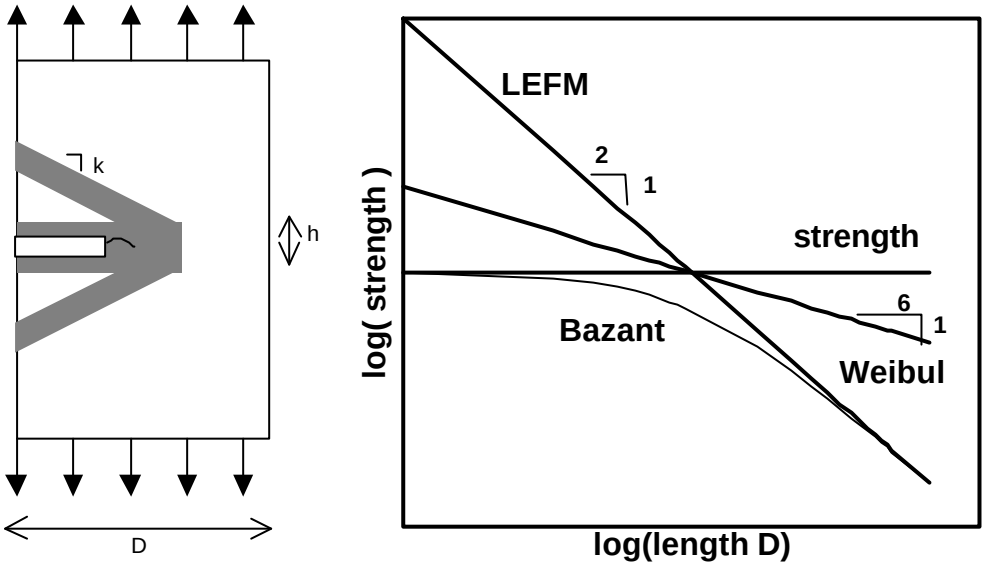

Figure 3.1.1.1 a: Structure used to develop size effect law (after Bazant and Chen,1997). b: Schematic diagram of size effect laws

A statistical theory of material strength and size effect was proposed by Weibull in 1939 (see Jager and Cook, 1979 for discussion of this theory). The main assumption underlying the Weibull law is that the number of flaws in any material is proportional to the volume of the material. Weibull's theory of statistical size effect is based on the assumptions that the structure fails instantaneously at the initiation and immediate propagation of the macroscopic fracture. There is a negligible process zone and no gradual crack growth with stress redistribution. The Weibull law then implies that the probability of failure increases with the increase in volume of the sample. Carpintieri et al. (1997) felt that the implicit assumption that there is a higher probability of finding a critical flaw in a large sample does not represent real materials. Bazant and Chen (1997) noted that the theory would not apply for quasi-brittle structures that are *designed* not to fail immediately after crack initiation. Obviously, for mining applications the notion of design for structural failure must be interpreted differently.

Jaeger and Cook (1979) considered that the size effect is due to the presence of stress gradients. Hodgson and Cook (1970) compared uniaxial tests that had only a small size effect with punch tests that showed significant strength decrease and concluded that the stress gradient within the punch test was responsible for the size effect. Carter (1992) discusses the application of the stress gradient theories to the borehole break out problem. Gonano and Brown (1975) concluded that the stress gradient theory of size effect is an oversimplification of the real response and cannot account for all the aspects of the size effect. They postulated that the size effect is induced because the energy requirements of the test machine depend on the size of the sample.

These implied links between the material structure, the material response, the representative volumes and the way that failure is defined emphasise that the understanding of the size effect is fundamental to the correct representation of material response. The definition of failure is also important to the definition of size effect. Weibull and statistical laws are relevant to structures that fail as soon as the most critical flaw propagation. Bazant's law requires that the sample does not fail immediately. The application of Bazant's method in compression is largely dependent on the assumptions regarding the failure mode.

The first question posed in this study was related to how the size effect affects the choice of material parameters. It would seem that most numerical modelling work is performed by assuming that the material parameters to be applied *in situ* are some fraction of the values measured in the laboratory. Scale effects arise in the laboratory from testing sub-parts of the representative volume. Rock is heterogeneous at small scales and often has a number of characteristic length scales defined by crystals, grains, joints, bedding planes and faults. Excavations and boundary dimensions, in the case of finite size structures, will introduce further length scales. Thus, small-scale samples usually form the stable part of the material, the weaker constituents being discarded during sampling, selection or preparation. Larger samples will be able to remain coherent in spite of the presence of weaker parts. Laboratory test results, therefore, will always form an upper bound to the strength envelope.

The data from rock tests has been analysed in detail by a number of authors and conferences (e.g. Pinto da Cunha, 1990, 1993, Mazars and Bazant, 1989, Jaeger and Cook, 1979, Heuze, 1980, Bandis, 1990, Panek and Fannon, 1992, Martin, 1997, Pinta da Cunha, 1993a,b, Bazant and Chen, 1997). In the literature referring to concrete, the size effect in bending is most often considered (e.g. Bazant and Chen, 1997). These results can be applied to rock in tension, and to understand the processes of quasi brittle fracture in tension. The conclusion of most of these studies is that a size effect with respect to strength is observed in many laboratory tests. The

most often studied test on rock is the uniaxial compression test because it is simple to perform and is analogous to the problem of pillar stability. The strength generally decreases with increasing size (Bandis, 1990, Martin, 1997, Bieniawski and van Heerden, 1975, Bieniawski, 1977, Hoek and Brown, 1980). Often it is observed that the strength reduction effectively ceases above a critical size, as shown in Figure 3.1.1.2a. The critical size is usually related to the test sample diameter and is never normalised to an intrinsic property of the rock e.g. the mean grain size. Hoek and Brown present an equation that suggests that the strength reduces to about a third of the UCS of a 50mm diameter sample, as shown in Figure 3.1.1.2. Martin (1997) studied tunnel and borehole breakouts and indicated that there is a further reduction in strength with the transition from large scale laboratory tests to field tests. Scale effects have also been observed in *in situ* stress measurements (Cusiat and Haimson, 1993).

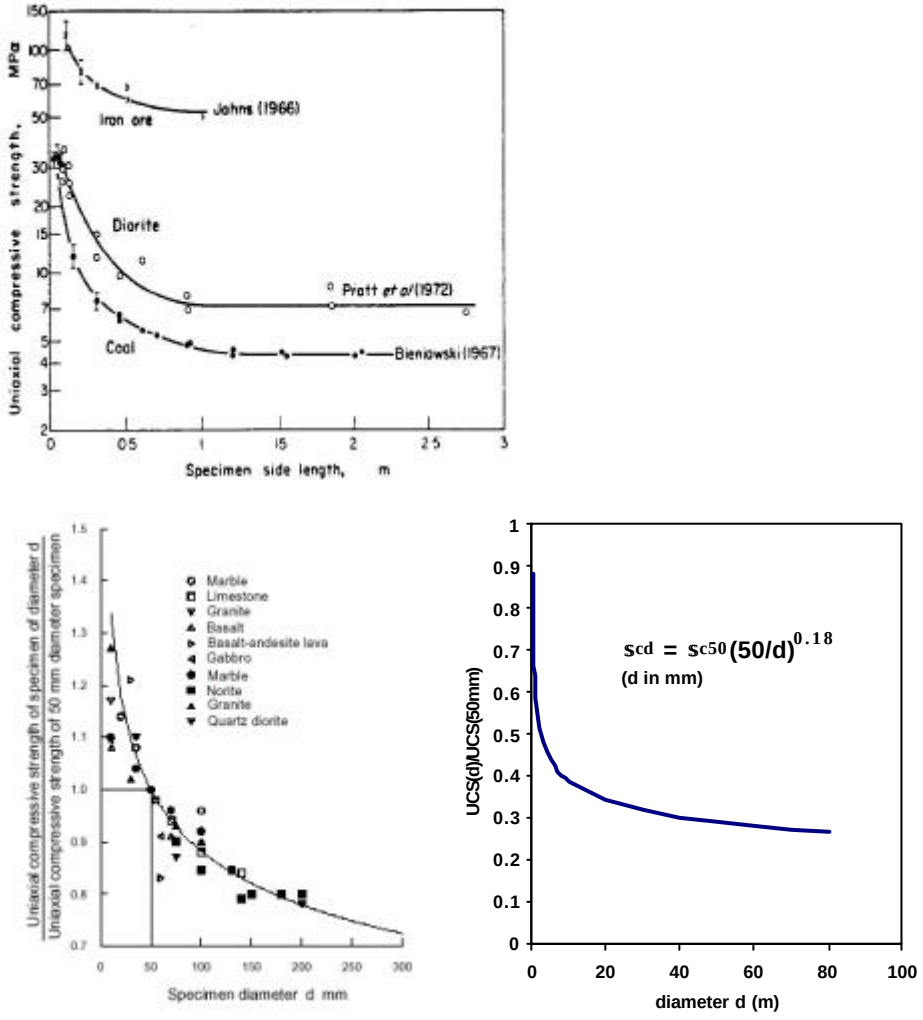

Figure 3.1.1.2 a) Example of experimental results showing the decrease in strength with size from Bieniawski and van Heerden (1977) and b) after Hoek and Brown (1980) and c) equation from Hoek and Brown extrapolated to 80m diameter

There is very little information on the size effect in triaxial compression. Baecher and Einstein (1981) found that the onset of crack initiation did not appear to result in a size effect, but the ultimate failure was dependent on the sample size. However, Singh and Huck (1972) found that

granite showed a strength decrease with size in triaxial compression, but that limestone did not. Most importantly for non-linear material modelling, there is very little experimental research on how the increased sample size affects the post- failure response. Hudson et al. (1971) concluded that the results of tests on different size samples, e.g. those shown in Figure 3.1.1.3, tended to indicate a strength decrease with increasing size and decreasing width to height ratio. The larger samples show a less ductile post failure response.

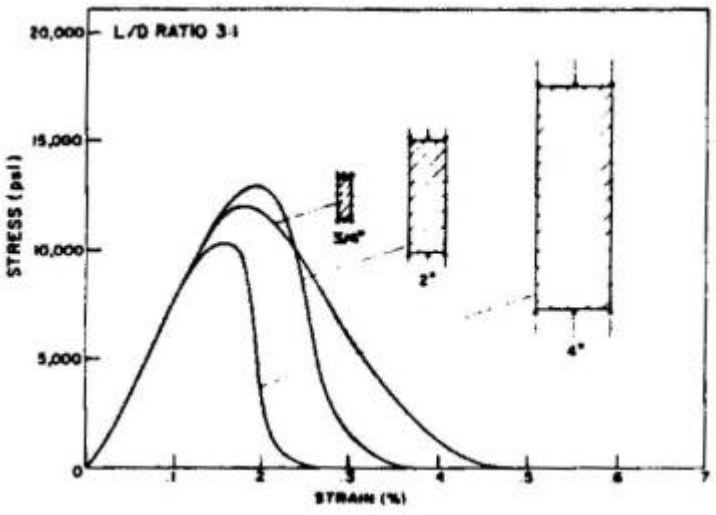

Figure 3.1.1.3 The effect of sample size and shape on strength and post failure response (after Hudson et al. 1971).

Discontinuities can also show many size effects and there is considerable controversy surrounding the measurement and description of the effect. Planar joints are expected to have strengths that are independent of size and in-filled joints will exhibit no size effect as long as the in-filling was thicker than the asperity height (Bandis, 1990). Rough joints will exhibit size effects as the behaviour depends on where the sample was taken (Bandis, 1990). If a sample is a small part of a larger undulation in the joint, testing the small specimen will give a different result than would be obtained from testing of the large joint. The increase in joint area leads to an increase in peak shear displacement, a transition from brittle to plastic response, a decrease in peak dilation, a decrease in apparent Joint Roughness Coefficient and a decrease in Joint Compressive Stress with size (Bandis et al. 1981). Hencher et al. (1993) repeated the experiments of Bandis et al. (1981), but could not confirm these size effects as shown in Figure 3.1.1.4.

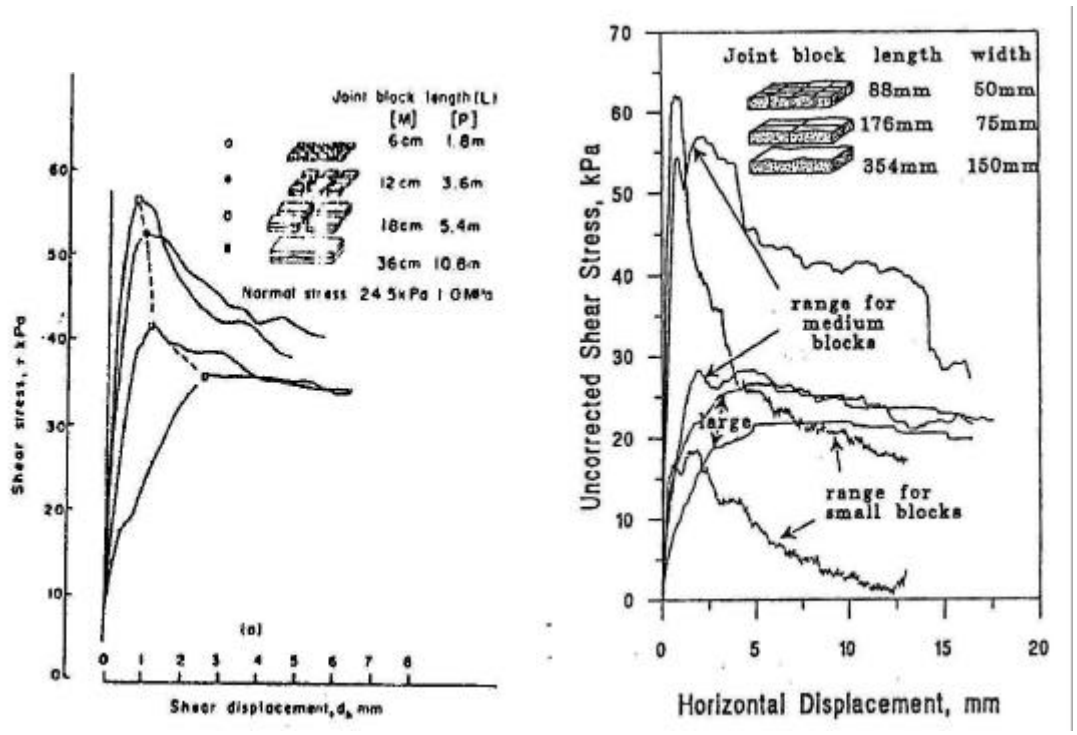

a: b:

Figure 3.1.1.4 Effect of sample size on joint shear behaviour. a: Consistent strength decrease and deformation increase with size from Barton et al. 1991. b: Variable response from Hencher et al. 1993.

Protodiakonov showed that the strength of a jointed rock mass depends on the number and spacing of the discontinuities (Jaeger and Cook, 1979). Moon and Kim (1993) showed theoretically that the strength and modulus decrease with increasing crack density.

Fault scaling laws usually consider infinite bodies and so the relationship between frictional strength and the crack length defines the size effect (Scholtz, 1990). Rate and state variable friction laws (e.g. Ruina, 1983) were developed because laboratory tests showed that the frictional strength depended on a number of state variables such as the critical slip distance and the velocity of the slip. Thus, it is important to determine how the critical sliding distance L scales with contact size. From laboratory experiments, L is calculated to be about 10 μm. However, to correspond with field observations, the length needs to be set to about 1 cm (Tse and Rice, 1986). Thus, the characteristic length increases with increasing size (Marone and Kilgore, 1993).

Thus, even after extensive research, a number of unresolved questions remain (Pinta da Cuhna, 1993a). These include

- Definition of laws describing trends in mean values and scattering
- Determination of test sizes beyond which there is little effect

- Relationships between laboratory and *in situ* tests to optimise selection of properties for jointed rock masses.

The aim of solving these problems would be to identify the selection of the size, type and number of tests to determine the parameters of numerical models and hence solve rock engineering problems in a cost effective and accurate manner.

The second issue relates to the prediction of *in situ* response from laboratory tests, which can be approached in four different ways:

- reduce the material parameters based on a size effect law developed from test results over a range of sample sizes, or assumed from the literature.
- test samples that are large enough to be above the critical size and hence are representative of the *in situ* response.
- perform large scale *in situ* tests.
- consider that the mean of the tests at small sizes represents the response at large sizes

All four methods have disadvantages. The first requires many tests or an assumption regarding the size effect law. The second requires large scale testing equipment. The critical size is about 1m for most rocks and is therefore impractical in most laboratories. Large scale *in situ* tests are possible, but require expensive equipment. The fourth method requires the assumption that the weaker samples of small size are tested, which is not the case unless special sampling techniques are applied, and in many cases the samples will be too weak to prepare for testing.

The third question asks whether numerical models are able to represent the scale effects without specifying or extrapolating a set of parameters that relate to a particular size. Some numerical models are able to do this, however a characteristic size must be included in the formulation. The methods that have been applied for this purpose include non-local damage Bazant and Oh (1996), crack band models (van Gils et al., 1996), gradient theories (e.g. Triantafyllidis and Bardenhagen, 1996) and Cosserat continua (Muhlhaus et al., 1991). Random particle models are also able to exhibit size effects (Jirasek and Bazant, 1995, Cundall et al. 1996, Potyondy et al. 1996). The spacing of the particles limits the localization width and controls the energy dissipation per unit length of fracture extension. With the correct choice of the particle size and the micro-strength parameters applied to the particle bonds, a size effect law can be reproduced.

The final question asks whether standard computational models can be modified to include size effect. Few computer models are able to exhibit a size effect. Most, especially the plasticity models with strain softening, require that the parameters be selected for a specific problem size. A number of techniques may be modified to include a size effect. The literature study has

highlighted that the understanding of the size effect is fundamental to the development of material models and to addressing issues of extrapolation of test data to the field scale. The study has also raised important questions about the relationship between the behaviour of the intact material, and the intrinsic length scales such as joint spacing, fracture spacing, and structure size. The size effect links the material and the structural response and is the key to the understanding and definition of failure and of post-failure response. These issues must be resolved in order to develop numerical representations of rock masses that are discontinuous at different scales

3.1.2 Experimental data on the size effect in rock

The deterministic size effect method of Bazant (e.g. Bazant and Chen, 1997) is based on the simple premise that larger structures are able to store greater amounts of energy and thus attain critical potential energy levels at lower stresses. The size effect manifests itself as a dependence of structural strength on the structure size. The structural strength is defined as a nominal stress given by the peak load normalised by a typical cross sectional area (Bazant and Planas, 1998)

$$\sigma_N = c_N \frac{P}{bD} \qquad \text{for 2D} \tag{3.1.2.1}$$

where P is the applied load, b is the structure thickness, D is a characteristic dimension and c_N is a dimensionless coefficient which is constant for self-similar geometries of different sizes. In the derivation of a simplified size effect law it is implicitly assumed that geometries of varying size are self-similar. The main assumption for quasi-brittle materials with microstructure and a characteristic length is that there exists a finite and constant process zone of length c_f ahead of a continuous crack. Along the process zone length the transverse normal stress deteriorates from the tensile strength f_t to zero. Adjacent to the crack and the process zone the material releases strain energy in a triangular area defined by the constant empirical gradient k_g. The energy balance condition is invoked such that the strain energy released for a unit increase in effective crack length is equal to the fracture energy dissipated. The basis of the size effect is apparent in the observation that for a unit increase in effective crack length Δa, the larger structure releases more energy.

Considering the experimental setup of a beam in three point bending, for a given ratio of span S to beam height D, the strength reduction with dimension D can be expressed as

$$\sigma_N = \frac{Bf_t}{\sqrt{1+D/D_0}} \tag{3.1.2.2}$$

where,

$$Bf_t = \sqrt{\frac{G_f E}{k_g c_f}} = \text{constant} \qquad (3.1.2.3)$$

$$D_0 = c_f \frac{D}{a_0} = \text{constant} \qquad (3.1.2.4)$$

b is the panel thickness, Gf is the fracture energy dissipated per unit area of crack, a_0 is the initial crack length, f is the tensile strength introduced for dimensional purposes, B is a dimensionless constant and D_0 is a constant with a dimension of length. For self-similar geometries both B and D_0 depend on the material properties and the geometry and not on structure size (a_0/D is constant for self-similar geometries).

Equation (3.1.2.2) is supposed be be applicable to quasi-brittle materials over a size range of approximately 1:20 provided the following hypotheses are fulfilled :

1. Gf is a material constant
2. Energy release is a function of the crack band and the process zone sizes
3. Failure mode remains consistent over the size range
4. The structure does not fail at crack initiation
5. The crack lengths in small and large structures are similar

A set of notched specimens of Elsburg Quartzite having various sizes, as shown in Table 3.1.2.1, were tested for their peak loads. Optimal least squares fitting of the nominal strengths with respect to the size data yields the size effect parameters B, D_0. The approximate size effect equation given in equation (3.1.2.2) can be rearranged into a linear form.

$$Y_j = AX_j + C \qquad j = 1,n \ , \ X_j = D_j, \qquad Y_j = \left(\frac{1}{ó_{N_u j}} \right)^2, \qquad Bf_t = \frac{1}{\sqrt{C}}, \qquad D_0 = \frac{C}{A} \qquad (3.1.2.5)$$

where n is the number of specimens tested. The RILEM methodology for the three-point bend specimen beam with mid-point load P_u gives the maximum normal stress as

$$ó_{N_u j} = c_N \frac{P_{u j}}{bD_j} = \frac{3S_j}{2D_j} \frac{P_{u j}}{bD_j} \qquad (3.1.2.6)$$

where S/D remains constant for self-similar geometries (See Figure 3.1.2.1b). The regression terms are given by Bazant and Planas (1998).

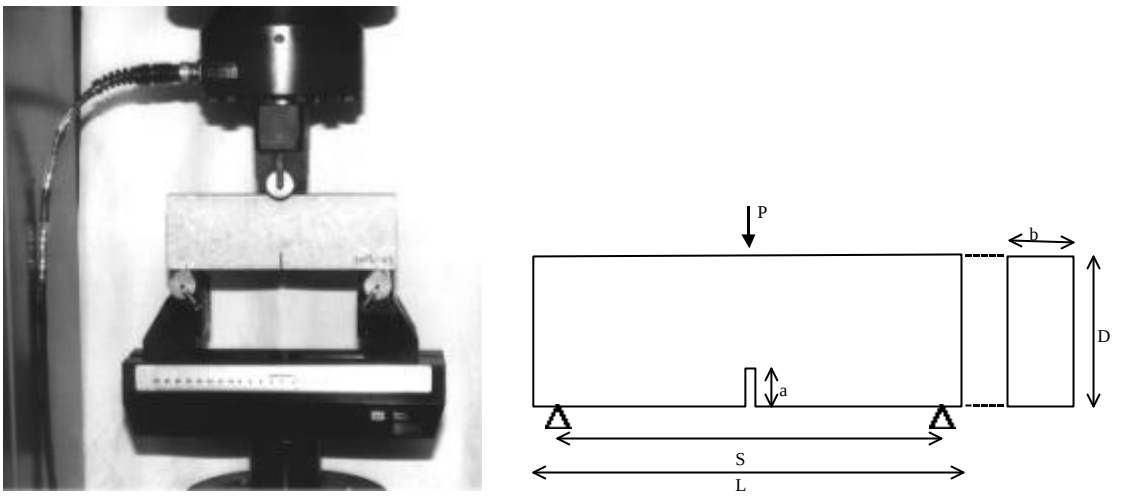

Figure 3.1.2.1 a) Photograph of the beam bending testing and b) schematic showing the dimensions of the beam.

The variation of the strength values and the fitted curved are shown in Figure 3.2.1.2. The results indicate that the tested beam sizes are too small to properly characterize the large scale asymptotic strength decrease with load. The strength is essentially constant within the inherent variation of the rock and falls in the small scale asymptotic region of Bazant's size effect law as shown schematically in Figure 3.1.1.1b. Attempts were made to prepare larger beams for testing, but these were unsuccessful due to the limited size of the available blocks and the presence of discontinuities.

Table 3.1.2.1 Dimensions of beam tests on Elsburg Quartzite.

TEST	b	D	S
	mm	mm	mm
12	18	9	27
11	18	9	27
10	18	9	27
9	18	18	54
8	18	18	54
7	18	18	54
6	18	36	108
5	18	36	108
4	18	36	108
3	18	72	216
2	18	72	216
1	18	72	216

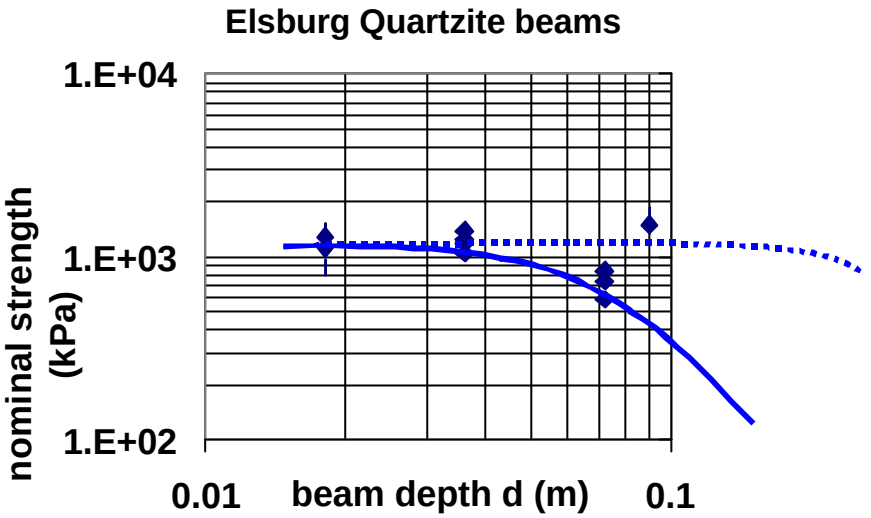

Figure 3.1.2.2 Strength change with beam size for Elsburg quartzite.

Figure 3.1.2.3 is a photograph of the beam close to failure during a test. The associated load deformation curve is given in Figure 3.1.2.4. When the beam is close to the ultimate load, a thin process zone is observed to develop at the pre-cut slot and this gradually extends across the beam width. Attainment of the ultimate load coincides with the process zone extending across the whole sample. The load continues to decrease, but the visible crack is not evident until the load has relaxed almost completely, as shown in Figure 3.1.2.4. This has implications for the observation and interpretation of cracks in the hangingwall of stopes. Cracks close to the stope face are often noted as white lines on the hangingwall. This suggests that they exist as process zones that may carry hangingwall-parallel tensile stresses. The stress in the hangingwall will only be relaxed completely once the cracks are open and are visible.

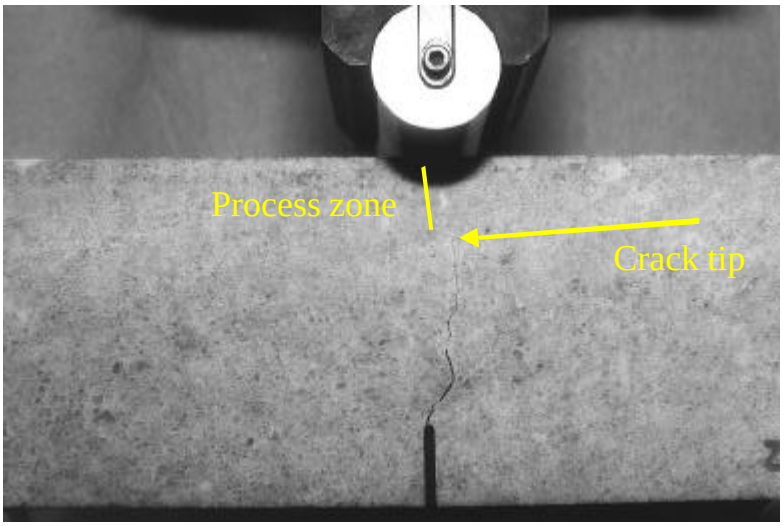

Figure 3.1.2.4 Photograph of failing beam showing the visible crack and the process zone.

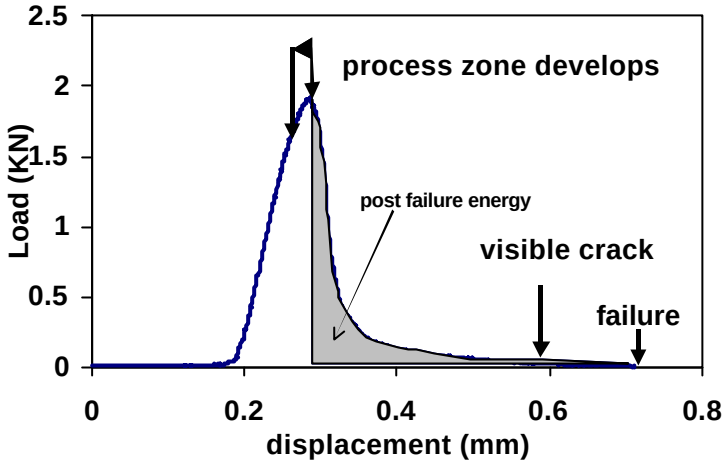

Figure 3.1.2.4 Typical load displacement curve from beam tests

A set of load – deformation curves are shown in Figure 3.1.2.5 to indicate how the load deformation response alters with increasing size. As suggested by Bazant and Chen (1997) amongst others, the beams become stronger and more brittle with increasing size. The post failure load deformation curve becomes steeper indicating increasing brittleness. The post failure energy is a parameter that is required in crack band models (e.g. Bazant and Chen, 1997, Klerck, 2000). The energy is defined as the area under the post peak load deformation curve, as shown in Figure 3.1.2.4, and is expected to be a material constant. This provides an explanation for the increasing brittleness observed in the post peak deformation as the sample size increases. The failure energy values are similar, but display some scatter over the range of sizes tested (see Figure 3.1.2.5b).

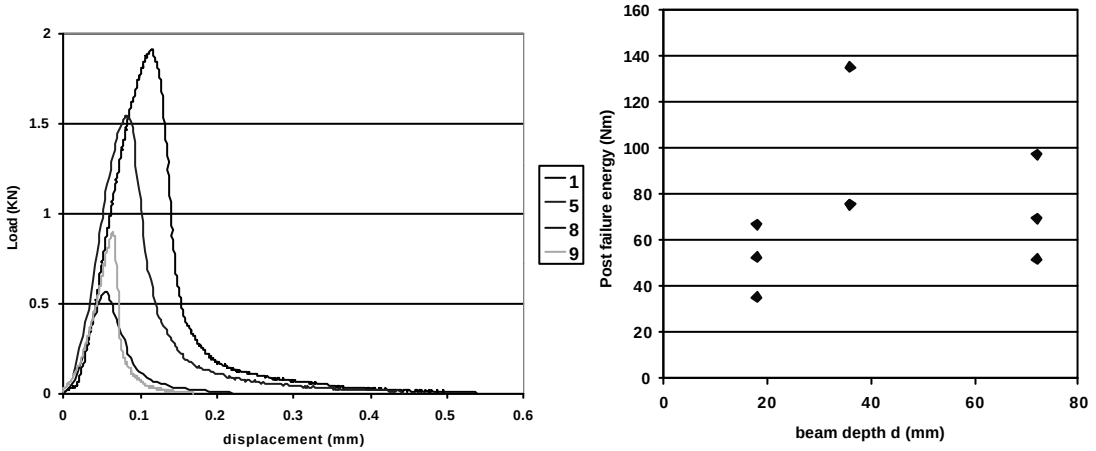

Figure 3.1.2.5 a) Load deformation curves for different size beams and b) the post failure energy related to beam size.

In order to investigate the size effect in compression, a number of uniaxial compression tests were carried out on Elsburg quartzite. Samples were tested in the AMSLER soft testing machine at the CSIR rock testing laboratory. The range of sample sizes was limited by the available block sizes and testing was confined to 25mm, 54mm and 96 mm diameter samples. As can be seen from Figure 3.1.2.7, there is no discernable size effect in this range of sample sizes. Fitting the Hoek and Brown (1980), or other size effect curves is therefore inappropriate. A series of results from indirect tensile tests is shown in Figure 3.1.2.7 and shows an apparently increasing strength as a function of the sample size. However, the size range and the variability in the test results shown in both Figures 3.1.2.6 and 3.1.2.7, tend to suggest that the results are strength rather than volume dominated and that the process zone size in these cases exceeds the sample size.

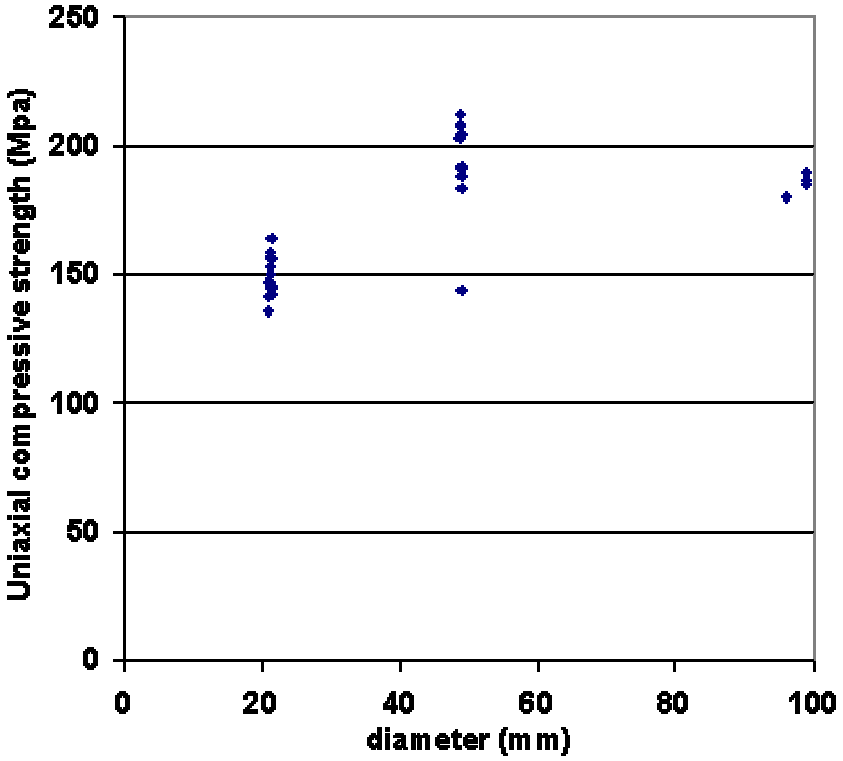

Figure 3.1.2.6 Variation in strength with diameter for Elsburg quartzite in unconfined compression.

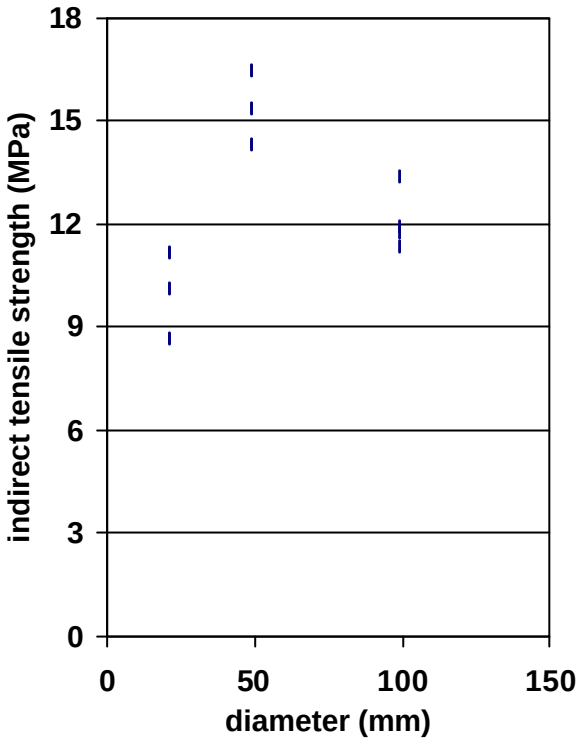

Figure 3.1.2.7 Variation in tensile strength (Brazilian test) with diameter for Elsburg quartzite.

A series of tests were done as part of SIMRAC project GAP 617 to evaluate the size effect for a Middle Elsburg conglomerate reef. The reef has a much wider variation in grain size and contains pebbles that vary from 1mm to 10 cm in diameter. In contrast to the Elsburg quartzite results of Figure 3.1.2.6, a size effect trend appears to be evident in the results of uniaxial compression tests on samples with 1:1 diameter to height ratios. There is considerable scatter in the results of the smaller diameter test results. There are too few large-scale tests to be able to properly compare the statistics of the strength values for each diameter, and the apparent decrease in the maximum strength with diameter may be due to inadequate sampling instead of an inherent size effect.

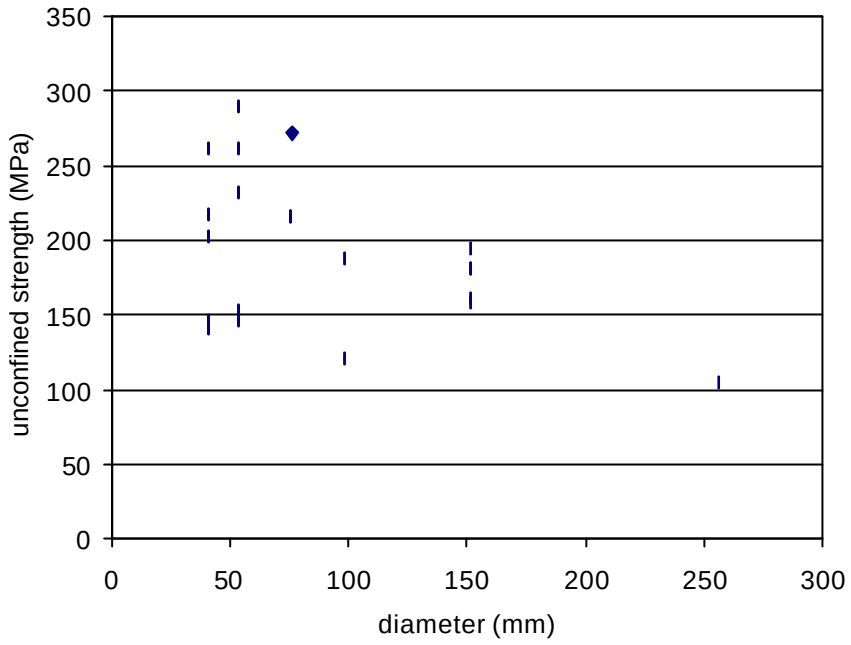

Figure 3.1.2.8 Variation in strength with diameter for Middle Elsburg conglomerate reef from unconfined compression of samples with 1:1 diameter to height ratios.

3.2 Computational methods to represent the mechanisms of failure at different size scales.

3.2.1 Slip and tension-weakening models

Linear slip and tension weakening laws have been incorporated in the DIGS code to enable the simulation of scale and size effects. In particular, a specific formulation has been introduced that can also allow coupled tension and slip weakening. The use of this form of model has important implications for both the simulation of fracture propagation and the replication of certain size effect phenomena. This essentially provides an explicit representation of the size effect theory of Bazant (Bazant and Chen, 1997) as presented in Section 3.1.1. The size effect arises because the energy "supply" is proportional to the strain energy available in a representative volume while energy "consumption" required to propagate fractures is proportional to a representative area of damage. A linear tension weakening model has been tested by attempting to simulate observed experimental results of the formation of "primary" tension cracks from the surface of boreholes drilled in limestone rock samples Carter (1992). Figure 3.2.1.1 shows the simulated size effect for samples with holes ranging from 3 mm to 30 mm radius. In this case, it was found that a number of sensitive factors have to be considered.

(a) The effective material modulus is important. In particular, it may be that the modulus in tension is smaller than in compression.

(b) Deviations from the predicted strength at small hole sizes (see Figure 3.2.1.1) probably arise from additional material failure not directly related to the presence of the hole. This is supported by numerical experiments in which additional failure sites, other than the borehole crown, are introduced. The effect on the simulated load-strain behaviour for a 3 mm radius hole is shown in Figure 3.2.1.2.

(c) The form of the law governing tensile strength as a function of crack opening may be important. The shape of the observed load vs strain curve shown by Carter (1992) for primary crack formation suggests that as crack opening proceeds, the tension-softening slope should increase. Figure 3.2.1.2 illustrates the effect of arbitrarily introducing an increase in the softening slope at a given point in the loading cycle for a 3 mm radius hole. This results in a rapid increase in strain change following the change to the softening slope parameter.

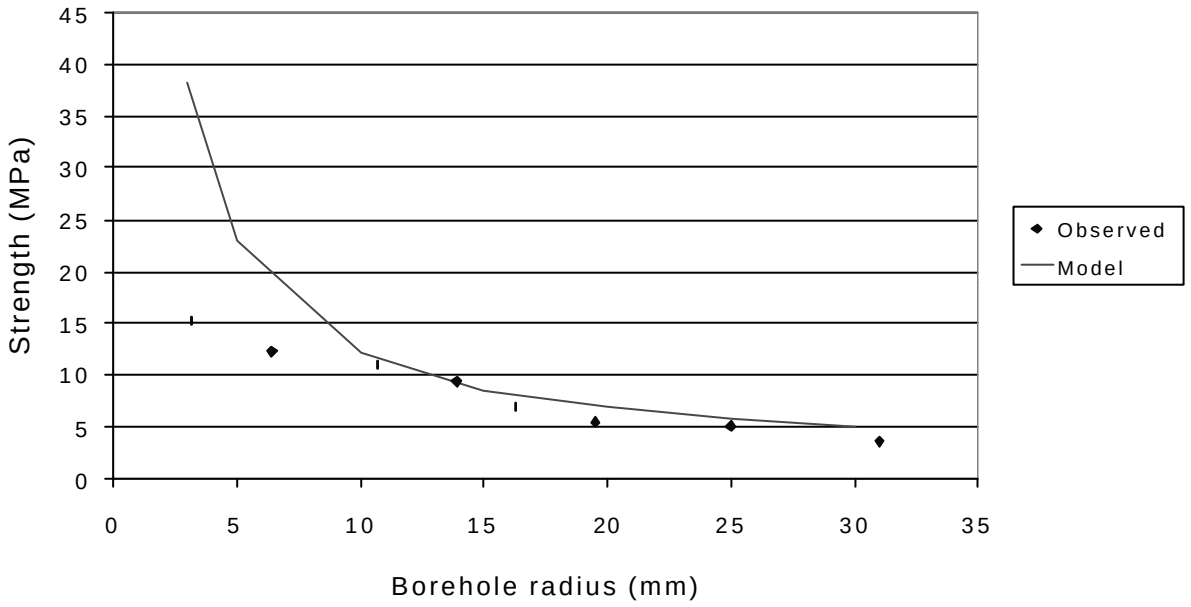

Figure 3.2.1.1 Simulation of size effect in primary crack formation, using a tension weakening model, from the crown of a circular hole in a uniaxially loaded rock sample. (Experimental data points from Carter, 1992)

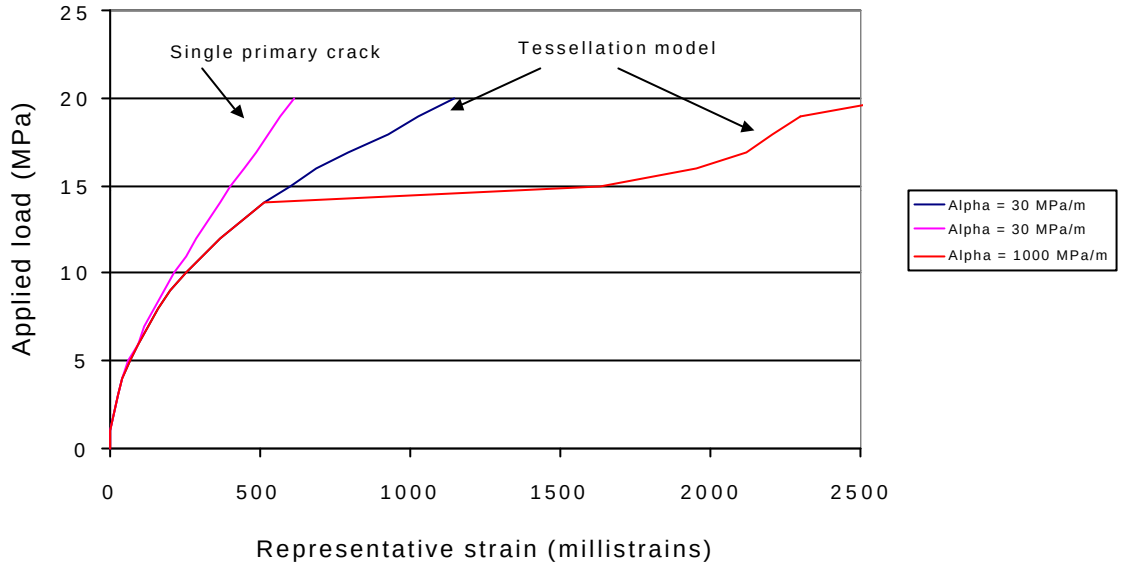

Figure 3.2.1.2 Load vs strain across a representative averaging length above the crown of a circular hole showing the effect of additional fracturing from sites in a tessellation mesh and the effect of suddenly increasing the slope of the tension weakening law (hole radius = 3mm).

A more effective implementation of the weakening behaviour described in point (c) is to assume that tension weakening increases more rapidly, but smoothly, as the crack opening displacement increases. This can be described by assuming that the slope of the tension weakening function is proportional to some power of the crack opening displacement. It is found that such a power law imposes a sharper “kink” in the modelled stress-strain relation for single cracks forming from the 25mm hole in the series of tests described by Carter (1992). However, the most important test of this weakening law is in the simulation of the strength of test blocks containing smaller sized holes where the nominal strength is over-estimated as shown in Figure 3.2.1.1. As noted by Carter, this over-estimation is probably due to additional failure in the sample besides the primary crack features. In order to test this hypothesis, a numerical experiment was performed in which a 20mm X 20mm square block was loaded with a rigid frictionless platen that was displaced in a series of small increments. In one set of experiments, failure was allowed to occur only from the primary crack positions.

The results are shown in Figure 3.2.1.3 for the curves marked “no tessellation” which compare the load vs strain response for linear and power law tension weakening. There is clearly very little difference between the two cases. The simulated loading test was terminated at a stress of about 24 MPa as it appeared that the sample load would have continued to increase indefinitely as the platen displacement was increased. Introducing a random mesh of possible failure positions around the hole, allows additional failure to occur. If the cohesion weakening slope, β,

is assumed to be100 MPa/mm the sample exhibits a peak load of approximately 22 MPa as shown in Figure 3.2.1.3. In the reported experiment, additional secondary fracturing is observed at loads of 29.1 and 33.5 MPa. The value of β appears, therefore, to be too high but it is interesting to note that the power law response shows a small but significant change in slope at an applied load of about 17 MPa, which is close to the observed primary fracture load of 15.2 MPa observed in Figure 3.2.1.1. (This is marked "power law initial failure" in Figure 3.2.1.3). It is found as well that the fracture pattern resulting from the power law weakening test appears to be more strongly "localised" (qualitatively more "brittle") than the more diffuse failure pattern corresponding to the linear tension weakening law.

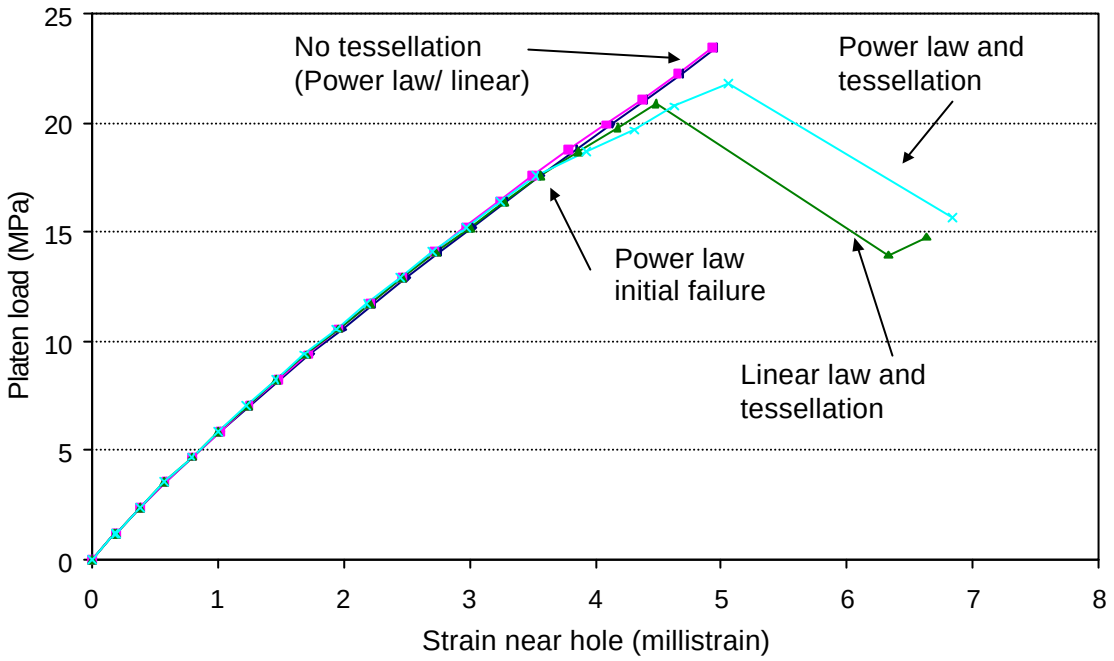

Figure 3.2.1.3 Comparison of linear and power law tension weakening laws applied to a 3 mm borehole in a square specimen.

3.2.2 Implications of time-dependent behaviour

Time-dependent damage sequences in rock are generally reflected in measurements of acoustic emission rates in laboratory scale samples (Shah & Labuz, 1995, Hazzard et. al., 2000) and more dramatically in the seismic monitoring of earthquakes. An intermediate problem scale concerns deep level mining operations. Numerous studies have been carried out to

interpret the observed mining induced seismic activity. (See, for example, Kranz et. al., 1994,1995). It is apparent that, even in hard rock mining environments, significant time-dependent deformations occur (Malan & Drescher, 2000) and that seismic event activity can display creep-like decay patterns following incremental excavation steps (Kranz, et. al., 1994,1995). From the viewpoint of the mining engineer, it is essential to determine whether mine layout sequence changes, regional support configurations, rock breaking methods or variations in the mining rate can be used to modify the hazards of sudden and uncontrolled rock failure. In terms of the design of large underground chambers, it is equally important to understand both the long-term behaviour of such openings and the impact of dynamic excitations on their stability. The consequences of introducing slip weakening behaviour in addition to time-dependent slip are described in this section. Elastodynamic effects are not considered and friction is assumed to be independent of the slip velocity.

Suppose that the resistance to slip (or strength) of a discontinuity is given by a Coulomb relation of the form

$$\tau = S - m\sigma_n, \tag{3.2.2.1}$$

where S is the cohesion, m is the coefficient of friction and σ_n is the stress normal to the discontinuity surface (assumed to be negative in compression). Assume that S and m depend on the magnitude of the relative slip, y, at the interface according to the linear relations,

$$S = S_o - by, \tag{3.2.2.2}$$

$$m = m_o - my, \tag{3.2.2.3}$$

where S_o and m_o are the "intact" cohesion and friction coefficient respectively. b is the slip weakening slope which can be defined in terms of a critical slip value y_c and the residual cohesion S_f as follows.

$$b = (S_o - S_f)/y_c. \tag{3.2.2.4}$$

For simplicity, it is convenient to assume that the coefficient m is such that the friction coefficient m will vary between the extreme values m_o and m_f congruently with the change in the cohesion between its extreme values. Thus, assume that

$$m = b(m_o - m_f)/(S_o - S_f). \tag{3.2.2.5}$$

The relaxation of an assembly of discontinuity segments depends on the detailed stress interaction between each discontinuity and on some rule governing the rate at which each

discontinuity will slip. Consider, as a basic phenomenological postulate, that the rate of change of the slip magnitude at a given point on the crack surface is governed by

$$\frac{dy}{dt} = \kappa(\tau - \rho)\,;\ \tau > \rho$$

$$\frac{dy}{dt} = 0\,;\ \tau \le \rho\,, \tag{3.2.2.6}$$

where κ is a surface "fluidity" term, τ is the shear stress imposed on the crack and ρ is the slip resistance given by equation (3.2.2). The shear stress magnitude, τ, is given by

$$\tau = -(C/g)y - eE_s\ , \tag{3.2.2.7}$$

where C is an influence coefficient depending on the local crack element shape function, g is the crack length and E_s is an externally imposed shear traction. The variable e is used to indicate the slip direction and is defined by

$$e = -sign(E_s)\,. \tag{3.2.2.8}$$

The validity of equation (3.2.2.6) has to be justified by application of the proposed model to the analysis of results from physical experiments. For a piecewise constant displacement discontinuity shape over the whole crack, the influence coefficient C in equation (3.2.2.7) depends on the elastic constants of the host material according to

$$C = E/\pi(1-\nu^2)\,, \tag{3.2.2.9}$$

where E is Young's modulus and ν is Poisson's ratio. Assembling the relationships defining τ and ρ and substituting these into equation (3.2.2.6) yields the discontinuity slip rate equation in the form:

$$\frac{dy}{dt} = \kappa\big[-(C/g)y - eE_s - S_o + \beta y$$

$$+ m_o\sigma_n - m\sigma_n y\ \big]. \tag{3.2.2.10}$$

Grouping terms gives

$$\frac{dy}{dt} = \kappa(-by + \tau_e^o)\,, \tag{3.2.2.11}$$

where,

$$b = C/g - \beta + m\sigma_n \tag{3.2.2.12}$$

and

$$\tau_e^o = -eE_s - S_o + m_o\sigma_n\,. \tag{3.2.2.13}$$

Equation (3.2.2.11) has the explicit solution

$$y(t) = (\tau_e^o / b)\left[1 - \exp(-\kappa b t)\right]. \qquad (3.2.2.14)$$

Equation (3.2.2.14) possesses some interesting properties that determine the crack sliding stability, depending on the sign of the coefficient b. From equation (3.2.2.12), b can be considered to be the difference between the "system" stiffness, C/g, and the weakening slope $\beta - m\sigma_n$. For large crack lengths (large g), the system stiffness is small. This is depicted qualitatively in Figure 3.2.2.1.

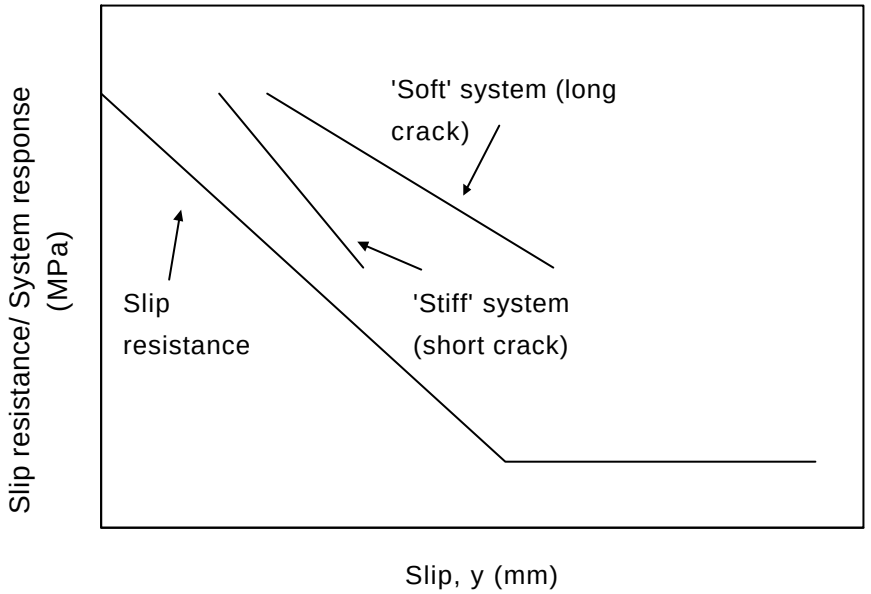

Figure 3.2.2.1 Qualitative response of a crack to slip weakening.

In the case of a very "stiff" system, a sufficiently small value of g in equation (3.2.2.12) will ensure that the coefficient b is positive and the slip rate dy/dt will decrease as a function of time. However, for a "soft" system (large crack size) the coefficient b will initially be negative and the slip will increase exponentially with time. It should be noted that when the cohesion has decreased to the specified residual value, S_f, the system will again become stable in the sense that the system stiffness exceeds the, now zero, rate of slip weakening. For a growing crack, the increase in crack length, g, causes the stiffness C/g to decrease progressively and, consequently, can lead to unstable growth unless some arrest barrier is encountered. Figure 3.2.2.2 shows the response (in terms of the strain energy release in each time step) of a 100 m

long straight fault that is modelled using the DIGS code with 20 linear variation displacement discontinuity elements, each of length 5 m. The total number of collocation points, where the fault slip values are calculated, is equal to 40. The formula used to estimate the energy release increments in each time step is given by equation (3.2.2.18) below. Each curve in Figure 3.2.2.2 is for a different value of the slip weakening parameter, b, defined in equation (3.2.2.2). The fault is loaded with a uniform shear stress of 50 MPa and clamped with a uniform normal stress of 10 MPa. The friction angle is assumed to be 45 degrees and the initial cohesion is 25 MPa. It can be seen from Figure 3.2.2.2 that as b is increased, the initial rate of strain energy release increases. The peak value is reached at the time when the residual cohesion falls to zero. At later times, the energy release is seen to decay exponentially in a stable manner. This behaviour is predicted by equation (3.2.2.14) with *g* set equal to the fault length of 100 m.

It is essential to quantify both the cohesion weakening slope, b, and the slip "fluidity" parameter, k, that is postulated to link the slip rate to the "driving" shear stress across a discontinuity as defined in equation 3.2.2.6. In order to achieve some initial quantification of these parameters, the simplified analytical model of slip that has been described here has been extended to model some results obtained previously by Bieniawski (1970) on the unconfined loading of small sandstone samples at different rates of loading. (Simulation of these results using the FLAC code has also been carried out by Malan and Drescher, 2000). The parameters in this simplified model were chosen to give an approximate match to the load-deformation curves observed by Bieniawski. The values of the estimated parameters are shown in Table 3.2.2.1.

Table 3.2.2.1 – Parameter estimation of Bieniawski's sandstone loading experiments, using a simple analytical model.

Loading rate (strain/sec)	Fluidity parameter, k (m / MPa.sec)	Slip weakening slope, b (Mpa / mm)
36.0e-8	4.4e-8	241
0.464e-8	6.43e-10	141

These results show that the slip weakening slope parameter b is relatively insensitive to the loading rate and is of the same order of magnitude as the 100 MPa/mm value estimated for the limestone sample in Section 3.2.1. However, the massive difference in the fluidity parameter k, as a function of the applied loading rate indicates that the postulated slip rule is incorrect or that the simple analytic model is inadequate for the analysis of the sample geometry used by Bienawski. (The sample was a squat cylinder with a width to height ratio of two). Further laboratory tests are required to confirm the trends observed by Bieniawski (1970).

Consider now the more general case where multiple discontinuity elements are used to represent an assembly of interacting fractures. The rate of change of the slip y_i at the i^{th} collocation point in the system is assumed to be given, from equation (3.2.2.6), by

$$\frac{dy_i}{dt} = \boldsymbol{k}(\boldsymbol{t}_i - \boldsymbol{r}_i)\,, \tag{3.2.2.15}$$

where $\boldsymbol{t}_i$ and $\boldsymbol{r}_i$ are the local shear stress and slip resistance at point *i*. These quantities are related by influence matrices to the remaining slip and crack opening discontinuity values. In general, adapting equation (3.2.2.10) yields

$$\frac{dy_i}{dt} = \boldsymbol{k}\left[-\sum_j K_{ij} y_j - e_i P_i - S_{oi} + \boldsymbol{b}_i y_i \right.$$

$$\left. + m_i Q_i + m_i \sum_j M_{ij} y_j \right], \tag{3.2.2.16}$$

where K_{ij} are shear stress influences and M_{ij} represents the influence of the shear slip at point j on the normal stress at point i. P_i and Q_i are the shear and normal components of the field stress at point *i*. Equation (3.2.2.16) can be written more compactly in matrix form as

$$d\mathbf{y} / dt = \boldsymbol{k}\left[-(\mathbf{K} - \mathbf{B} + \mathbf{M})\mathbf{y} + \mathbf{T}\right] \tag{3.2.2.17}$$

where **y** is a vector of slip values, **K** = $\{K_{ij}\}$, **B** is a diagonal matrix of the weakening coefficients b_i, **M =** $\{M_{ij}\}$ and **T** is the vector of driving shear tractions.

The strain energy release at time step, *t*, can be estimated by summing the contribution from each collocation point, i, in the system according to

$$\Delta E(t) = \tfrac{1}{2}\sum_i A_i\left[\boldsymbol{t}_i(t) - \boldsymbol{r}_i(t)\right]\Delta y_i(t) \tag{3.2.2.18}$$

where A_i is the area associated with point i and $\Delta y_i(t)$ is the incremental slip in time interval *t*.

The stability properties of the system depend on the eigenvalues of the matrix $\mathbf{K} - \mathbf{B} + \mathbf{M}$. If the smallest eigenvalue of this matrix is positive, the system is stable and moves towards a point of equilibrium. From a detailed eigenvalue analysis, it is found that the magnitude of the minimum eigenvalue for the 100 m sliding crack is approximately equal to 420 MPa/m. If the slip weakening coefficient is set equal to 400MPa/m the slip response is as shown in the lowest curve of Figure 3.2.2.2. It can be seen that this curve comprises a very slowly decaying initial response, as the cohesion is destroyed, followed by a more rapidly decreasing response when

the residual cohesion is zero. In each case the response is “stable” as predicted by the eigenvalue analysis. Although the eigenvalue analysis provides an elegant tool for the instantaneous analysis of the stability of equations (3.2.2.17), it is apparent that if an assembly of cracks is analysed in which the number of elements in the system is increased progressively, according to specified growth rules, the instantaneous stability can fluctuate depending on the specific configuration of the element population at any given time. If the elements are drawn from a random mesh assembly, it can be expected that the accompanying energy release cycles may behave in a manner that is analogous to observed seismic activity.

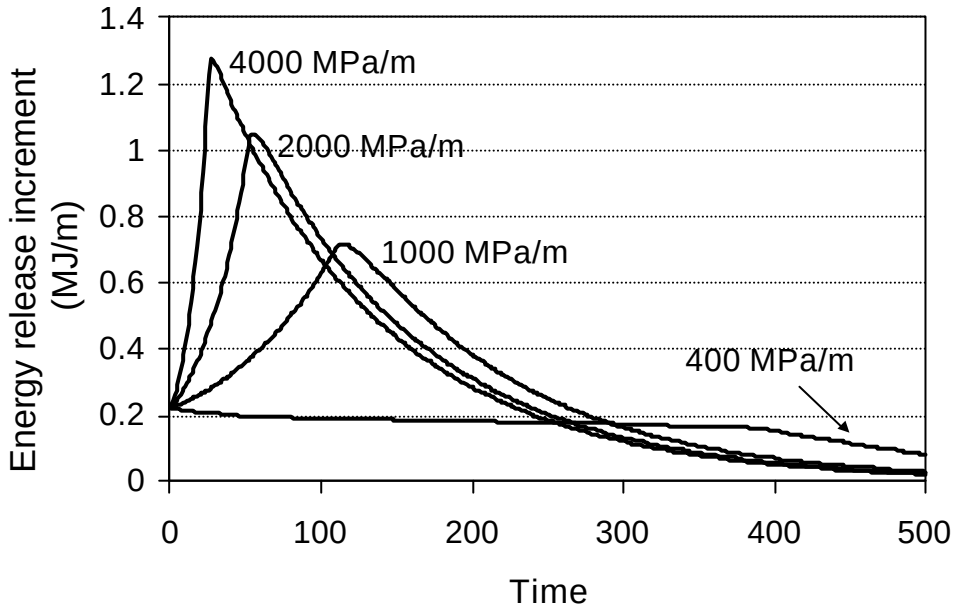

Figure 3.2.2.2. Time response of a single crack uniformly loaded in shear with different slip weakening parameter values.

The incorporation of the slip weakening logic also implies the existence of scale effects as explained by Palmer and Rice (1973), Bazant (1986) and demonstrated experimentally by Labuz and Biolzi (1991). The inclusion of the time-dependent slip relaxation, described by equations (3.2.2.17), in turn implies some scaling effects that can arise in addition to the classic volumetric supply/ surface absorption mechanism described by Bazant (1986). To illustrate this, consider the sudden shear loading of two collinear faults of length 100 m and separated by a 20 m “asperity” where the cohesion is four times greater than in the adjacent faults. The incremental energy release response in each time step is shown in the lower curve of Figure 3.2.2.3. (The particular material properties are given in Table 3.2.2.2).

Table 3.2.2.2. Material properties for fault slip scaling tests.

Property	Value
Young's modulus (MPa)	70000
Poisson's ratio	0.2
Crack cohesion (MPa)	25
Asperity cohesion (MPa)	100
Friction angle (degrees)	45
Fluidity parameter, (m/MPa-t)	0.00001
Slip weakening rate (MPa/m)	4000

It is interesting to observe, in the lower curve of Figure 3.2.2.3, that the first peak in the energy release plot corresponds to the progressive loss of cohesion in the weaker fault regions adjacent to the central asperity. These fault sections continue to creep, increasing the load on the asperity region. The cohesion in the asperity also decreases as a function of time and this leads, eventually, to the second peak in the incremental strain energy release values recorded in each time step. In a second problem, the fault and asperity lengths were doubled to 200 m and 40 m respectively. Applying the same shear load and normal clamping stress to this system yields the response shown in the upper curve of Figure 3.2.2.3. The interesting result here is that the second peak of the energy release increments occurs later than for the case of the 100m fault geometry shown in the lower curve of Figure 3.2.2.3. This result is due to the slip rate control implied by the deformation rate law expressed by equation (3.2.2.16). It appears that the fraction of the asperity, where the cohesion has been destroyed, increases at a similar rate in each case and, consequently, the larger size asperity requires a greater length of time to be broken. Similar experiments can be formulated in relation to the loading rate of laboratory scale samples, which can be used to validate the assumed slip rate law of equation (3.2.2.16).

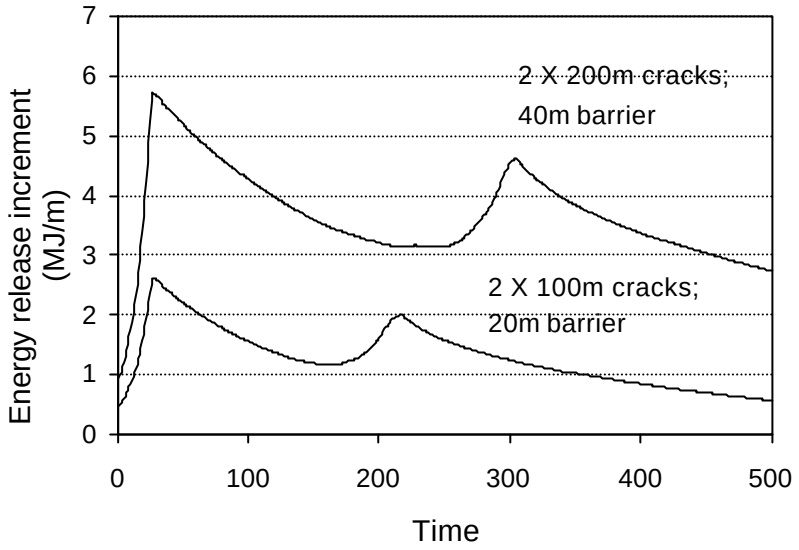

Figure 3.2.2.3. Effect of scale on the response of two faults separated by a strong asperity. (Time units unspecified).

3.2.3 Implications for foundation failure and preconditioning

Studies were carried out to investigate the effect of different tessellation mesh densities on the response of a rectangular shaped sample with nominal dimensions of 104mm X 52mm and having a lateral confinement of 10MPa. A “coarse”, “intermediate” and “fine” triangular Delaunay mesh was used to cover the sample with nominal mesh sizes of 13mm, 6.9mm and 3.8mm respectively. Figure 3.2.3.1 shows the axial load vs axial displacement response for these cases with two choices of the cohesion weakening parameter, b (designated as b in Figure 3.2.3.1). It is apparent that the mesh density has some effect on the response of the sample but that the weakening parameter b has a strong effect on the peak load and on the post-peak slope. This has important implications in assessing the effect of scale on both the regional stability of proposed mine layouts and the stability of the mining face and pillar edges in relation to the stope width. As an example, a study was performed in which three sets (A, B and C) of parallel-sided strike stopes were mined. In each case the panels were separated by pillars having different widths but arranged to ensure a nominal extraction of 84 percent. The specific layout dimensions are shown in Table 3.2.3.1. It was assumed that pillar foundation failure could occur on shear planes above and below the reef plane, dipping from the edge of each pillar towards the centre of the pillar as shown in Figure 3.2.3.2. The “wedge” angle $\grave{e}$ was assumed to be 30 degrees. In each case, the critical slip weakening slope b was varied until the slip planes became unstable and foundation failure occurred. The range of b values at which this was observed are shown in the right hand column of Table 3.2.3.1. It is apparent that as the pillar/

panel sizes are increased, the overall layout becomes progressively less stable (decreasing critical b slopes).

An assessment of an appropriate field value of b is required if this approach is to be used to design the dimensions of a mine layout to achieve a particular stability performance. However, it seems more practical to propose that the critical weakening slope b could be used as a novel measure that could provide a ranking between different layout geometries with respect to foundation failure stability.

Table 3.2.3.1 Critical stability of different pillar layouts.

RUN	Number of Pillars	Pillar width (m)	Total Pillar (m)	Number of panels	Panel span (m)	Total span (m)	Critical slope b
A	9	18	162	10	84	840	600-650
B	5	32	160	6	140	840	550-560
C	3	52	156	4	210	840	500-550

This procedure effectively provides a method for determining a lower bound to the magnitude of the softening slope at which unstable behaviour will arise. Consequently, the layout which displays the highest value of this bound is implicitly the most stable (Layout A in the example shown in Table 3.2.3.1).

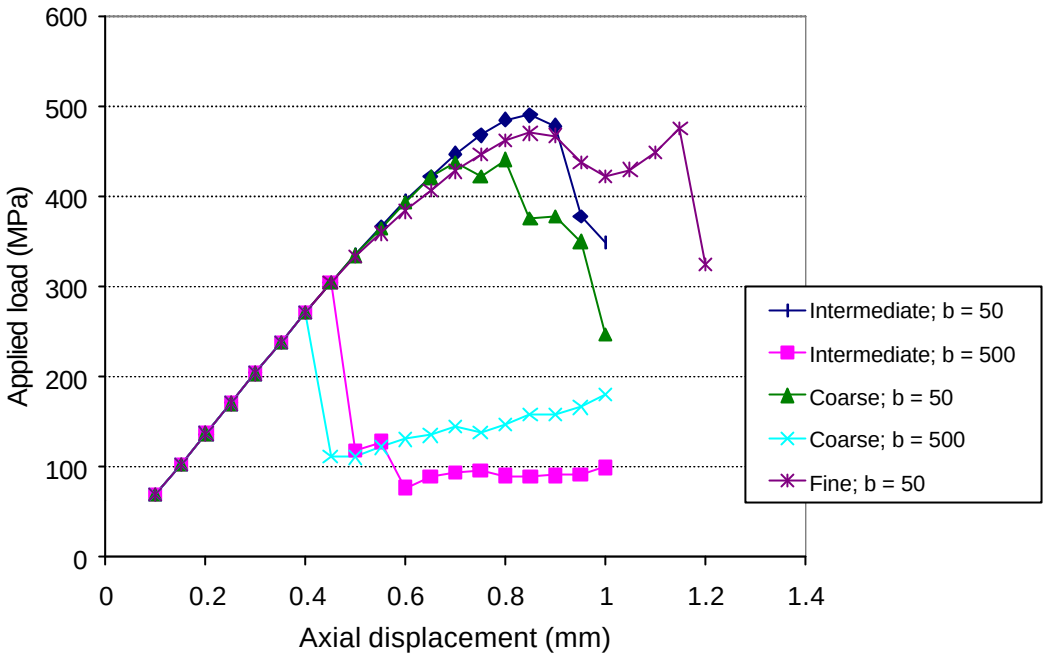

Figure 3.2.3.1 Sample loading test with different tessellation mesh densities.

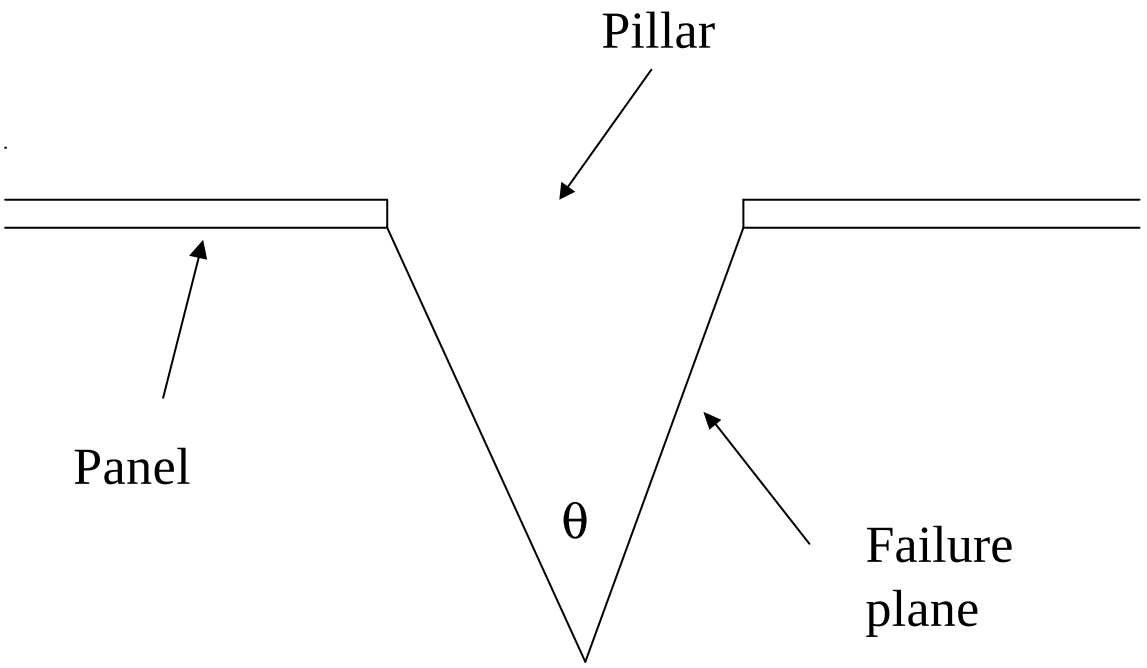

Figure 3.2.3.2 Schematic pillar layout showing two of four failure planes forming a potential wedge-shaped foundation failure mechanism.

Time-dependent relaxation of discontinuities in the stope fracture zone can lead to a buildup of stress concentrations that may lead to intermittent failure episodes. An important objective of the present work is to represent these mechanisms explicitly in numerical codes and then to study the stability of the mining face and the clamping stress in the stope hangingwall. Following the implementation of the tension and slip weakening time-dependent behaviour in the DIGS code, it is now possible to address some of these problems. In particular, it is of great interest to understand the interactive effect of variations in the mining rate, the excavation procedure (drill and blast or continuous mining), the geological environment and the stope width. A study was initiated to examine, firstly, the effect of the geological environment on the closure rate response and the possible consequences of implementing preconditioning blasting in different stope widths. A random mesh of potential failure planes was specified in a small region near the face of a parallel-sided panel. Parting plane weaknesses near the mining face were simulated by assigning zero cohesion to all discontinuities that lay within an angle of fifteen degrees to the reef plane. Figure 3.2.3.3 shows the simulated stope closure at a point initially 2m behind the advancing face, in a reef having a mining height of 2m, and having either a fully layered structure in, both the hangingwall and the footwall, or only layering below the reef plane in the footwall. The response, corresponding to four face advance steps, is shown in Figure 3.2.3.3 and shows significant differences in these two cases. This response is in very good qualitative agreement with time-dependent closure observations that have been made in different geological areas with and without strata layering by Malan (1999).

An attempt has been made also to simulate the effect of preconditioning blasting. This is clearly a formidably difficult problem. A simplified model of the blast is proposed in which a small rectangular region ahead of the stope face is selected and all discontinuities that fall within this region are dilated by a specified amount for a short period of time. Following this dilation, the discontinuities are allowed to relax and further mining steps are executed. Figure 3.2.3.4 shows the closure response following two different selections of the blast “dilation” parameter in the case where there are no parting planes in the hangingwall. The results are clearly very sensitive to the blast magnitude (“dilation” parameter) and do not show very good agreement to the observations of Malan for the closure response after preconditioning blasting in the VCR. (The behaviour observed by Malan (1999) indicated that the closure rate tended to increase after the preconditioning blast. The mining was, however, in an up-dip orientation). It is of great interest to examine the effect of the preconditioning blast on the hangingwall horizontal (“clamping”) stress. This is plotted in Figure 3.2.3.5 after three mining steps have taken place following the preconditioning blast. The most interesting result is that before the preconditioning blast, the average hangingwall clamping stress is approximately 5 MPa. Following the strong blast (“dilation” = 20mm), the stress is reduced to a smaller, uniform level of approximately 1 MPa to 2 MPa. However, after the small blast (“dilation” = 5mm), the back area clamping stress is

strongly increased (peak values exceeding 40 MPa) although the stress near the face is slightly tensile. Clearly, these results have considerable potential significance but at present must be regarded with extreme caution. Additional studies will have to be carried out to check the validity of the numerical simulations in relation to available field observations.

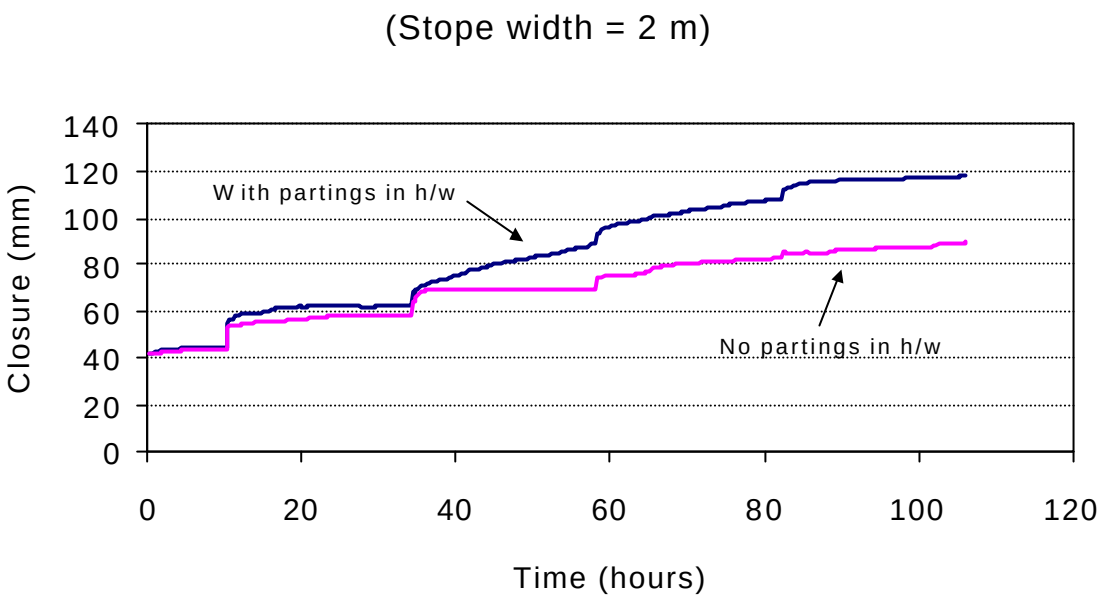

Figure 3.2.3.3 Simulated stope closure profiles following four successive mining steps of a parallel-sided panel in two geological environments in which parting plane weaknesses are present and are absent in the hangingwall region.

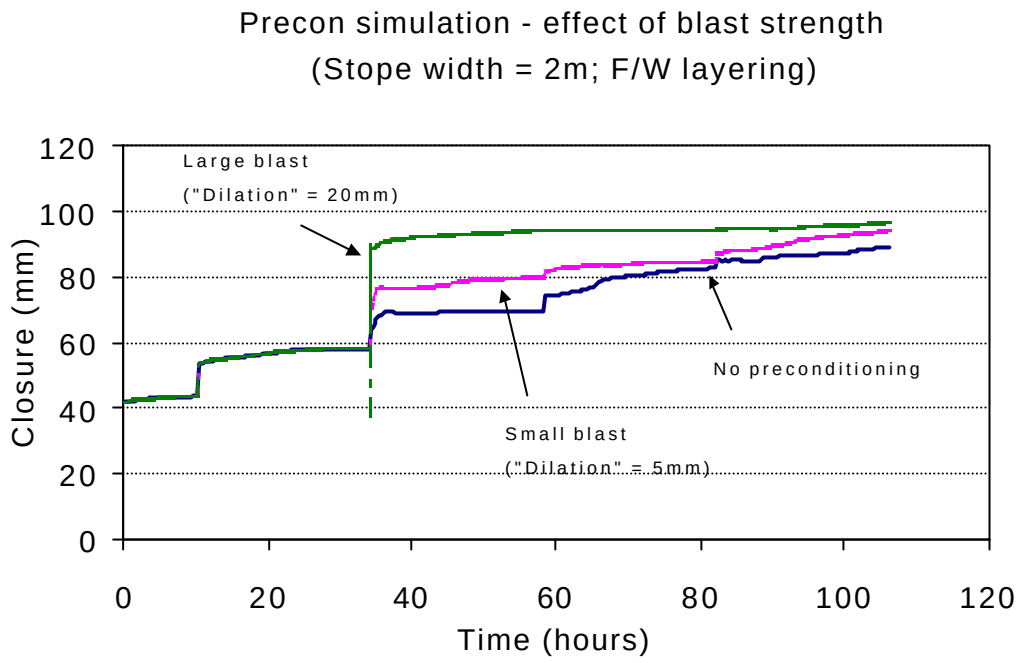

Figure 3.2.3.4 Effect of simulated preconditioning blast magnitude on the closure response in a stope with weak footwall parting plane but having no weak parting planes in the hangingwall.

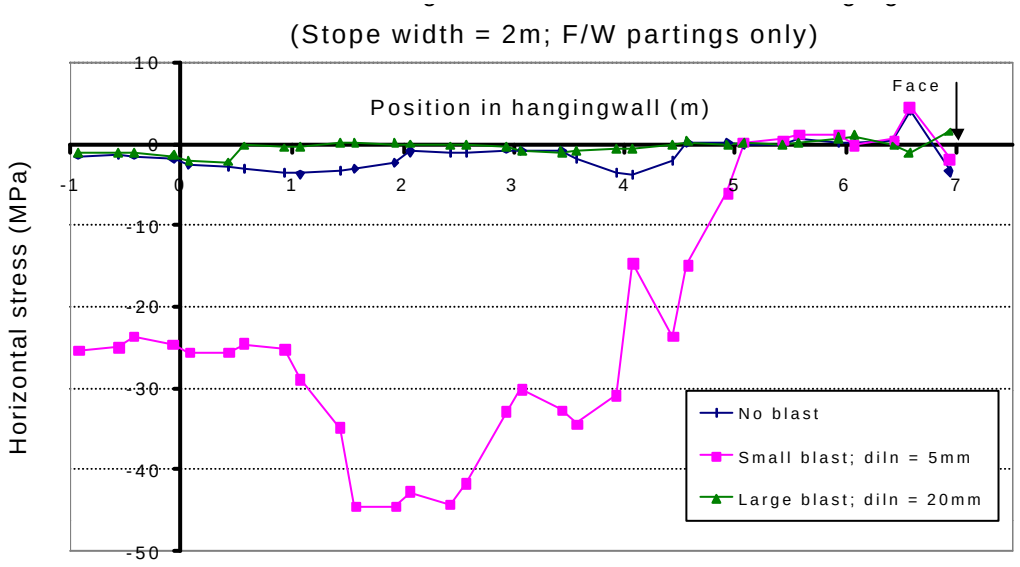

Figure 3.2.3.5 Effect of simulated preconditioning blast strength on the stress induced in the stope hangingwall behind an advancing stope face.

4.0 Seismic wave transmission through fractured rock and two and three dimensional fracture propagation

4.1 Seismic wave interaction with underground openings

The detail of this work is covered in the thesis “Wave interaction with underground openings in fractured rock”, (Hildyard, 2001). Some of the main results and conclusions are summarised here, and the thesis is presented in its entirety as a supplementary document.

One aspect of addressing the rockburst problem in deep-level mining is to develop numerical models of rockbursts which project the amplitudes, distribution and detailed seismic wave motion around an excavation. The results in this section seek to evaluate and improve models of wave propagation around underground openings. In particular, evaluating the damage potential of a rockburst requires the accurate modelling of the full wave motion and not simply the first motions. Comparisons were made between simulated and measured waveforms for a large amplitude underground experiment. These results show the need for more tightly constrained data. Comparisons are therefore made between models and data from controlled experiments at the Underground Research Laboratory (URL) in Canada. The implications of the excavation on the amplitude and distribution of ground motion, and in particular, the potential importance of surface waves is then established using studies on a typical mining layout. Important conclusions are presented and recommendations made.

4.1.1 Review of previous modelling

A great number of static and pseudo-static numerical models have been applied in studying the rockburst problem. A number of studies have also been made using dynamic numerical models. These mainly focus on the mechanisms rather than the effects of rockbursts. Nevertheless, many of these calculate the seismic waves at some distance from the event. Cundall and Lemos (1990) model dynamic events for different models of failure on a pre-existing fault subjected to the stress field induced by an excavation. Resulting seismic waveforms are calculated in the roof of the excavation. Brady (1990) applies a distinct element formulation to study a number of dynamic rock mechanics problems including an underground excavation in

jointed rock, recording numerical waveforms at a distance from the events. Dowding et al. (1983) investigate the effect of low frequency loading due to an assumed earthquake or nuclear blast on a cavern in a jointed rockmass represented using rigid blocks. Mack and Crouch (1990) describe a boundary element method for modelling wave propagation and demonstrate its usefulness through comparison with an analytic solution. Müller (1991) applies a continuum model to simulate an idealised rockburst in a coal-mine, recording the simulated velocity waveforms at the coal-face. Siebrits et al. (1993) simulate a mining excavation and use three different representations of a fracture zone to demonstrate that waves from a seismic event are larger due to propagation through the fracture zone. Hildyard et al. (1995) demonstrate a mechanism of dynamic triggering for a model of a mining excavation and a stressed fault, where seismic waves from slip on the fault trigger a much larger event.

These applications show that there is potential for models, which can simulate wave propagation from rockbursts. However, the usefulness of most of the above models is seriously limited by two factors. Firstly, wave propagation was modelled in two-dimensions. Rockbursts are fundamentally three-dimensional and meaningful calculation of the effects of a rockburst and the resulting distribution of ground motion requires three-dimensional simulation. Secondly, although many of the studies show waveforms at surfaces within an excavation, there is little emphasis on establishing the accuracy of the wave propagation or on comparing motions with observed seismograms. Before conclusions can be reached from such models, it is important that they are demonstrated to correspond closely to observed ground motions.

Previous studies have demonstrated that modelled wave behaviour agrees well with experimental observations of wave propagation in a photoelastic material. Daehnke et al. (1996) simulated experiments of wave interaction with a slot, Daehnke and Hildyard (1997) simulated wave interaction with discrete fractures intersecting a slot, and Uenishi (1997) simulated Rayleigh wave propagation causing slip along an interface. These cases show a striking resemblance between the simulated and observed wave patterns. Again, however, these are for two-dimensional wave propagation. The experiments validate the elastodynamic behaviour of the models. However, since they employ a more ideal elastic material than is typical of a rockmass, the results do not indicate that the models can realistically simulate wave behaviour around an excavation in fractured rock. This can only be evaluated by comparison of simulations with recorded wave motions in rock.

Simulation of seismic events and comparison with observed seismograms is widespread in studies of large earthquakes. For example both the Loma Prieta (e.g. Wald et al., 1991; BSSA, 1991), and the Kobe (e.g. Pitarka et al., 1996; Motosaka and Nagano, 1996) earthquakes, were extensively modelled to back-analyse the recorded strong and far-field ground motions. These

have demonstrated a close correspondence between the simulated and observed waveforms, and have aided in inferring mechanisms of the events, the regions of damage and in understanding the geometry and geology near the event and how this contributes to the damage.

Back-analyses of rockbursts have mainly focused on using the observed damage and seismic data to propose mechanisms and causes of the rockburst (Durrheim et al., 1995; Hagan et al., 1999). In cases where numerical modelling has been employed, it has typically been a static analysis attempting to understand the stress conditions which have led to the event. Very little published work has attempted to apply numerical models to simulate an actual rockburst event, or to compare directly the simulated wave motions with those recorded around an underground opening. One case study simulating a specific seismic event is reported by Tinucci and Spearing (1993). They used a two-dimensional, stress-driven, asperity model of fault slip to simulate the wave motions in a region of mining. They conclude that “dynamic asperity models of fault-slip can reasonably reproduce peak particle velocities (PPVs) and dominant frequencies of seismic events”, and “the most significant results presented in this study are contour plots of PPVs and induced shear stresses. Such plots offer the ability to identify possible locations where rockburst damage might be expected ...”. Notably, however, no direct comparison was presented between measured and modelled seismograms for different geophone positions.

Handley et al. (1996) used a three-dimensional model to simulate actual seismic events in a deep-level gold mine, to understand what information seismograms contain on the state of closure in mining stopes. They compare waveforms from the simulation with the recorded data, and conclude that “while correspondence between seismic traces is generally very poor, there are several simple measures that can be used to show good correspondence, such as P-wave arrival times, arrival sequence at the geophones, and first motions.” Two of their comparisons are reproduced in Figure 4.1.1.1.

In summary, a number of models have demonstrated the potential value of simulating seismic waves from a rockburst. They have indicated that calculating PPVs and induced stresses can aid in interpreting and anticipating damage. Brady (1990) concludes that not only the peak velocity but the full wave motion is important in determining damage. However, no study has successfully related the simulated wave motions from mechanistic models of a rockburst, to actual recorded waveforms in the vicinity of deep excavations. It has therefore not been demonstrated that wave motions around an excavation due to a seismic event can be reliably estimated by a numerical simulation.

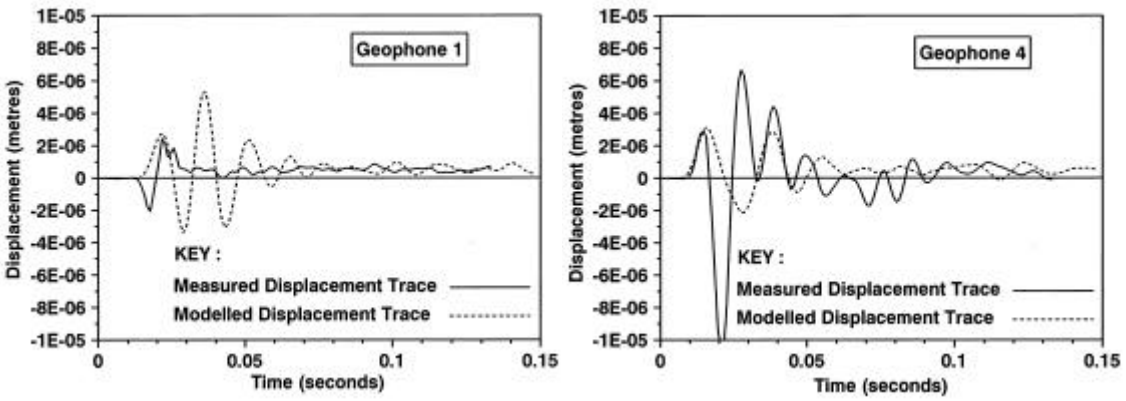

Figure 4.1.1.1 Comparison of displacement waveforms for two geophone positions (from Handley et al., 1996).

The lack of evidence of reliable simulation is partly due to the complexity of the mining region. This complexity includes the influence of the excavations voids, the highly fractured nature of the surrounding rock and the proximity of the opening to the source of the event. Another reason is simply that three-dimensional representation of wave propagation through complex regions is only now becoming computationally viable. (Hazzard, 1998; Hildyard and Young, 2002). Possibly the most important reason, however, is a lack of suitable data for calibration. Evaluating models of this nature requires a seismic event where there is a detailed knowledge of the excavation geometry and the surrounding rock, good coverage of recordings both near the surfaces of excavations and in the solid rock, knowledge of both the source location and the mechanism, and a knowledge of the rock condition before and after the event. Data with these properties is more likely to be obtained in a simulated rather than a natural event. The next section reviews in detail results from modelling such a simulated seismic event.

4.1.2 Modelling an underground experiment at Kopanang

This section summarises some of the results and conclusions of modelling wave propagation from an underground experiment, in particular those results which pertain to the accurate modelling of seismic wave propagation at the surfaces of underground excavations. Some of this work has been presented in the report of the SIMRAC project GAP332 (Napier et al., 1999), but the full results and final conclusions are now available in two papers (Hildyard and Milev, 2001a; Hildyard and Milev, 2001b) on the pre- and post-modelling of seismic wave propagation from this experiment.

The experiment was conducted at the Kopanang mine in South Africa (Hagan et al., 2001), and used a controlled blast to induce damage in a nearby tunnel. Full details can be obtained in the

above papers. The blast was made in solid rock and was designed so that direct gas-driven damage did not extend to the tunnel, ensuring that damage at the tunnel surface was due to seismic waves. The tunnel was pre-instrumented with geophones and accelerometers. The experiment also included a small calibration blast at the opposite end of the tunnel from the main blast. Extensive comparisons were made between the recorded and modelled waveforms. These are examined here as a measure of the capacity to simulate ground motion near underground openings. Figure 4.1.2.1 is a plan view showing the layout of the experiment, the positions of the calibration and main blasts and the positions of the instruments. The model coordinates are such that the x-axis is normal to the tunnel, y-axis is vertical and z-axis is parallel to the tunnel.

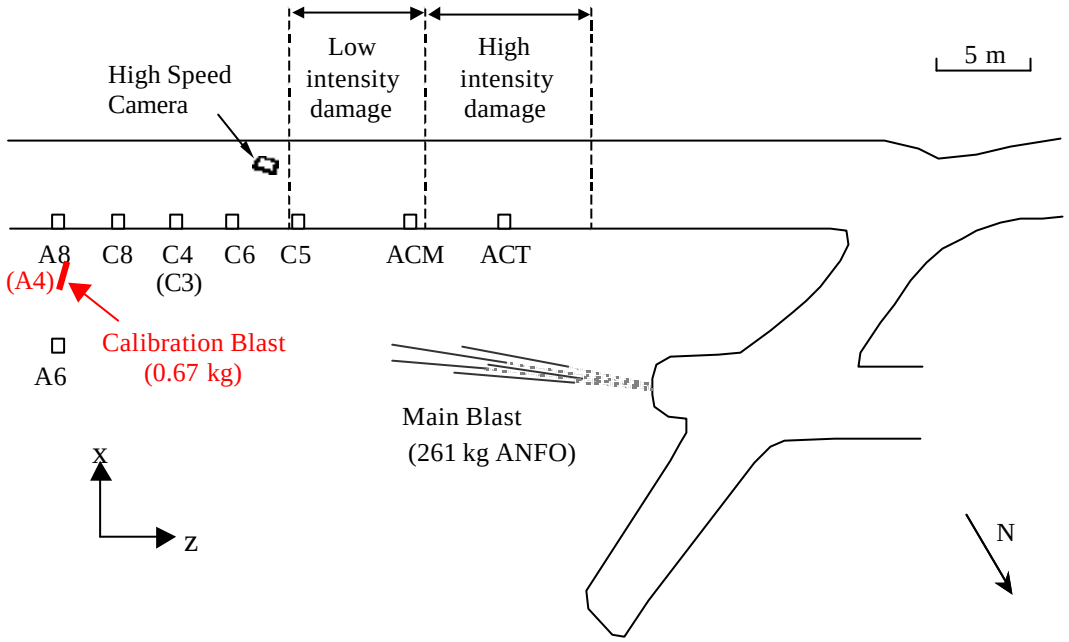

Figure 4.1.2.1 Plan view of the tunnel-site for the rockburst experiment, showing the excavation and positions of the main blast, calibration blast, accelerometers ACT and ACM, geophones mounted on the side-wall C5, C6, C4, C8 and A8, and geophone A6, sited 5 m into the solid rock. (Geophone names in brackets indicate a different name for the calibration blast).

Hildyard and Milev (2001a) first develop a model for simulating wave propagation from a blast detonating in a borehole, where the detonation speed is comparable to the P- and S- wave speeds of the medium, and the borehole length is of similar order to the region of interest. The model was developed by comparison with a limited number of recorded waveforms close to a detonating blast in solid rock. The final comparisons are shown in Figure 4.1.2.2 and indicate that some uncertainty is immediately introduced by the modelling of the blast source.

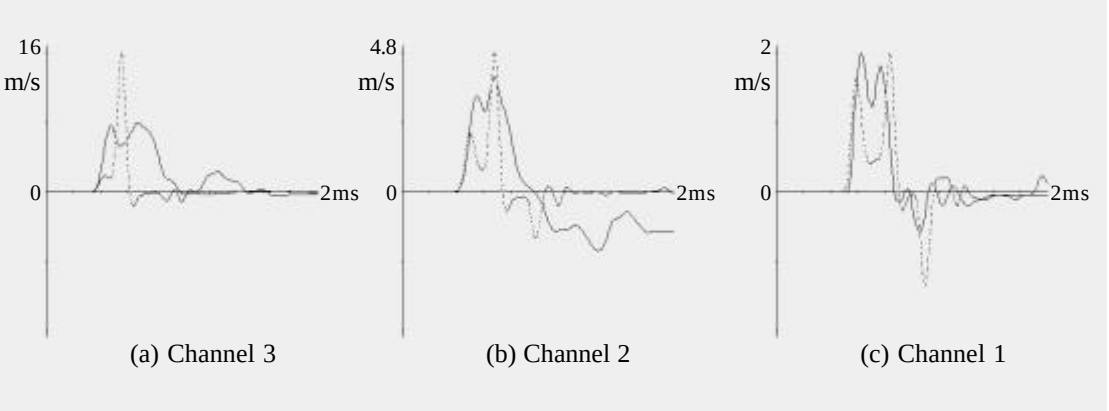

(a) Channel 3 (b) Channel 2 (c) Channel 1

Figure 4.1.2.2 Test blast in solid rock: Comparison of the recorded (solid line) and modelled (dotted line) velocity seismograms at distances of 0.6 m, 1.2 m and 1.8 m from the blast.

The model for the small calibration blast appeared to be a reasonable model of the real wave propagation. Figure 4.1.2.3 shows modelled and measured waveforms at different distances along the tunnel wall for motion normal to the tunnel wall. Qualitatively, this shows an acceptable correspondence in the waveforms and in the amplitudes and the relative amplitudes of the tunnel surface waves at different positions. Figure 4.1.2.4 compares a triaxial set of geophones very close to the blast. There is good correspondence for two of the components and the discrepancy in the vertical velocity probably indicates that the blasthole was not truly aligned to the horizontal as was modelled. However, Figure 4.1.2.5 compares modelled and observed waveforms for a triaxial set of geophones mounted 5 m into the tunnel wall in solid rock, and these show considerable differences, particularly for the vertical velocity.

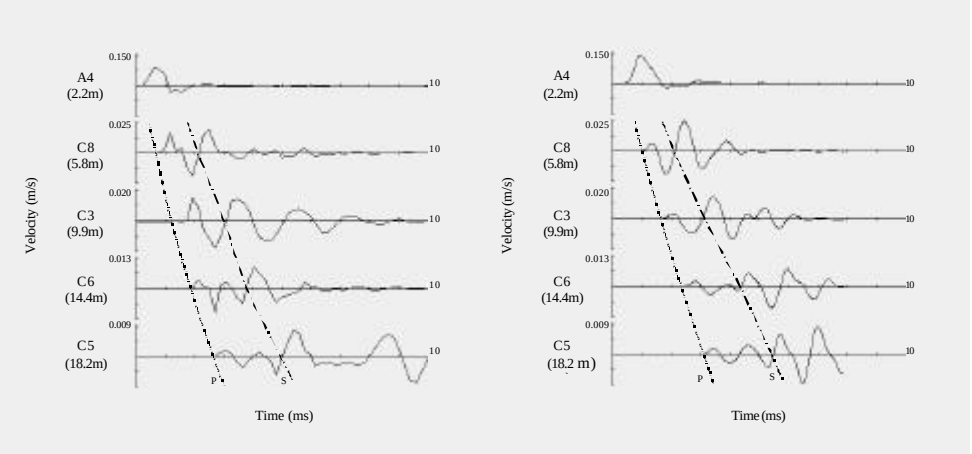

(a) Experiment (b) Model

Figure 4.1.2.3 Comparison of velocity seismograms for the calibration blast at varying distances along the tunnel near wall. Motion is normal to the tunnel surface. Approximate P-wave arrivals and the position of the S wave, are identified.

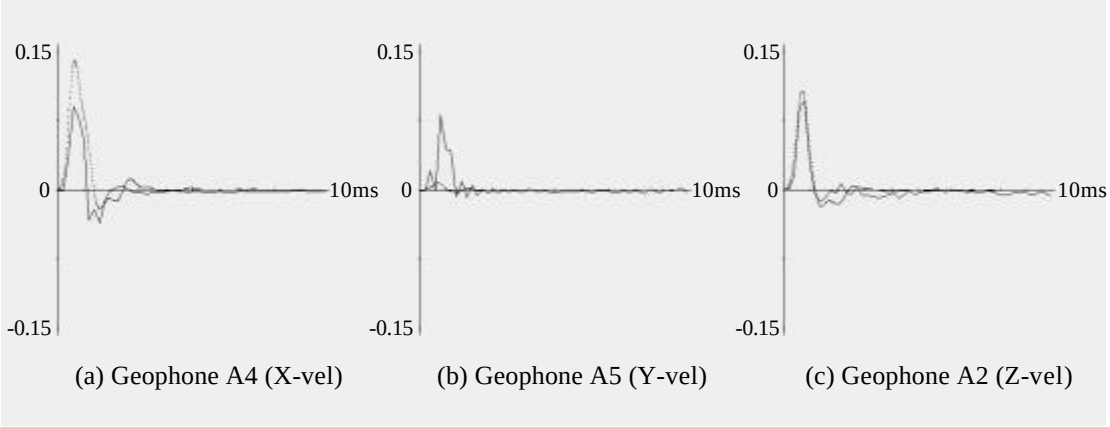

(a) Geophone A4 (X-vel) (b) Geophone A5 (Y-vel) (c) Geophone A2 (Z-vel)

Figure 4.1.2.4 Recorded (solid line) and modelled (dotted line) velocity waveforms for the calibration blast, compared for geophones A4, A5 and A2 which were a triaxial set mounted on the tunnel wall 1.7 m ahead of the calibration blast.

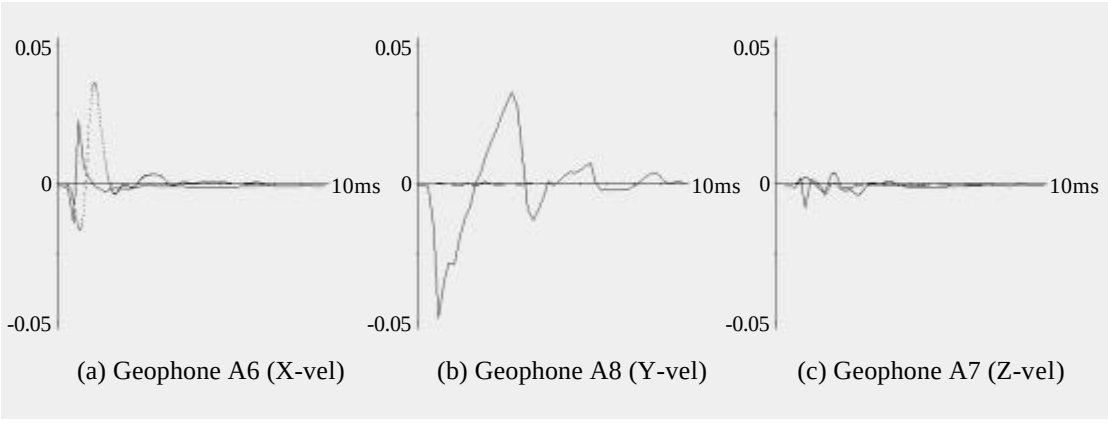

(a) Geophone A6 (X-vel) (b) Geophone A8 (Y-vel) (c) Geophone A7 (Z-vel)

Figure 4.1.2.5 Recorded (solid line) and modelled (dotted line) velocity waveforms for the calibration blast, compared for geophones A6, A7 and A8 which were a triaxial set mounted 5 m into the tunnel wall in solid rock, 1.5 m ahead of the calibration blast.

The main blast consisted of five blast holes with a total charge of 261 kg of explosive, triggered in sequence with a 70 μs delay. Models of this detonation sequence led to complex wave behaviour with multiple incident P- and S- waves, reflected waves and Rayleigh waves. Figure 4.1.2.6 compares the waveforms from the main blast at different distances along the tunnel wall for motion normal to the tunnel wall. Although the first motions are similar, it is clear that the match is very poor. P-wave amplitudes are about 2 to 3 times less in the model. More importantly, the largest motions in the model are associated with the later arrivals of the shear and Rayleigh waves, which are considerably smaller or hardly evident in the recorded waveforms. Figure 4.1.2.7 indicates that the match is no better for recordings 5 metres into the

tunnel wall, 30 metres ahead of the source blast. Hildyard and Milev (2001b) go on to note the similarity between the distribution of maximum velocity and induced tensile stress with the regions of observed damage, but indicate that this is misleading since the maximum motions in the model are associated with completely different wave mechanisms than those measured.

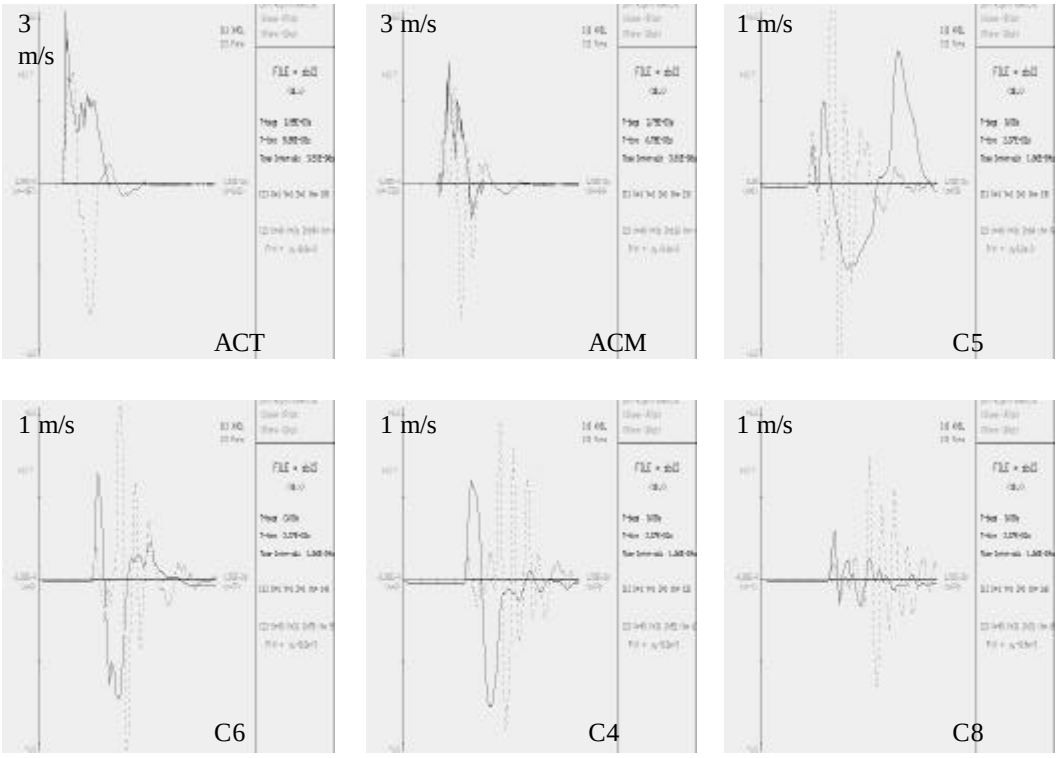

Figure 4.1.2.6 Comparison of the recorded (solid line) and modelled (dotted line) velocity seismograms for the main blast, at ACT, ACM, C5, C6, C4 and C8. (Time windows are 15 ms, and modelled waveforms were time shifted by up to 0.5ms for the first arrivals to coincide).

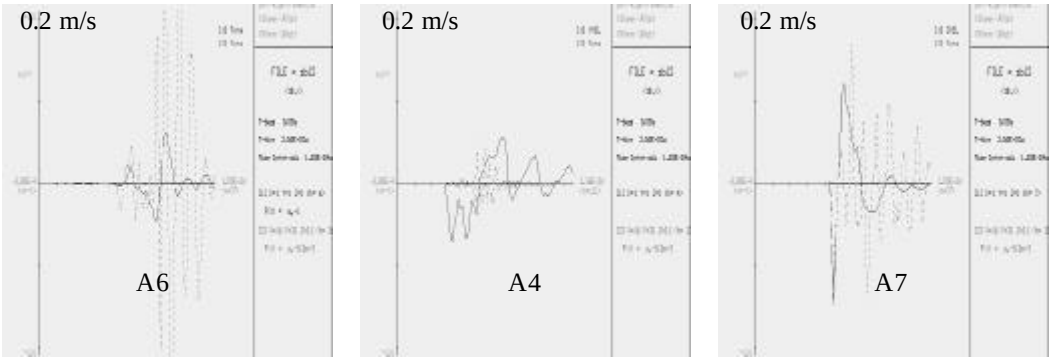

Figure 4.1.2.7 Comparison of the recorded (solid line) and modelled (dotted line) velocity seismograms for the triaxial geophones A6, A4 and A7. These were mounted 30 metres ahead of the blast and 5 metres into the tunnel wall. A6, A4 and A7 are respectively the tunnel-normal, vertical, and tunnel-parallel components. (All time windows are 15ms, and modelled waveforms were time shifted by 0.3ms for the first arrivals to coincide).

In summary, the experiment leads to mixed conclusions. Modelling the small amplitude calibration experiment shows a reasonable but not a perfect correspondence with the recorded data. Modelling the large amplitude experiment corresponds poorly with the recorded data. These differences could be due to problems in the data acquisition, a poor source model, or the inelastic behaviour of the medium.

Although this experiment provided a number of advantages for a case study over a natural event, the number of unknowns is still considerable. There is uncertainty in the wave motion caused by a single detonating blast and in the waves caused by the interaction of multiple blasts. There is a clear lack of coherence in both amplitude and form between recordings measured at different distances along the same ray-path. It is uncertain whether this lack of coherence indicates real behaviour due to large amplitude wave propagation, or errors in the data. There are three possible sources of error in the recordings - poor coupling, the high value of damping in the geophones required to record large ground motion, and poor frequency content with the loss of information due to filtering. Alternatively, the source and data are adequate, and the complex behaviour in the recordings is due to the influence of fractured rock or the influence of new fracturing due to damaging waves.

The above case study motivates the need to first model more tightly constrained data, which isolates a single aspect of complexity. Experimental data is sought for cases which are well-controlled and of limited complexity, and where the data is known or expected to be “clean” and accurate. This is attempted in the next section using data from the URL. It also highlights the need for models of detailed studies on the effects of fractures under idealised experimental conditions, as covered in Section 4.2.

4.1.3 Modelling an underground Experiment at the URL, Canada

Based on the results of section 4.1.3, better-controlled *in-situ* data was required to evaluate model capabilities. Such waveform data was available from *in-situ* recordings in a tunnel at the URL in Canada. This section describes comparisons from an elastic model of the experiment. Comparisons with the recorded waveforms show many similarities such as the correct polarities for all P- and S- waves. However, all paths oblique to the tunnel surface have significant differences in speed and amplitude. This indicates the presence of fracturing and the work is extended in section 4.2.3 to model fracturing to account for this behaviour.

A large number of carefully controlled *in situ* experiments were made at the Underground Research Laboratory in Canada, during the period 1990 to 2000. A fundamental component was the monitoring and collection of microseismic and acoustic emission data. One experiment, forming part of the Mine-by phase of excavation, used an acoustic array to study changes in a small volume of rock, approximately $1\,m^3$, near the face of an advancing tunnel (Carlson and Young, 1992). The experiment included active velocity scans where each sensor in turn is activated as a seismic source, while the other sensors record the response of the rock. These showed variations in both wave-speed and amplitude for different paths, and waveforms altered after face advance due to changes in stress or further fracturing.

The waveforms from these velocity scans were used to evaluate models of wave propagation near the surface of an excavation and through fractures. The experiment was chosen because of well-defined waveforms for both P and S waves, while being of a suitable size, wave frequency, and limited geometric complexity to be studied numerically. In addition, since it occurred within a particularly well-studied region, the stress-field, elastic parameters, geology and geometry were all established.

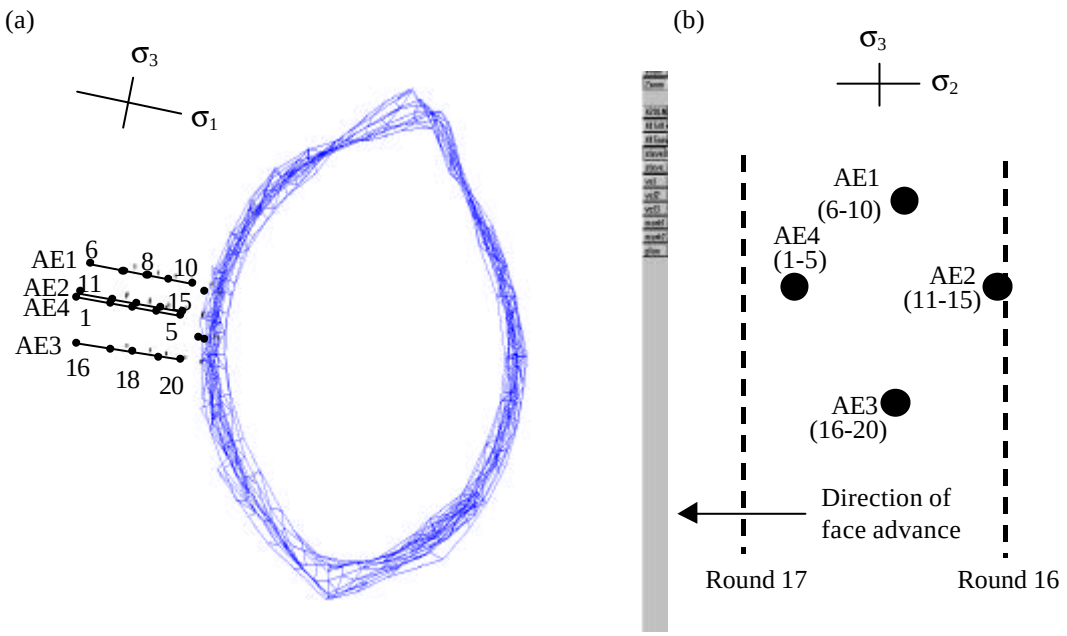

Figure 4.1.3.1 Acoustic emission array showing positions of boreholes AE1-AE4, sensors 1-20, and the orientation of the far-field principal stress tensor. (a) End on view of the Mine-by tunnel (looking from the face back into the tunnel). (b) View from the tunnel surface looking down the boreholes into the solid.

The experimental layout is shown in Figure 4.1.3.1, with an end-on-view of the tunnel, and a side-view of the tunnel surface, indicating the positions of the boreholes, the sensors and the orientation of the stress tensor. The sensors were Panametrics V103 1.0 MHz compressional

transducers. There were 23 sensors in total with 3 mounted on the wall of the tunnel. Sensors were oriented in the boreholes such that they faced the diagonally opposite borehole. The data analysis (Carlson and Young, 1992) identifies a number of trends: (i) significant anisotropy in seismic velocities, with the slow direction orthogonal to the tunnel wall and the intermediate and maximum velocities parallel to the tunnel wall (Figures 4.1.3.2 and 4.1.3.3). (ii) P- and S- wave-speeds decrease with proximity to the tunnel wall (Figures 4.1.3.2b and 4.1.3.3) (iii) velocities change with tunnel advance, dropping with initial advance and then rising again with further advance (Figure 4.1.3.2a). They conclude that the reduced velocities are due to micro-fractures with a maximum crack density of 0.12, and mostly orientated parallel to the tunnel surface (Figure 4.1.3.4).

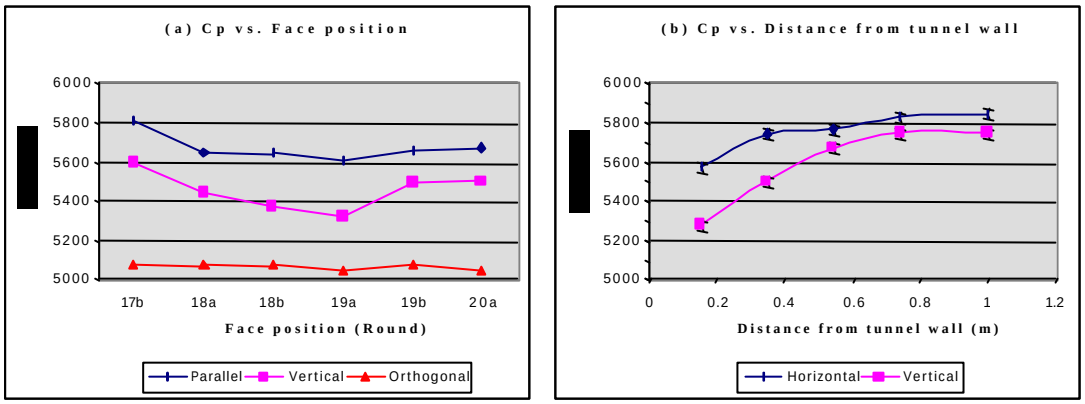

Figure 4.1.3.2 P-wave velocity. (a) Ellipsoidal model with three orthogonal directions of wave-speed calculated for different face positions (b) Variation of C_p with distance from the tunnel wall for paths approximately parallel to the tunnel surface - horizontal paths (AE4-AE2) and vertical paths (AE1-AE3). (From Carlson and Young, 1992).

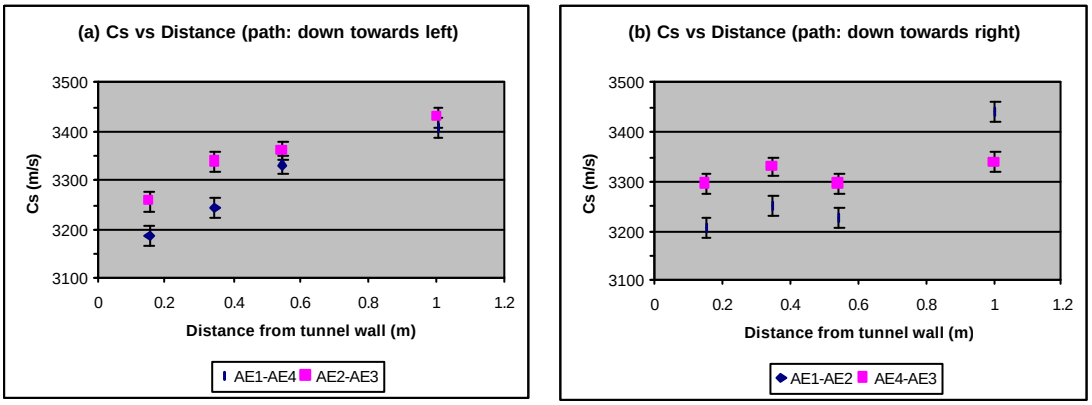

Figure 4.1.3.3 S-wave velocity. Variation of C_s with distance from the tunnel wall for paths approximately parallel to the tunnel surface (a) paths downwards towards left (AE1-AE4 and AE2-AE3) (b) paths downwards towards right (AE1-AE2 and AE4-AE3). (From Carlson and Young, 1992).

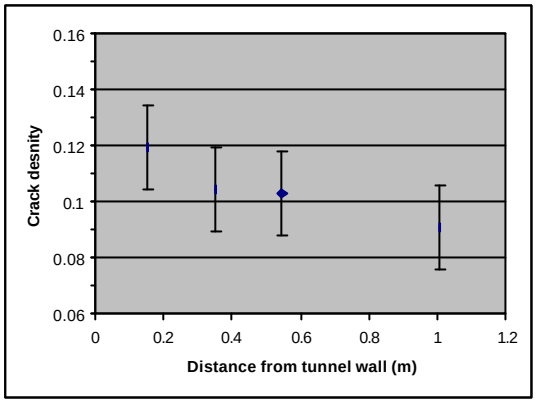

Figure 4.1.3.4 Crack density variation with distance from the tunnel wall, calculated from the measured values of C_p and C_s (From Carlson and Young, 1992).

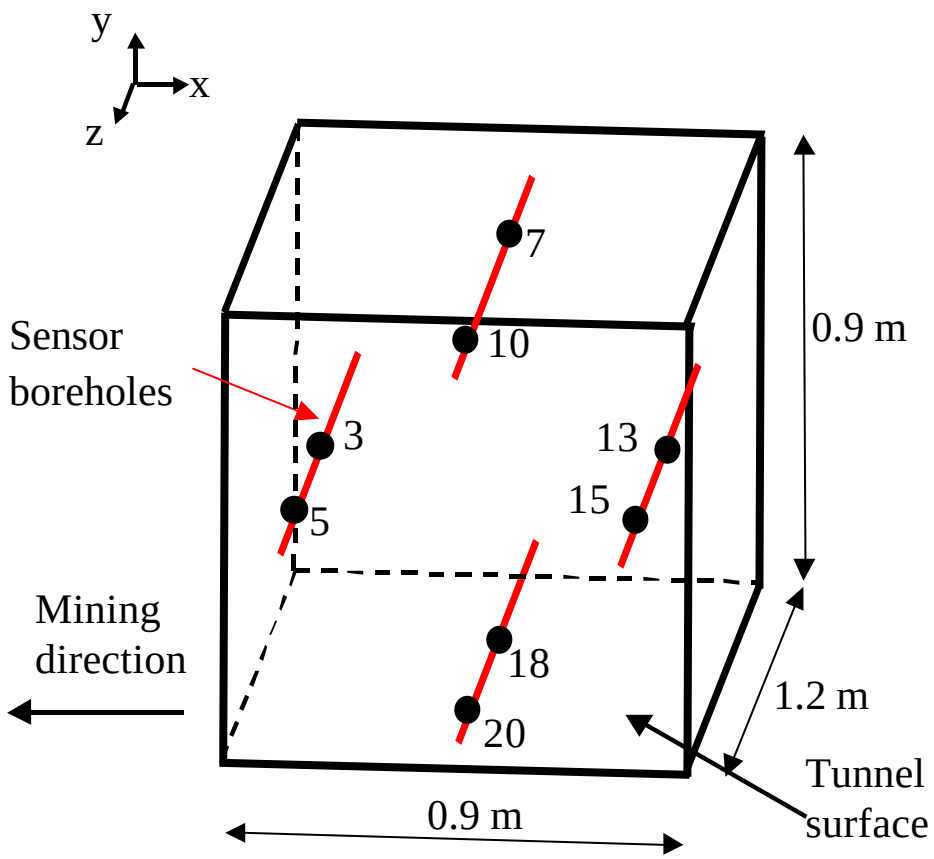

Figure 4.1.3.5 Sketch of the model of the acoustic array. The full array consisted of 4 boreholes each with 5 sensors spaced at 0.2 m starting at 0.2 m from the tunnel surface. The model used a reduced 8x8 array and the positions of the sensors used are shown. For the model, the boreholes were rotated into a diamond pattern as shown. The block indicates the model boundaries.

The original waveform data was used to evaluate the ability to model the wave behaviour. The experiment was modelled in three dimensions using WAVE (Figure 4.1.3.5). Approximately 8 million grid-points with a 5 mm grid-spacing were used to cover the volume of approximately 1 m^3. The tunnel surface was approximated by a flat, stress-free surface. A reduced data-set of 8 sensors was used, giving an 8x8 array. Recorded waveforms are really voltages. As the same sensors are used as sources and receivers, the assumption is made that whatever physical property is influenced by the sensor when used as a source, is equivalently measured by the sensor when used as a receiver. For example, if velocity is applied as the source, then velocity is measured by the receiver. It is also assumed that the source and receiver response can be built into the source time function, and that only the medium response needs to be modelled. A range of studies were made to determine the appropriate source. It was found that applying a normal velocity accounted for the correct polarity of all P- and S- waves, and approximately accounts for the variation in amplitude for different ray-paths. In spite of a relatively large model of 8 million grid-points, the frequency of the model source needed to be lower than the physical source to avoid dispersion. This limited the ultimate accuracy of the model.

The initial model consisted of an isotropic elastic medium, with the elastic wave-speeds of the intact rock. The full set of waveform comparisons are presented in Figure 4.1.3.6 for the source at sensor 3. This case was chosen as it clearly indicates the differences between paths approximately parallel to the tunnel face 3:7, 3:13 and 3:18, and those oblique to the tunnel surface 3:5, 3:10, 3:15 and 3:20. All three cases parallel to the surface are close to the data in terms of the wave-speed and amplitude of both P and S waves, and are similar in the total waveform. The worst match are the amplitudes in path 3:7, and this path is more oblique than the other two paths. Since waveforms for different source-receiver angles are well matched by the model, it is assumed that the source model is an acceptable approximation of the real source, and that deviation of the recordings from the elastic model is due to wave interaction with the medium. The comparisons for paths oblique to the tunnel surface are strikingly different. All recordings have much later arrivals, and significantly lower amplitudes than the elastic model. We therefore need to account for waveform changes in this direction of propagation, with propagation parallel to the surface remaining relatively unaffected. This is done in section 4.2.3.

This exercise provided a number of insights. Primarily, it shows that it is feasible to model wave behaviour in real rock. It also highlights the practical need for very large models, as even models with millions of elements may not be sufficient to model the true frequency content. Significant insight was also gained on source modelling for these types of experiments. The most important conclusion though is that even where a dilute crack density is expected, it is not possible to simulate waveforms or amplitudes without modelling the cracking in the material.

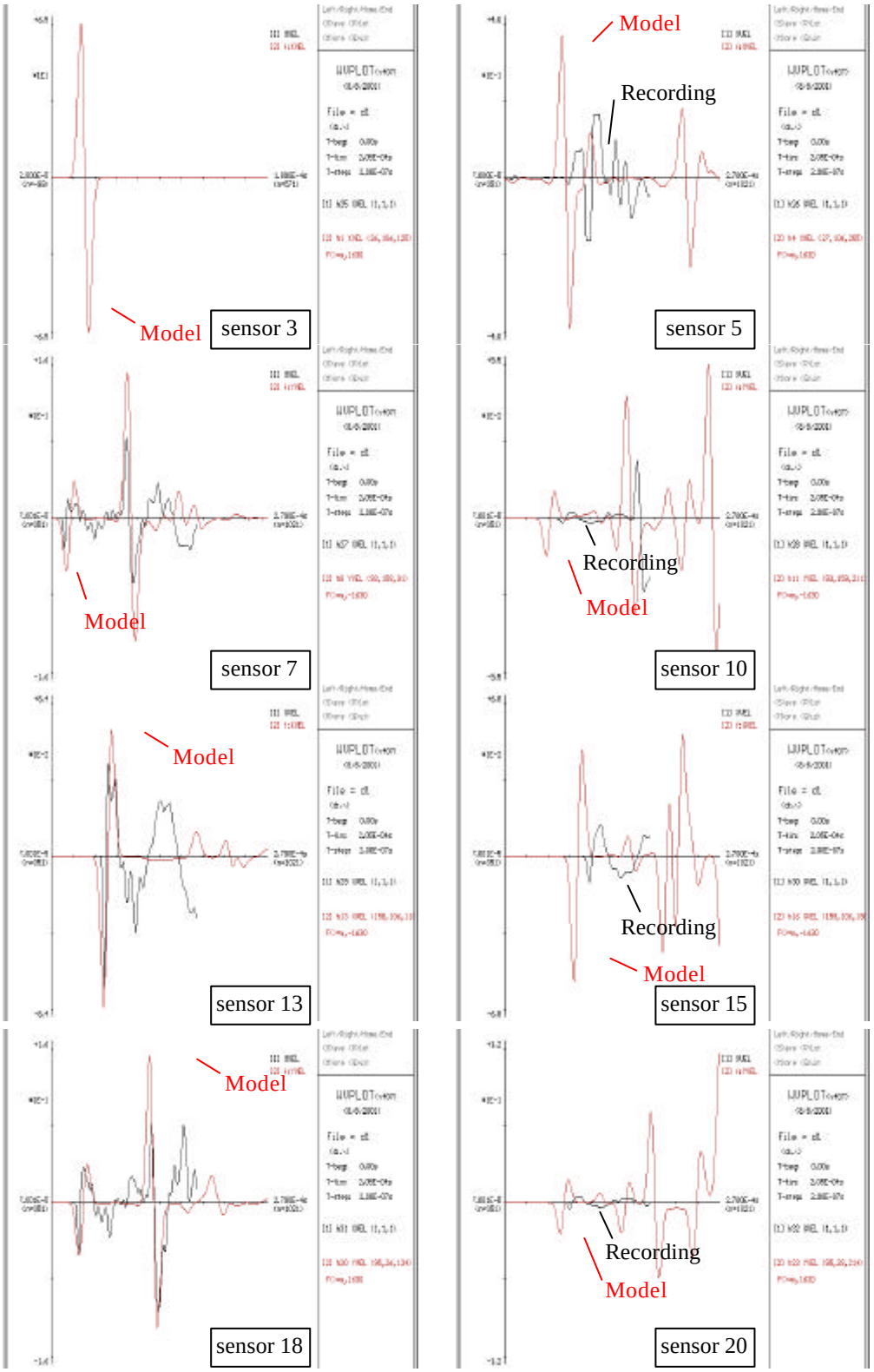

Figure 4.1.3.6 Elastic model (red line) compared to velocity scan AT01 (black line) for source at sensor 3 - sensors 3, 5, 7, 10, 13, 15, 18, 20. Model scaled such that peak P-wave amplitude of sensor 18 matches the data.

4.1.4 The influence of excavation free surface on the distribution and amplitudes of ground motion

Understanding the maximum ground motions due to a rockburst, its decay and the regions of large ground motion, has important consequences for hazard analysis and support design. However, a number of questions remain unanswered in the field of rockburst study. What are the maximum in-stope amplitudes caused by a seismic event? What mechanisms lead to motions in stopes being much larger than those in the solid rock? What affects the observed distribution of damage?

The first uncertainty is in the peak ground motion. Current rockburst support in South African mines are designed to yield at rates of up to 3 m/s (Jager, 1992). McGarr (1993) concludes that velocities of up to 4 m/s can be expected in the near-source region. Spottiswoode et al. (1997) note that such estimates omit the effects of the excavation, the fractured rock around it, and the relative motion of the stope surfaces. Hemp and Goldbach (1993) tabulate in-stope velocities from near-field events, which they define as having hypocentral distances of less than two source radii, and note that these are considerably lower than projections of the peak amplitude. The maximum velocity they report is 0.45 m/s at a distance of approximately 1.5 source radii, from a magnitude 1.9 event. Jager and Ryder (1999) state that “actual observations, from instruments installed in stopes and tunnel sidewalls, have so far indicated ground motions of no more than 2 m/s associated with nearby seismic events”. Projections inferred from observations such as ejected rock have however suggested the possibility of much larger motions (e.g. 8 m/s, Ortlepp, 1993).

The second uncertainty is understanding the effect of the excavation. Researchers who have recorded ground motion inside excavations have observed that these are many times larger than the ground motions in the solid. Hemp and Goldbach (1993) compared on-reef and off-reef velocities and accelerations. After multiplying by the hypocentral distance, they indicate that the motions in stopes were five to ten times higher than those in the solid rock. Milev et al. (1999) recorded ground motion at 2 m intervals in a borehole drilled 10 m vertically into a stope hanging-wall. They conclude that “ground motion at points on the skin of a stope hanging-wall was found to be some four to ten times larger than at a point 6.5 m into the hanging-wall”. It has been hypothesised that such observations result from amplification due to fracturing in the rock surrounding the stope (Hemp and Goldbach, 1993; Spottiswoode et al., 1997; Milev et al., 1999).

Another uncertainty is what influences the distribution of damage. Investigations of rockbursts have indicated that positions of damage can vary greatly, and damage can occur at large

distances from the original event. Durrheim et al. (1997a) summarise conclusions from twenty-one rockburst investigations over a three year period, and state: “The severity of rockburst damage often varies greatly. One panel in a longwall may be severely damaged, while an adjacent panel (perhaps even closer to the focus of the seismic event) is unscathed”.

This section uses models to evaluate the effect of the excavation on ground velocity and in so doing attempts to address these questions. It first evaluates the influence of the stope free surface alone and highlights certain features of Rayleigh waves. It then examines the effect of variations in the geometry and source on the amplitude of ground motion. The additional contribution of fracturing is studied in section 4.2.5.

An idealised mining layout was used to examine the effects of an excavation on wave propagation. This consisted of a long-wall tabular stoping geometry with a vertical slip event in the foot-wall of the pillar. The region of slip was a square area 28 m by 28 m, extending down from the plane of the stope and along the edge of the pillar. A plan view of the layout is shown in Figure 4.1.4.1.

It was found that even a relatively small event (M=1.3), produced stope velocities of 0.1 m/s hundreds of metres from the event. Particle velocities at a remote pillar were found to be up to six times that of a model which took no account of the excavation. The excavation significantly influenced both the amplitude and the distribution of the largest motions, with maximum amplitudes following the face outline. The particle velocities declined with depth, but were not less than half of the surface value at 10 metres depth. However, this is highly dependent on the source size and wavelength, and velocities at the surface are up to 8 times those deep in the solid material.

An even more marked effect was noted when the tensile stresses were examined. The same event (M=1.3), induced tension of 2 MPa at the stope surface hundreds of metres from the event, and the induced tensile stress was up to twenty-five times that of a model which took no account of the excavation. Figure 4.1.4.1 shows the distribution of maximum induced tensile stress at the surface and is very similar to that of the maximum velocity, but decays much more sharply with distance from the free surface. It is hypothesised that this induced stress may be significant in triggering falls of ground in the low stress failed regions of the stope hangingwall and footwall, or energy release in the highly stressed regions of the pillars.

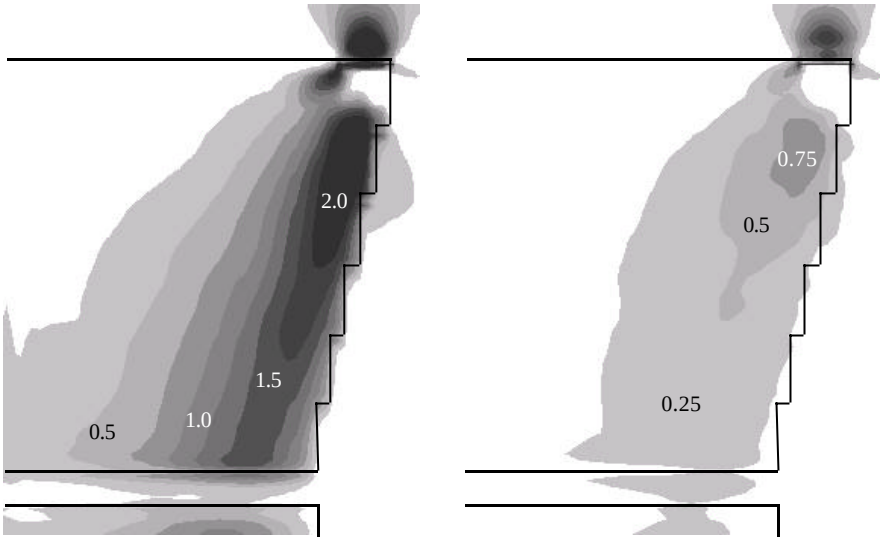

(a) 2m below stope (b) 6m below stope

Figure 4.1.4.1 Maximum induced tensile stress (in MPa) for s_{zz}. Plan sections are shown for two distances below the excavation, and indicate that horizontal tensile stress of up to 2 MPa is induced close to the surface, and that this falls off rapidly with distance from the surface.

The above analysis provides one explanation for apparent velocity amplification at stope surfaces. The amplitudes of velocities measured in the stope a number of source radii from the event are many times higher than would be expected in solid rock. This effect is due to Rayleigh waves propagating along the free surface of the stope, although for these wavelengths and distances the shear and Rayleigh waves do not separate, and motion is made up of both body and surface waves. It is significant that the effect of just a 1.3 magnitude event near the edge of a stope can lead to significant motions and induced stress hundreds of metres from the event.

A number of features of a Raleigh wave propagating along a hangingwall surface were analysed - in particular how the particle motions relate to induced stress, how motions and stress decay with distance from the surface, and how this decay depends on the wavelength of the incident wave. The study here, as in most mining scenarios, includes the combined effects of both body and surface waves. The Rayleigh wave speed is 91% of the shear wave speed and separation from the shear wave occurs only after a distance of at least ten wavelengths. For a distance of 200 m, only wavelengths less than 20 m or frequencies greater than 150 Hz will separate in the time domain. For many mining events, separation will therefore not be evident in the seismograms.

The studies were made with two different source frequencies of 330 Hz and 120 Hz, equating to wavelengths of approximately 10 m and 27 m respectively. The particle motion is retrograde at the surface but reverses direction for points further into the solid, which also have decreasing amplitude. The velocity was scaled to give a peak of 0.1 m/s, which resulted in a peak tension of 1.8 MPa at the surface. The waveforms for both stress components are closely related to that of the horizontal velocity at positions close to the surface. Figure 4.1.4.2 examines how the different components of velocity and stress decay with distance from the surface in the case where the dominant wavelength is 10 m. Horizontal velocity decays to zero and changes direction at a distance of $\lambda/4$, and reaches a maximum in the opposite direction at $\lambda/2$. The vertical and total velocity decay more slowly, and the amplitude decays to approximately 50% of the surface value at a distance of $\lambda/2$, and 20% of the maximum at λ. The above is consistent with theoretical results (e.g. Graff, 1975).

Induced tensile stress declines more rapidly than velocity and is 50% of the surface value at $\lambda/10$. The direction of maximum tension at the surface is horizontal, but at a distance of approximately $0.15\,\lambda$, the induced vertical tension is greater than the induced horizontal tension. This would affect the direction which is conducive to damage. Maximum velocity and the induced maximum tension are therefore not directly related, which is important if either is used as an indicator of likely damage.

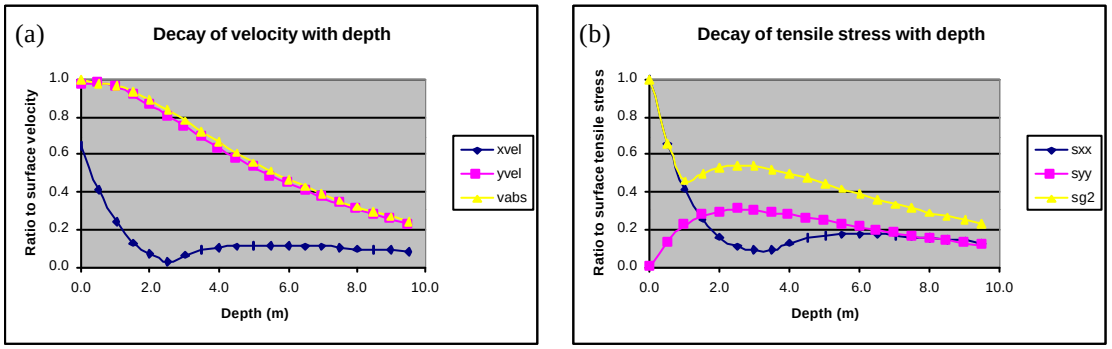

Figure 4.1.4.2 Decay of velocity and stress with depth into the hanging-wall. The peak frequency was 330 Hz, with a wavelength of approximately 10 m. (a) Decay of the peak horizontal velocity (xvel), peak vertical velocity (yvel), and peak total velocity (vabs). (b) Decay of the peak horizontal tensile stress (sxx), peak vertical tensile stress (syy), and peak tensile stress (sg2). The results shown are normalised to the maximum velocity and tensile stress, which were 0.1 m/s and 1.8 MPa respectively.

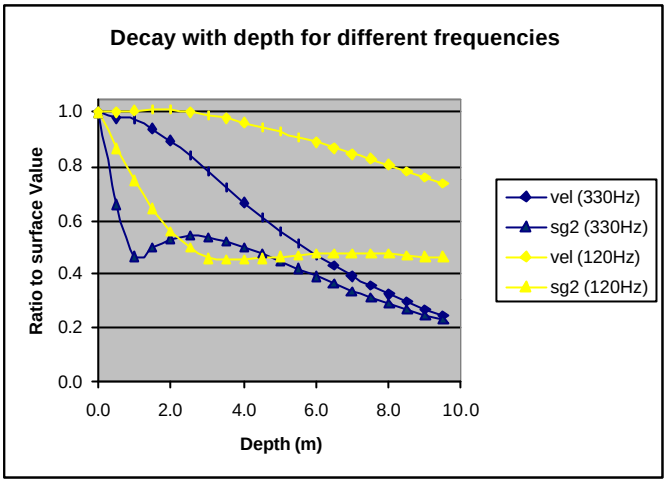

Figure 4.1.4.3 Decay rate of velocity and maximum tensile stress for different frequencies. (a) Peak frequency of 330 Hz (l » 10 m) (b) Peak frequency of 120 Hz (l » 27 m)

Figure 4.1.4.3 compares the velocity and tensile stress decay for two different sources, with peak frequencies of 330 Hz and 120 Hz corresponding to wavelengths of 10 m and 27 m respectively. At a distance of 10 m, the higher frequency source has decayed to a peak velocity and tension of less than 25% of the surface values, whilst the lower frequency source is still 75% of the surface velocity and nearly 50% of the surface tensile stress. For smaller, higher frequency events, the decay is even more rapid, leading to the velocity at the surface being many times more than that a few metres into the solid. Measurements have been made in the stope fracture zone in which particle velocities are many times higher at the surface than a few metres into the fracture zone (e.g. Milev et al., 1999). This has been interpreted as amplification due to the fracture zone. Some of this apparent amplification may be explained by Rayleigh waves rather than by the effect of the fracture zone.

A number of further models were made of the pillar event, varying the characteristics of the source and its position relative to the excavation, and studying the effect on the apparent amplification for both near-source and far-field motions. The most significant control on amplitude was the peak stress-drop. The distance of the stope from any part of the region of slip was more important than it's distance to the source centre. The position of the event relative to the stope face influenced the amplitudes although the actual face shape had little effect for this size event. The sense of vertical slip had no influence on velocity amplitudes but a significant influence on induced tension. It is important to note that both senses of slip are of practical importance as typically there is excavation on both sides of the pillar. Horizontal (ride) slip induced greater near-source tension, but lower velocities and tension at more distant parts of the stope, indicating that the effect of surface waves is not as great for this direction of slip.

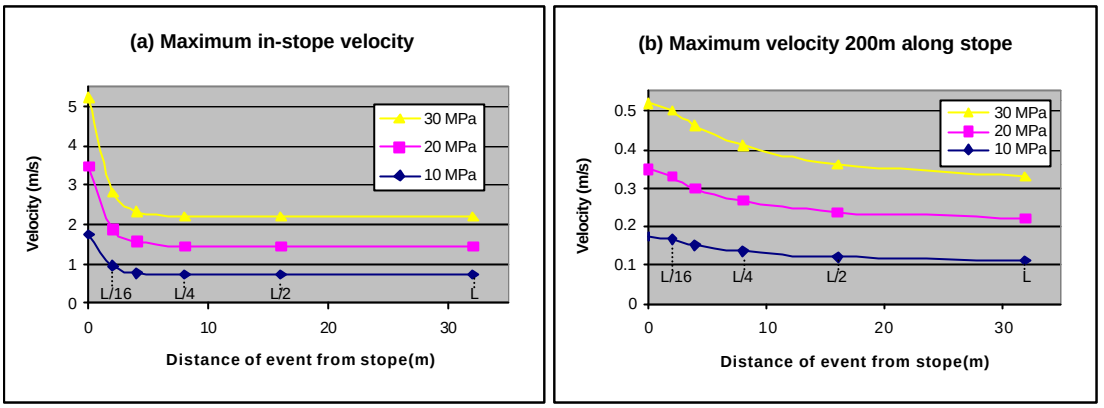

Figure 4.1.4.4 Relationship of stress-drop and source distance to velocities in the stope. Results are based on a vertical slip source with a square area of 32 m side-length, initiating at the centre and propagating up to the stope plane. Resulting magnitudes range from 1.83 to 1.76, 1.71 to 1.64 and 1.51 to 1.44, for stress drops of 30 MPa, 20 MPa and 10 MPa respectively. The maximum velocities are valid for any source size (L), where the distance of the source to the stope is expressed in terms of L. In this case (b) indicates the velocity at a distance of 6.25 L.

The most important influences on near and far-field stope velocities are the stress-drop and the proximity of the event to the stope. These effects are summarised in Figure 4.1.4.4. For these models, the source comprised vertical slip on a square area of 32 m, with stress-drops of 10 MPa, 20 MPa and 30 MPa. The position of the source plane ranged from 32 m ahead of the stope, to 0 m (daylighting). Results show that the maximum stope velocity is linearly related to the stress-drop. The results also indicate that there is a significant increase in the maximum velocity as daylighting is approached. This is only partly due to closer proximity to the source as the seismic moment also increases. For daylighting, the moment is approximately 20% higher than the same stress-drop event at a distance of 32 m, as greater proximity to the stope causes increased slip. The maximum velocities in Figure 4.1.4.4 apply to any source size, if the distance of the source to the stope is expressed in terms of the source size (L). In this case Figure 4.1.4.4(b) indicates the velocity at a distance of 6.25 L. The results are not a true upper limit on the velocity, as this also depends on the rate of slip. In this model the stress-drop for a 2 m by 2 m area took 2 ms and the rupture propagated at 3000 m/s. Faster rates of slip lead to higher particle velocities.

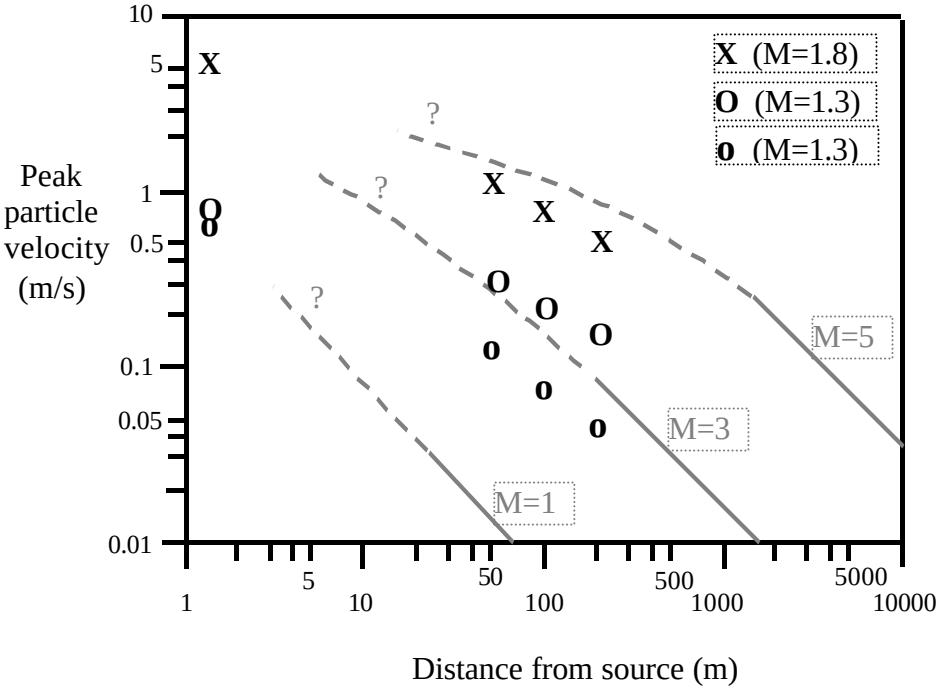

Figure 4.1.4.5 Velocities for three modelled events superimposed on a graph (from Jager and Ryder, 1999) of far-field and projected near-field velocities for different magnitude events. 'X' is for the 30 MPa daylighting event of Figure 4.1.4.4; 'O' is for the M=1.3 event of Figure 4.1.4.1a; 'o' is the same event as 'O' without the influence of the stope. The presence of the stope, and cases with a high stress-drop, lead to in-stope velocities associated with much larger magnitude events in current guidelines.

The maximum velocities produced in this work were up to 70% greater than the upper limits commonly estimated using the formula ($V_{max} \approx 1.1\tau_e/(G\beta)$), (Jager and Ryder, 1999), where τ_e is the stress-drop, G is the shear modulus, and β is the shear wave velocity. Figure 4.1.4.5 shows present estimates of far-field and near-field velocities for different magnitude events (Jager and Ryder, 1999). Velocities for three of the modelled events have been superimposed on the original graph. The two modelled events which include the excavation, have velocities much higher, and decay more slowly than that projected by Jager and Ryder. Their estimated curves correspond more closely to the solid model. The presence of the stope, and a high stress-drop, therefore lead to in-stope velocities normally associated with much larger magnitude events.

The peak amplitudes modelled here should not be seen as an indication of the maximum velocities possible. Quite small magnitude events were modelled, and both larger magnitude or higher stress-drops would lead to larger amplitudes. Secondly, in all cases a uniform stress drop

was assumed across the slip region. If the stress drop was less evenly distributed, this would likely lead to larger peak velocities.

This work indicates that the amplitudes in both the near-field and the far-field are influenced in a complex manner by the following factors: the stress drop, the sense of slip, the excavation surface, the excavation outline, and the proximity of any part of the source, rather than the source centre, to the excavation. The conclusion from the above is that the damage potential from an event near an excavation cannot be readily inferred from measures such as moment, magnitude and the proximity to the source centre. Explicitly modelling the event and mining geometry may be the only way of evaluating the damage potential of an event. For the near field, the cases studied indicated an increase in peak particle velocities of up to 40% due simply to the influence of the stope geometry. Considering just the source may therefore give too low an estimate of the peak velocity. If the effect of the excavation is ignored, the decay of ground motion with distance is over-estimated, and the induced tensile stress is grossly underestimated.

4.2 Interaction of seismic waves with fracture assemblies

The previous section identified the difficulties and limitations encountered in modelling seismic waves around mine openings. An important contributor to this complexity is the effect of fracturing on the seismic waveforms and distribution. In particular, it is necessary to develop and to demonstrate whether models can accurately reproduce observed behaviour when waves interact with fracturing. The detail of this work is covered in the thesis “Wave interaction with underground openings in fractured rock”, (Hildyard, 2001). Again, only some of the main results and conclusions are summarised here, and the thesis is presented in its entirety as a supplementary document.

It was shown in the review that while theoretical models have been developed and many laboratory experiments have been performed, numerical models have not yet been demonstrated to be able to accurately model wave interaction with widespread fracturing. This work develops numerical models capable of studying wave propagation through fractures, evaluates the capacity to simulate wave propagation through large numbers of fractures by direct comparison with experimental and *in situ* data, and demonstrates the contribution that these models can make to understanding the distribution of ground motion due to underground seismic events, and aiding interpretation of the fracture state from observed waveforms.

4.2.1 Overview of previous research on wave propagation through fracturing

One feature of deep underground excavations is a highly fractured rock-mass. This excavation-induced damage may extend many metres into the rockmass (e.g. Adams and Jager, 1980; Napier et al., 1997). This leads to complex wave motions and complicates the task of modelling wave propagation. A wide body of literature deals with studies of wave propagation through fractured rock. Much of this research has been focussed toward exploration applications such as in the oil industry, with emphasis limited to accurate simulation of first arrivals. However, for the purposes of understanding or projecting rockburst damage, accurate simulation the full wave behaviour is essential.

A displacement discontinuity has been proposed as a suitable discrete representation of a fracture (Schoenberg, 1980; Myer et al., 1985). Experimental studies have indicated that this representation captures many of the frequency dependent effects of fracturing on waves (Pyrak-Nolte, 1990a, 1990b). Numerical studies using this representation have however tended to be made with assumptions of plane waves, two-dimensional modelling, or contain very limited numbers of fractures (e.g. Gu et al., 1996; Cai and Zhao, 2000).

The alternative approach to a discrete fracture representation attempts to encapsulate the effects of large numbers of fractures into the behaviour of the medium. This approach considers the fractured rock as an effective elastic medium, with the elastic constants related to the density of fracturing, and typically leads to anisotropy in the seismic velocities (e.g. O' Connell and Budiansky, 1974; Crampin, 1981; Sayers and Kachanov, 1991). Expressions for the effective attenuation have also been developed (Hudson, 1981; Liu et al., 2000). The main restriction is that this representation is valid only for wave propagation of long wavelengths much greater than the fracture size. There are also restrictions limiting the density of fracturing.

Most numerical studies of waves through fractures therefore make some of the following assumptions: two-dimensional wave-propagation; plane wave propagation; small amplitude motions; low frequencies relative to the crack-size; dilute crack concentration; uniform stress state, or are only accurate for first arrivals. Many of these assumptions are poor in the context of real problems involved with wave propagation around underground openings. Excavations are firstly in a highly non-uniform stress-field. In the case of deep-level mining, the excavation surface is highly fractured, wave amplitudes may be large, sources are in the near-field and wave motion is non-planar. Microseismic and ultrasonic recordings used to monitor excavations and infer the rock-mass state, contain frequencies which do not satisfy low frequency or plane

wave assumptions. Accurate simulation is required over the full duration of dynamic motion and not just for the first arrivals, so that the full effect on the rockmass can be assessed.

There is a significant gap therefore between what has so far been demonstrated in numerical studies and what is required for models of wave propagation around underground excavations. In particular it remains to be demonstrated through comparison of simulations with observed behaviour, that such models are capable, appropriate and accurate for simulating wave motion in the zone of highly fractured rock surrounding a typical underground excavation.

4.2.2 Laboratory measurements of seismic waves in quartzite

In order to quantify the ground motion caused by rockbursts or slip on geological structures in a mine, it is necessary to model the attenuation characteristics of seismic waves. The attenuation of both the P- and S- wave components are relevant in the context of determining hazard due to rockbursts since high-frequency ground motion is generated by P- waves and the large amplitude ground motion is produced by the S- waves. Considerable work is required to apply the available numerical modelling methods and compare the results with laboratory tests and in-situ seismic recordings for further understanding of wave attenuation. This will improve our understanding of seismic wave propagation in the fractured rockmass around the stope (Sellers, 1995).

Wave propagation velocity and attenuation have been used to determine dynamic properties of rock (Siggins, 1993). Both wave propagation velocity and attenuation parameters seem to be sensitive to weathering conditions (Klimis, 1991), anisotropy (Tao and King, 1990), grain dimension (Klimis, 1991 and Tao and King, 1990) of a rock. Ultrasonic waves of low amplitude and with a frequency of around 50kHz can be easily generated under laboratory conditions using piezoelectric actuators. Ultrasonic measurements in the laboratory can be used for material characterization and non-destructive evaluation (Lockner et al., 1977) and during mechanical or thermal tests in order to find correlations with cracking, compaction and pore collapse (Lockner et al., 1977; Klimis, 1991; Thimus, 1993; Moustachi et al., 1995; Jones and Moral, 1989; and Rao and Ramana, 1992).

The propagation of seismic waves in a quartzite rock sample was investigated experimentally using standard laboratory techniques (ASTM, 1994; Rummel et al., 1981, Couvreur and Thimus, 1996). The waves are generated by a PUNDIT UNIT (Portable Ultrasonic Non-destructive Digital Indicating Tester) which can transmit and receive P and S waves using two 50 mm

diameter transducers. The waves are generated at the top of the specimen, so that the wave propagation
is mainly in the loading direction. The waves are recorded by transducers that are in contact with the bottom of the specimen. The output signals are recorded by a digital oscilloscope and a PC computer (sampling frequency of 20 MHz) and saved at several intervals during the test to permit further analysis. In subsequent tests, the rock specimen was sliced and the sliced rock pieces placed on top of each other to mimic a cracked rock.

The peak particle velocity (PPV) can be expressed as a function of the distance R_s to the source of an event by a relationship of the form

$$Log(PPV) = A - \alpha Log(R_S) \qquad (4.2.2.1)$$

where the intercept A depends on the event magnitude and the constant α is the distance attenuation coefficient with respect to the scaled distance, R_s (e.g. Srinivasan et al., 2001). Expressions for the constants can be obtained for various situations, especially with respect to blast vibrations monitored essentially for determining safe levels of ground motion response in surface mining (Nicholls, 1971; Dowding C.H., 1985 and 1992). Similar relationships have been arrived at in the context of mining induced seismicity by other authors (e.g., McGarr et al. (1981), Wagner, (1984), Gibbon, et al. (1986)) when attempting to assess the damage potential of rockbursts in stopes and tunnels in South African mines. The form of this relationship is then given as

$$Log(R\bar{V}) = 3.95 + 0.57M \qquad (4.2.2.2)$$

where $\bar{V}$ is the peak ground velocity and M is the event magnitude.

The waveforms transmitted through solid and cracked rock samples have been analysed to study attenuation in the time domain. The peak amplitude of waveforms from samples of different lengths were compared to investigate how the wave attenuated with distance. As shown in Figure 4.2.2.1, the waveforms from the longer samples are more attenuated and the pulse shapes are also affected by the sample length. The presence of cracks in the rock was simulated by placing shorter samples together to make up a length equivalent to that of the uncracked sample. Tests were done with one, two and three cracks within the sample. The waveform amplitudes were highly diminished in the cracked rock samples. With three or more cracks, no signal could be determined within the resolution of the data acquisition system. As shown in Figure 4.2.2.2, the first arrival amplitude was so low that it could not be distinguished clearly from the background noise. The regular oscillations observed in the seismogram after 90 milliseconds appear to be due to resonance of the transducer. The study of the seismograms indicates that the waves from the cracked rock are also slowed (i.e., arrive later compared to solid rock).

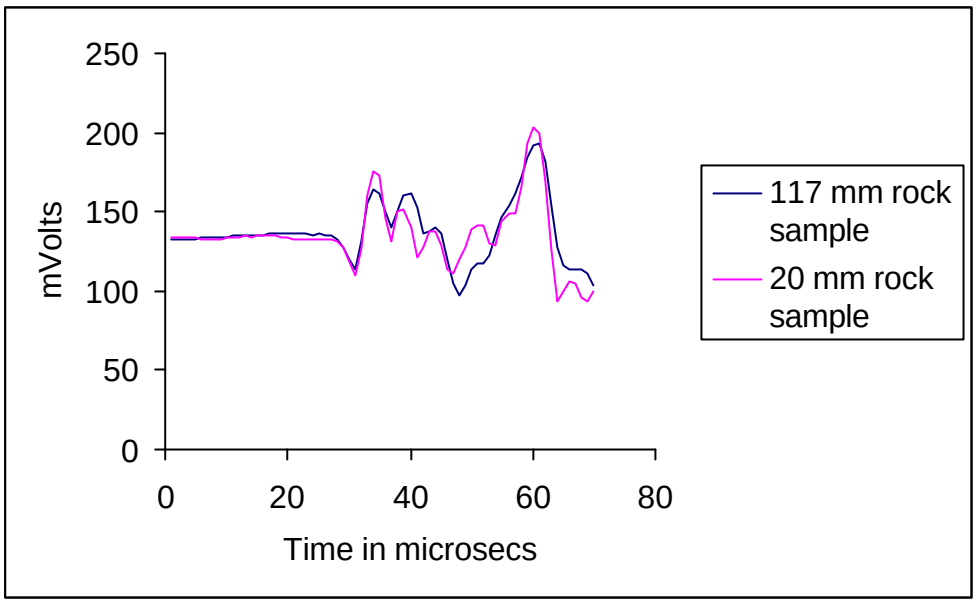

Figure 4.2.2.1 Waveforms from solid rock samples of 20 mm and 117 mm lengths.

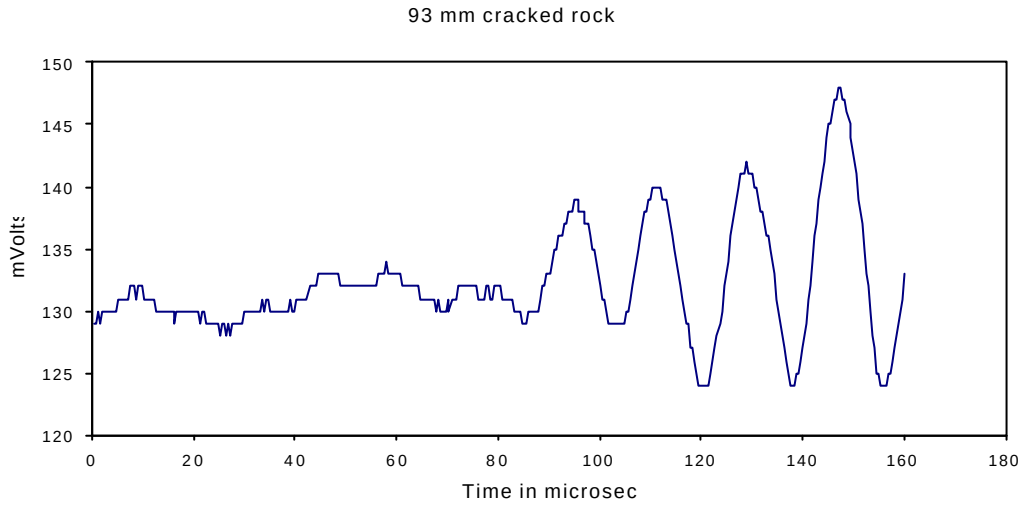

Figure 4.2.2.2 Waveforms for a 93 mm long rock sample containing 3 cracks.

Figure 4.2.2.3 shows a plot of the log(amplitude) in milliVolts vs the log of the sample length. The slope of this plot corresponds to the distance attenuation coefficient α in equation 4.2.2.1. The attenuation with sample length is linear for uncracked samples. The introduction of a single crack into the rock sample reduces the magnitude of the output signal and thus causes considerably more attenuation. The results for the cracked rock sample have a considerable drop in amplitude that can be attributed to attenuation by the cracks. The presence of two cracks does not result in much further attenuation. However, three cracks caused complete destruction of the output wave. The attenuation of cracked samples tends to be bi-linear over

the entire range of sample lengths that can be tested, and the slope increases significantly for longer samples.

.

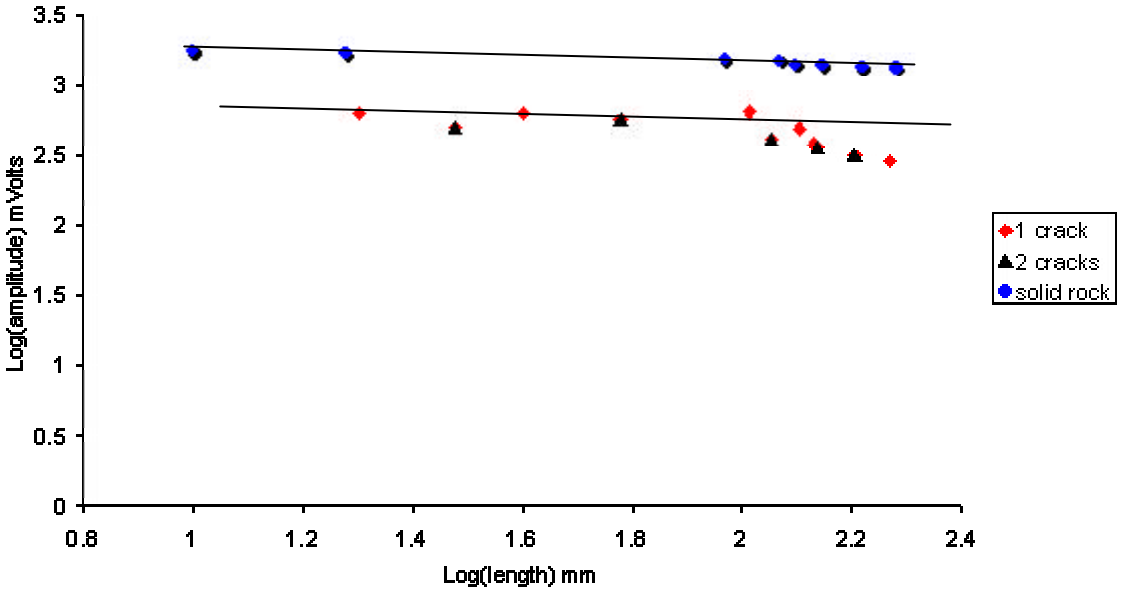

Figure 4.2.2.3 Plot of Log amplitude verse Log distance from the source for a solid and cracked samples.

The Fourier power spectral amplitude was analysed for waveforms from a 120 mm long steel sample, 119 mm full rock sample, 93 mm full rock sample and 93 mm cracked rock sample. It is observed that the rock exhibits much more attenuation than steel (see Figure 4.2.2.4). The results also indicate that more attenuation, especially of the higher frequencies, occurs in the presence of cracks. Seismic waves are highly attenuated in cracked rock because of the wave distortion caused by cracks. As the wave propagates through a cracked solid, multiple scattering processes take place and incident wave energy is transferred to the scattered waves. Consequently, the wave decay will depend on the size distribution of cracks. The decay rate increases with increase in frequency, and the effective wave (pulse) velocity, decreases with an increase in frequency. The wave attenuation and dispersion, constitute a radical difference between wave propagation in a cracked solid and in an uncracked solid (Gross and Zhang, 1992). The observations in this study are in agreement with results from some numerical models (e.g., Cai and Zhao, 2000).

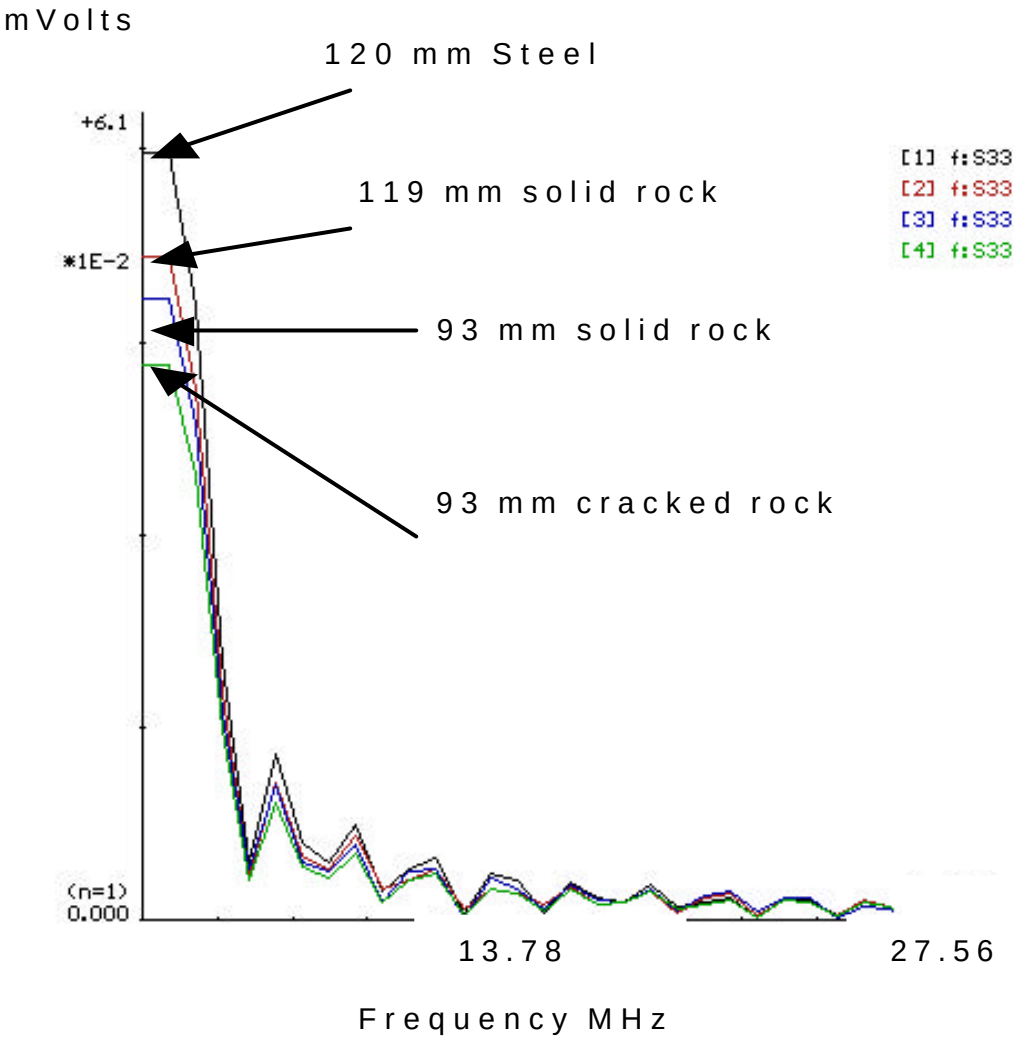

Figure 4.2.2.4 The linear-linear plot of amplitude spectra for waveforms from steel of 120 mm length, 119 mm of length full rock, 93 mm of length full rock and 93 mm of length for cracked rock sample. Notice that the high frequencies are strongly attenuated for the cracked rock sample and the rock is more attenuated than steel.

These studies have shown that as a wave propagates through a cracked solid, multiple scattering processes take place and scattered waves are induced. The wave amplitude as well as the wave speed decreases with increase in sample length (distance). High frequencies are eliminated by cracks and with distance from the source. This study has provided preliminary data that can be used in the calibration of numerical models.

4.2.3 Models of laboratory experiments with fractures

This section presents the conclusions from modelling laboratory experiments of wave propagation through fractures. Some of these results have been presented in the final report of SIMRAC project GAP332 (Napier et al, 1998), but the full results and conclusions are now available from the thesis by Hildyard (2001) that is attached as a supplementary document.

In the late 1980s experiments were performed by Pyrak-Nolte et al. (1990a, 1990b) recording wave propagation through single and multiple fractures. The importance of these experiments was that they recorded detailed and precise waveforms for both P- and S- wave propagation through different orientations of the fracturing. Their work shows significant changes in both the amplitude and wave speeds due to fracturing. The fractures had significant effects on the total waveforms including wave propagation parallel to fractures, even when the apparent arrival or peak amplitude was not significantly altered. The results indicate that amplitude and wave-speed in a fractured medium are frequency dependent. It was shown that an approximate analytic model using multiple displacement discontinuities with uniform fracture stiffness, had a similar frequency behaviour to the multiple fracture experiment.

The waveforms from these experiments present extremely good data with which to evaluate numerical models of wave propagation through fractures. A number of features make this data particularly attractive for modelling:

- the existence of a control experiment through unfractured material
- significant and complex differences between waveforms for each variation
- high quality sensors with good frequency behaviour over a broad frequency range.
- frequency range chosen appropriately for the geometry
- a well-constrained and relatively simple experimental geometry

The multiple fracture experiments were therefore modelled and it was shown that the behaviour for all types of waves could be accurately reproduced in terms of the effects on amplitude, frequency and indeed the total waveform. A sample result is shown in Figure 4.2.3.1 for four different cases of shear wave propagation. However, it was also shown that it was not possible for a single value of fracture stiffness to account for the correct amplitude and dispersion behaviour for both P- and S- wave propagation across the fractures. A model was proposed for non-linear fracture stiffness, which would account for the stress loading of individual fractures. It was shown that this model could account for the observed behaviour.

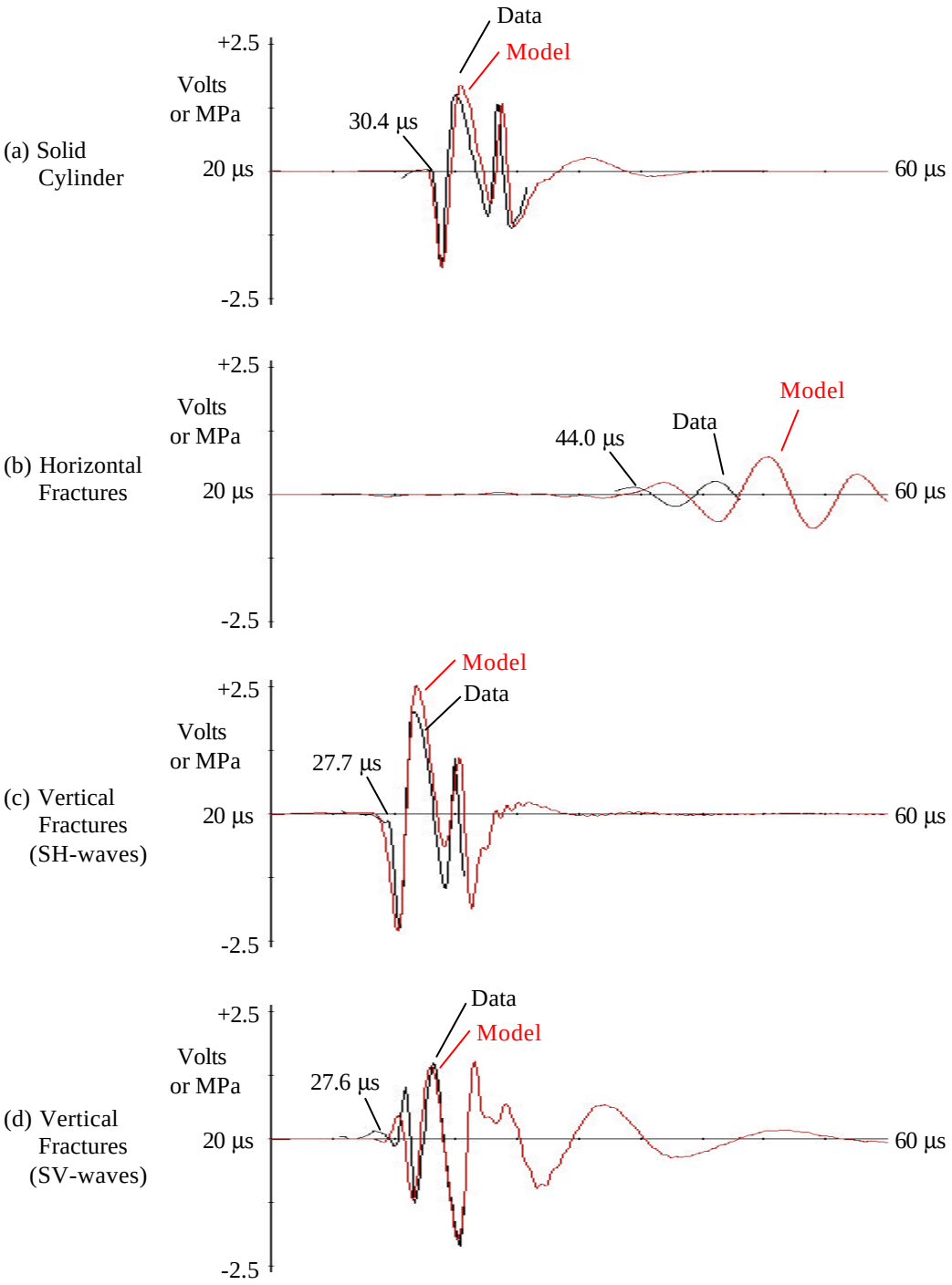

Figure 4.2.3.1 Shear-wave comparisons for experimental and modelled waveforms, for the different fracture orientations. Waveforms from the experiment recorded voltage (Volts), while the model records stress (MPa).

The work shows that modelling wave interaction with displacement discontinuities appears to capture much of the physics observed in experiments with real joints and, by inference, with fracturing. A relatively simple model of a fracture convincingly matched the results of an experiment with many fractures. This work highlights the importance of the fracture stiffness in modelling waves through fractures, and hence for modelling waves around deep underground openings. The fracture stiffness has a significant effect on the waveforms, delay, amplitude and frequency, resulting in completely different behaviour from simply considering fractures as either open or closed.

An important conclusion however, is that except in a completely uniform stress field, modelling wave propagation without considering the stress variation around the fractures, will be inaccurate. The stress-dependence of the fracture can be accounted for with a stress-dependent fracture stiffness, and in a non-uniform stress field this stiffness may vary along a single continuous fracture. This has important consequences for modelling fractures around underground openings where stresses are highly non-uniform.

It is not a new concept that the fracture stiffness should be dependent on closure or normal stress. However, important conclusions can be reached from this modelling. Firstly it indicates that the stress state can significantly affect wave propagation, and it is important to consider the coupled problem of the *in situ* stress together with the seismic loading, when a non-uniform stress distribution is expected. Secondly it is not sufficient to introduce stress dependence by allowing opening of fractures in tension, since significant differences in propagation are experienced even when all fractures are in compression. Finally, the use of a stress-dependent fracture stiffness provide promising results that account for observed behaviour.

The work also investigated how varying fracture stiffness, and varying stress-dependent stiffness parameters, affect waveforms. The stiffness was shown to account for attenuation of high frequencies as well as amplification of lower frequencies. It was noted that for P-waves, amplitudes of first arrivals are dependent not only on the normal fracture stiffness, but also on the shear fracture stiffness. This is an important result for multiple fractures, as it is not predicted by the theory for a single fracture.

An approach to inverting the source was developed, which could be useful in future models of experiments. Although nothing can be said about the real source, some interesting aspects were noted such as the apparent greater efficiency of the S-wave source.

Investigations were also made into how the model behaves for large amplitude waves where non-linear behaviour is to be expected - i.e. the fracture stiffness changes during passage of the wave, and hence the fractures respond differently for different wave amplitudes. An interesting result was observed in the model, where the relative amplitude of the wave is increased for larger amplitude waves in the phase causing decreased compression (tensile pulse), but is decreased in the phase causing increased compression (compressional pulse). Further investigation is needed to explain this phenomenon.

In summary, there are a wide variety of interesting results in this work. The most important is that repeated use of a fairly simple model of a fracture, very accurately reproduced experimental recordings of wave propagation through a large number of fractures. The stiffness of a fracture was shown to affect amplitudes causing both attenuation and amplification. In particular, the importance of stress-dependence on the fracture stiffness was established, even for modelling what was a weakly non-uniform stress distribution. The stress distribution around underground excavations is extremely non-uniform. Taking into account the stress-dependence of the fracture stiffness can therefore be expected to be extremely important for modelling wave propagation around these openings.

4.2.4 Models of *in-situ* experiments with fractures

Section 4.2.3 showed that by using a numerical implementation of fractures with a fracture stiffness, it was possible to accurately model laboratory experiments of waves propagating through fractures. The degree to which the modelled waveforms matched the experiment is very encouraging for the modelling of such behaviour. However, the usefulness of such crack models needs to be established for wave propagation around a real excavation in rock and with excavation-induced fracturing. In essence, sufficiently controlled and well-measured *in situ* data is required to bridge the gap between the laboratory results and the plethora of unknowns in an active excavation. This work returns to the URL experiment of section 4.1.3, and applies these fracture models to account for the observed amplitude and wave behaviour.

The elastic model presented in section 4.1.3 showed two main trends - waveforms for paths parallel to the tunnel surface are similar to the recordings, while those for paths oblique to the tunnel surface are significantly higher than the observed data in both wave-speed and amplitude. This indicates a fractured medium, with fractures aligned approximately parallel with the tunnel surface. Carlson and Young (1992) estimated the crack density to range between 0.12 and 0.09 in the first metre of the tunnel wall. They also reported evidence of new fracturing

with 199 acoustic emissions locating within 0.75 m of the centre of the array. An elastic model of stress distribution around the Mine-by tunnel actually indicates that the tangential stress is more tensile than the radial stress, which would suggest a very different orientation of fractures. This section uses models of the fracturing to attempt to match the wave-speed and amplitude behaviour, and in so doing characterise the size and orientations of open fractures. Two models of fracture were investigated: random assemblies of open cracks with a particular fracture density, and large fractures with a fracture stiffness as used in section 4.2.3.

One conceptual model of fracturing is a collection of flat openings. O'Connell and Budiansky (1974) used energy considerations to develop a dimensionless quantity describing the relative effect of a collection of cracks on a medium. This crack density is proportional to the cube of the crack radius. One consequence of this definition is that it is dimensionless. Self-similar geometries at different scales have the same crack density, although their frequency response will differ. A simple program was written to generate random crack assemblies in WAVE. It allows three orthogonal directions of cracks with a specified crack density for each direction. Cracks are rectangular with side-lengths varying between specified limits and with a linear size distribution. Different crack assemblies were added to the URL model with different crack sizes and an average crack density of 0.1. Figure 4.2.4.1 shows two example distributions.

Table 4.2.4.1. shows the P- and S- wave amplitudes for the path 3:18 (*cf*. Figure 4.1.3.5) once fractures were introduced. This indicates that the fractures influence the wave propagation even for paths parallel to the fractures. Of interest is that the small fractures amplify the waveform. Figure 4.2.4.2 compares the waveforms for two paths for models with different crack-sizes, the elastic model and the data. All cases change the wave-speed and the relative amplitudes of waveforms. The oblique path (3:20) is most affected with significant changes in wave-speed. This confirms that this orientation of fracturing is the most consistent with the waveform data, since the alternative directions would have a greater effect on the wave-speeds for the path 3:18. The wave-speeds for path 3:20 are slower than the data for all crack sizes. For the large crack cases, this may be due to a higher crack density in the central region due to the non-uniform crack density discussed above. However, this is not the case for the smaller cracks, which also have a slower wave-speed than the data. This implies that the true crack density is less than 0.1. The larger cracks significantly change the waveform for the path parallel to the fractures (3:18), while the waveforms for 36.5 mm and 26.5 mm cracks are little changed and best match the data. The best overall match is for 26.5 mm cracks. This is a probable indication that in general the size of open cracks in the rock is smaller than 26 mm.

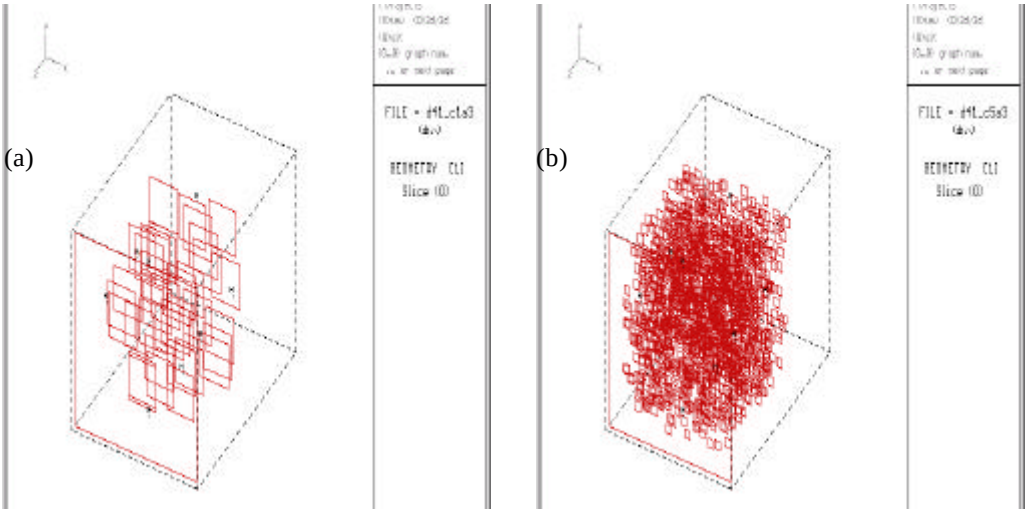

Figure 4.2.4.1 URL model with the addition of open cracks with an average crack density of 0.1. (a) 38 40x40 element cracks (196.5 mm x 196.5 mm) (b) 6061 8x8 element cracks (36.5 mm x 36.5 mm).

Table 4.2.4.1 Relative P-wave and S-wave amplitudes for path 3 to 18 for varying crack-sizes. Amplitudes are relative to the elastic model which was chosen to match the P-wave amplitude of the data.

Model	N	Average crack density	Peak crack density	% of elastic P-wave amplitude	% of elastic S-wave amplitude
Data				100%	54%
Elastic				100%	100%
196.5mm	38	0.1	0.465	69%	38%
96.5mm	320	0.1	0.186	90%	92%
76.5mm	645	0.1	0.162	74%	96%
56.5mm	1611	0.1	0.142	81%	78%
36.5mm	6061	0.1	0.125	110%	94%
26.5mm	16089	0.1	0.118	121%	100%

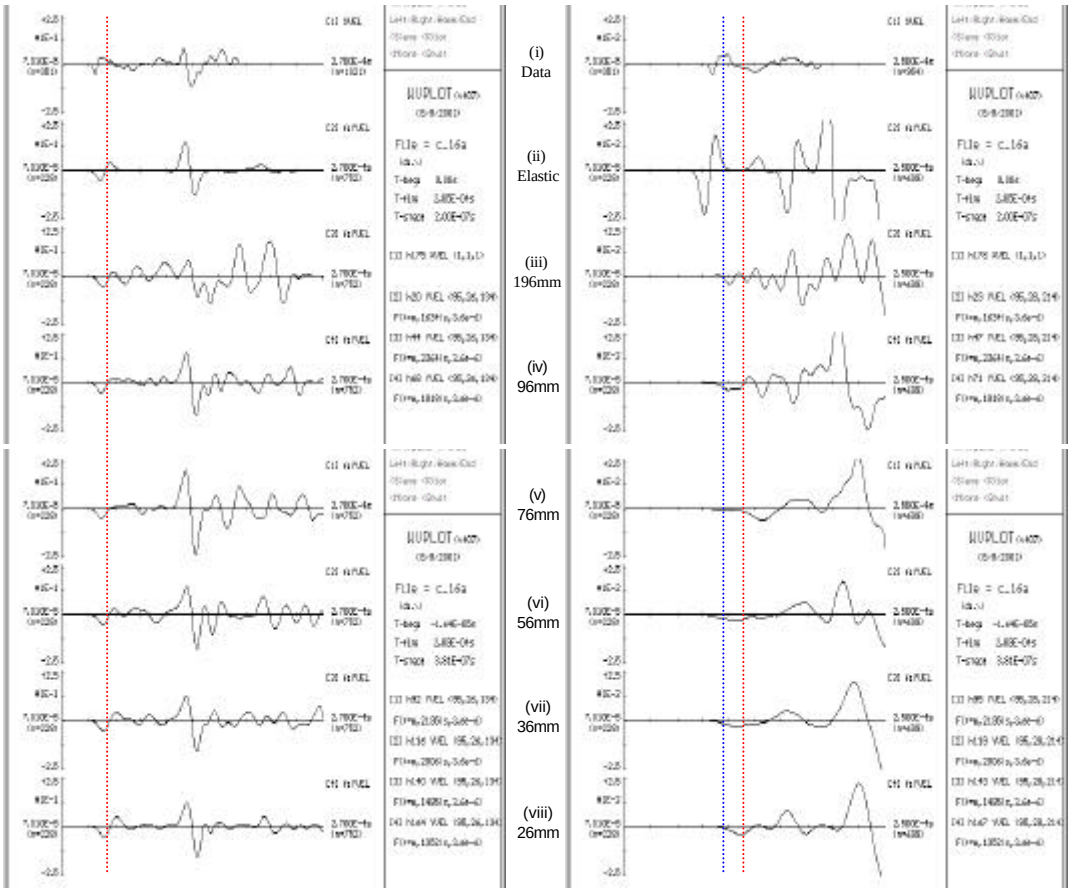

(a) Path 3 to 18 (b) Path 3 to 20

Figure 4.2.4.2 Comparison of wave-forms for different crack models with sizes ranging from 196 mm down to 26 mm. All crack models have an average crack density of 0.1. Source amplitudes are scaled such that all models match the P-wave amplitude of the data for path 3 to 18. Red and blue lines indicate the P-arrival in the data and elastic model respectively.

An alternative representation of the fracturing is to capture the behaviour of the fractured rock by using large fractures with a fracture stiffness. The fracture stiffness accounts for areas of solid and areas of crack opening, provided wavelengths are much larger than the openings. This has more naturally been applied as a model of a single fracture with contacts (section 4.2.3). Hildyard (2001) also explored whether it is useful as an effective fracture, where it represents a collection of openings throughout a volume, rather than in a single plane. This is a potential method for modelling the effects of a volume of fractures, but does not have a direct relationship to the physical state. It can only be truly useful if a relationship can be also established between it and the underlying physical and geometrical state of fractures.

The aspects of the model which influence the wave propagation are the fracture spacing and the fracture stiffness. Fracture spacings of 80 mm and 40 mm and four variations of fracture stiffness were examined, using a normal fracture stiffness of $8*10^{12}$, $4*10^{12}$, $2*10^{12}$ and $1*10^{12}$ Pa/m, with the shear fracture stiffness equal to half that of the normal fracture stiffness.

Both methods of representing fracturing caused changes in the wave-speed and amplitude of waveforms, of the order of that observed in the data. It appears from the modelling of open fractures that the recorded behaviour is more consistent with models of smaller open fractures (26 mm) than with that of larger open fractures (196 mm). The practical numerical limits did not allow smaller cracks to be investigated, particularly down to grain size. The modelling confirms that the only single orientation of fractures consistent with the data for these paths, are fractures approximately parallel to the surface. The modelling also suggests that the crack density was over-estimated in the original analysis.

The representation of the fracturing using large stiff fractures caused wide variation in wave-speed and amplitude. A qualitative study indicated that decreasing either fracture spacing or fracture stiffness decreased the wave-speed, but that the fracture stiffness had the greatest influence on the amplitude. The fracture spacing had only a weak effect on amplitude. In a coarse sense, the fracture stiffness may be related to the sizes of openings, while both fracture stiffness and fracture spacing relate to the crack density. Although best-fit cases were identified, the source in the numerical simulations did not contain sufficiently high frequency content (due to current computational limitations), for absolute conclusions to be made on the comparisons.

The representation using stiff fractures does not suffer from the numerical resolution difficulties associated with the attempts to represent the true size of crack openings. It could therefore be a useful model of effective fracturing for matching the wave behaviour for large scale models. A link then needs to be established between the effective representation and the underlying assembly of fractures. This can be explored in smaller scale models, which allow greater resolution and sufficiently small sizes of open cracks.

The studies have shown the capability for models of fractures to represent the effects of fracturing on wave propagation. Results of these studies of *in situ* data from a deep-level excavation give some confirmation that the models can be used to study wave propagation around an excavation in fractured rock. Models using explicit representations of fracturing accounted for the discrepancies of the elastic model with observed behaviour.

The study also indicates that coupling modelling with the measurement of seismic waveforms will aid in interpreting the rock mass condition. It is not a new concept to use wave-speed and

attenuation to infer fracture states (e.g. Young and Hill, 1986). However, the ability to model the inferred fracture states allows such ideas to be tested and modified. The modelled fracturing causes both wave-speed and amplitude changes. This provides a method of verifying the consistency of conclusions and inversions acquired through seismic monitoring. Such modelling also allows greater insight into the underlying fracture state - in this case, it gave estimates for upper limits on the size of open fractures which would cause the wave-speed and amplitude changes. It was also found that it is presently impractical to model the true openings in the material to account for waveform changes in *in situ* monitoring - since many openings may be micro-fractures and of the order of the grain-size. Yet such openings influence the macro behaviour and these effects need to be included in the model. It was shown that the wave propagation changes on the larger-scale could be better accounted for using a distribution of stiff rather than open fractures. Such “stiff” fractures account for a number of smaller surrounding open fractures. Having matched the behaviour using such effective fractures, smaller-scale models can be used to investigate how the effective fractures relate to the underlying physical fracture state. A possible strategy is therefore to characterise the behaviour of various models of fracturing including idealised assemblies of open fractures, and stiff fractures. Relating these results allows inference of the possible state of fracturing in the larger scale problem.

4.2.5 Wave behaviour through random fracture assemblies

Development of the ability to accurately model waves through fracture assemblies is important for a number of practical problems. It would aid in the interpretation of rockmass structure from recorded waves. It would improve the ability for forward modelling to project amplitudes and distribution of motions around excavations, and could help develop appropriate representations of wide-spread fracturing without modelling each individual micro-fracture. It could even be used as a diagnostic for simulations of fracture development, where waves are passed through both a fractured experiment and the simulated fracturing to determine if the seismic behaviour is similar.

A method was developed to study the frequency dependence of both wave speed and amplitude for different fracture sizes and fracture assemblies. A large body of research has focussed on these issues including analytical, experimental and, more recently, numerical studies. These include developing analytical expressions for wave-speed and attenuation due to fracture assemblies, studying wave propagation through single and multiple aligned stiff fractures, and the relationship of fracture stiffness to areas of contact and opening. The

numerical approach developed here offers benefits over these studies. Expressions are obtained for both attenuation and phase velocity, and these are presented as a function of frequency. The expressions are not limited to wavelengths much larger than the fracture sizes. The analysis is not necessarily limited to the study of plane waves. Finally, most cases necessarily require a three-dimensional treatment, which has not been attempted in other numerical studies.

The approach used is to perform numerical simulations of plane wave propagation through the fracture set and to record the waveform on both sides of the fractured region. An expression was developed (Hildyard, 2001) for the phase velocity (wave-speed) as a function of frequency:

$$c(\omega) = \omega(x_2 - x_1)\left[\frac{-(\phi_2 - \phi_1) - iLn\left(\frac{A_2}{A_1}\right)}{(\phi_2 - \phi_1)^2 + \left[Ln\left(\frac{A_2}{A_1}\right)\right]^2}\right] \qquad (4.2.5.1)$$

where $A_1(w)$ and $A_2(w)$ are the Fourier amplitude functions and $\phi_1(w)$ and $\phi_2(w)$ the Fourier phase functions of the elastic and recorded waveforms respectively, x_1 and x_2 are the positions of the recorded waveforms and $c(w)$ is the phase velocity.

Similarly, an attenuation function can be defined as simply the ratio of the two amplitude functions normalised per unit distance and given by

$$A(\omega) = \left(\frac{A_2}{A_1}\right)^{\frac{L}{x_2 - x_1}} \qquad (4.2.5.2)$$

where L is the unit distance of interest. This is more convenient for these purposes than Q, as it readily gives the attenuation of all frequencies at a particular distance. The attenuation at any distance (x) can be calculated by raising the function to the power of (x/L). $Q(\omega)$ can be calculated from the amplitude functions and the phase velocity.

The procedure is demonstrated in Figures 4.2.5.1-3. A fracture model is constructed such as that shown in Figure 4.2.5.1. A broad-band, plane wave is passed through this model and a waveform recorded at the end of the fractured region. An input waveform is calculated for the beginning of the fractured region with the reflections from the fracturing removed. The time

domain waveforms are shown for a variety of crack models of different crack size and density in Figure 4.2.5.2a. Using Fourier Transforms we calculate the phase difference (Figure 4.2.5.2b), and the amplitude spectrum for the output and input waveforms (Figure 4.2.5.2c). Applying equations (4.2.5.1) and (4.2.5.2) yields the phase velocity and the attenuation spectra (Figure 4.2.5.3).

Example results are shown in Figures 4.2.5.3 for the cases of 3.3 mm and 11.3 mm open cracks and for varying fracture densities. The curves show that the wave-speed decreases with increasing fracture density. However, the wave-speed is not constant, but decreases from its low frequency value by another 30-50%, and then increases back toward the elastic wave-speed such that high frequencies are attenuated but not slowed. The amplitudes are unattenuated at low frequencies and highly attenuated at high frequencies, but the decay occurs over a wide frequency range. The frequency at which high attenuation occurs and at which the wave-speed returns to its elastic value decreases with increasing crack-size. Results for different crack sizes were fairly consistent and estimates of phase velocity are 93% decreasing to 90%, 87% to 82%, 81% to 75% and 77% to 69% in the low frequency region for crack densities of 0.025, 0.05, 0.075 and 0.1 respectively.

An important result is that the time domain waveforms do not show a clear difference in the arrival time (Figure 4.2.5.2a), due to the high frequency content which is not completely attenuated. The calculated phase velocity clearly indicates a reduction in velocity for the low frequency region. This indicates that time domain analysis is not a reliable indicator of the wave-speed and hence not a reliable diagnostic of the fracture state.

A range of studies were made for various sizes and densities of open fractures, different orthogonal orientations, and large fractures with varying fracture stiffness and fracture spacing. This method has potential for studying the behaviour of much more complicated fracture assemblies, once this becomes computationally viable. The approach could also be applied to other topics of research, such as understanding the relationship between contact spacing and fracture stiffness. The method was shown to be consistent although sensitive to a number of numerical issues such as boundary influences, and requires a sufficiently large number of cracks. Typically, such problems can be avoided by using sufficiently large models, but while practical limits exist, care needs to be taken in applying the technique.

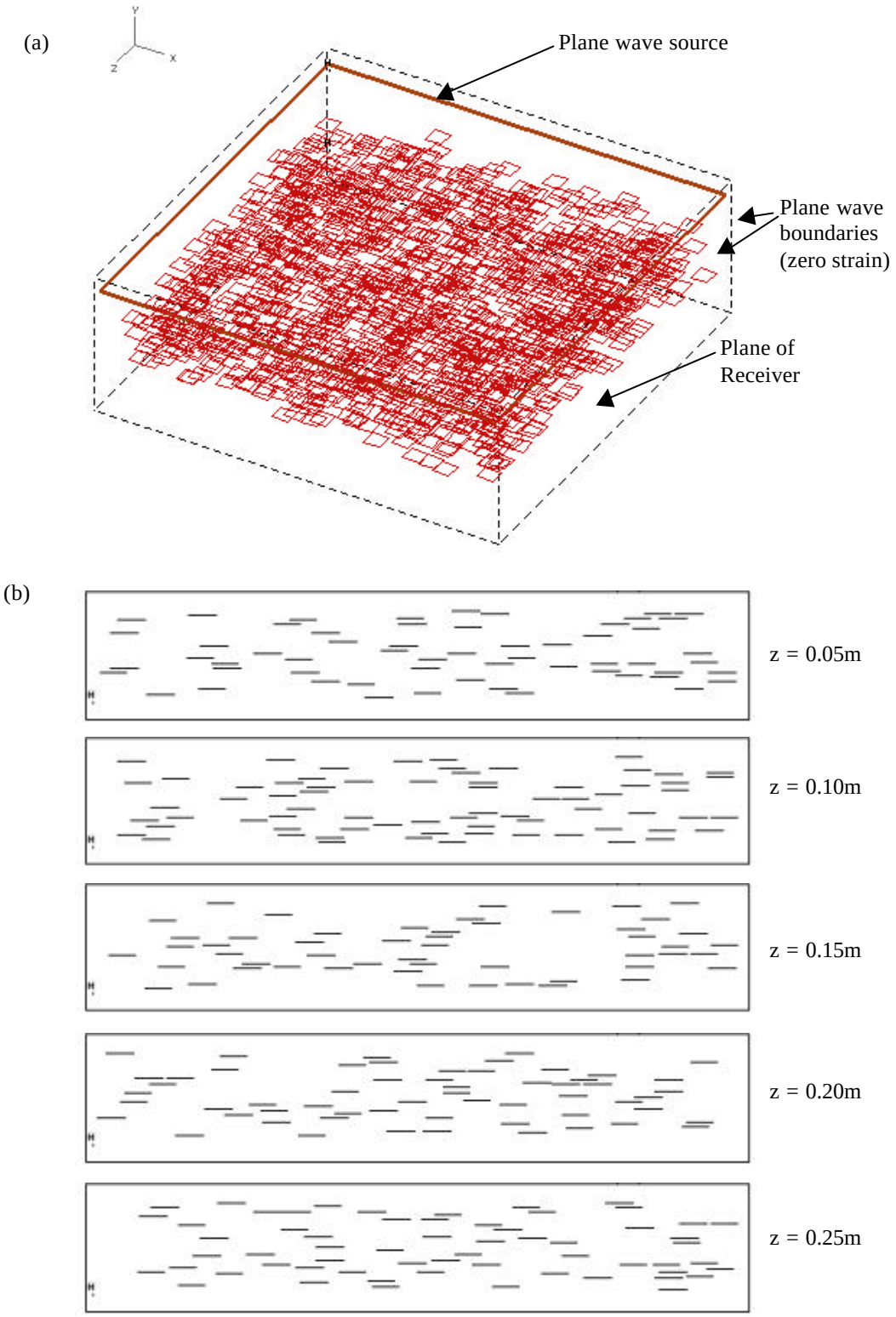

Figure 4.2.5.1 Model geometry to calculate phase velocity and attenuation for 11.3 mm cracks with a central crack density of 0.1. The crack volume consists of 288 mm by 39 mm by 288 mm, and contains 1182 cracks. (a) Three-dimensional view (b) Two-dimensional cross sections at different positions along the z-axis.

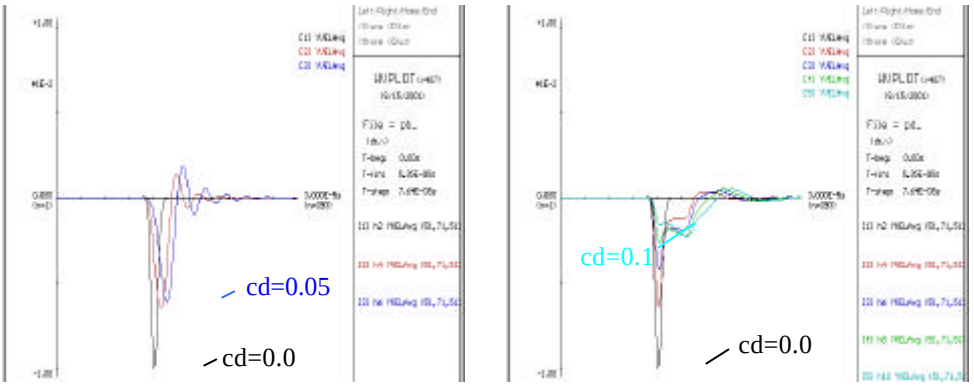

(a) Time domain waveforms

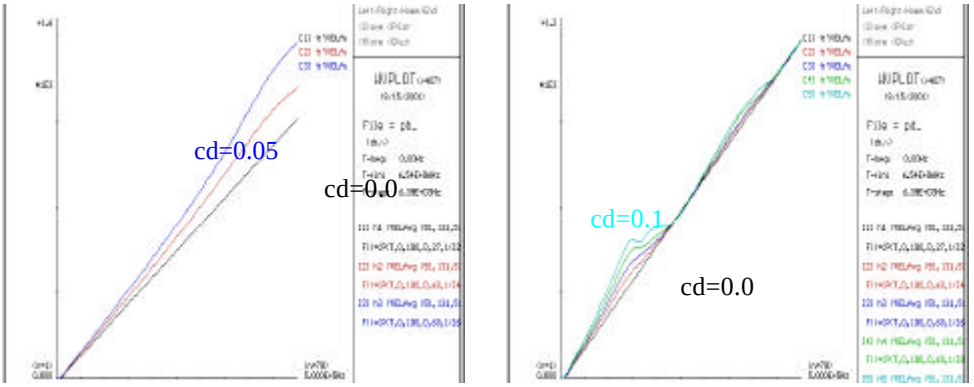

(b) Phase difference between output and input waveforms

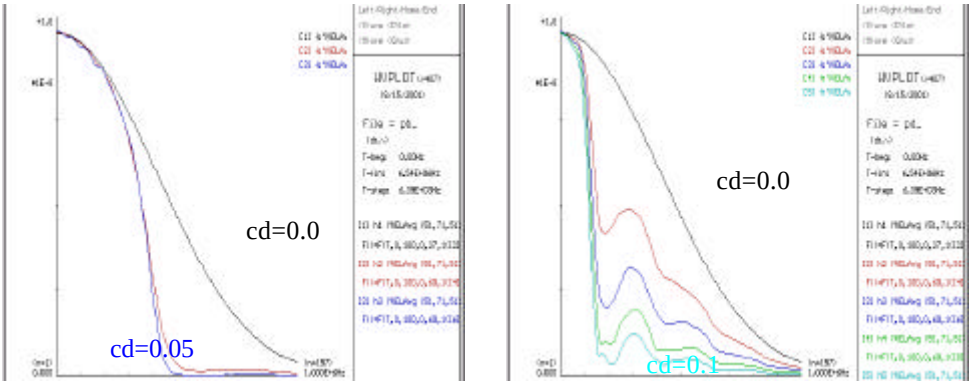

(c) Fourier amplitude spectrum

Figure 4.2.5.2 Stages for calculating phase velocity and attenuation (a) Produce the time domain waveforms for the crack models (b) Calculate the difference between the Fourier phase spectrum of the emerging waveform and the input waveform (c) Calculate the Fourier amplitude spectrum. Results are shown for models with two different crack lengths and with central crack densities of 0.025 (red), 0.050 (blue), 0.075 (green) and 0.1 (cyan), and are compared to an uncracked (c.d.= model (black). (i) L.H.S. Models with 3.3 mm cracks with 13366 and 26732 cracks respectively (ii) R.H.S. Models with 11.3 mm cracks with 296, 591, 887 and 1182 cracks respectively. Equations 4.2.5.1 and 4.2.5.2 are then applied giving the results in Figure 4.2.5.3.

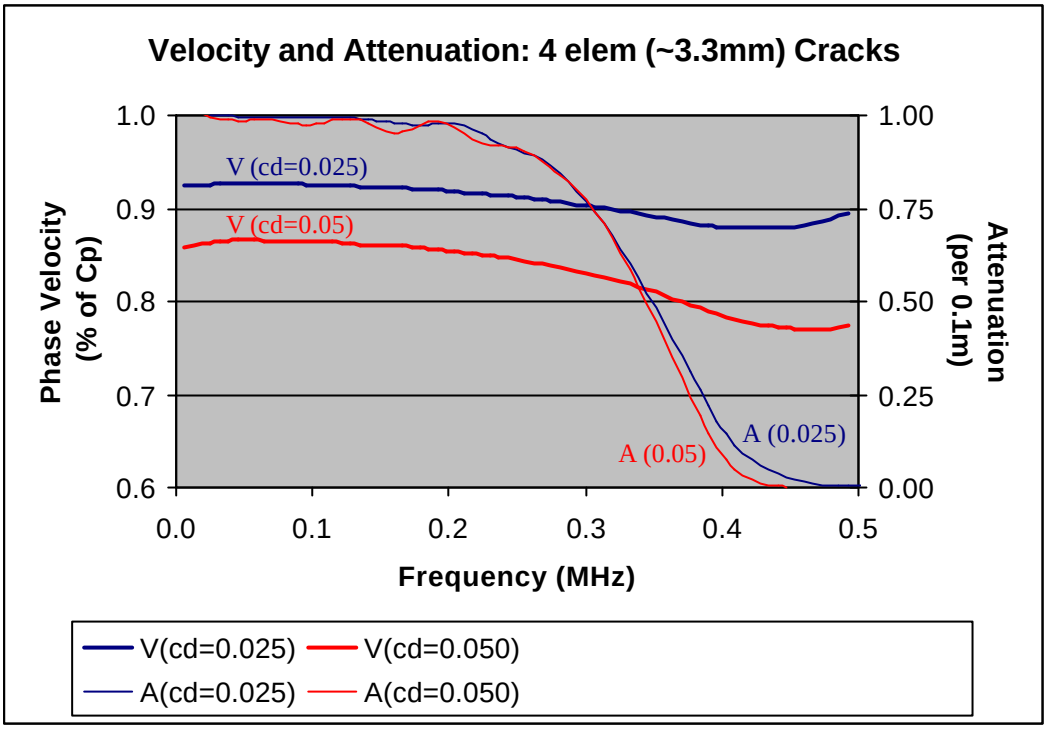

Figure 4.2.5.3 Velocity and attenuation spectra for a distribution of 4 element (3.3 mm) open cracks with a crack density of 0.025 and 0.05.

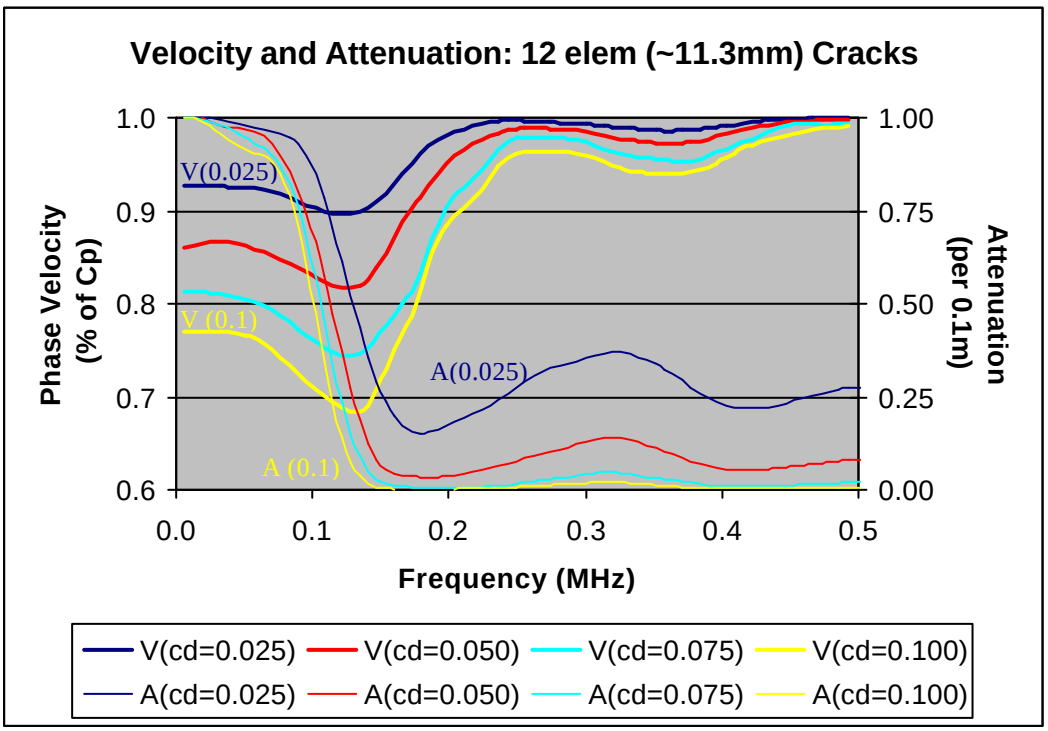

Figure 4.2.5.4 Velocity and attenuation spectra for a distribution of 12 element (11.3 mm) open cracks with a crack density of 0.025, 0.05, 0.075 and 0.1.

4.2.6 The effect of fracturing on amplitude and distribution of motion in stopes

The hanging-wall and foot-wall of deep-level mining stopes are highly fractured due to stress-induced fracturing. There are also natural discontinuities such as joints and bedding planes. Such fractures cause waves to attenuate due to scattering of high frequencies. However, fractures also cause a reduction in the effective stiffness of the rock, and for longer wavelengths this can increase the amplitude of ground motion. In section 4.1.4, it was shown that the excavation increases ground motion significantly both in the near-source region, and the distant areas of stopes due to the propagation of Rayleigh waves. This section uses the results on fracturing from sections 4.2.3 to 4.2.5 to extend these stope studies to examine the effect of the fracture zone on the wave propagation, including the propagation of surface waves, and whether the fracture zone alters the amplitude of the ground motion.

The models were based on the long-wall stoping geometry and M=1.3 pillar event described in Section 4.1.4. The models separately evaluate the effect of stope-normal and stope-parallel fracturing. The fracturing consists of random rectangular cracks, with edge-lengths varying between 4 m and 14 m, in a band located between 4 m and 18 m below the stope. Figure 4.2.6.1 shows two cases for stope-normal fracturing with crack densities of 0.01 and 0.1. The crack density is based on the definition of Budiansky and O'Connor (1974), modified for square cracks in section 4.2.5. The fractures are represented by linear stiffness displacement discontinuities.

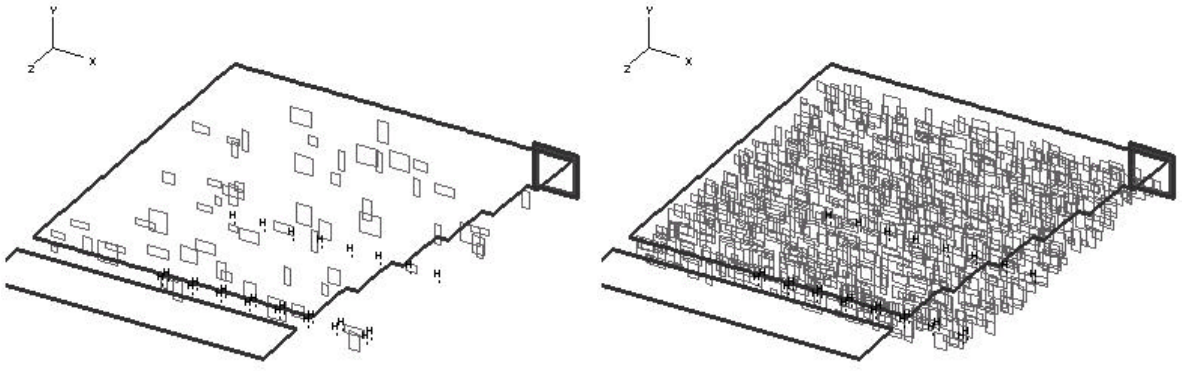

(a) (b)

Figure 4.2.6.1 Stope model with vertical fractures in the foot-wall of the stope. The fractures are rectangular with edge-lengths between 4 m and 14 m, and are in a band between 4 m and 18 m below the stope. (a) Fracture density of 0.01 (b) Fracture density of 0.1

Table 4.2.6.1 Maximum in-stope velocity and induced tensile stress at 40 m and 200 m from the event, for different models of the fracture zone. All models use the same event. Values are given as a ratio to that of an unfractured model. (B) is the unfractured model. (E) Horizontal fractures parallel to the stope and extending across the same area as the stope. (F) Smaller, random horizontal fractures. (G) Random vertical fractures (H) A reduced modulus in a zone around the stope.

	Model	Fracture Stiffness		Ratio to unfractured model			
				(Max. at 40 m)		(Max at 200 m)	
		Normal (Pa/m)	Shear (Pa/m)	Vel.	Tens. stress	Vel.	Tens. stress
B: Unfractured model							
	B1	-	-	1.00	1.00	1.00	1.00
E: Horizontal fractures (extensive)							
	E1	$1*10^{16}$	$1*10^{11}$	1.00	1.00	1.18	1.03
	E2	$4*10^{10}$	$2*10^{10}$	1.19	1.07	1.21	1.03
	E3	$1*10^{10}$	$5*10^{09}$	1.50	1.11	1.12	0.63
F: Horizontal fractures							
	F1	$1*10^{10}$	$5*10^{09}$	1.16	1.07	1.45	0.94
G: Vertical fractures							
	G1	$1*10^{16}$	$1*10^{11}$	1.00	1.00	1.09	1.03
	G2	$4*10^{10}$	$2*10^{10}$	1.00	1.00	1.10	1.00
	G3	$1*10^{10}$	$5*10^{09}$	1.00	0.96	1.09	0.88
	G4	$1*10^{10}$	$5*10^{09}$	1.00	0.96	1.24	0.88
H: Reduced modulus							
	H1	-	-	1.28	0.89	0.77	0.56

Table 4.2.6.1 summarises the effect of this fracturing on the amplitudes of velocities and stresses in the model. All cases are based on the same event, and the near-source and far-field values are shown as a ratio relative to a model without any fracturing. The first set of horizontal fracture models (E) considers the effect of bedding planes and contains three extensive plane fractures parallel to the stope and spaced at 6 m intervals below the stope. The second set of horizontal fracture models (F) considers random rectangular cracks with a crack density of 0.1. The Vertical fracture cases are for a crack density of 0.1 (Figure 4.2.6.1b). A crack density of 0.01 (Figure 4.2.6.1a) had negligible effect on the amplitudes. The third fracture direction, vertical and parallel to the stope face, is not tabulated. Fractures with this orientation had a negligible effect for this source position as the wave propagation is approximately parallel to the fractures - however the face-parallel fractures are very important when the source locates ahead of the stope face. For each model, three different cases of fracture stiffness were studied.

For the case of extensive horizontal fractures (Table 4.2.6.1E), the near-source stope velocities and tensile stress (at 40 m) are larger by up to 50% and 10% respectively, and increase with decreasing fracture stiffness. The fractures also increase the velocities further along the stope (at 200 m) by up to 20%, although the tensile stress is reduced. This effect is not monotonic, and as the fracture stiffness falls below a certain value, the far-field velocity amplitudes decline. For random horizontal fractures with low fracture stiffness (Table 4.2.6.1F1), the near-source velocities are increased, and the distant stope velocities are increased by nearly 50% in certain areas. Vertical fractures (Table 4.2.6.1G) had no effect on the near-source amplitudes. Distant velocities were increased due to the fracturing, although again the amplitudes decline below a certain fracture stiffness. (Table 4.2.6.1G4) is the case for increased crack density of 0.15, and indicates that the effects are more marked for higher crack density. In general the effects of vertical fractures were less marked than those of horizontal fractures.

The above cases were limited in the degree of fracturing. Numerical constraints meant that fractures were far from the stope surface, and intersection of fractures with the surface and other fractures was avoided. An alternative representation of fracturing is a reduction in the modulus of the host material. This reduction does not capture the frequency dependence of the fracturing and hence the scattering of higher frequencies. However, it is a convenient way of considering the effect of more dense, randomly-orientated fractures. A third representation of the fracture zone therefore comprised a softened elastic modulus in a zone 12 m above and below the stope. The Young's modulus was dropped in 2m intervals from 80 GPa 12 m from the surface to 30 GPa at the surface, while the Poissons ratio was increased from 0.2 to 0.37. This results in the P-wave and S-wave velocities at the surface being 77% and 57% that of the virgin rock. The effect on amplitude is shown in Table 4.2.6.1H, with a 30% increase in near-source stope velocities, but a decrease in distant velocities and induced tensile stress.

While all models of fracture affect the distribution of maximum motions, the patterns are similar to that of the elastic model, with increases in amplitude and the region of high amplitude. The cases with distributions of fractures (c,d,e) lead to less smooth distributions, with pockets of higher amplitudes. Comparing seismograms of vertical velocity (Figure 4.2.6.2a), indicates that the fracturing causes a large decrease in the wave-speed, and a small increase in the amplitude.

The above models all considered linear fracture behaviour, where the passage of the waves does not alter the state of the fracture. However, for large ground motion the amplitude of the

induced stress may be large, leading to non-linear behaviour - altering the stiffness of the fractures, or causing slip or opening of fractures, that can potentially release further energy.

Although the earlier models have shown that even small magnitude events can account for maximum velocities of more than 1 m/s, much larger velocities have been inferred in observations of failed rock. Ortlepp (1993) examined ejected rock and inferred ejection velocities of at least 8 m/s. The linear models so far have not been able to account for surface velocities of this magnitude. One explanation for large velocities is that the waves may trigger failure in a highly stressed region (e.g. within a buckling slab, McGarr 1997). Another model proposed by Linkov and Durrheim (1998), involves the possibility of amplification of the waves due to additional energy release as waves pass through the fracture zone which is in a post-failure strain-softening state.

Models were used to investigate a related mechanism - whether the passage of the waves can cause slip on fractures and whether this additional energy release increases the amplitude of the wave motions. The free surfaces of a stope are not highly stressed, so the model evaluates whether small amounts of stress released on large numbers of cracks, can progressively increase the wave amplitude. This assumes the existence of stresses on already failed fractures near the surface of the excavation. Although elastic theory suggests tensile horizontal stress near the surfaces of the hanging- and foot-wall, it is generally accepted that the real horizontal stresses parallel to the stope surface, are slightly compressive. For example, measurements by Squelch (1994) found that one component of the horizontal stress varied from 2 MPa to 20 MPa compression within the first 2 m of the hanging-wall.

A simplified model was used to investigate the mechanism, and is not intended to represent a real fracture zone or the real stress state. The model consists of the random non-intersecting vertical fractures from model G1 (Table 4.2.6.1). All fractures were assigned a uniform pre-existing normal and shear stress - a 6 MPa normal stress (horizontal in the stope plane), and a vertical shear stress of 5 MPa. The fractures have a Mohr-Coulomb failure law with a friction coefficient of 0.58 (friction angle of 30°), and a cohesion of 2 MPa. The excess shear stress on each fracture is 0.5 MPa, requiring an increase of 0.5 MPa in shear stress, or 0.8 MPa decrease in the normal stress, for failure to occur. Fractures were assigned a high normal and shear fracture stiffness of 10^{16} Pa/m and 10^{11} Pa/m respectively, to decouple the failure effects from the softening effects. Since the event in earlier linear models induce tensile stress of more than 1 MPa, the waves from the event should cause some of the fractures to fail.

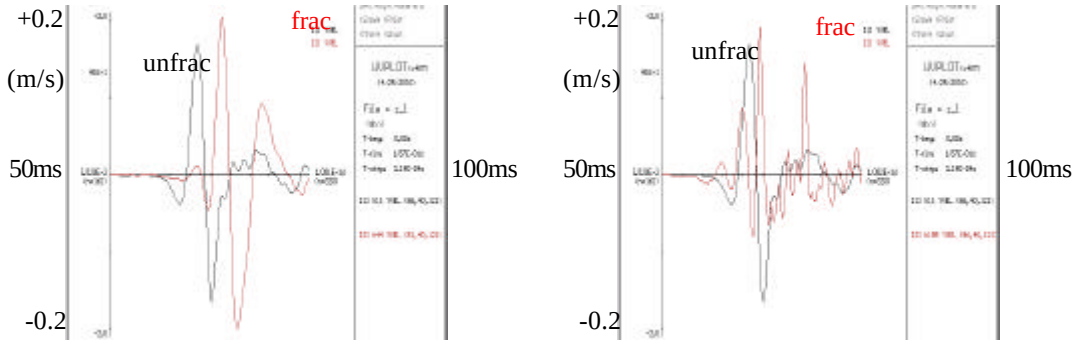

Figure 4.2.6.2 Effect of fracturing on the vertical velocity seismograms 200 m along the stope. (a) Horizontal fractures parallel to the stope free surface, with a low linear fracture stiffness (Table 5.3-E3). (b) Pre-stressed random vertical fractures with a capacity for failure. Each case is compared with that of an unfractured stope.

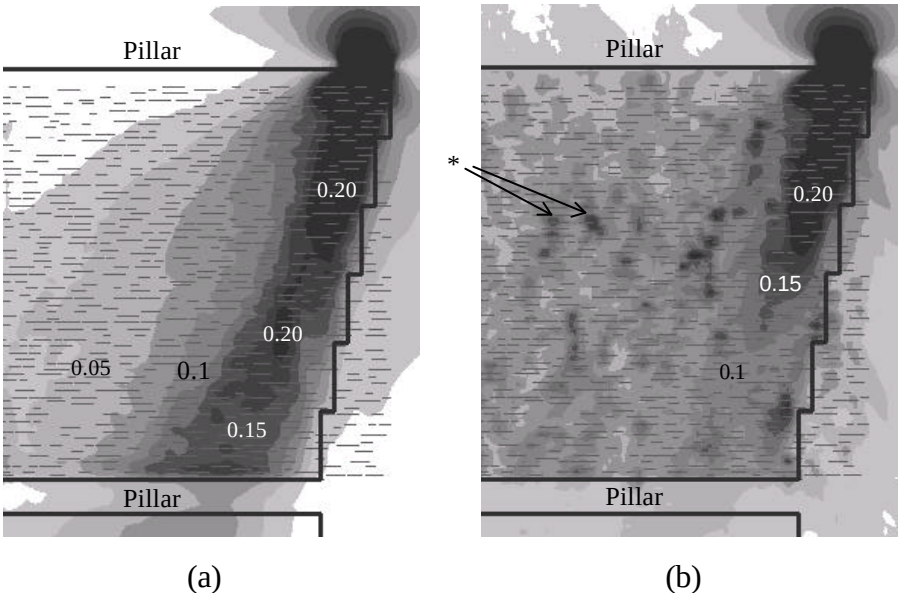

Figure 4.2.6.3 The influence of vertical fracturing. Contours indicate the maximum velocity (in m/s) induced by event #1 (magnitude 1.3) in a plane 2 m below the excavation. (a) Random vertical fractures with a normal and shear fracture stiffness of $1*10^{10}$ Pa/m and $5*10^{9}$ Pa/m respectively (Table 5.3-G3). (b) Random vertical fractures which are pre-stressed and allowed to fail due to induced stresses. The '*' indicates examples of further energy release on fractures.

The results were that some failure took place on all 712 fractures, generating magnitudes on individual fractures ranging from -2.5 to 0.35. The total moment for all fractures was 6.10^5 MNm, which is 5 times that of the original event. Nevertheless, the distribution of maximum velocity (Figure 4.2.6.3b) is no larger than the original event, and in fact the motions are generally smaller than that obtained with soft, linear fractures (Figure 4.2.6.3a). What is noticeable is that there are pockets of high velocity associated with triggered events in areas where there was previously low ground motion. Figure 4.2.6.2b compares a seismogram with that of the unfractured model, indicating that failure on the fractures alters the waveform considerably without significantly increasing the peak amplitude. This is in contrast to the model with 'soft' linear fractures where the wave-shape is not altered, but the wave-speed is slower and the amplitude increased. The conclusion is that although considerable energy release occurs, this is not coherent and does not lead to the amplification of the original wave, but rather manifests itself in localised pockets of large motions, sometimes in unexpected areas. This may relate to the observation of uncorrelated ground falls following seismic events in deep-level mining.

Results of section 4.1.4 indicated the importance of Rayleigh waves. A model was investigated to examine the effect of Rayleigh wave motion along an otherwise intact hangingwall containing a single block. A 2D simulation was carried out with a 1m by 1m block, and a Rayleigh wave pulse width of 3ms and a vertical velocity of approximately 1m/s. The block sides were assumed to have a compressive horizontal in-situ stress of 0.1MPa and a friction angle of 30 degrees. The top of the block was assumed to have a 0MPa in-situ (vertical) stress, 30 degree friction, and was allowed to open under tension. The motion of the centre of the block was compared with that of the intact hangingwall without the block.

An interesting effect was observed where the block "ratchets" downwards relative to the surrounding hangingwall. During downward motion of the hangingwall the block moves downward, but during upward motion of the hangingwall the block slips resulting in a net downward displacement. This occurs for both senses of shear event (Figure 4.2.6.4a,b), and for cyclic motion, the block progressively ratchets downwards (Figure 4.2.6.4c). Of interest is that the block failure essentially occurs during upward rather than downward motion of the hangingwall (again for both senses of the event). The effect can be understood with reference to Figure 4.2.6.5, which compares the horizontal tension with the downward motion for the intact hangingwall. During downward motion the horizontal stress is compressive and the block moves downward with the surrounding rock. During reverse and upward motion there is horizontal tension or reduced compression and the block continues to move downwards or at least slips relative to the rest of the hangingwall.

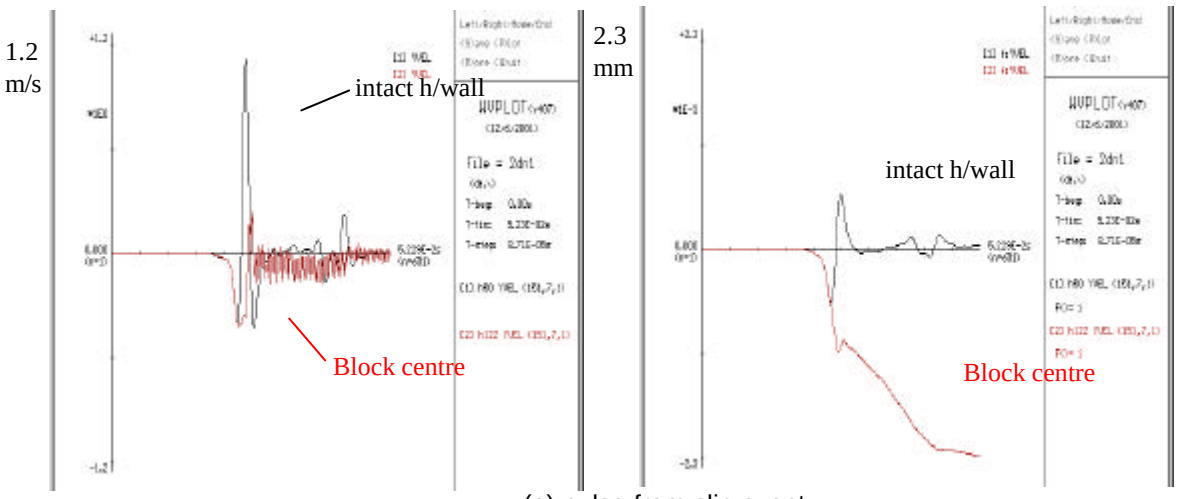

(a) pulse from slip event

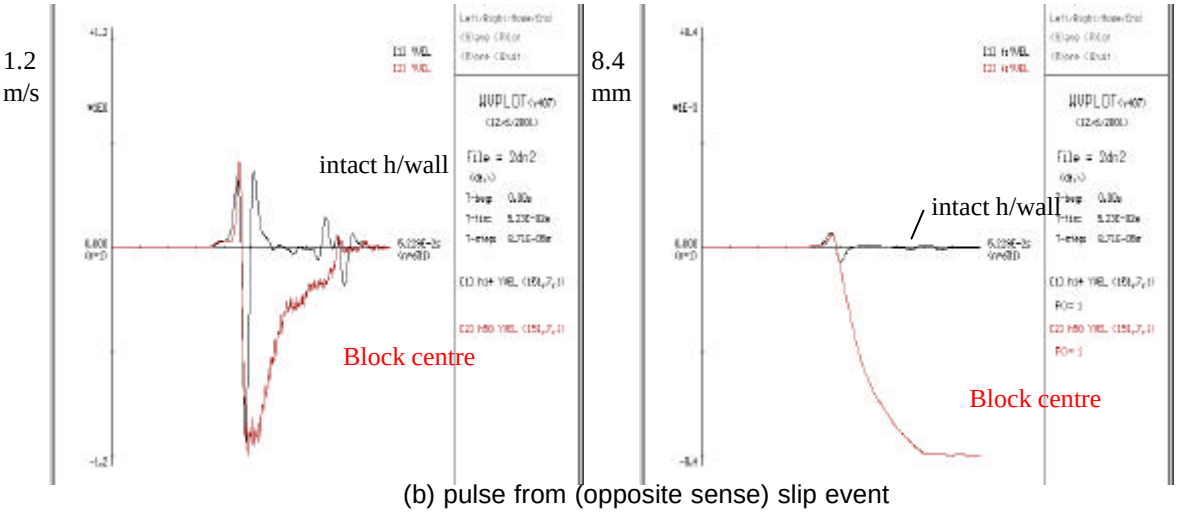

(b) pulse from (opposite sense) slip event

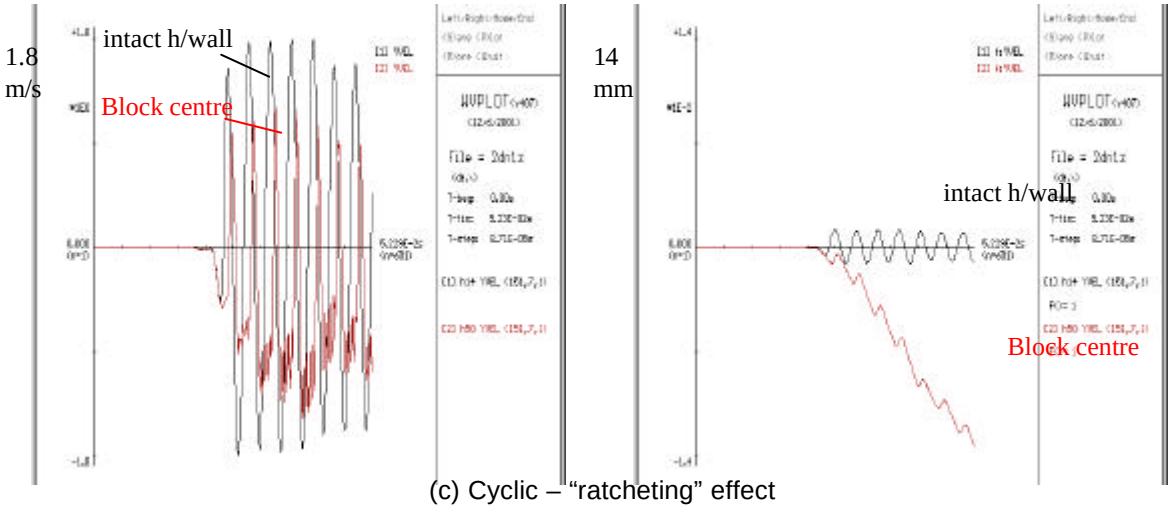

(c) Cyclic – "ratcheting" effect

Figure 4.2.6.4 Comparison of the motion of the block versus the intact hangingwall, for Rayleigh wave propagation induced by three types of loading. Waveforms on the L.H.S. are velocity, and those on the R.H.S., displacements. Comparisons are for a point in the centre of the block and for the same position in an intact hangingwall. There is a nett displacement, and for cyclical loading (as in (c)), the block "ratchets" downwards.

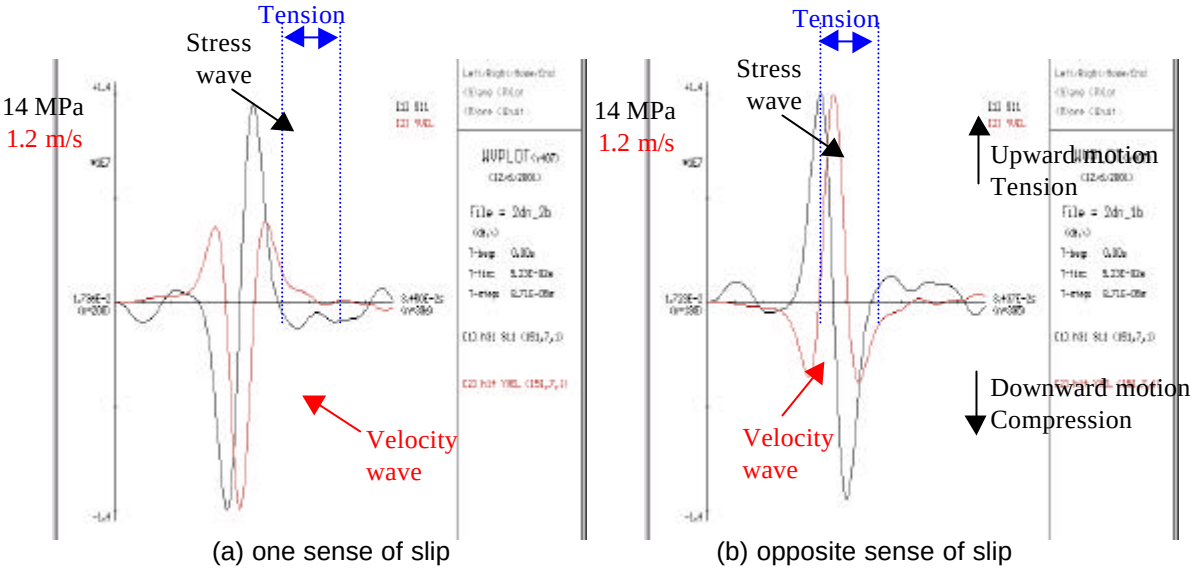

Figure 4.2.6.5 Comparison of vertical motion and Horizontal stress for Rayleigh wave propagation in an intact hangingwall. Horizontal tension for both senses of slip event tends to occur during reverse or upward motion. As a result a block will tend to slip during upward motion of the hangingwall.

In summary, it has been shown that horizontal fracturing and general softening can account for increased amplitudes of ground motion in the stope close to the source. All representations of fracturing indicate increased amplitudes at more distant parts of a stope. The amplitudes decrease beyond a certain fracture stiffness, which may indicate that the propagation of surface waves is inhibited by open fractures. The maximum apparent amplification caused by fracturing in the cases studied was limited to 50% for both near and far stope velocities. This effect may be greater if a higher density of fracturing is assumed.

A model was studied where waves from the main event triggered energy release on numerous fractures in the foot-wall and hanging-wall, which were assumed to be in a low stress regime. Although a large amount of energy was released from these fractures, this did not increase the maximum motions over the whole region. This probably indicates that the energy release is not coherent and does not lead to the amplification of the original wave, but rather manifests itself in localised pockets of large motions, sometimes in unexpected areas. The potential for triggering energy release in a high stress regime was not studied.

An important effect was established in the analysis of Rayleigh wave interaction with a block in a hangingwall – tension during upwards motion of the hangingwall results in the “ratcheting” downwards of the block. The problem could not be studied in three-dimensions, and it is recommended that this should be done in the future along with investigating the effects of other

waves such as incident P and S waves on such a block. It is noted that this has important consequences for work on the Simrac project “GAP709”.

Overall the above work has shown that fractures can have a significant influence on the amplitude and distribution of ground motion. Little has been done in rock engineering to measure the degree of fracturing and the effective moduli in stopes. This should be more routinely measured and estimated, as it has an influence on the expected amplitudes. It is recommended that seismic methods of measuring and quantifying the fracturing around stopes are developed and utilized.

4.3 Numerical methods for three-dimensional fracture propagation and assessment of dynamic effects.

4.3.1 Numerical issues relating to dynamics

A dilemma exists in the mesh-based (finite difference and finite element) solution of dynamics problems as to how to support an acceptable resolution for the analysis, while supporting sufficient flexibility which allows analysis of real mining problems. There are two competing requirements: A consideration of the frequencies involved shows that very large numbers of elements are required for meaningful analyses due to the inefficiency caused by the phenomenon of dispersion. For example, the solution of relatively simple models in sections 4.1 and 4.2 required meshes with many millions of elements. Such large meshes can best be obtained using simple and restrictive mesh-schemes that also use high-order approximations. However, analysis of real mining problems also requires flexibility, such as the arbitrary orientation of stopes and fractures. Programs which allow this tend to use very inefficient grid-schemes and are incapable of accommodating the large number of elements required for a meaningful analysis.

A new method was developed for quantifying the dynamic performance of a computer code without needing to understand the internal and theoretical behaviour of its grid scheme. The method was used to quantify the mesh-size capabilities and performance of different computer codes which are available for the dynamic analysis of mining problems. It was found that codes which allow general solutions, are restricted to problem sizes of up to two orders of magnitude less than special-purpose codes which use restrictive grid-schemes, specifically the staggered

grid. Methods, to extend the staggered grid scheme to allow general geometric shapes to be modelled, were developed and evaluated. An alternative grid scheme to the staggered grid was also developed, which has a similar performance to the staggered grid, yet should more readily allow transformation to allow analysis of general problems.

Methods for quantifying dispersion behaviour

One reason necessitating large meshes in dynamic problems is that a wave propagation analysis will require a particular frequency range. Higher frequencies require smaller elements and hence larger mesh sizes. The dispersion behaviour of a grid scheme however, limits the frequency range for which the wave propagation is accurate, requiring the use of smaller elements and a larger number of elements, to obtain the correct frequency range. Analytical methods can be used to derive the dispersion behaviour of a particular finite difference or finite element scheme. This requires a detailed knowledge of the internal grid scheme. Theoretical results also assume the simplest uniform meshes, while many practical models have mesh distortions and non-constant element sizes. A practical method was therefore developed for measuring the dispersion caused by a grid scheme. This method can be applied without knowledge of the internal grid scheme, and without restrictions on the uniformity of the mesh.

The method involves passing a broad-band, high frequency plane wave through the mesh. Two alternative approaches can be used to characterize the dispersion: either, recording spatial waveforms at different times, or recording time waveforms at different positions. Figure 4.3.1.1 indicates the waveform data from which dispersion curves are obtained.

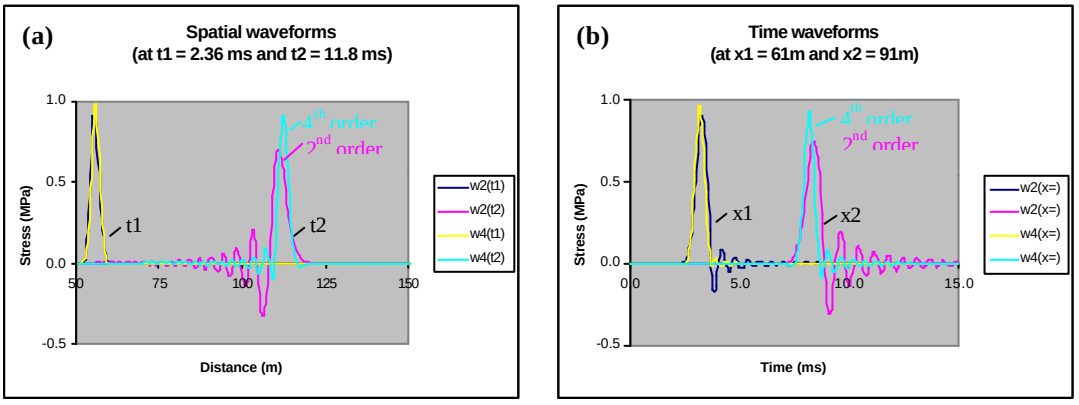

Figure 4.3.1.1 Waveforms from which the phase and group velocities are calculated. (a) Spatial waveforms at two different times used in the first method for calculating dispersion (b) Time waveforms at two different positions used in the second method for calculating dispersion. Waveforms are shown for both a 2^{nd} order and 4^{th} order staggered grid.

The first approach takes Fourier Transforms of the two spatial waveforms, transforming the spatial variable x to wave-number γ. Denoting A_1 and A_2 as the amplitude and ϕ_1 and ϕ_2 as the phase functions of these transforms, yields the following expressions for phase and group velocity as a function of wave-number.

$$c(g) = \frac{1}{g(t_2 - t_1)}\left[-(f_2 - f_1) + iLn\left(\frac{A_2}{A_1}\right)\right] \tag{4.3.1.1}$$

$$\frac{\partial w}{\partial g} = c(g) + g\frac{\partial c(g)}{\partial g} \tag{4.3.1.2}$$

The second approach is to take Fourier Transforms of the two time waveforms, transforming the time variable t to frequency ω. Again, denoting A_1 and A_2 as the amplitude and ϕ_1 and ϕ_2 as the phase functions of these transforms, yields the following expressions for phase and group velocity as a function of frequency.

$$c(w) = w(x_2 - x_1)\left[\frac{-(f_2 - f_1) - iLn\left(\frac{A_2}{A_1}\right)}{(f_2 - f_1)^2 + \left[Ln\left(\frac{A_2}{A_1}\right)\right]^2}\right] \tag{4.3.1.3}$$

$$\frac{\partial w}{\partial g} = \frac{c^2(w)}{c(w) - w\frac{\partial c(w)}{\partial w}} \tag{4.3.1.4}$$

The second approach (Equations 4.3.1.3 and 4.3.1.4) is the most useful, as time waveforms are more readily obtained than spatial waveforms. However, phase and group velocity are usually given as functions of spatial frequency or wave number not as a function of frequency. $c(\gamma)$ can be readily obtained from $c(\omega)$ numerically (Hildyard, 2001).

The dispersion characteristics for the 2nd, 4th and 8th order staggered grids were obtained used spatial waveforms. These are compared in Figure 4.3.1.2. The graphs are plotted against $\gamma/2\pi$, which is the inverse of the wavelength, and are based on a spatial discretization of $\Delta x = 1$ m. Only the frequency range for which the phase velocity is within a few percent of the true wave-speed can be considered sufficiently accurate. Results indicate that the higher order schemes have significantly improved frequency behaviour, with the accurate frequency range of the 4th order mesh being at least twice that of the 2nd order mesh. The graph "w-4s" is for a 4th order mesh with half the resolution in each dimension (i.e. $\Delta x = 2$ m) as the 2nd order mesh. It is important to note that this coarse 4th order mesh has a more accurate phase velocity for frequencies below 15% of the maximum frequency of the more refined 2nd order mesh. It is highly recommended that any mesh-based dynamic code make use of higher-order approximations.

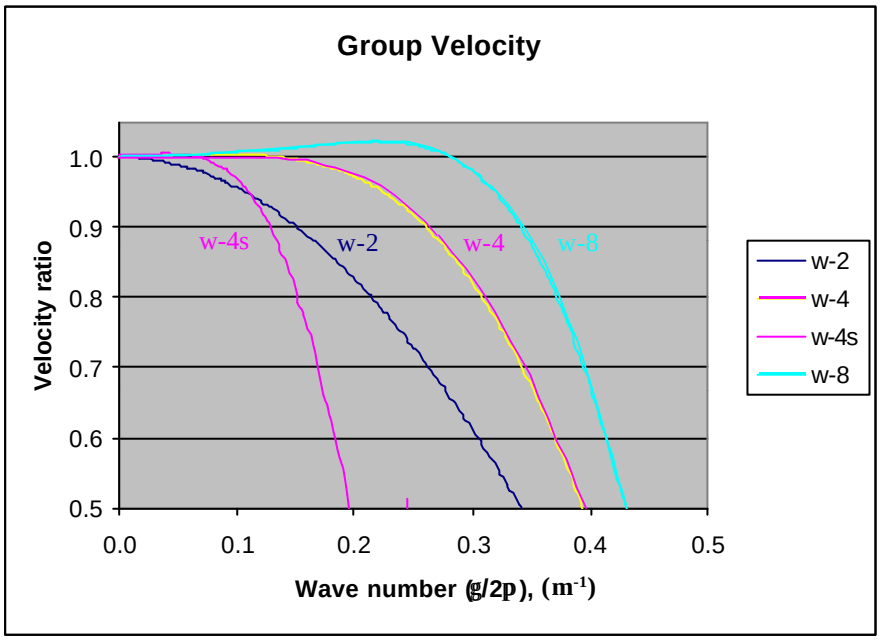

Figure 4.3.1.2 Group velocity calculated from spatial waveforms for the 2nd order (w-2), 4th order (w-4) and 8th order (w-8) staggered mesh. The graph (w-4s) is for a 4th order mesh with half the resolution in each dimension as the other meshes.

Performance and model-size capabilities of different computer codes

A number of finite difference and finite element codes exist in rock mechanics which can be used to study dynamic problems (e.g. UDEC (Itasca, 1993a), FLAC (Itasca, 1993b), ELFEN (Rockfield, 1999)). In contrast to the staggered-grid scheme of WAVE, these codes employ schemes where the different components of stress are coincident at a given point in space. This simplifies the treatment of cracks and cavities, and readily allows a non-uniform mesh, allowing very general geometries to be modelled. This section shows however, that these more general schemes are orders of magnitude less efficient in memory and run-time than the regular 4^{th} order staggered mesh scheme, and that they cannot support a sufficient number of elements to solve many of the problems studied in sections 4.1 and 4.2.

UDEC and ELFEN use triangular elements, while FLAC uses four-noded quadrilaterals with a mixed discretization to avoid spurious deformation modes ("hour-glassing"). The performance of a regular grid in two-dimensions was compared for each of these codes against that of the staggered mesh. The accuracy of the grid-schemes was evaluated by measuring the dispersion using the previously described method. The performance was evaluated by comparing the computer memory and run-times required to obtain the same degree of accuracy in these dispersion curves. Results were normalised to the 4^{th} order staggered-grid (WAVE).

Dispersion results are shown in Figure 4.3.1.3 and the performance summarised in Table 4.3.1.1. These show that a combination of the basic grid scheme and the use of a fully general mesh, causes the UDEC, FLAC and ELFEN grids to be nearly an order of magnitude less efficient than the 2^{nd} order regular staggered mesh. In addition, since these schemes are limited to 2^{nd} order, they are nearly two orders of magnitude less efficient than the 4^{th} order staggered mesh. This difference in efficiency increases with dimension, and is expected to be greater than two orders of magnitude for three-dimensional grids. These general-purpose codes would not support a sufficient number of elements to solve many of the problems dealt with in sections 4.1 and 4.2. The results highlight that while it is important to find a grid scheme which permits mesh deformation, for dynamics it is important that the scheme is efficient and that it can be readily formulated with at least 4^{th} order accuracy.

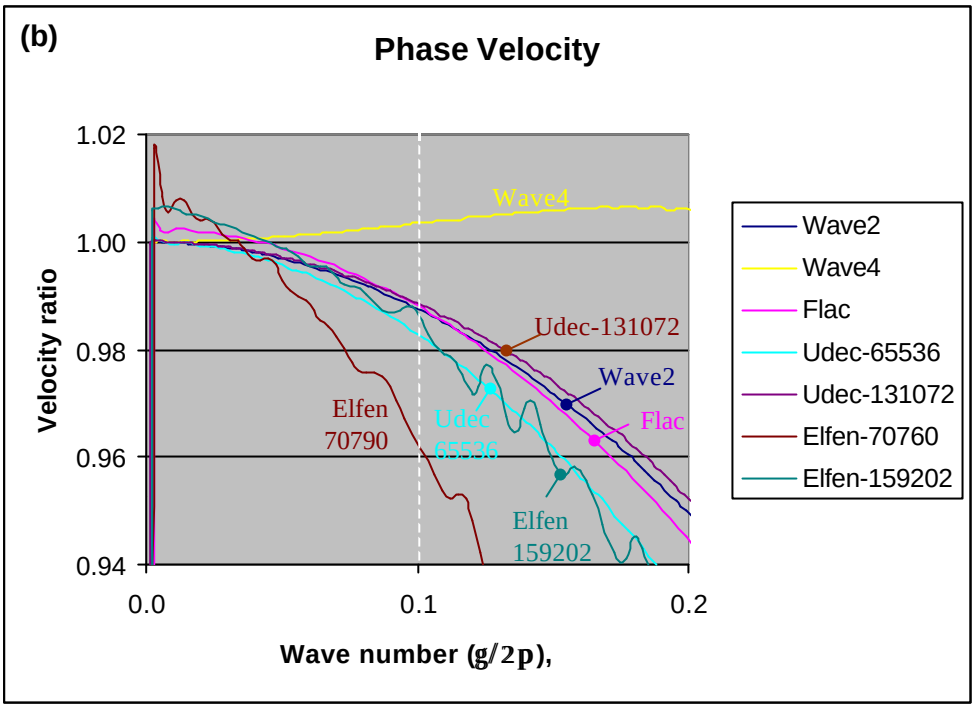

Figure 4.3.1.3 Phase velocities for different codes and grid schemes, with the dotted line indicating the accurate frequency range normally assumed for the 2nd order staggered grid. Results are based on a 1 m grid spacing for WAVE and FLAC (i.e. an area of 1 m^2 per zone). Two different ELFEN and UDEC results are shown, one for an element area of approximately 1.2 m^2 the other for an element area of approximately 0.6 m^2.

Table 4.3.1.1 Comparison between different codes and grid schemes, for memory and run-times required to obtain the equivalent dispersion accuracy as shown in Figure 4.3.1.1. Values are relative to that of a 4th order staggered mesh with 2 metre grid-spacing.

Mesh Scheme	Accuracy (Order)	Two-Dimensions			Three-Dimensions	
		Memory ratio	Run-time ratio	Zone size (m^2)	Memory ratio	Run-time ratio
Wave4	(4)	1	1	4.00	1	1.0
Wave2	(2)	4	7	1.00	8	15
Flac	(2)	34	115	1.00		
Elfen-159202	(~2)	238	555	0.57		
Udec-131072	(~2)	43	1053	0.61		
NuWave4	(4)	1.4	2.5	4.00		

Methods for generalising the staggered mesh

One limitation of the program WAVE is that it has a regular and orthogonal grid. This severely restricts the orientations of fracturing and cavities that can be modelled. Nevertheless, it has significant advantages over more general programs in terms of the sizes of meshes and accuracy for which seismic problems can be solved. An unfortunate consequence of the staggered grid is that different components of stress are located at different spatial positions. Similarly, different components of velocity are located at different positions. This complicates the treatment of cracks, and it the rotations of stresses or velocities into other co-ordinate systems. This, in turn, complicates the treatment of general fracturing and cavities.

Hildyard (2001) evaluated three options for adapting the staggered mesh to more general geometries. The first approach used a localised distribution of a transversely isotropic material for modelling discrete fractures in any orientation (Coates and Schoenberg, 1995). However, this was shown to be unacceptable for low-stiffness or open cracks. A second approach developed expressions for an explicit angled crack which approximately satisfies the boundary conditions at the crack surfaces. This implements a 45° crack in a regular mesh, while other angles can be modelled by varying the grid-spacing. This approach to angled cracks has the advantage that no changes are required to the mesh equations, and it is therefore potentially very efficient. However, it appears difficult to accommodate crack intersections in this method, and it is not suited for providing completely general fracture models. A third method is to map a curvilinear grid of the problem space to the orthogonal grid, and is discussed in more detail.

A similar though less complex problem than modelling arbitrary fracture orientations, is the modelling of an irregular free-surface topology. Recently, a number of methods have been proposed which allow the modelling of an irregular free-surface topology for seismic applications. Most of these are based on “vacuum formalism” ((Zahradnik et al., 1994; Oprsal and Zahradnik, 1999; Pitarka and Irikura, 1996; Robertsson, 1996), where the wave-speeds and density of the material above the surface tend toward zero. However, models with flat surfaces have shown that it is more accurate to enforce the stress free boundary condition explicitly (Graves, 1996). An approach which allows surface boundary conditions to be enforced, is to solve the wave equation on a general curvilinear grid. Non-orthogonal and curvilinear grids were first introduced for modelling electromagnetic wave propagation on staggered grids (Holland, 1983; Lee et al., 1992; Jurgens et al., 1992;). Hestholm and Ruud (1994) applied a mapping to a staggered grid finite difference formulation for seismic wave propagation, to model a stress-free, curved surface topography.

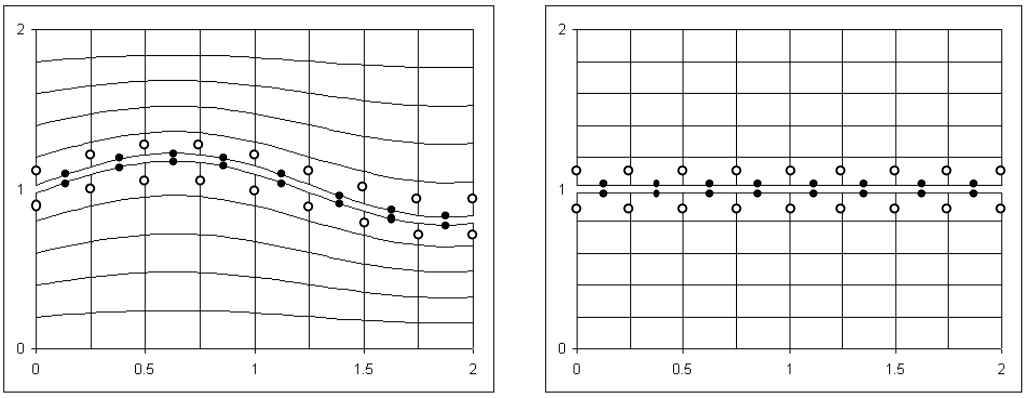

(a) x-y coordinate system (b) ξ-η coordinate system

Figure 4.3.1.4 Example mapping, showing position of a crack in the two coordinate systems. ‘ ’ indicates position of velocity u1, while ‘ ’ indicates position of velocity u2. Note that u1 is dual-valued on the crack. Stress positions are not shown.

The approach used by Hestholm and Ruud was extended to the case curved cracks. Hildyard (2001) outlines the details of this formulation. However, a number of potential problems were identified in the implementation of this approach. Firstly, the mapping introduces certain derivatives into the mesh equations which are not present in the rectilinear grid formulation. These derivatives do not have “natural” difference approximations within the staggered grid and will lead to a reduction in the overall accuracy. An even more important limitation was encountered in the crack boundary conditions. Some of the expressions do not have a suitable implementation in the staggered grid, and may need to be approximated with first order differences. The above are serious and perhaps prohibitive limitations. However, it is recommended that further investigations be made, since mapping the staggered grid is otherwise a very attractive way of obtaining an efficient solution for general crack orientations. Alternatively, this mapping approach is potentially very useful for a grid scheme whose components are co-incident, where the above short-comings do not apply.

Alternative grid schemes

From the previous section it is apparent that although the staggered grid is very efficient and allows for large problem sizes, it cannot easily be adapted to model general fracturing and cavities. Both the efficiency and the difficulty in generalising the program result from the use of a staggered grid – where the components of stress (and similarly, the components of velocity) are

not coincident. A new grid scheme was developed which avoids the staggering, while having similar memory and run-time requirements to the 4th order staggered mesh.

A family of schemes was investigated based on the quadrilateral element used in FLAC (Cundall, 1992), which uses the mixed discretization scheme of Marti and Cundall (1982). Based on ideas from Cundall (1998), it was shown that this approach can be recast into a far more memory efficient scheme for uniform elements, where the number of solution variables is significantly reduced by the elimination of stresses from the calculation cycle.

However, there are advantages to using a method where stresses are calculated, particularly for the application of high order differencing. It was shown that the grid scheme can instead be recast as a velocity-stress finite difference scheme, requiring just two more grid-variables than the staggered mesh, and that this can be extended to higher order accuracy. The full details of this proposed method are given in Hildyard (2001).

The above investigations resulted in two formulations named “NuWave2” and “NuWave4”, indicating 2nd and 4th order accuracy respectively. These schemes were tested, and dispersion curves indicate that they correspond to the accuracy of the staggered mesh. Table 4.3.1.1 shows that the “Nuwave4” scheme is very efficient, with the memory and run-time efficiency approaching that of the staggered mesh.

It has been shown that general-purpose finite-difference and finite element programs are severely limited in their model sizes, and hence incapable of studying many problems relating to wave propagation and dynamics. The above grid-scheme provides a potential approach for studying more general fracture geometries, while retaining the efficiency to support large numbers of elements. It is recommended that further work is carried out to determine if this grid scheme can indeed be readily mapped to a curvilinear mesh, and whether it can be extended and still be efficient in three-dimensions. If this proves possible, then it has the capacity to displace the staggered grid scheme both in mining applications and more widely.

4.3.2 Attenuation of a seismic wave in WAVE

The general problem of understanding the seismic source is of great interest in mining seismology. Every seismogram carries implicit information about the source and the structure of the medium through which the seismic wave has propagated. Hence, explaining the observed motion can give information about the source and ground structure. However, in solving this

problem, there are also related aspects that have to be understood, e.g., the scaling relations of earthquake parameters. Previous work from acoustic emission testing, described in Section 2.1.1, has shown that laboratory scale, mining-induced and natural earthquakes exhibit self-similar behaviour (Sellers and Kataka, 2001). Numerical modelling can also be used to generate ground motions of an event associated with a given mine layout. The use of numerical modelling can allow the identification of hazardous stope regions subjected to high velocities or large induced tensile stresses.

The elastodynamic finite difference program WAVE was written to model wave propagation in a two- or three- dimensional elastic medium (Hilyard et al 2001). Wave propagation can be followed in detail from the source taking into account any subsequent reflections and refractions from surface boundaries and fault structures. A variety of dynamic sources can be simulated in WAVE, but it must be noted that the finite difference scheme used by WAVE can suffer from the dispersion of high frequencies. Dispersion implies that different frequencies are propagated at different velocities and, as a result, any source signal is distorted with distance from the source. The specification of the source frequency structure therefore has far-reaching consequences on the validity of a WAVE simulation.

Previous work by Daehnke (1996) has shown that Brune's model correspond reasonably well with the results of WAVE analyses if the fault cohesion is eliminated instantaneously. This work aims to investigate more general mining situations in which stopes may alter the wave dynamics. The study also aims to simulate the numerical output in the same manner as a seismic system would work on a mine. This will provide an assessment of whether the rock mass response predicted by WAVE is relevant for mining back analyses.

In Brune's (1970, 1971) model the near-field velocity is shown to decay as R^{-2} and the far-field velocity decays to R^{-1}. The "far-field" assumption in fact involves two conditions, firstly, that the observational distance (R) should be much greater than maximum wavelengths of interest in the radiated field and, secondly, that R should be much greater than the dimensions of the source. The most fundamental limitation of the Brune model comes from its failure to account for the effects of rupture propagation (Boatwright and Boore ,1982, Koyama and Izutani, 1990). Directional dependence and the effect of asperities are also not included explicitly in the model (Boore and Joyner, 1989, Koyama and Izutani, 1990). Nonetheless, Brune's source spectrum with a constant stress drop gives a useful "reference" for comparing different events and has been adopted in this study.

To test the attenuation response of a simulated, mining induced seismic source, a simple WAVE model of a cubic volume of rock without a stope was constructed with a grid size of 1m. The source (termed Event 1), was assumed to be a horizontal slip event at a depth of 71 m and located at the centre of a cubic volume. The shear source was assigned a stress drop of 18.4 MPa and a ramp-like source time function. The transient period characterising the source duration was assumed to be Tmin = 32e-3 seconds, implying a corner frequency, fc, of 311Hz, typical of a mine source event. A line of point histories were recorded to analyse the attenuation from the source to the sensors. The amplitude decay of the first pulse with distance was analysed to see how the near-field and far-field compared with the Brune's model. Figure 4.3.1.1a shows the log(Amplitude) vs the log(distance to source) for histories located up to 110m from the source. A linear regression fit to the points indicated a decay with an exponent of -1.6 (i.e. amplitude decays with $R^{-1.6}$). Figure 4.3.2.1b shows the readings between 110m and 290 m from the source with a decay exponent of -1.2. These findings can be compared to the theoretical the near-field and far-field exponents in the Brune model of –2 and –1, respectively.

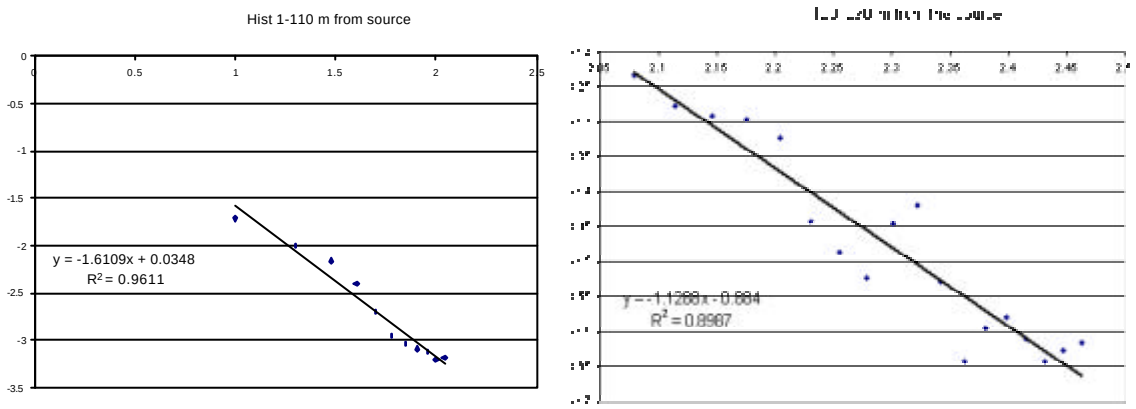

Figure 4.3.2.1. Log amplitude of the first pulse versus log distance for a) waveforms from 0 to 110 m away from the source and b) waveforms from 120 to 296 m away from the source

The Fourier spectral amplitudes were also analysed for waveforms at various distances from the source to study the attenuation behaviour. The results indicate that high frequency content decreases with distance from the source (see Figure 4.3.2.2).

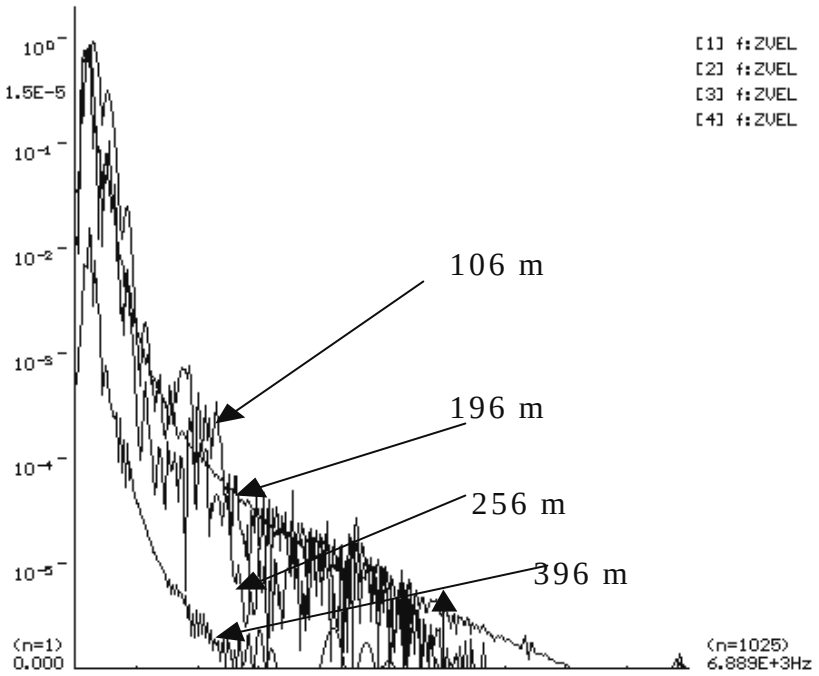

Figure 4.3.2.2. The Fourier spectral amplitudes for waveforms at stations 106m, 196m, 256m and 396m away from the source. Notice that the high frequencies are strongly attenuated for events further away from the source.

Using the same model, synthetic seismograms were generated and recorded by sensors placed around the cube for good azimuthal coverage to improve location and other source parameter calculations. This exercise was carried out to see if the simulated event specified in WAVE could be "located" by the PSS seismological software. The results have shown that the event could be located within an error of 7 to 8 m (see Figure 4.3.2.3). The location error of the events will depend on the resolution of the wave speed or time step i.e., a slight error of 1 time step (7.258 e-4 seconds) in the picking of the P-wave onset can cause a location error of 4.5 m (assuming the P-wave velocity to be 6200 m/s).

A source radius of 9.8 m was estimated for the event using the PSS seismic software, compared to the input source dimensions of 7m by 15 m. For a circular crack, the equivalent area of the event would be $105m^2$ resulting in a radius of 5.8m. The PSS seismic software underestimated the corner frequency of the event generated by WAVE. The reason for this underestimate is that the PSS seismic software is based on a spectral fit of the Brune (1970, 1971) model so the reduction in high frequency content due to numerical dispersion (as shown in Figure 4.3.2.2) causes an underestimate of the corner frequency. The spectral amplitude plot shows that Event 1 actually has a corner frequency of about 220 Hz. This gives a source radius of 5.8 m in agreement with the rectangular input source size.

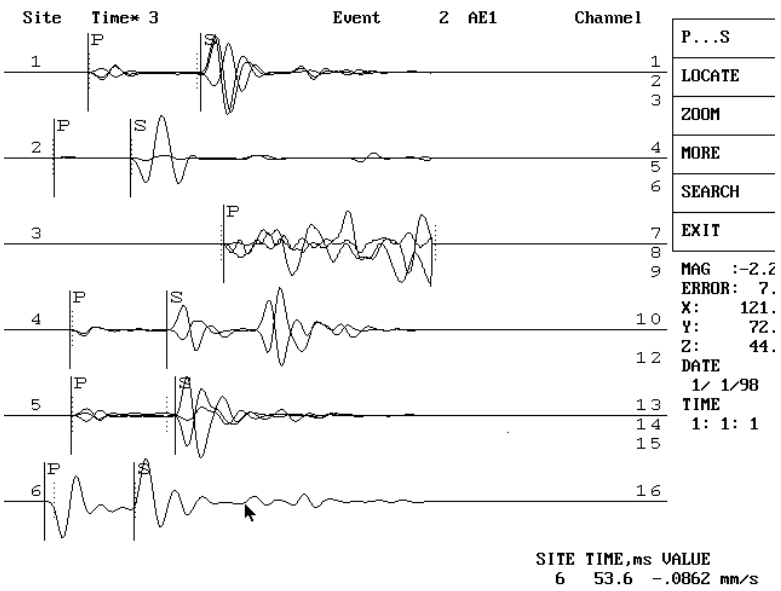

Figure 4.3.2.3 The waveforms used for location for event 2. The event is located at (121, 72, 44) with an error of 7 m. This event is supposed to be at (116, 76, 40).

To investigate the effect of a stope on the numerical predictions of wave propagation, models were constructed with a tabular stope at different positions relative to the events and the sensors (Figure 4.3.2.4). A comparison was made between the situation without a stope to a model where the stope was situated above the event. The comparison was also made for two different stations one above the stope and another below the stope. As shown in the spectral density plots of Figure 4.3.2.5, the presence of a stope introduces a considerable number of high frequencies into the wave spectrum. Without the stope, the waveform was found to have a lower corner frequency. Thus, the presence of the stope reduces the reported event radius.

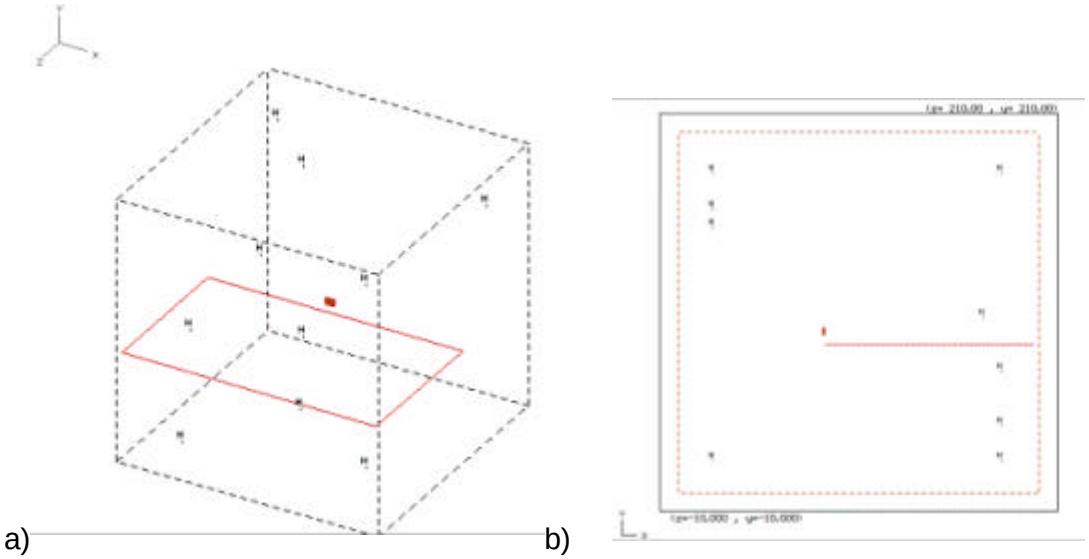

Figure 4.3.2.4. Wave models showing a) a 3-D view and b) a 2-D section of the model for a typical configuration of event, stope and sensors.

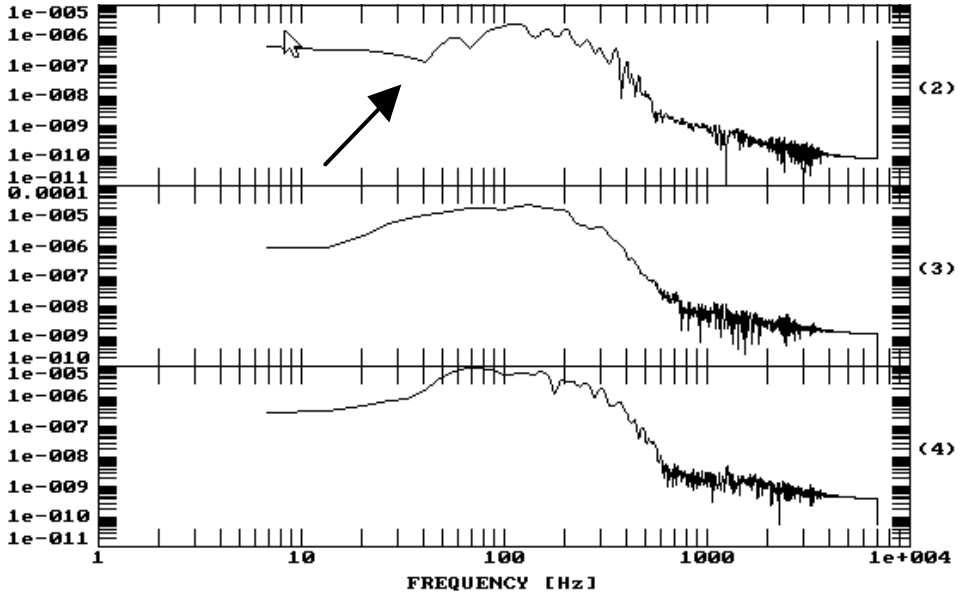

Figure 4.3.2.5. Spectral amplitude fit for event 1 on the log-log scale. Channel 2 is above the stope and the event. Channels 3 and 4 are between the stope and the event. Notice that the lower frequencies are affected by the stope (see arrow).

The moment tensor solution gives information about the orientation and deformation characteristics of the source (Aki, 1982). A moment tensor solution was computed for the Event 1 simulation from WAVE, in a cubic volume with stations uniformly placed for good azimuthal coverage using Relative Moment Tensor Inversion software (Andersen, 2002). The event was orientated in a vertical direction. An analysis with the source region sheared in the vertical direction was compared with an analysis having the source sheared in the horizontal direction. The focal plane solutions calculated from the moment tensors are given in Figure 4.3.2.6. The moment tensor reports two focal planes, and additional information is needed to distinguish the source plane (Kataka, 2002). The results from the vertical shear (Figure 4.3.2.6a) indicate that focal plane 2, with a strike of 94^{o} within 4^{o} of the input event. The rake of –90.4^{o} indicates the direction of shearing to be within 0.4^{o} of the input. The division of the stereoplot into two equal halves for the tensile and compressive region is typical of a vertical dip slip event. The case with the horizontal shear indicates poorer agreement between the estimated moment and input event. The strike of plane 1 is given as 77^{o,} which is about 13^{o} different from the expected 90^{o} strike. The dip is also reported to be 10.3^{o} from the input vertical dip. However, the focal pattern, involving the division of the stereoplot into quarters is typical of a vertical strike slip event, as was input.

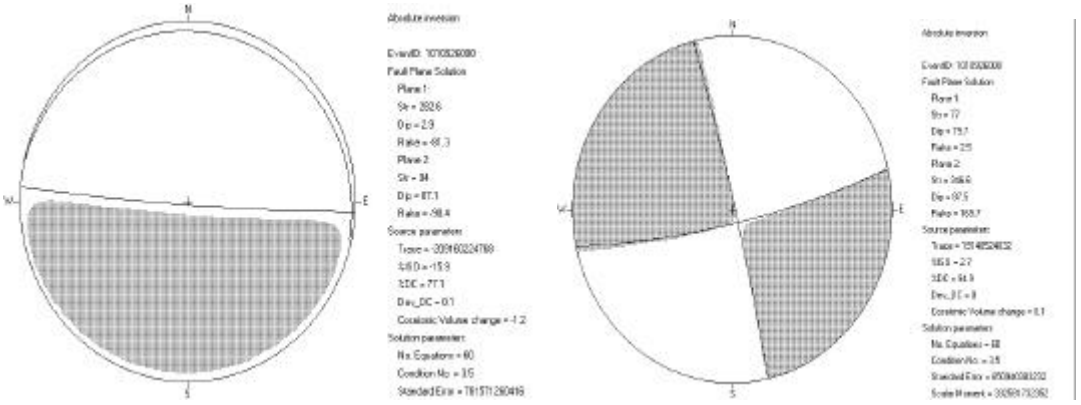

a) b)

Figure 4.3.2.6 Moment tensor solution from WAVE for an event a) sheared in the vertical direction and b) sheared in the horizontal (X) direction.

Using the same grid size, the same event was studied with a rectangular stope at different positions relative to the event . The waveform pulse shapes and polarities are different in the two models and show that the presence of a stope has an influence on the wave propagation. The moment tensor mechanisms obtained when the stope was placed 8 m to the right of the event are shown in Figure 4.3.2.7. Both moment tensors produced the correct slip pattern, but the reported fault plane and slip directions had significantly more deviation from the ideal input source than for the events without a stope, shown in Figure 4.3.2.6. This is further evidence that the stope does affect the waveform.

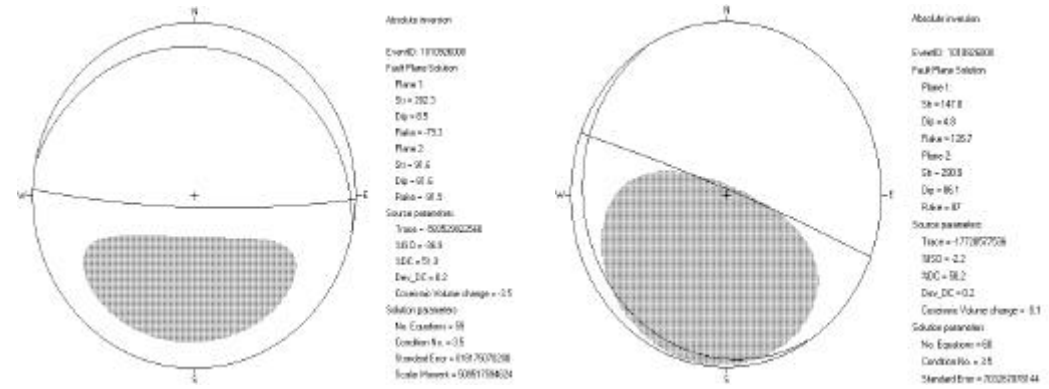

a) b)

Figure 4.3.2.7 Moment tensor solution from WAVE for an event with a stope 7 m west of the event a) sheared in the vertical direction and b) sheared in the horizontal (X) direction.

This modelling exercise has provided a better understanding of the propagation of seismic events in the numerical code WAVE. The testing has been performed with less than ideal sensor positions, as could be expected in a mining situation. The study has shown that the frequency content of the transmitted wave is sensitive to the grid size, the distance to the

source and the source frequency. The source parameters can be back calculated using seismic software and moment tensor analysis. This correlation between the input source and the output waveform and particle velocities is a pre-requisite for the application of the numerical technique to back calculate the effect of a seismic event on a mine stope. Integration techniques for correlating the observed mine seismicity and the stress state predicted by numerical models (e.g. those discussed in project GAP 603) should consider the dynamical response of the rock mass. These preliminary studies have indicated that it is extremely important to represent the rock mass with a sufficiently fine grid and to correctly represent the source dimensions, frequency content and slip directions in order to obtain meaningful correlations with observed seismological parameters.

4.3.3 Lead-lag geometry modelling

Large scale mine modelling is carried out regularly on mines, using elastic boundary element methods (Napier and Stephansen, 1987). These models can identify areas of high stress concentration, but cannot describe the rock failure processes and subsequent stress re-distributions. Considerable effort has been made to develop numerical models and constitutive equations that can represent the nonlinear fracture processes. These have currently only been applied to laboratory test situations (e.g. Sellers and Napier, 1997) and some two-dimensional models of the fracture processes around deep level mining excavations (Sellers et al, 1998, Van de Steen, 2001, Van de Steen et al, 2001, Klerck, 2001).

As an example for comparison with the observed fracture patterns, the boundary element program DIGS (Napier, 1990) has been applied to solve a two dimensional problem. A square sample is constructed that has a side length of 80 mm. The slot is represented by a line of boundary elements through the centre of the block, as shown in Figure 4.3.1.1. These elements have zero normal or shear stresses acting on the surfaces and closure is limited to the specified width of the slot. The cut surface forming the contact between the upper and lower blocks is represented with boundary elements having a friction angle of 30 degrees. A tessellation approach (e.g. Napier, 1990, Sellers and Napier, 1997) is applied to represent fracture growth.

A Delaunay triangulation of the sample, was created with an average triangle side length of 1mm. The side of each triangle is assumed to be a potential fracture path and is assigned a failure criterion based on the Mohr-Coulomb model. At each loading increment, all potential fracture sites are searched and the site with the highest excess shear stress is activated and can then transmit its influence to the other elements. The inclusion of an active element causes stress redistribution and other sites may activate. Once all sites have been activated for a given

load, the load is incremented and the process repeated. The final fracture pattern is shown in Figure 4.3.1.1. The pattern is representative of the fracture induced in the Elsburg quartzite (Sellers et al, 1999). The modelling of fracturing in three dimensions is still at an early stage (Napier 1998, Potyondy and Cundall, 1998, Sellers, 2001). Preliminary studies (Sellers, 2001) have shown that the three-dimensional variations in the fracture surface may be modelled using the ELFEN finite/discrete element technique.

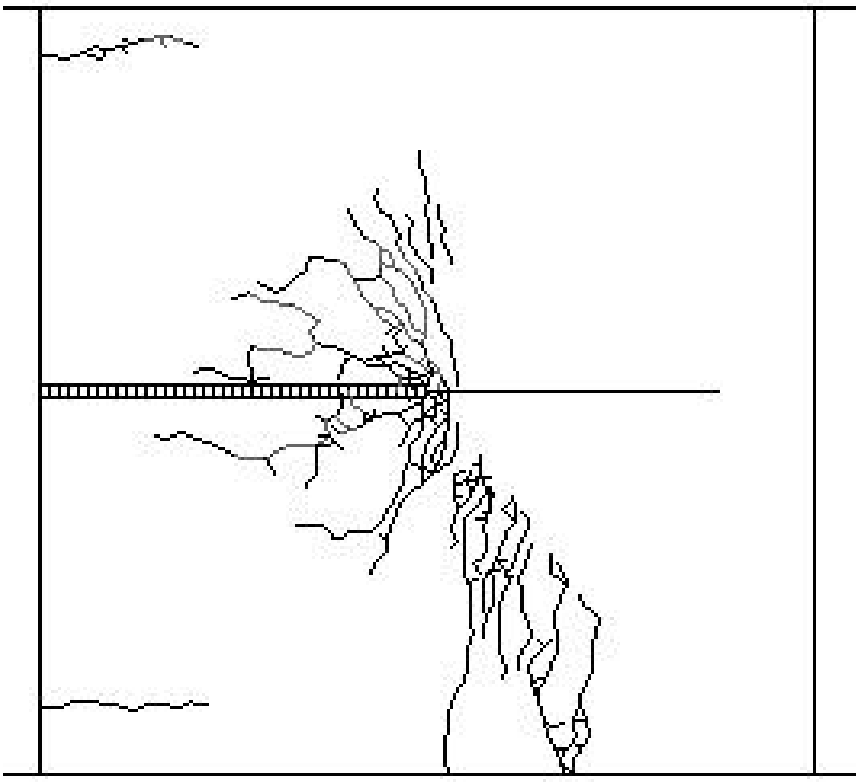

Figure 4.3.1.1 Example of numerical prediction of the fracture pattern in the experimental samples using the two-dimensional boundary element program DIGS.

Triaxial tests have been used extensively to test the response of various material models. However, the cylindrical shape and loading symmetries mean that the results are difficult to interpret for understanding of the growth of fractures in three dimensions. Thus, a series of tests have been performed on cubic samples with slots cut to simulate stress raising effects that are similar to those caused by the corners of the excavation in mine situations. A schematic of the test setup is shown in Figure 4.3.1.2a. The cube is cut in half. Part of the lower surface is ground down to form the outline of a tabular excavation, leaving a shaped pillar of rock to support the load, as shown in Figure 4.3.1.2a The sample used in the numerical modelling simulates a tabular excavation with two mine “panels”. One “panel” leads the other by 10mm. This situation of a lead-lad panel layout is typical in gold mines and is designed to reduce the

chance that a single long face is parallel to a geological feature such as a fault or dyke, and is also beneficial for removal of rock along periodic strike gulleys (see e.g. Jaeger and Ryder, 1999). Thus, understanding the effect of the lead-lag distance on the formation of fractures around the stope, and hence the potential for limiting the rockburst hazard is very important for mine safety.

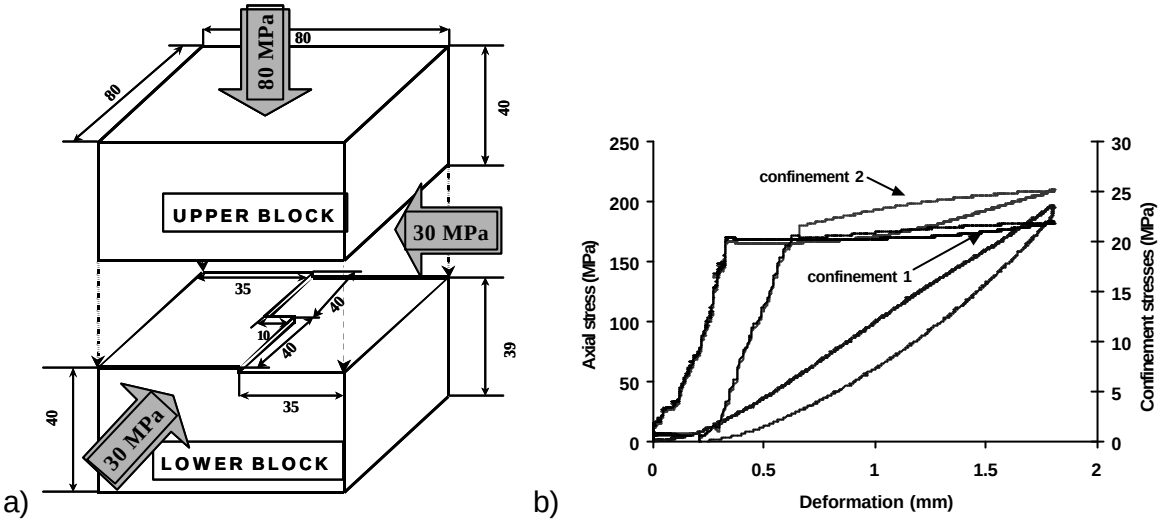

Figure 4.3.1.2. a) Schematic of block test sample and b) actual loading data

In the physical experiment, the confinement is applied via stiff steel platens. As shown in Figure 4.3.1.2b, the confinement is increased with the vertical load to a selected pressure and then the vertical load is increased until failure occurs. Ten acoustic emission sensors are incorporated into the platen to record microseismic activity due to fracture formation. These AE sources can be located within the sample and the fracture mechanism can be determined using moment tensor analysis, providing real time information about the fracture pattern developing within the sample.

The finite element model of the sample contains 31415 elements. A plot of the damage pattern at a load level of 100 MPa is shown in Figure 4.3.1.3a. The damage originates at the slot and extends towards the sample boundaries as the loading increases. This agrees with the results of acoustic emission monitoring. The damage contours observed on the top surface of the sample follow the general pattern of the mine layout shape shown in Figure 4.3.1.2a. However, when discrete fracturing is allowed to occur during the loading the damage zone does not extend outwards from the slot. A large mass of self-sustaining fracturing forms near the initiation point and the solution rapidly diverges. This is an artefact of the penalty contact algorithm.

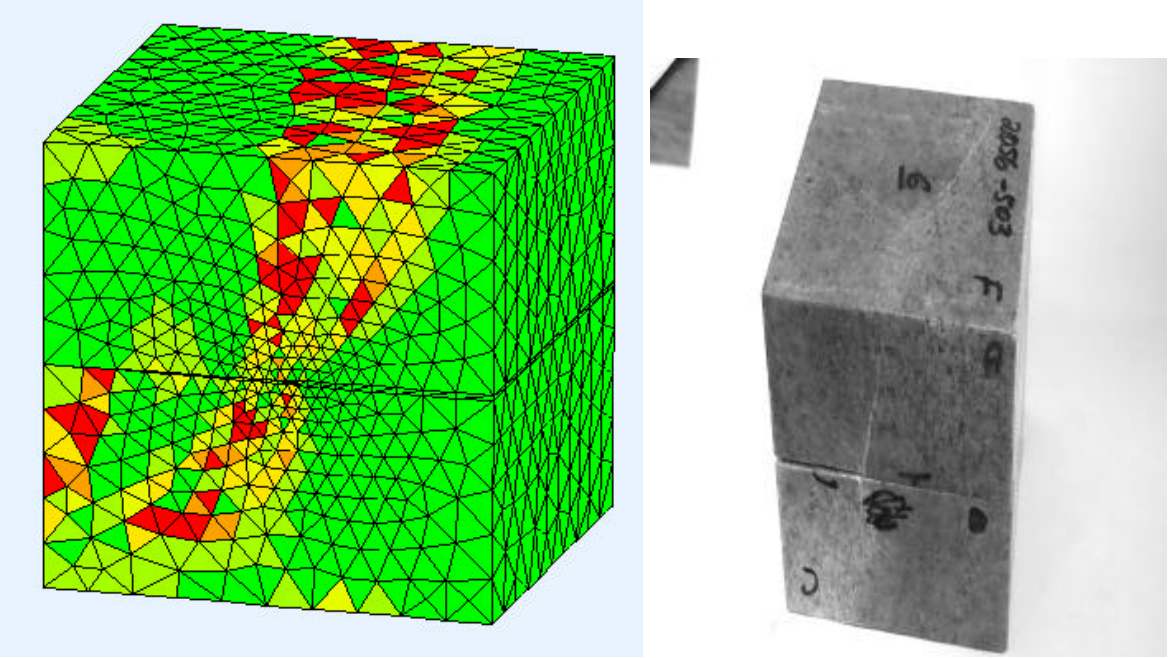

Figure 4.3.1.3. a) Coarse mesh and damage pattern at 100 MPa vertical load and b) observed fractures.

Discrete fracturing can be introduced, as shown in Figure 4.3.1.4a, by specifying continuum damage only until a specified load level and then switching on the discrete fracturing facility to determine where discrete fractures would form. The discrete fracture state shown in Figure 4.3.1.4a relates to the damaged state at 100 MPa as shown in Figure 4.3.1.3a. The model was allowed to run for 10 000 time steps as the load was increased to 100 MPa and then discrete fracturing was allowed to develop over thirty time steps until the numerical divergence occurred.

The observed fracture pattern can be seen in Figure 4.1.3.4b, but this view only gives a limited view of the complete trace of the fracture on surface. A digital image of the fracture surface within the actual rock sample was reconstructed using x-ray tomography (CT scanning) (Sellers et al., 2000) and is shown in Figure 4.3.1.4b. In the centre of the block, near the plane of the slot, the fracture closely follows the stepped lead-lag pattern of the edge of the excavation. Gradually, the fracture surface forms a curved shape that defines an average line across the face of the excavation. The damaged zone (Figure 4.3.1.3a) and discrete fracturing (Figure 4.3.1.4a) predicted by the coarse model followed an average line throughout the entire block and did not closely follow the edge of the excavation. A finer mesh was constructed in an attempt to determine whether this was due to the coarse finite element grid averaging the stress concentration in the region of the edge of the slot. The finer mesh contained 159 150 elements and required 226 Mb of memory. As shown in Figure 4.3.1.5, the damage contours follow the face at the plane of the excavation and follow the average face shape at the surface of the

block. There was insufficient computer memory available to allow the simulation of discrete fracturing.

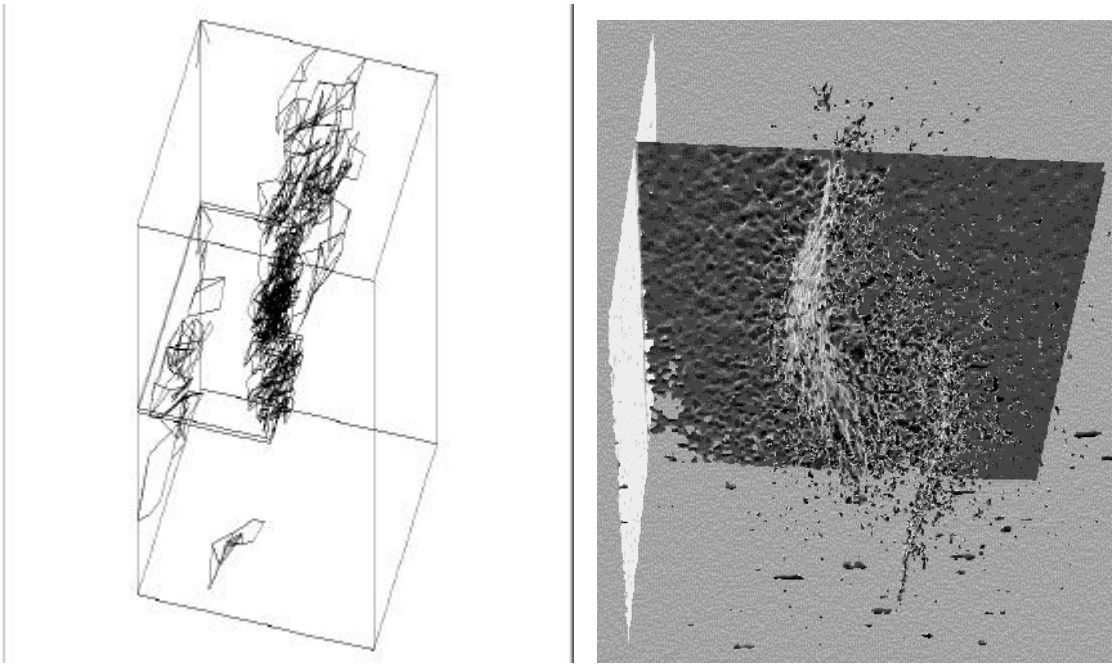

Figure 4.3.1.4. a) modelled fracture pattern with coarse mesh and b) observed fracture pattern reconstructed from x-ray tomography

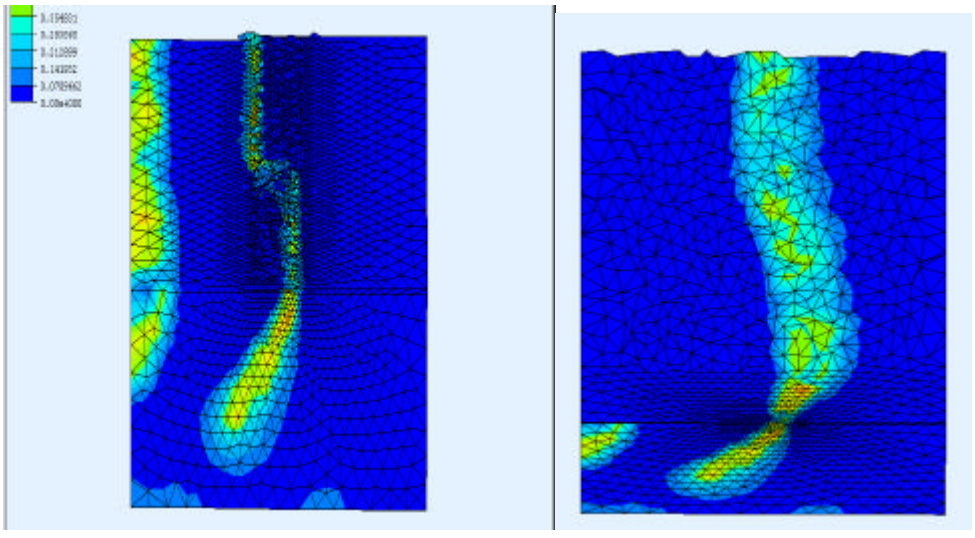

a) b)

Figure 4.3.1.5 Cut-away views of the refined mesh model showing damage contours. a) at the slot level b) near the sample surface

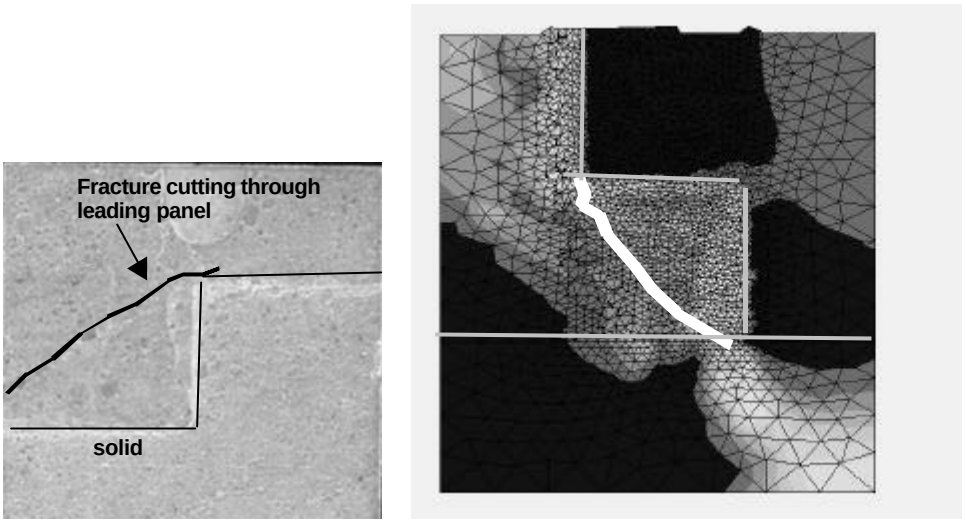

Figure 4.3.1.6 a) Photograph of test sample with 30mm lead lag layout indicating the fracturing along the edges of the stress raiser and with annotation indication the position of the fracture that cuts through the leading panel. b) a section view of the ELFEN model of the sample, which produced damage contours that indicate a similar fracture pattern.

Figure 4.3.1.6a shows the results of an experiment with a 30mm lead lag layout. In this case, the fracture surface is unable to follow the sharp angles of the edge of the slot. The fracture surface therefore cuts through the leading “panel”. The experimental sample was modelled with ELFEN. The resulting damage contours indicate that fracturing initiates at the edge of the slot in the lagging “face” as observed in the experiment. Figure 4.3.1.6b shows that the majority of fracturing, expressed as damage contours, in the leading “panel” is located behind the slot edge as the three-dimensional fracture surface cuts across the “panel” in agreement with the experimental observations.

Three-dimensional numerical models for rock fracture processes are still under development, but examples are shown that can reproduce the observed fracture patterns. Whilst this study has concentrated on South African gold mining conditions, x-ray tomography provides a unique means of visualising the fracture pattern within rock test samples and the methodology presented has many other applications and provides new avenues for the study of rock fracture processes.

Three-dimensional dynamic Particle Flow Code (PFC3D) models were used to examine the three-dimensional fracture processes in the experimental samples Three-dimensional models obviously present a much more realistic representation of rock volumes than the two dimensional models. The individual grains within a modelled rock volume are able to move in any direction and fractures may propagate out of the plane as is observed in tests on real rocks.

More realistic seismic sources can be generated that have an out of plane component which will allow direct comparisons between the energy release estimates obtained from the PFC^{3D} models and the actual seismicity (AE) recorded in laboratory experiments. Assuming that the PFC^{3D} models satisfactorily reproduce the mechanical and acoustic behaviour of actual rocks undergoing stress, they can then be used to examine in detail some of the micromechanics involved in the cracking and failure of the rock samples.

In general, a PFC model of rock consists of a collection of particles bonded together in a dense assembly. The micro-properties of the particle bonds can be adjusted to simulate the desired rock type. The various microproperties that can be specified are the particle size distribution, the normal and shear stiffness, the density, the friction angle, the normal bond strength scale factor, the shear bond strength scale factor and the strength deviation. The choice of these microproperties influences the macroproperties (e.g. strength and stiffness) of the modelled 'rock' . The general steps required to for create a model of a laboratory rock sample are given by Hazzard (1998). These steps involve: compacting the initial assembly, installing the isotropic stress state, expanding certain particles to ensure that all particles have three or more contacts and then applying the bond strength law. The bond average normal and shear strength must be specified and a variation in bond strengths about the mean may be applied. The overall strength of the material depends on the particle radii. The bond strength must be scaled directly with the particle size in 2D and with the square of the particle size in 3D. Loads are then applied to the walls of the cube to simulate the experimental loading conditions. The appearance of cracks in the material can be monitored during loading by using the internal macro language (FISH) to record bond breakages. Another series of FISH functions have been written to monitor and display cracking in PFC models and to represent them in terms of acoustic emission parameters (Hazzard, 1998). Groups of simultaneous or subsequent bond breakages can be collected into macro events using a clustering algorithm (Hazzard, 1998)

A PFC model with approximately 70000 particles was set up using particle sizes ranging from 0.65 mm to 1.2 mm. The smaller particles were used near the excavation (in the middle of the sample) and the size was gradually increased away from the excavation plane to limit the memory requirements of the model. The model was loaded normal to the plane of the excavation up to 210 MPa, while keeping the lateral confinement constant at 30 MPa in the same way as the laboratory experiments carried out previously. The final fracture pattern is shown in Figure 4.3.1.7a. Figure 4.3.1.7b and 4.3.1.7c show the laboratory acoustic emission locations for the same experiment. The general trend is quite similar as far the final stage of fracturing shown in Figure 4.3.1.7b.

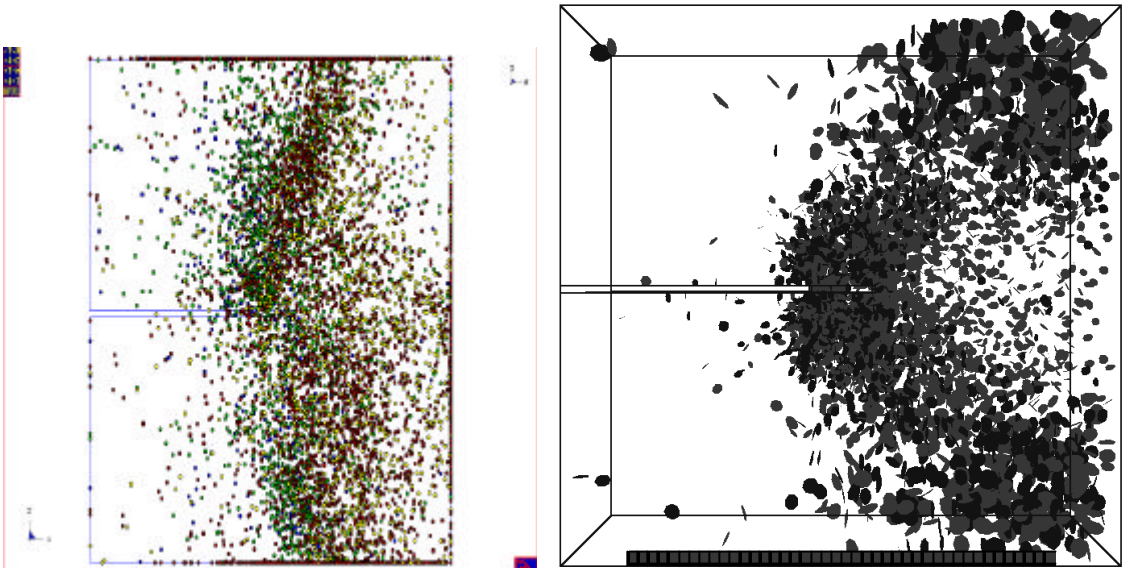

Figure 4.3.1.7. Section view through the block model indicating a) the located acoustic emission and b) the acoustic emission predicted by the PFC3D model.

A clustering algorithm (Hazzard, 1998) was used to correlate bond breakages that occurred close together in space and time into clusters. These clusters represent the equivalent seismic event that would be registered by a seismic system in the field or the AE location software in the laboratory. Figure 4.3.1.8 shows how the clusters of events initiate at the edge of the slot when the applied stress is about half the final value. The clusters increase in size and the number of increases with increasing applied load until the final state as shown in Figure 4.3.1.8b.

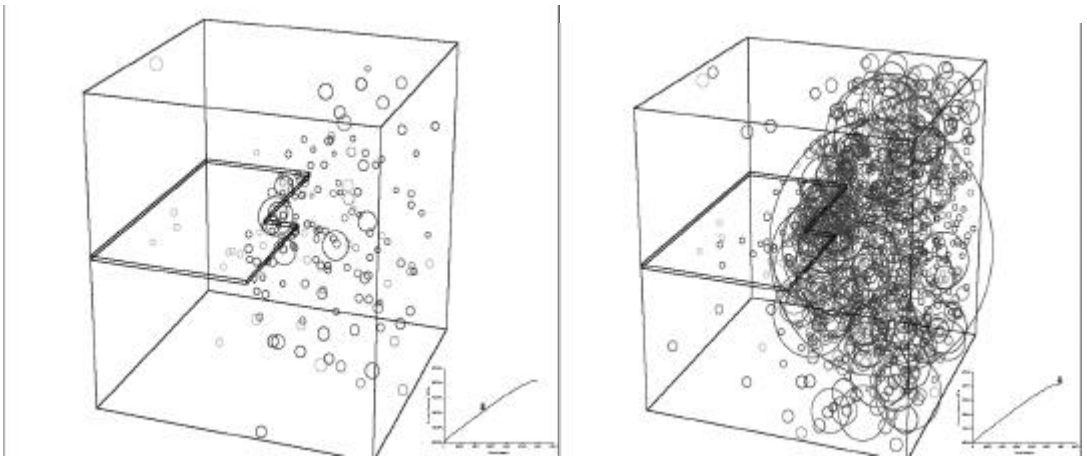

Figure 4.3.1.8. Perspective view of the PFC model indicating the cluster size and position at two stages in the model analysis. a) At about half the applied load and b) at the maximum applied load.

The equivalent energy release can be calculated for each cluster. Figure 4.3.1.9a shows the incremental energy release rate observed from the acoustic emission events in the laboratory test. Figure 4.3.1.9b shows the equivalent energy release rate for the PFC3D model. In both cases, the energy release begins to increase exponentially when the load is abot 50% of the ultimate value. Also of interest is the exponential decay in the energy release when the load is held constant at the maximum vale. The exponential decay of the number of events with time is in agreement with Omori law for aftershock frequency.

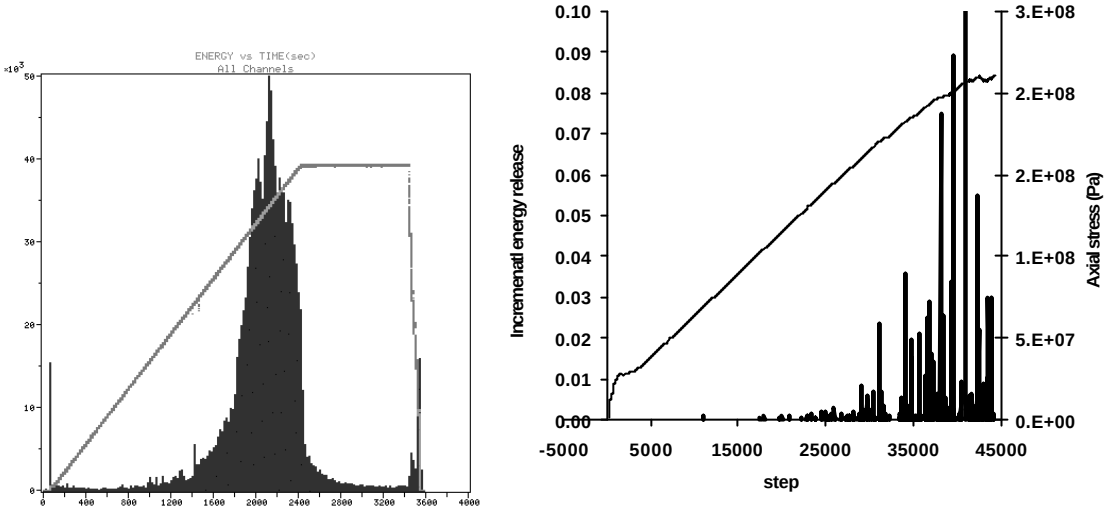

Figure 4.3.1.9. Comparison of the variation in the a) observed and b) predicted incremental energy release rates with time (steps in the model are equivalent to a time increment). Also shown is the applied stress increase with time.

The three-dimensional fracture analysis code 3DIGS has been developed to solve incremental crack growth problems using rectangular or triangular shaped elements with polynomial variation of the discontinuity values. It has been found that in most cases the classic Gauss-Seidel with SOR provides a good choice of iterative solver. A 3D tetrahedral mesh generator was developed to allow the possibility of extending the 2D tessellation method to three-dimensional problems. The implementation of this scheme has proved to be disappointing. In particular, the complexity of triangular facets can lead to severe numerical difficulties even with higher order element variations. An alternative approach has been adopted in which the possible fracture positions are generated by extending a 2D random mesh in the direction perpendicular to the plane of the mesh. Initial steps to develop an explicit crack front growth algorithm that will be appropriate for general fracture growth simulations are described in the

next section.

A number of explicit test runs have been analysed using the pseudo-3D mesh generation scheme. One series of runs has investigated axi-radial fracture growth from the surface of a borehole with encouraging initial fracture patterns. A second series of tests has been carried out to check the growth of fractures ahead of a small horizontal stope. The results of the analysis are shown in Figure 4.3.1.10. In this case, a horizontal stress of 5 MPa was applied to the vertical boundary plane shown on the right hand side of Figure 4.3.1.10 to approximate a wide span condition. The stope was modelled as a rectangular, horizontal slit adjacent to this plane with dimensions of 20m along the mining “face” and 6m perpendicular to the face. The region in which fracturing could occur was positioned to allow fracture growth over a length of 10m around the central region of the mining face. It was found that fractures initiated first from the face and then grew at a steep angle above and below the mined region. In all cases, the fractures propagated predominantly in mode III parallel to the face until terminated by the available face-parallel extent of the tessellation region. Subsequent fractures are observed to form in planes at a low angle to the stope and may be tensile in nature. These growth patterns will be different if parting planes are introduced. The general pattern of fracture development is encouragingly similar to the physical modeling results shown in Figure 2.1.3.3.

The left hand edge of the stope face shown in Figure 4.3.1.10 was extended by 1m over a distance of 10m to form a jog in the face shape. The resulting cumulative pattern of fracture growth is shown in Figure 4.3.1.11 and the incremental extent of fracturing is shown from a different view point in Figure 4.3.1.12. It was observed that the additional fracture growth initiated in the vicinity of the new face edge. Much more significantly, it can be observed in Figure 4.3.1.12 that additional fracturing was initiated ahead of the old lagging face position. This clearly presents a mechanism of face fracture growth that is not present in a 2D analysis. This analysis has significant implications for the detailed face conditions arising from lead/ lag face geometries as well as the selection sequence of stope faces that would be made, for example, for preconditioning blasts. It must be noted though that the physical modeling results shown in Figures 2.3.1.1 and 2.3.1.2 suggest that fractures form along the overall face edge but no incremental mining step was tested in this case. Fracturing along the strike direction may suppress the fracturing ahead of the lagging panel face. The mechanism identified here warrants further investigation.

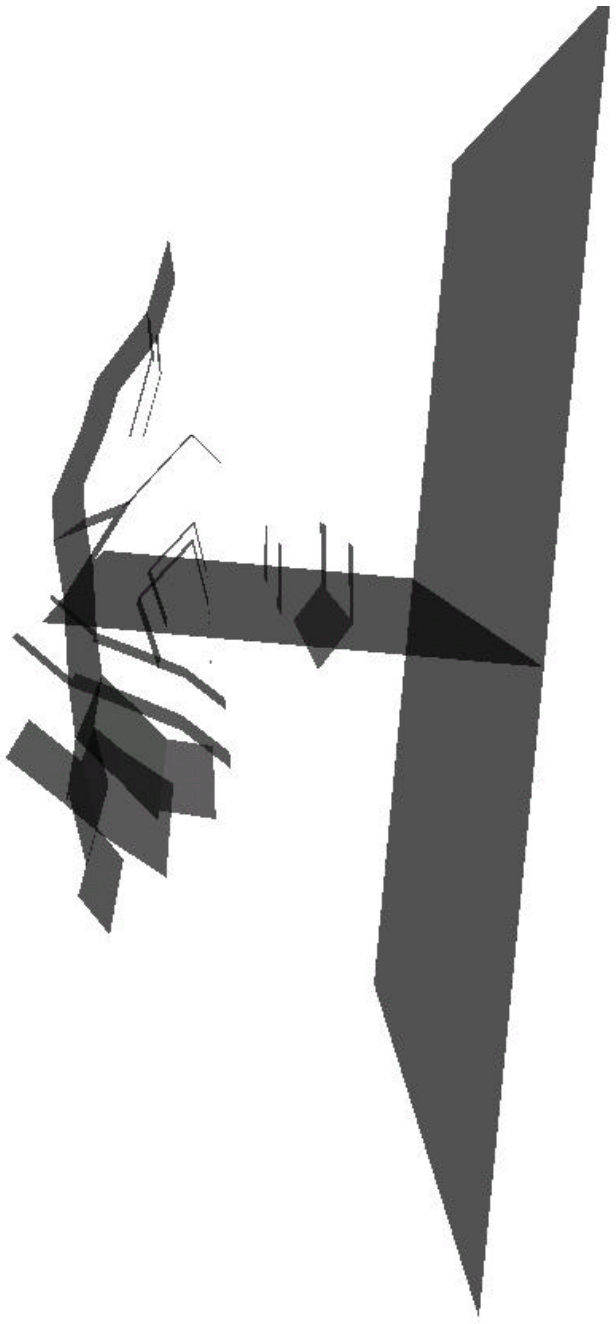

Figure 4.3.1.10 Orthographic view of fractures developed from a horizontal stope plane.

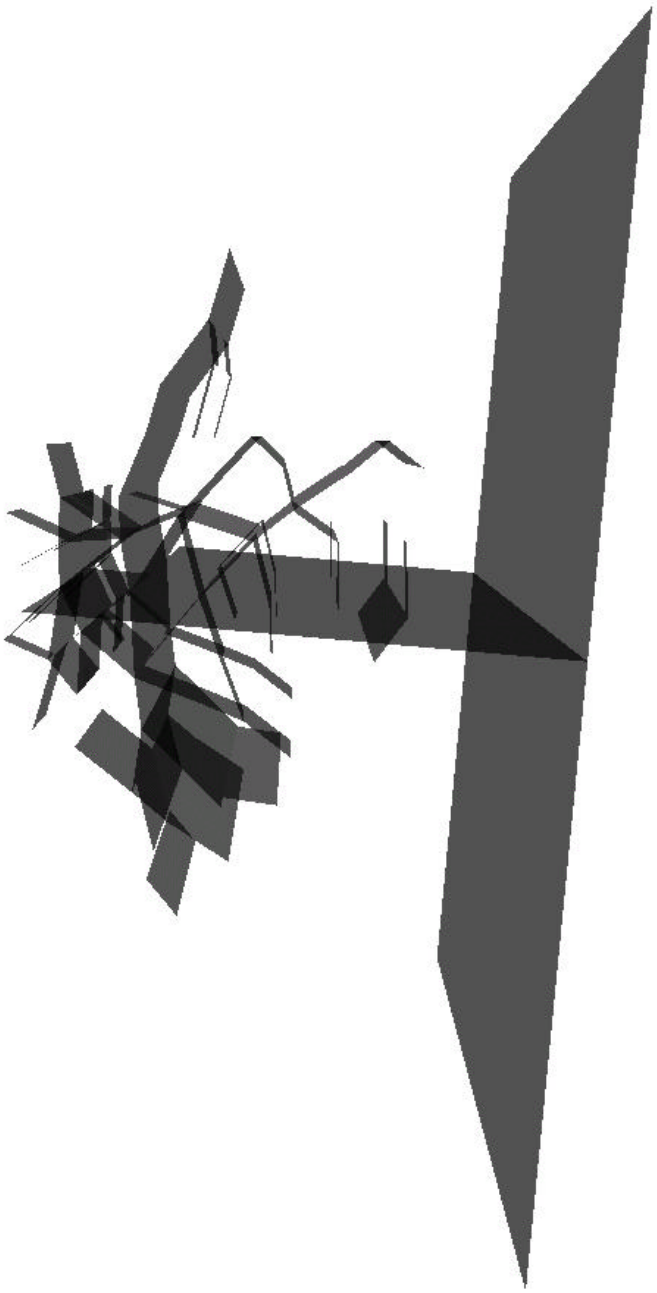

Figure 4.3.1.11 Cumulative fracture growth following an extension of one half of the stope face by 1m.

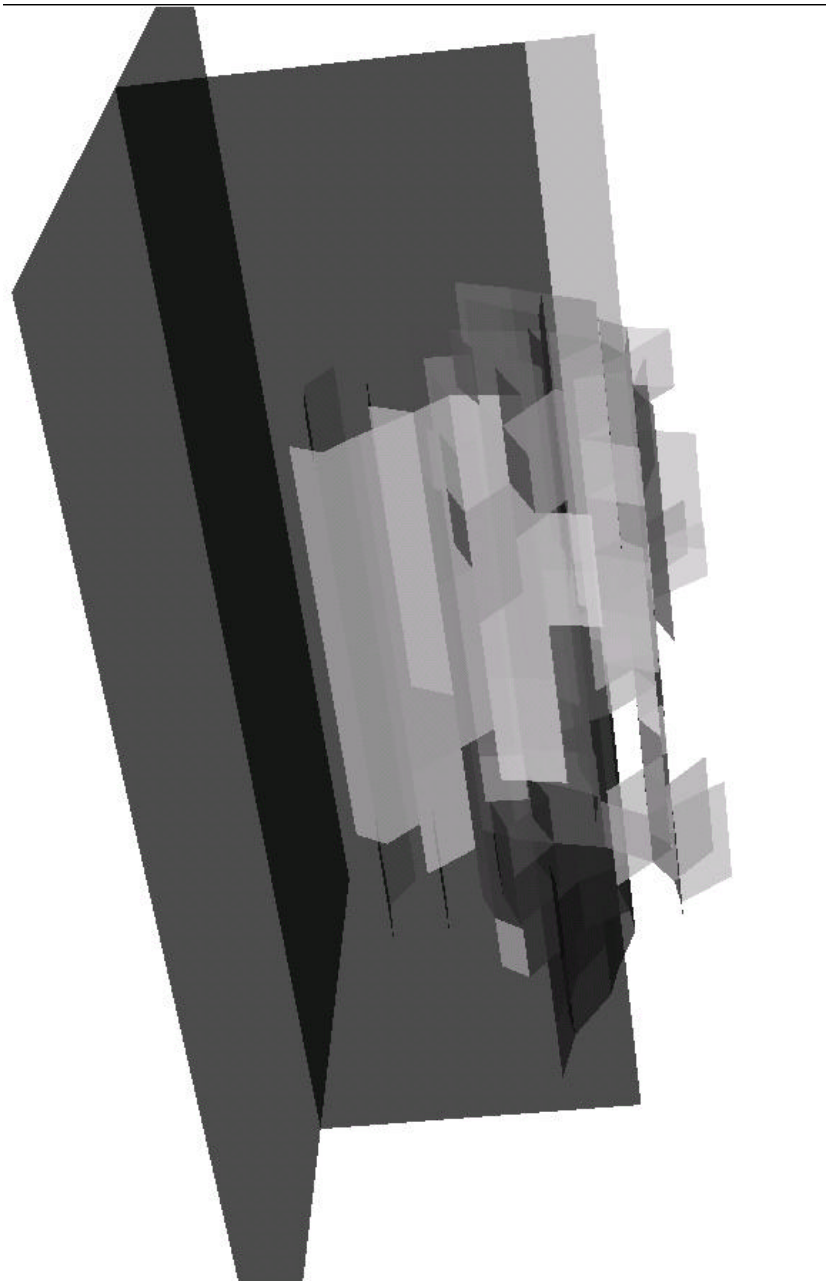

Figure 4.3.1.12 High angle view of incremental fracture growth following a 1m mining step. The mining increment is at the top right hand edge of the stope.

4.3.4 Mesh-free method for fracture propagation

In order to make progress in understanding the mechanics of complex fracture propagation processes that arise in lead-lag panel mining, fault slip propagation and blast-induced fracturing, it has been necessary to develop a conceptually new displacement discontinuity method in which crack surfaces are defined by the progressive propagation of the crack edges in space. The main feature of the new approach is that points falling on successive edge positions are used to define the topography of the crack surface rather than constructing and extending a fixed set of covering elements. This “meshless” scheme offers a number of computational advantages in providing a flexible representation for both blast-induced fracture propagation and for studies of fault rupture. However, a number of formidable difficulties remain in formulating appropriate local representations of curvilinear and intersecting crack surfaces. To provide some insight into the merits of this approach, a Phase I test code has been written to analyse, initially, fracture propagation on a flat surface. This employs local least squares fitting to evaluate the crack displacement discontinuity “shape function” at each point on the surface and a semi-analytical scheme to evaluate the local self-effect influence coefficient. Examples of the application of this approach, when tensile loading is applied in a direction perpendicular to the crack surface, are shown in Figures 4.3.4.1 and 4.3.4.2. In the first case (Figure 4.3.4.1), the initial crack outline has a re-entrant corner. Crack growth proceeds most rapidly from this corner as would be expected. Simple rules are used to control the spacing of the marker points along the crack front. These include the ability to introduce additional points or to eliminate points when the spacing becomes too small. In the secaond example, shown in Figure 4.3.4.2, the crack is arrested by an “asperity” at position (10, 0) that is modelled as a local region of high compressive stress normal to the crack surface. The momentary interruprion of the crack front and subsequent growth advance is illustrated in Figure 4.3.4.2.

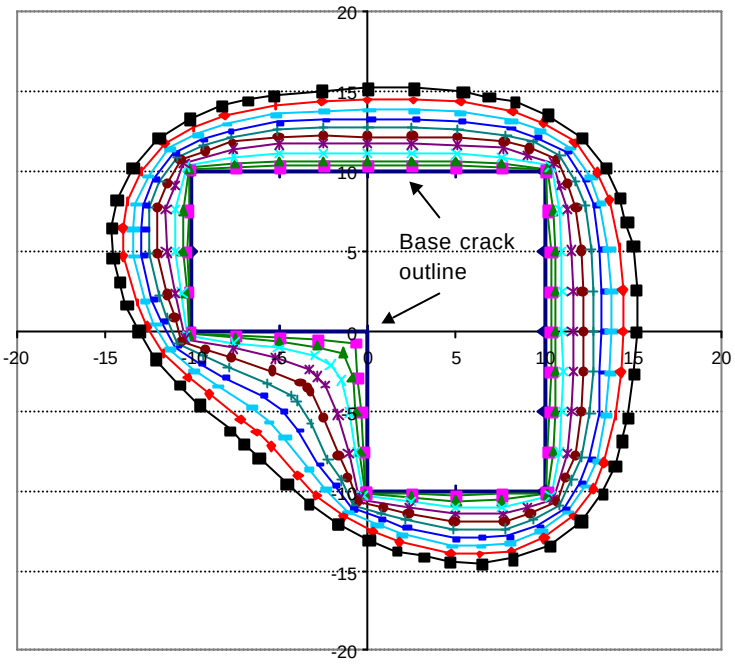

Figure 4.3.4.1 Illustration of fracture propagation under tension from an initially re-entrant crack.

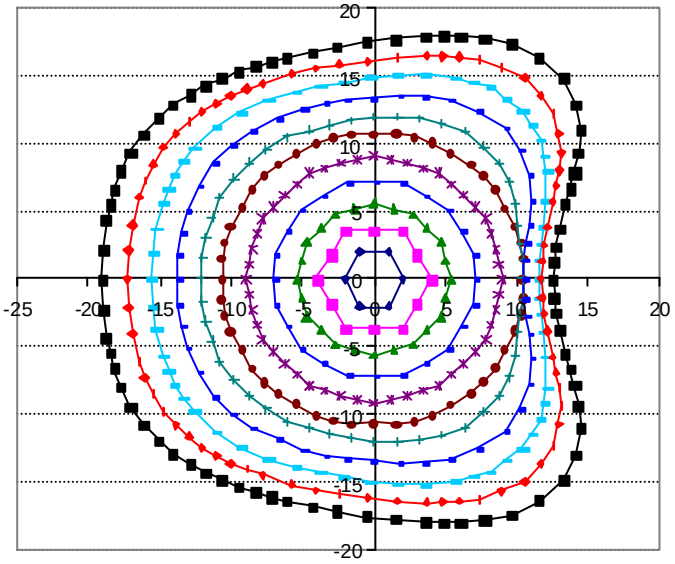

Figure 4.3.4.2 Fracture propagation past an asperity illustrating the progressive crack front evolution.

4.4 Modelling of blast-induced fracture propagation.

4.4.1 DIGS model with simplified pressure distribution

Blasting is the most widely used method for deep level tunnel development and stope excavation. The blast has a considerable effect on the response of the rock mass. This can be seen in the way that the seismicity observed underground is strongly correlated to the time of the blast (e.g. Stewart and Spottiswoode, 1993). The stope exhibits a considerable amount of closure in a very short time due to the rapid removal of the rock in the region ahead of the face (Malan, 1998). The blast imparts considerable energy into the rock mass in order to break the rock, but some of this energy may be diverted into dynamic waves that travel through the rock mass and can cause spalling at exposed faces. Blasting may cause additional fracturing that may damage the rock and alter the stability of the hangingwall (Brost, 1970).

The blast involves a number of coupled physical processes that involve the high-pressure response of the rock including the effect of the thermal gradients induced by the explosive and penetration of gas into the fractures. High pressures and rapid fracture propagation cause the rock to be thrown some distance at high velocities. The main questions that arise in dealing with blast modelling relate to the choice of the most efficient method of modelling the process of explosive detonation and the subsequent fracture propagation. The explosive and detonation processes are not considered here as the main objective is to evaluate and predict the effect of the growing cracks.

Simple models of blast fracturing were developed for the DIGS boundary element program and were presented in Project GAP 029. These have been updated to consider more realistic data for the relationship between the explosive pressure and the borehole volume. The extent of gas penetration into the fracture has also been considered, by using a simple approximation. During the explosive detonation, gases are generated that apply pressure to the borehole walls. The simplest model for gas behaviour is the ideal equation of state

$$PV = n\,RT \qquad (4.4.1.1)$$

where P is the pressure, V is the volume, n is number of moles of gas, T is the temperature and R is the ideal gas constant. However, most gases are not ideal and can be better described by the BKW equation of state that is expressed as

$$PV = nRT(1 + xe^{bx}) \quad where \quad x = \frac{k}{V_g (T + q)^a} \tag{4.4.1.2}$$

and the x is calculated for each gas produced by the explosive reaction. This can be difficult to determine, as the composition of the explosive is often a trade secret for the particular explosive manufacturer. This equation is therefore developed from empirical evidence based on actual explosions performed in a steel cylinder confined by a piston. The measurement of the pressure and the expansion of the piston leads to an equation for the pressure decrease with relative expansion of the volume. Simple models have been developed to estimate the detonation pressure when the gas products are unknown. The detonation pressure P_d can be estimated from

$$P_d = \rho_o D^2 / 4 \tag{4.4.1.3}$$

where ρ_o is the initial density of the explosive and D is the hole diameter. A more complicated equation of state, based on the Mie-Gruneisen equation was developed by Heuze (2001). This states that

$$\begin{aligned} P(V,E) &= P_k(V) + \frac{\Gamma(V)}{V}[E - E_k(V)] \\ E_k(V) &= y\left[l\left(\frac{\rho}{\rho_r}\right) + m \ln\left(\frac{\rho}{\rho_r}\right)\right] \\ P_k(V) &= \Gamma \rho E_k(V) + \rho y\left[l\left(\frac{\rho}{\rho_r}\right) + m\right] \end{aligned} \tag{4.4.1.4}$$

and implies that the pressure P is a function of the internal energy E, the relative density ρ / ρ_r and a number of material constants that can be relatively easily obtained from experimental results. Other important considerations are the amount of tamping and the time for the tamping to be expelled. The gas flow is not one-dimensional and gas will flow towards the excavation limiting the gas pressure and penetration. The effect of the momentum imparted to the rock mass should also be considered when determining the crack opening volume as the model must be able to consider the dynamics and interactions of the expanding region of fractured rock.

The DIGS boundary element program (Napier and Hildyard, 1994) was modified to be able to model blast fracturing in a quasi-static manner. The DIGS code requires that boundary elements are placed along the borehole and excavation boundary. The user places seed point at the sites of potential cracks. The program calculated the stress state surrounding the seed points and if the stress is greater than the tensile strength, the program inserts a new fracture element in the

direction of the maximum tensile stress. Thus, the growth of fractures can be explicitly modelled. The time increment Δt is related to the change in crack length ΔL and the crack velocity c_v as

$$\Delta t = \frac{\Delta L}{c_v}$$

The crack velocity can be related to the P-wave velocity c_p by the relationship

$$c_V = 0.38 c_p ,$$

developed from experimental evidence by Bieniawski (1967).

Blast modelling was performed by Turner as part of SIMRAC project GAP 029. In these models, only the borehole was pressurised and the effect of far field stress anisotropy was studied. Considerable attention was given to the development of a blast model that included gas pressure effects in the SIMRAC project GAP 332. An analytical model was developed by Daenkhe et al. (1996), based on the model originally developed by Nilson (1981). The model predicts the growth of a penny shaped crack from a single borehole and produces pressure profiles of the gas penetration as a function of crack length. An enhanced model (e.g. Daenkhe et al, 1996) also considered the effect of different thermal models on the thermal energy losses into the rock and the extent to which the gas will penetrate into the crack. Based on these results, an approximate model of blast fracturing parallel to the axis of the shothole (axi-radial fracturing) was proposed to obtain estimates of the fracture extent as a function of the mass of the explosive charge.

As part of the current project, the original DIGS program was modified to permit a semi-coupled analysis with a simplified gas pressure distribution. The approach is indicated in the flow diagram of Figure 4.4.1.1. The boundary elements provide a convenient way of applying and modelling the blast gas pressure penetration along the fractures. The gas pressure is applied as a pore pressure to each crack element that connects to the borehole. However, as the boundary element code considers each element separately, additional data structures were needed to associate elements with a specific borehole and blast model.

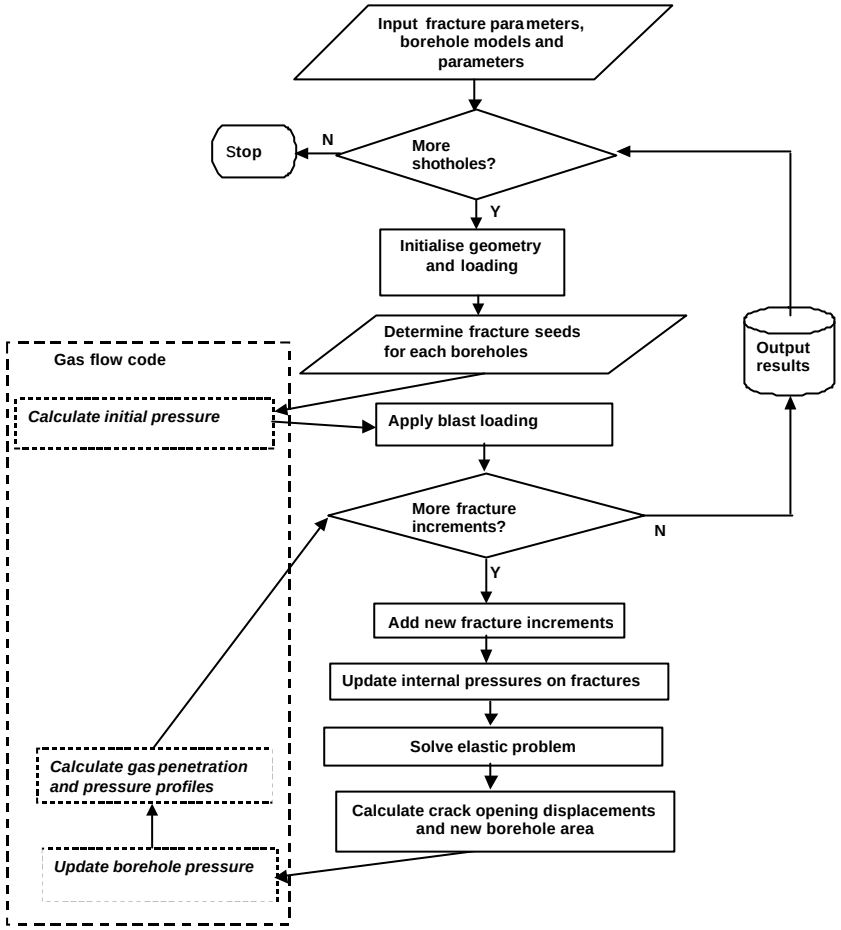

Figure 4.4.1.1 Flow chart of DIGS code with semi coupled gas flow calculations

Two different assumptions of the borehole and crack pressure distributions were compared. The first was developed by Swenson and Taylor (1983) as a simplification of the analytical solution of Nilson (1981). The Swenson-Taylor model prescribes that the pressure in the borehole decreases linearly over a specified time. The penetration of gas into the crack is assumed to follow a simple rule that requires the specification of the pressure in the cracks as a fraction of the borehole pressure and the fraction of the crack length that the gas will penetrate. The gas pressure is assumed to remain constant throughout the pressurised length of the crack.

The formulations by Nilson (1981) and Daenkhe et al (1996) provide more complex solutions for the pressure distribution in the crack. An assumption that is intermediate between the Swenson Taylor model and the Nilson/Daehnke model is to simplify the relationships between the pressure distribution and the crack length as presented by Nilson (1981) so that the gas pressure reduces linearly to zero along the crack. These semi-analytical models could be coupled to the DIGS code but this has not been done due to time constraints.

As an alternative to the linear pressure decrease in the Swenson-Taylor model, empirical distributions of borehole pressure against relative volume were provided by Cunningham (2002) for different explosive types. The data are shown in Figure 4.4.1.2 along with some power laws fitted to the curves to facilitate implementation in the DIGS model. Note that although the R^2 values are high, the curves are bilinear in log-log space, which is why the trend lines do not fit the curves well when the a relative volume exceeds 2.5. The DIGS program was modified to be able to use these models by considering the volume of cracks being formed. In addition, the borehole data structure had to keep track of the crack segments that were associated with each borehole. The borehole area is represented as a polygon comprising a connected sequence of the relevant elements, taking into account the expansion of the borehole due to the pressurisation. The increase in crack volume is accounted for by integrating the crack opening displacement over the pressurised region of the cracks.

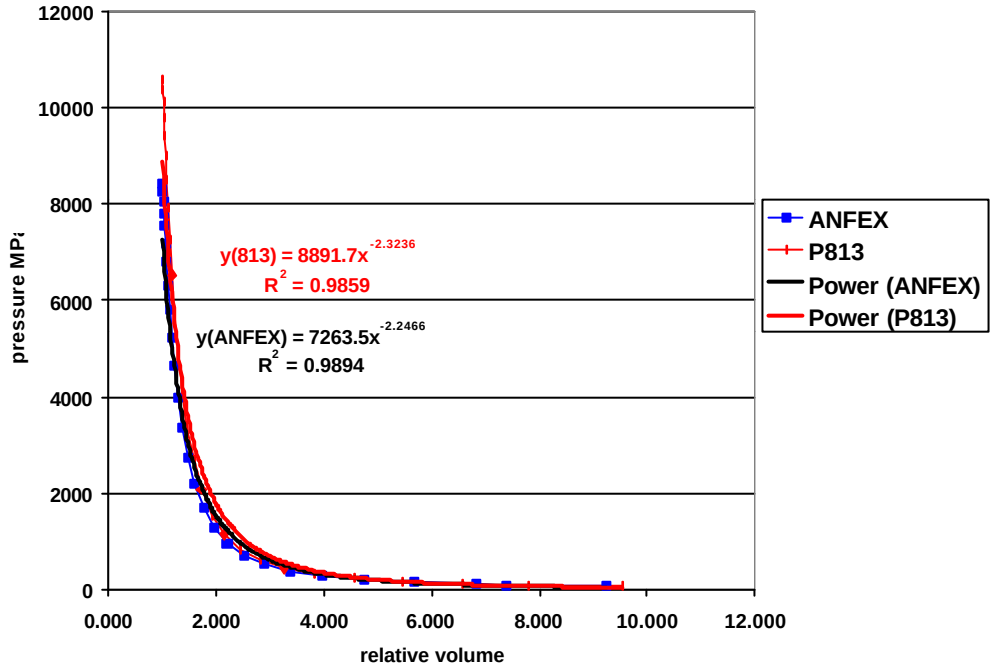

Figure 4.4.1.2 Generic pressure – relative volume curves for two explosive types.

The pressure time curve obtained from a DIGS analysis is shown in Figure 4.4.1.3. There is an overall decrease in the pressure as the cracks extend. However, unexpected oscillations occur in the pressure – time response, because the elastic rock mass acts to close the fractures. When the borehole pressure is lower than the in situ stress, the cracks close, the relative volume decreases and the pressure increases.

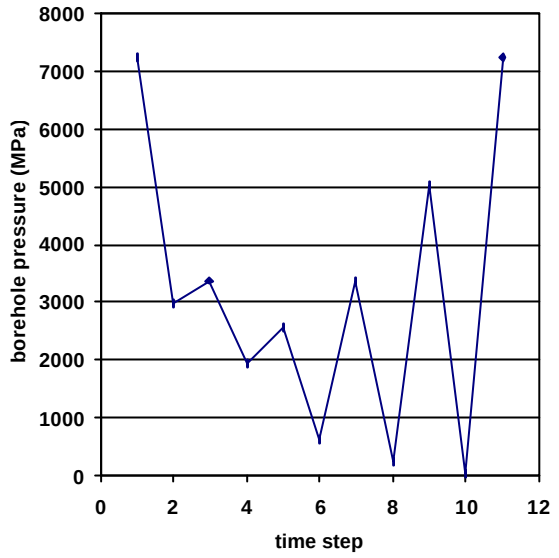

Figure 4.4.1.3 Pressure time curve for DIGS model with borehole pressure calculated from empirical data

The correct solution would be to couple the DIGS program with a gas dynamics code to properly consider all the possible interactions of the blast gases and the expanding cracks. These effects should include consideration of the different crack lengths, the borehole, the pressure drop from the borehole into the cracks, the flow of gas in two dimensions inside the expanding fractures, the flow of gas into pre-existing fractures, the change in borehole volume due to the expulsion of the tamping and the fragmentation of the rock mass. For example, Brinkman (1986) reports that 90% of the gas escapes through the hole collar, and the rest through cracks in the burden rock. Brinkman and Gibson (1985) report that blast gases vent from pre-existing fractures within one millisecond of the blast. All these effects are three-dimensional in nature and can only be considered once the three-dimensional version of the code (3DIGS) is available.

Observations of blast induced fractures in low stress situations or regions of hydrostatic stress distributions show that the fractures extend radially from the shot hole. The length of the fractures is approximately constant in all directions. Underground observations in deep level mines indicate that the majority of fractures extending from the shothole grow towards the maximum compressive principal stress (Turner, 1995). The fractures can extend as far as one metre from the shothole. When the minor principal stress is less than the major principal stress, the fractures growing towards the minor principal stress are suppressed. These fractures seldom grow more than four diameters from the shothole. In addition, predictions using simple DIGS modelling and the underground observations showed that cracks from a previous shothole may be reactivated and extend in another direction, towards a subsequent blast.

A DIGS model with the Swenson –Taylor gas pressure law was constructed to evaluate the effect of a production blast on the fracturing in a stope face and hangingwall. The model was based on the guidelines for blasting in narrow stopes that suggest that the holes should be positioned about 0.15m from the hangingwall and the footwall and the spacing between blastholes should be about 0.5 to 0.6m.(Brinkmann et al, 1990). The model, shown in Figure 4.4.1.4., represents a dip section through the rock mass just ahead of the face with the stope assumed to dip at 20^{o}. The vertical free face indicates where the rock ahead of the face has been removed by the ignition of the previous set of shot holes. The example with the higher blast pressure, shown in Figure 4.4.1.4a, demonstrates that the fractures are controlled initially by the stress field of the blast and grow radially from the shothole, until the pressure has dropped and the fracture directions are controlled by the stress state surrounding the free face. When the blast pressure is low, the fracture directions are controlled by the existing stress state as shown in Figure 4.4.1.4b. The blast generates fractures in the hangingwall that grow towards the shothole. The position and direction of these fractures is influenced by the blast pressure, duration and the position of the shothole. Thus, the stability of the fractured hangingwall is affected considerably by the blasting. The amount of gas penetration into the mining induced fractures and pre-existing discontinuities will also affect the hangingwall stability.

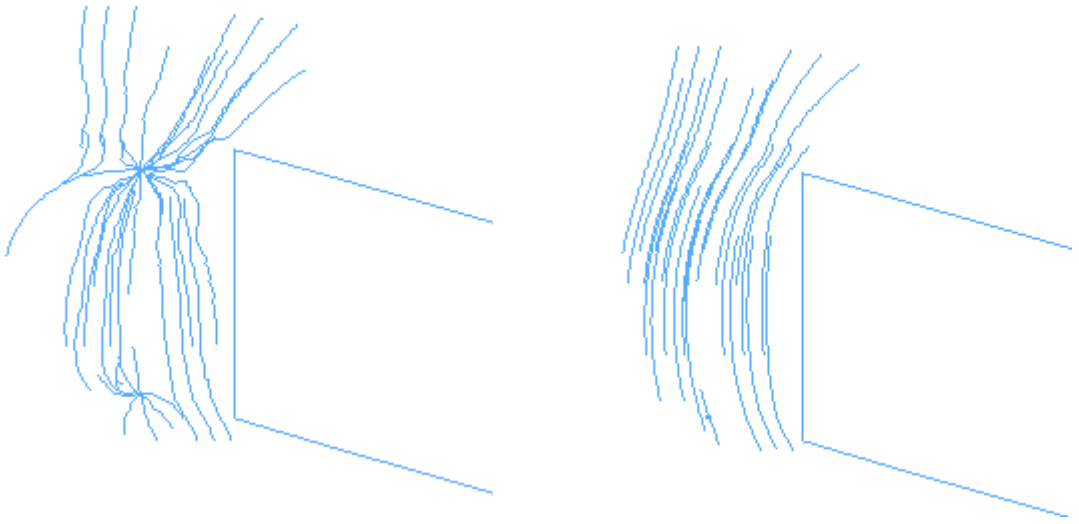

a b

Figure 4.4.1.4 Fracture formation around a production blast for a) 1000 MPa blast pressure and b) 40 MPa initial blast pressure

Pre-split blasting and smooth wall blasting are two important methods that are used to control the profile of a tunnel. Smoother sidewalls are important for improving the effectiveness of support and for reducing the potential for unravelling of the rock mass during seismic events (Brost, 1970). In both techniques, the explosive is decoupled from the borehole by reducing the diameter of the explosive charge. In smooth wall blasting, the explosive will have a diameter of

about 1cm (Turner, 1995). The holes are spaced more closely (usually about 300mm apart) and are drilled with more precision that the holes for the burn cut that removes the majority of the rock in the central portion of the region to be excavated. The effect of smooth blasting can be simulated using the DIGS model and the P-V/Vo blast model. Consideration of the pressure – relative volume relationship in Figure 4.4.1.2, indicates that the increase in equivalent area from a 25mm diameter explosive to a 38mm hole results in a relative volume change of about 2.3 times. This would lead to a reduction in pressure from 8400 MPa to 800 MPa for the ANFEX and from 10 000 MPa to 400 MPa for the P813 explosive. Crack growth will reduce these pressures even further. Thus, in a similar way to the fracturing pattern shown in Figure 4.4.1.4b, the fracturing due to the decoupled explosive would be more constrained by the *in-situ* stress state than by the borehole pressure. The fracturing would tend to follow the curve of the opening creating the required smooth surface.

Preconditioning has been investigated as a proactive method for reducing the potential for rockbursts in mines and has proved to be successful in narrow tabular stopes (Adams et al, 1993, Rorke and Brummer, 1990). The method relies on additional blasts within the fractured ground ahead of the face to induce slip along pre-existing fractures and hence transfer stress away from the working face (Kullmann et al, 1996). Preconditioning has been shown to create a well-defined hangingwall surface. The method is currently being extended to consider wide reef stopes in SIMRAC project GAP 811. A simple example of blasting in a wide reef stope was investigated with DIGS, using the Swenson Taylor gas pressure model. The crack velocity was assumed to be 2000m/s and the gas pressure as assumed to last for 250 milliseconds. The initial borehole pressure and the position relative to the hangingwall were varied. The properties of the hangingwall were also varied. Fracture patterns for different pressure profiles are shown in Figure 4.4.1.5.

Figure 4.4.1.6 shows how the different blast parameters induce slip along the hangingwall parting. The parting was assumed to have no cohesion and a friction angle of 35 degrees. The amount of slip depends on the borehole position, the borehole pressure P, the percentage of the pressure that enters the fractures (%P), the gas penetration along the fractures (%L) and the percentage of the blast duration (%T). The amount of slip on the parting palne is very sensitive to the specified cohesion. A higher initial gas pressure and greater gas penetration is required if the borehole is positioned further away from the hangingwall parting. More extensive fracturing occurs as the pressure increases.

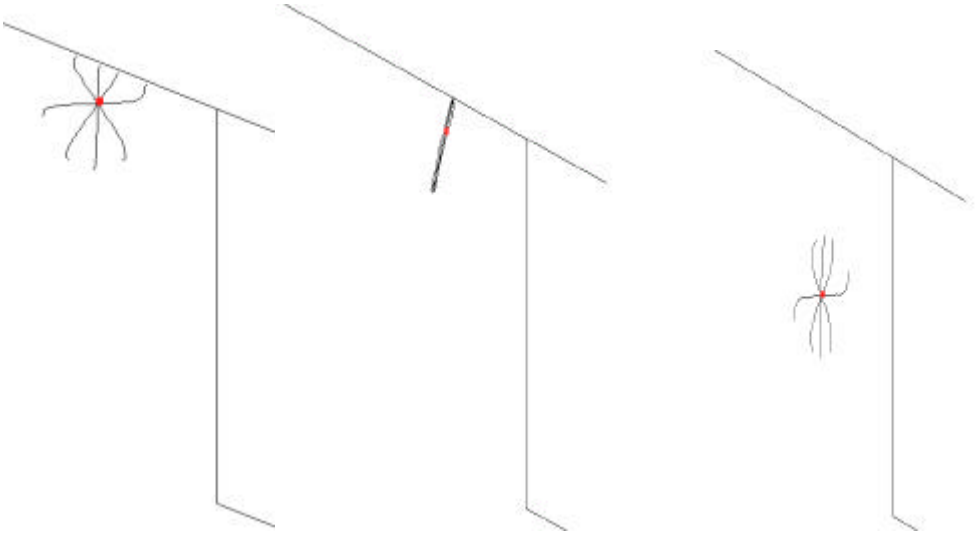

a b c

Figure 4.4.1.5 Effect of blast pressure and shothole position on fracturing due to preconditioning blast with a) 1000 MPa at 300m from the hangingwall, b) 100 MPa at 300mm from the hangingwall and c) 1000 MPa at 1.5m from the hangingwall

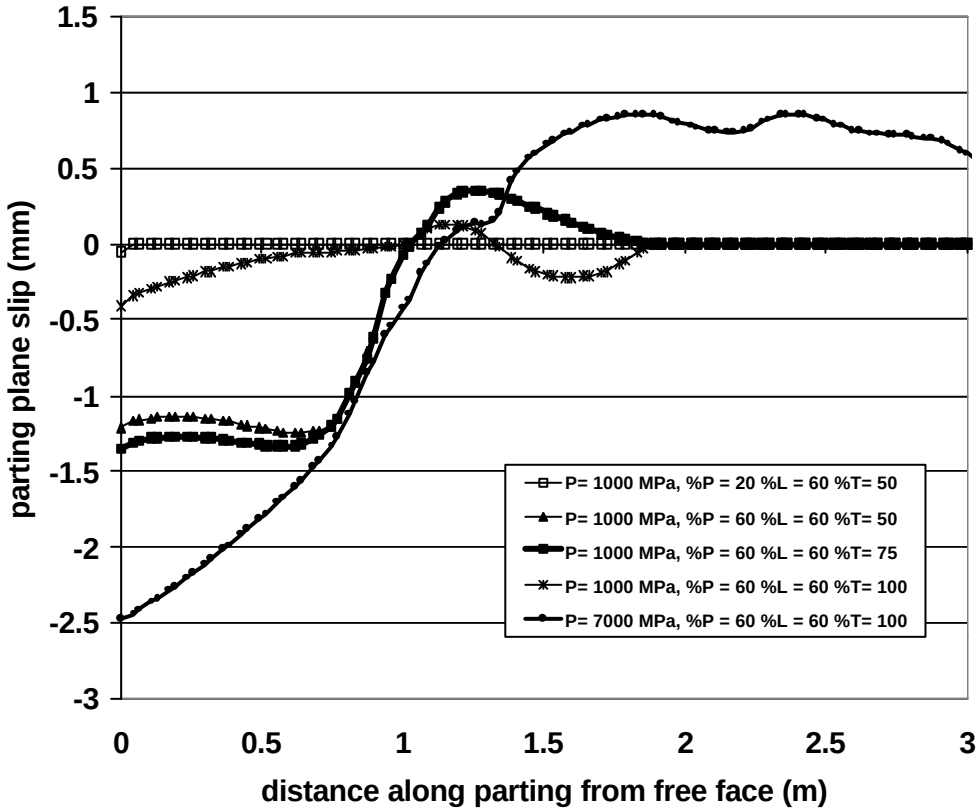

Figure 4.4.1.6 Effect of blast pressure and gas flow model parameters on the slip on the hangingwall parting. All boreholes 300mm away from the hangingwall.

An initial attempt was made to simulate three-dimensional blast-induced fracturing from a short shot-hole using the 3DIGS program. Figure 4.4.1.7 shows the fracture pattern that develops within a tessellation mesh comprising rectangular, flat elements surrounding the hole. The primitive stress field was assumed to have vertical and horizontal compressive components of 80 MPa and 40 MPa respectively. A pressure of 500 MPa was applied to the surface of the borehole to simulate the stress induced by the explosive charge. All fractures are constrained to grow in directions that are sub-parallel to the axis of the borehole. In this study, fracture growth was simulated by examining each element in the tessellation mesh in turn and determining the total tensile stress normal to the element surface. These stresses were evaluated at four points (collocation points) within each element. The element having the highest tensile stress was introduced as a new growth increment. It was observed that fractures grew initially along the length of the hole and subsequently extended away from the hole surface. The fracture pattern (see Figure 4.4.1.7) shows clearly that the growth direction is predominantly in the major (vertical) stress direction as observed in practice.

The three-dimensional model described here is clearly very simplistic. The run time efficiency is currently low (the simulation with about 80 incremental crack growth steps required approximately one hour on a 450 MHz desk top computer). Further development of the 3DIGS code is required to allow more flexible growth patterns and fracture intersection features.

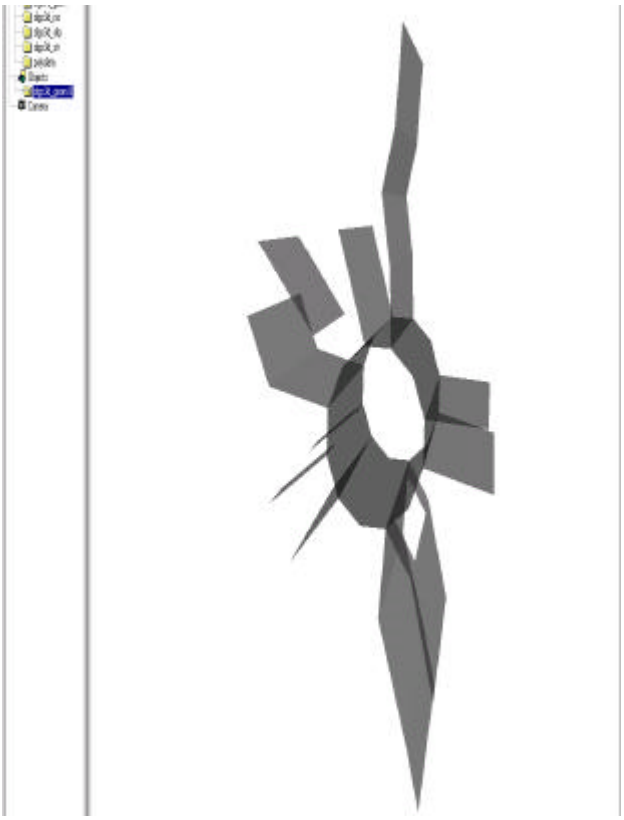

Figure 4.4.1.7 Three dimensional fracture pattern obtained from 3DIGS model.

5.0 Conclusions

Extensive laboratory experiments were carried out to study the creep behaviour of quartzite and lava rock specimens in compression. For a given stress level, close to the peak strength, the axial and lateral creep rates of the quartzite are orders of magnitude greater than the axial and lateral creep rates of the lava at an equivalent stress level. Since the strength of lava is more than twice as high as that of the quartzite, the strain at failure of the lava is more than that of the quartzite. It is also observed that the onset of unstable fracture propagation for lava occurs at a higher ratio of the applied stress to the rock strength than for the quartzite. This implies that in lava there is more energy available for violent failure than in quartzite and, consequently, a rockburst in lava is perceived to be more violent than a rockburst in quartzite.

Further laboratory experiments were carried out to quantify the time-dependent characteristics of shear-loaded discontinuities. Most experiments display a characteristic behaviour in which the slip resistance appears to increase as the joint shear displacement is increased for both filled and unfilled joints. The test results also show that the shear creep mechanism is governed by the ratio between the thickness of the infilling and the grain size distribution of the infilling as well as by the moisture content of the infilling. It was found that this behaviour could be described by a simple constitutive model in which it is assumed that the friction builds up as a function of the amount of shear slip over a given critical slip distance. This model was implemented in the DIGS computer code was and found to be able to reproduce the observed laboratory results of time-dependent slip resulting from step increases in applied shear stress.

Tests were also carried out to quantify the post-failure relaxation behaviour of specimens of quartzite and lava subjected to confined loading and a fixed displacement of the axial loading platen. It is concluded that the post-failure relaxation times for hard rocks under a high confinement are orders of magnitude greater than the relaxation periods for softer rocks under uniaxial compression conditions. In the mining context, this implies that the state of confinement plays a strong role in determining how much strain energy will be stored in the rock mass. Comparing the behaviour of quartzite and lava, the test results show that during a relaxation period of 24 hours the total stress relaxation for the failed quartzite is approximately twice that of the failed lava. The relaxation rate in the subsequent time period is more than three times higher for the quartzite than for the lava. The quartzite shows a well-developed fracture pattern while the lava shows only a few cracks, i.e. the damage to the lava is significantly more localised than the damage to the quartzite.

Acoustic emission (AE) in tests were carried out on loaded rock samples. In this study, it was established that a frequency magnitude relationship holds with a b- value close to unity. These results are similar to those observed from mining induced events and provides objective evidence that rock fracture processes observed in the laboratory are relevant to the understanding of mining induced fracturing and seismicity. Although some authors have suggested that earthquake self-similarity can break down at very small magnitudes, the present study seems to suggest that self-similarity still holds for very small magnitudes and that the AE processes on a localised fracture plane scale in a similar way to mining induced earthquakes and natural earthquakes.

Loading tests were carried out on cube-shaped samples, containing stress-raising slots, in order to study the formation of three-dimensional fracture structures. Different slot shapes were studied to determine the effect of geometrical perturbations analogous to lead-lag longwall panel layout geometries. Medical X-ray tomography was applied to reconstruct a digital representation of the three-dimensional fracture surfaces formed in the samples. The observed fractures tend to follow a uniform two-dimensional pattern in section, when there is no lag between the simulated panels. When a lead-lag jog is introduced along the edge of the slot, the fracture surface is observed to follow the edge of the slot in the centre of the sample. As the distance from the plane of the slot increases, the surface becomes s-shaped. It is also observed that the fracture curves below the leading panel, especially in the region adjacent to the other panel. In the underground situation, this would represent a great hazard. Due to the relatively low dip of the fracture at this point, the process of fracture formation and any subsequent slip displacement in this region would transmit seismic waves directly upwards at the edge of the panel and the gully with a consequent risk of injury or loss of life**.**

Underground experimental work was carried out to investigate the time-dependent “unravelling” of the stope hangingwall and the effect of mining rate on the occurrence of falls of ground. At a site on the Vaal reef it was observed that the hangingwall-parallel stresses appeared to decrease as a function of time. Data from extensive time-dependent closure and face advance measurements have also been used to assemble an empirical model that can be calibrated to represent the functional dependence of stope closure on the face advance rate and on elapsed time from the initial mining of a given position in the stope. This relationship provides a practical input for the evaluation and design of support equipment.

The assessment of stope face stability forms a vital theme in fundamental studies of the stope fracture zone. Some simple models of stope face fracturing were examined to clarify the role and meaning of stope face stiffness. It was demonstrated how the presence of a fault could lead to a degrease in stiffness as the stope approached the fault. In order to “sense” the proximity of

the fault to the mining face it is useful to monitor trends in the rate of stope closure and to track trends in the face “stiffness”. More generally, it has been shown that if a time-dependent slip model can be used to describe the movements on a set of interacting discontinuities, it is possible to analyse the stability properties of the system in terms of the eigenvalues of the governing matrix. Although the eigenvalue analysis provides an elegant tool for the instantaneous analysis of the system evolution, it is apparent that if an assembly of cracks is analysed in which the number of elements in the system is increased progressively, according to specified growth rules, the instantaneous stability can fluctuate depending on the specific configuration of the element population at any given time. If the elements are drawn from a random mesh assembly, it can be expected that the accompanying energy release cycles may behave in a manner that is analogous to observed seismic activity.

A number of numerical studies were performed to clarify whether it would be feasible to predict the time of failure of a stressed sample as a prototype problem to prediction of unstable rock failures at the stope scale. The main conclusion from these experiments is that the observed energy release (seismic) signals did not yield clear-cut patterns preceding the failure time. A more detailed knowledge of the distribution of damage in the material is required to identify the onset of sudden failure. One measure of this damage is the frequency distribution of damage cluster sizes in a given region of interest as possibly evidenced by the spatial distribution of seismic activity near the stope face. The hypothesis that still has to be tested is whether the emergence of a connected region of damage occurs just prior to the time of occurrence of a major event.

The spatial variation in Shore hardness has been applied for a statistical evaluation of the variability of rock properties for four rock types at the laboratory scale. The implication of these studies is that the rock behaviour is controlled by variability that occurs on a relatively small scale depends on the relationship of the sample size to the grain size distribution. The study illustrates that the inherent variability in different rock types can be quantified and should be accommodated in numerical models. Numerical models of the large scale rock mass must consider these small scale variation, as well as the variations such as veins, joints and faults that exist on intermediate scales.

A combined meshed/meshless methodology was developed that incorporates meshless representation of slip and fracturing on multiple interacting discontinuities using point kernel approximations of displacement discontinuity influences combined a with standard boundary element based mine planning software. The point kernel approach has shown that large numbers of faults and discontinuities can be considered in a single analysis. However, care is required in positioning of the elements as the stress singularities induced by the point or

constant elements may result in overestimates of the extent of failure. The ability to input a statistical distribution of input data for the position and properties of geological discontinuities implies that the point kernel method could provide a good starting point for the application of reliability based procedures in the design of tabular openings at depth and for calculating the risk related to seismic events.

Slip and tension weakening models were formulated and implemented in the DIGS code in order to allow the simulation of scale effects. Attempts were made to calibrate these models using reported experimental data. The slip and tension weakening behaviour was found to provide a partial explanation to the observed behaviour. A more important application is to the evaluation of the stability of mine layouts. This in turn suggests a possible criterion that could be used to evaluate the relative stability of competing layouts. In this procedure, the slip weakening parameter is varied in a series of simulation runs for each layout to determine a lower bound to the weakening parameter at which a large-scale instability, such as foundation failure, will occur. The layout having the largest value of critical slip weakening is the deemed to be the most stable. Further studies on the merits of this criterion would have to be pursued.

Numerical studies of three-dimensional fracturing near lead-lag stope panel geometries were initiated using several computer codes. These included the finite element code ELFEN, the particle flow code PFC3D and the boundary element code 3DIGS. Certain difficulties were encountered in each case although the ELFEN code yielded some qualitatively satisfactory results with rather diffuse damage localisation. Results from the PFC3D analyses also displayed very diffuse failure regions. The 3DIGS code, applied within a restricted random mesh showed fairly coherent localisation of fracturing but is currently unable to analyse full spatial fracture growth simulations. An interesting result suggested by the 3DIGS analysis is the formation of additional fracturing ahead of the lagging face position, after the leading face is advanced. This clearly presents a mechanism of face fracture growth that is not present in any 2D analysis and has significant implications for the detailed face conditions arising from lead/ lag face geometries as well as the selection sequence of stope faces that would be made, for example, for preconditioning blasts. However, fracturing along the strike direction, which could not occur in the 3DIGS analysis, may inhibit the formation of fracturing ahead of the lagging panel face. The mechanism identified nevertheless warrants further investigation.

Extensive studies of wave propagation through fractures and the interaction of seismic waves with excavations were carried out. An overview of the literature identified a number of deficiencies in previous attempts to simulate wave propagation around underground openings – in particular a lack of direct comparison with waveforms collected near the surfaces of real openings, and hence the lack of evidence that numerical models can reproduce such wave

behaviour accurately. Models were constructed of real events and these simulated waveforms were compared directly against those measured. There is a sufficient correspondence in the waveforms to indicate that the simulations approximate real wave behaviour. Detailed comparisons, however, showed mixed results, with some models producing good fits and others corresponding poorly. Not all differences reflect on the accuracy of the models, but on the lack of good measurements, uncertainty in the source, and current computational limitations. Specific studies included the analysis of observations of wave propagation from a simulated test blast near a cross-cut in a deep level gold mine and analysis of field data made available from a detailed investigation of wave propagation effects near the surface of a deep level tunnel in Canada. (The Underground Research Laboratory (URL) sponsored by the Atomic Energy Corporation Limited in Canada).

These studies indicate the numerical feasibility of modelling waves around underground openings provided that the numerical grid is sufficiently refined, which requires many millions of elements. While the studies were made at different scales, even the small scale URL experiment provides information that is relevant to larger scale problems – i.e. a maximum frequency of 100 kHz in a 1 m cube, is self-similar to 1 kHz in a 100 m cube, which is the appropriate frequency range for many practical mining problems.

Comparison of numerical models with reliable measurements of ground velocity in relatively unfractured ground emphasised the need to incorporate the effect of fracturing to reduce the discrepancies between modelled and observed amplitudes and wave-speeds.

Mechanisms leading to amplification of particle velocities were studied in detail. Models showed that one mechanism, which leads to the apparent amplification of particle velocities, is simply the propagation of surface waves along the excavation free surface. In the models, the presence of an excavation could cause an increase of up to fifty percent in ground velocities near the stope and up to a six fold increase for more distant positions in the stope.

Although considerable attention has been directed previously to the estimation of peak ground velocities, it was also found that the tensile stress induced by a seismic event can be many times larger at the free surface of an excavation than in the solid, both at positions close to the source and at more distant positions in the stope. This effect is important for understanding the damage caused by rockbursts.

Aspects of Rayleigh wave propagation were studied, such as the decay of different components of velocity and stress with distance from the free surface. The Rayleigh wave amplitude decays from the surface to 20% of its surface value within the distance of the dominant wavelength.

This is of the order of 10m for a typical mine seismic event. This leads to lower amplitudes deeper into the stope hangingwall and footwall. The induced tensile stress decays more sharply than the velocity. The amplitudes of ground motion in both the near-field and the far-field were influenced in a complex manner by the following: the stress drop, the sense of slip, the excavation surface, the excavation outline, and the proximity of any part of the source, rather than the source centre, to the excavation. The coupled influences of all these factors on both the peak amplitude and on the distribution of motions, is not intuitive.

Modelling a specific event and the excavation layout appears to be necessary to obtain a meaningful evaluation of the damage potential of an event. Considering the source to act in a solid, infinite rock mass gives too low an estimate of the peak velocity. Ignoring the effect of the excavation also over-estimates the rate of decay of ground motion with distance from the source, and grossly under-estimates the induced tensile stress.

A number of specific conclusions on the modelling of fracturing are important for the modelling of waves around openings. Modelling wave interaction with displacement discontinuities having a stress dependent stiffness captured much of the physics observed in experiments with real joints and, by inference, with fracturing. The stiffness of a fracture has a significant effect on the waveforms, delay, amplitude and frequency content and this has important consequences for modelling waves around underground openings. Large fractures must be modelled with the appropriate interface stiffness and not simply be considered as open or closed when modelling wave propagation.

It was found that fracture stiffness can influence both the attenuation of high frequencies and the amplification of lower frequencies. In addition, it was found to be important to develop models in which the fracture stiffness increases with increased loading on the discontinuity, even for modelling a weakly non-uniform stress distribution along the discontinuity. The stress distribution around underground excavations is extremely non-uniform. Taking into account the stress-dependence of the fracture stiffness can therefore be important for modelling wave propagation around these openings. It was also demonstrated that it is not sufficient to introduce stress dependence simply by allowing the opening of fractures in tension.

A combination of computational modelling with the measurement of seismic waveforms will aid in interpreting the rock mass condition. The modelled fracturing causes both wave-speed and amplitude changes and provides a method of verifying the consistency of conclusions acquired through seismic monitoring.

It was found to be impractical, with current computational capabilities, to model the true micro-scale crack openings in the material for *in situ* monitoring. A two-stage approach was proposed, using larger stiff fractures in full-scale models and relating this to the true crack openings using smaller-scale models.

A numerical technique was developed to characterise the wave dispersion behaviour of different assemblies of fractures across a wide frequency band. A numerical technique ultimately has advantages over theoretical analyses, as it allows less restrictive cases to be studied and can be readily applied to alternative models of fracture. The method involves simulating plane wave propagation through an assembly of fractures and extracting the frequency variation in phase velocity and attenuation from the resulting waveforms. The method was shown to be consistent although sensitive to a number of numerical issues. Phase velocity and attenuation spectra were calculated for various sizes and densities of open fractures, as well as for large fractures with varying fracture stiffness and fracture spacing. The technique can readily be applied to study a much wider range of fracture models.

The modelling of wave interactions with fractures places great demands on computational capacity. For example, the URL study was limited to a minimum crack-length of 20 mm. This is self-similar to being limited to 2 m cracks in a 100 m cube in a practical mining problem. The model used many millions of elements. A greater capacity for treating sufficient numbers of grids is required to solve realistic dynamic problems.

Models have indicated the necessity for very large numbers of elements in dynamic studies of wave propagation. A method was developed to characterize the dispersion behaviour of numerical codes. This method was used to evaluate the computational requirements of a number of finite element and finite difference computer codes. It was found that those codes which are currently capable of modelling fully general geometries are severely limited in problem-size. For the same computer resources, these general codes can only solve problems which are two orders of magnitude smaller than those possible with the specialised WAVE code. WAVE's limitation however, is that it cannot accommodate general orientations of geometry. A number of methods were investigated for generalising the WAVE-code while maintaining it's large problem-size capability. The two most promising methods are to apply a curvilinear mapping to the existing staggered grid scheme, or to use an alternative high-order non-staggered grid to which a mapping can also be readily applied. It is recommended that these two methods should be investigated further. The development of these improvements, which should allow both general studies and large accurate grids, is crucial to the future of dynamic modelling in mining.

The models of fracture were applied to examine the influence of the excavation fracture zone on the distribution and amplitude of ground motion. Fractures were shown to influence the amplitude of ground motion in both the near-source and far-field regions. The results indicate that a combination of surface waves and the presence of fractures provides an explanation for documented observations of velocity amplification. The models showed increases in near-source in-stope amplitudes of up to 50% due to the free surface alone, and 50% more due to fracturing. In the far-field, the in-stope amplitudes were again increased for certain fracture cases. The effect was dependent on the orientation and density of fracturing.

A model was studied where waves from the primary event triggered energy release on numerous fractures in the footwall and hangingwall, which were assumed to be in a low stress regime. Although a large amount of energy was released from these fractures, this did not increase the maximum motions over the whole region. This indicates that the energy release is not coherent and does not lead to a general amplification of the original wave, but rather manifests itself in localised pockets of large motions, sometimes in unexpected areas. The potential for triggering energy release in a high stress regime was not studied.

A study was carried out to determine the effect of a Rayleigh wave on a block in the hangingwall. This hangingwall was found to be in tension during upward motion and the block did not move upwards with the rest of the hangingwall. As a result the block tended to “ratchet” downwards for successive loading/ unloading cycles. This is an important mechanism in explaining potential rock falls triggered by seismic activity.

Since fracturing affects the amplitudes of ground motion, measuring the extent of fracturing is important for estimating maximum motions due to potential events. It is recommended that attempts should be made to characterize the degree of fracturing in particular stopes. One means to accomplish this, is to make detailed seismic measurements of wave-speeds and attenuation, quantifying how these vary with distance from the excavation. This requires active measurements with a known source, and careful choice of the appropriate frequency range. Models can be used to aid in the interpretation of the fracture state.

6.0 References

Adams, G.R. and Jager, A.J., 1980. Petroscopic observations of rock fracturing ahead of stope faces in deep level gold mines, *J. South African Inst. Min. Metall.* vol. 80 (6), 204-209.

Adams. D.J. , Gay, N.C. and Cross, M. 1993. Preconditioning – a technique for controlling rock bursts. *Proceedings of 3rd International Symposium on Rockbursts and Seismicity in Mines, ed.* Young, Balkema, 29-33.

Amadei, B., 1979. Creep behaviour of rock joints. *M.Sc. Thesis,* University of Toronto, Toronto, Canada.

ASTM., 1994. Standard test method for laboratory determination of pulse velocities and ultrasonic elastic constants of rock. In *annual Book of ASTM standards.* vol. 04.08, 242-246.

Atkinson B.K. and Avdis, V. 1980. Fracture mechanics parameters of some rock forming minerals determined using an indentation technique. *Int. J. Rock Mech Min Sci. 383-386.*

Baecher G.B. and Einstein H.H., 1981. Size Effect in Rock Testing, *Geophysical Research Letters*. vol. 8, No 7, 671-674.

Bandis S C., 1990. Scale Effects In The Strength And Deformability Of Rocks And Rock Joints. *Scale Effects in Rock Masses* , Pinto de Cunha (ed.)

Bandis, S., Lumsden, A.C., and Barton, N.R., 1981. Experimental studies of scale effects on the shear behaviour of rock joints. *Int. J. Rock Mechanics Mining Science,* 18: 1-21

Bazant Z. and Chen E-P., 1997. Scaling of structural failure*. Appl. Mechanics Rev* 50: 593-627.

BAŽANT, Z.P. and Planas, J., 1998. Fracture and size effect in concrete and other quasibrittle materials, *CRC Press LLC.*

Bienawski, Z.T. 1967. Mechanism of brittle fracture of rock, *Int. J. Rock. Mech Min Sci*, Vol 4, 395-406.

Bieniawski Z.T. and van Heerden, W.L., 1975. The significance of in situ tests on large rock specimens. *Int. J. Rock.Mechanics. Mining Science*. 12: 101-113.

Bieniawski, Z.T., 1977. Discussions: A review of coal pillar strength formulas by W.A. Hustrulid. *Rock Mechanics*. 10: 107-110.

Bowden, R.K. and Curran, J.H., 1984. Time-dependant behaviour of joints in shale. *In Proceedings of 25th Symposium. Rock Mechanics edited by C. H. Dowding & M. M. Singh*: 320-

327.

Brady, B. H. G. and Brown, E. T., 1993. *Rock Mechanics For Underground Mining, published by Chapman and Hall, London,* 354-356.

Brady, B.H., 1990. Dynamic performance and design of underground excavations in jointed rock. *In Static and dynamic considerations in Rock Engineering,* ed. Brummer, Balkema, 1-11.

Brinkman, J.A. and Gibson, P.A. 1985 High speed photography of stope blasting in South African gold mines. *Proceedings,* 11th Conference on Explosives and Blasting Technique.

Brinkmann, J.R., Giltner, S.G., Critcher, P.R. 1990. The development of effective blasting systems for South African gold mines. *Int. Deep mining Conf. Technical challenges in deep level mining.* SAIMM.

Brinkmann. J.R. 1986. Blasting Technology in stoping and development. *SAIMM School : Drilling and blasting in underground mining.* SAIMM.

Brost. F.B. 1970. A study of blasting phenomena and problems of blasting under high stress. *PhD. Thesis.* University of the Witwatersrand.

BSSA., 1991. The 1989 Loma Prieta, California, earthquake and its effects. *Special Issue: Bulletin of the Seismological Society of America*. vol. 81 (5), 415-2166.

Cai, J. G and Zhao, J., --. Effects of multiple parallel fractures on apparent attenuation of stress waves in rock masses. *Int. J. Rock Mechanics Mining Science*.

Carlson, S.R. and Young, R.P., 1992. Acoustic emission and ultrasonic velocity study of excavation-induced microcrack damage in the mine-by tunnel at the underground research laboratory. *Report #RP015AECL to Atomic Energy of Canada*. 1-50.

Carlson, S.R. and Young, R.P., 1993. Acoustic emission and ultrasonic velocity study of excavation-induced microcrack damage at the underground research laboratory. *Int. J. of Rock Mechanics.* vol. 30 (7), 901-907.

Carter, B.J., 1992. Size and stress gradient effects on fracture around cavities. *Rock Mechanics. Rock Engineering*. Vol. 25, no. 3, 167-186

Castaing, C., Genter, A., Chiles, J-P., Bourgine, B., and Ouillon, G., 1997. Scale effects in natural fracture networks. *Int. J. Rock Mechanics Mining Science* 34: 3-4, Paper No 045.

Coates, R.T., and Schoenberg, M., 1995. Finite-difference modelling of faults and fractures. *Geophysics*. vol. 60 (5), 1514-1526.

COMRO., 1988. Industry guide to methods of amelioration of rockfalls and rockbursts. *Research Organisation of the Chamber of Mines of South Africa.*

Couvreur, J. F. and Thimus, J. F., 1996. The properties of coupling agents in improving ultrasonic transmission. In *J. Rock Mechanics Mining Science & Geomech.* Abstr., 33, 417-424

Crampin, S., 1981. A review of wave motion in anisotropic and cracked elastic-media. *Wave Motion*. vol. 3, 343-391.

Cuisiat F.D. and Haimson B.C.,1993. The scale dependency of in situ rock stress measurements. *Scale Effects in Rock Masses*, Pinto du Cunha, 15-26.

Cundall, P.A., 1992. Theoretical basis of the program WAVE. *Unpublished internal report, COMRO* (now CSIR Division of Mining Technology, South Africa). 1-12.

Cundall, P.A., 1998. Personal communication on finite-difference grid schemes.

Cundall, P.A. and Lemos, J.V., 1990. Numerical simulation of fault instabilities with a continuously-yielding joint model. *Proceedings of 2nd International Symposium. on Rockbursts and Seismicity in Mines,* Balkema, 147-152.

Cunningham, C. 2002. Personal Communication.

Daehnke, A. and Hildyard, M.W., 1997. Dynamic fracture propagation due to stress waves interacting with stopes. *Proceedings of 1st Southern African Rock Engineering Symposium (SARES),* Johannesburg, South Africa, 97-108.

Daehnke, A., Rossmanith, H.P., and Knasmillner, R.E., 1996. Using dynamic photoelasticity to evaluate the influence of parting planes on stress waves interacting with stopes. *Int. J. for Num. and Analyt. Methods in Geomech.* vol. 20 (2), 101-117.

Daenkhe, A., Rossmanith, R., and Kouszniak, N., 1996. Dynamic fracture propagation due to blast induced high pressure gas loading. *2nd North American Rock Mechancis Symposium.* Montreal, 19-21 June. Balkema.

Dowding, C. H., 1992. Suggested method for blast vibration monitoring. ISRM Commission on Testing Methods. (C. H. Dowding, coordinator*), Int. J. Rock Mechanics. Mining Science & Geomech.* Abstr. 29 (20), 1992.

Dowding, C. H., 1985. *Blast monitoring and Control*. Prentice-Hall. Englewood Cliffs, N.J.

Dowding, C.H., Ho, C., and Belytschko, T.B., 1983. Earthquake design of caverns in jointed rock: effects of frequency and jointing. *In Seismic design of embankments and caverns*, publ. ASCE. 142-156.

Durrheim, R., Haile, A., Roberts, M.C.K., Schweitzer, J.K., Spottiswoode, S.M., and Klokow, J.W., 1998. Violent failure of a remnant in a deep South African gold mine. *Tectonophysics*. 289. 105-116.

Durrheim, R.J., Jager, A.J., Klokow, J.W., and Booyens, D., 1995. Back analysis to determine the mechanism and risk of rockbursts - 3 case histories from South African gold mines. *Proceedings of 26th Conference of Safety in Mines Research Institutes, Central mining Inst.,* Katowice, 1995. vol. 5, 41-56.

Durrheim, R.J., Roberts, M.K.C., Hagan, T.O., Jager, A.J., Handley, M.F., **Spottiswoode, S.M., and Ortlepp, W.D., 1997a.** Factors influencing the severity of rockburst damage in Southern African gold mines. *Proceedings of 1st Southern African Rock Engineering Symposium (SARES),* Johannesburg, South Africa, 17-24.

Gay, N.C. and Jager, A.J., 1986. The influence of geological features on problems of rock mechanics in Witwatersrand mines. *In: Mineral Deposits of Southern Africa Vol I&II edited by C.R. ANHAEUSSER & S. MASKE,* Geological Society of South Africa, Johannesburg, 753-772.

Gibbon, G.J., De Kock, A., and Mokebe, J., 1986. Monitoring pf peak ground velocity during rockbursts. *Proceedings of 8th West Virginia University Institute Mining Electro- Technology Conference*, Morgantown.

Gonano, L.P and Brown, E.T., 1975. Stress Gradient Phenomena and Related Side Effects in Brittle Materials, *Fifth Australian Conference on the Mechanics of Structures and Materials* - Melbourne.

Graff, K.F., 1975. Wave motion in elastic solids, Dover publications, New York, 323-329.

Graves, R.W., 1996. Simulating seismic wave propagation in 3D elastic media using staggered-grid finite differences. *Bulletin of the Seismological Society of America.* vol. 86 (4), 1091-1106.

Gross, D. and Zhang CH. (1992). Wave propagation in damaged solids. *Int. J. Solids Structures, 29.* pp 1763-1779.

Gu, B.L., Nihei, K.T., and Myer, L.R., 1996. Numerical simulation of elastic wave propagation in fractured rock with the boundary integral equation method. *J. Geophys. Res.* vol. 101 (B7), 15933-15943.

Hagan, T.O., Durrheim, R.J., Roberts, M.K.C., and Haile, A.T., 1999. Rockburst investigation in South African mines. *Proceedings of 9th ISRM International Congress on Rock Mechanics*, Paris, 1089-1094.

Hagan, T.O., Milev, A.M., Spottiswoode, S.M., Hildyard, M.W., Grodner, M.W., Rorke, A.J., Finnie, G.J., Reddy, N., Haile, A.T., Le Bron, K.B., and Grave, D.M., 2001. Simulated rockburst experiment - an overview. J. *South African Inst. Min. Metall.* vol. 101 (5), 217-222.

Handley, M.F., Hildyard, M.W., and Spottiswoode, S.M., 1996. The influence of deep mine stopes on seismic waves. *Proceedings of 2nd North American Rock Mechanics Symposium (NARMS),* Montreal, 499-506.

Harr, M. 1977 The mechanics of particulate media – a probabilistic approach. McGraw Hill.

Harr, M.E. 1987. *Reliability based design in civil engineering*. McGraw-Hill. 290pp.

Hazzard, J.F., 1999. Numerical modelling of acoustic emissions and dynamic rock behaviour. *PhD Thesis, Keele University,* United Kingdom*,* 1-274.

Hemp, D.A., and Goldbach, O.D., 1993. The effect of backfill on ground motion in a stope. *Proceedings of 3rd International Symposium on Rockbursts and Seismicity in Mines, ed.* Young, Balkema*,* 75-79.

Hencher, S.R., Toy, J.P., and Lumsden, A.C., 1993. Scale dependent shear strength of rock joints. *Scale Effects in Rock Masses*, Pinto du Cunha, 233-240.

Henning, L.T., Els, B.G., Meyer, J.J., 1994. The Ventersdorp contact placer at Western Deep Levels Gold Mine – an ancient terraced fluvial system. *South Africa. J. Geology* 97, 308-318.

Hestholm, S. and Ruud, B.,1994. 2D finite-difference elastic-wave modeling including surface-topography. *Geophysical Prospecting.* vol. 42 (5), 371-390.

Heuze F.E., 1980. Scale effects in the determination of rock mass strength and deformability. *Rock Mechanics*. 12. 167-192.

Heuze, O. 2001. An equation of state of detonation products for hydrocode calculations. *12th biennial int. conf. of the APS topical group on shock compression of condensed matter. Bull Am. Phys. Soc.* V46. No 4.

Hildyard, M. 2001. Wave Interaction with Underground Openings In Fractured Rock. *PhD. Thesis, University of Liverpool*.

Hildyard, M.W. and Milev, A.M., 2001a. Simulated rockburst experiment: Development of a numerical model for seismic wave propagation from the blast, and forward analysis. *J. South African Inst. Min. Metall.* vol. 101 (5), 235-245.

Hildyard, M.W. and Milev, A.M., 2001b. Simulated rockburst experiment: Numerical back-analysis of seismic wave interaction with the tunnel. *J. South African Inst. Min. Metall.,* vol. 101 (5), 223-234.

Hildyard, M.W. and Young, R.P., 2002. Modelling wave propagation around underground openings in fractured rock. *Special issue on induced seismicity, ed. Trifu, Pure and Applied Geophysics.* vol. 159, 247-276.

Hildyard, M.W., Daehnke, A., and Cundall, P.A., 1995. WAVE: A computer program for investigating elastodynamic issues in mining. *Proceedings of 35th U.S. Symposium on Rock Mechanics, June 1995,* Balkema, 519-524.

Hodgson, K. and Cook, N.G.W., 1970. The effects of size and stress gradient on the stength of rock. *Proc 2nd Int. Congress ISRM*. Belgrade, 2, 31-34.

Holland, R., 1983. Finite-difference solution of Maxwells equations in generalized non-orthogonal coordinates. *IEEE Transactions On Nuclear Science.* vol. 30 (6), 4589-4591.

Hudson, J.A. and Brown, E.T., 1973. Studying the time-dependant effects in failed rock. *In: Proceedings of. Fourteenth Symposium on Rock Mechanics edited by H.R. HARDY & R. STEFANKO, American Society of Civil Engineers, New York*: 25-34.

Hudson, J.A., 1981. Wave speeds and attenuation of elastic waves in material containing cracks. *Geophysical Journal R.* Astr. Soc., vol. 64, 133-150.

Hudson, J.A., Brown, E.T., and Fairhurst. C., 1971. Shape of the complete stress – strain curve for rock. *Rock Mechanics*. 773-795.

International Society for Rock Mechanics. Commission on Standardization of Laboratory and Field Tests. 1978. Suggested methods for determining hardness and abrasiveness of rocks. *Int. J. Rock Mech. Min. Sci, & Geomech. Abstr*. Vol 15, pp. 89-97.

Itasca Consulting Group., 1993a. UDEC Version 2.0, *Minneapolis,* Minnesota.

Itasca Consulting Group., 1993b. *FLAC Version 3.2, Minneapolis*, Minnesota, 1 20.

Jager, A.J., 1992. Two new support units for the control of rockburst damage. *Proceedings* of *International Symposium on Rock Support, Sudbury,* June 1992, ed. P.K. Kaiser and D.R. McCreath, Balkema, 621-631.

Jaeger, and Cook N.C., 1979. Fundamentals of rock mechanics. *Chapman and Hall.* London.

Jager, A.J. and Ryder, J.A., 1999. A handbook on rock engineering practice for tabular hard rock mines. *Published by The Safety in Mines Research Advisory Committee (SIMRAC),* Johannesburg, South Africa.

Jirasek, M. and Bazant Z., 1995. Macroscopic fracture characteristics of random particle systems. *Int. J. Fracture*. 69 201-228.

Johnson, R.A. and Schweitzer, J.K., 1996. Mining at depth: evaluation of alternatives. 2nd North American Rock Mechanics symposium. *Montreal. June. Balkema. Rotterdam,* 359-366

Jones, C. and Murrell, S.A.F., 1989. Acoustic compressional wave velocity and dilatacy in triaxally stressed rock. *In Rock at Great Depth* (edited by Mauray, V. and Foutmaintraux, D), Balkema, Rotterdam, 214-247.

Jurgens, T.G., Taflove, A., Umashankar, K., and Moore, T.G., 1992. Finite-difference time-domain modeling of curved surfaces. *IEEE Transactions On Antennas And Propagation*. vol. 40 (4), 357-366.

Keller, A., 1998. High Resolution, non-destructive measurement and characterization of fracture apertures. *Int. J. Rock Mechanics Mining Science. 35:8,* 1037-1050.

Klerck, P.A., 2000. The finite element modelling of discrete fracture in quasi-brittle materials. *PhD* Dissertation University Of Wales, Swansea.

Klimis, N., 1991. Geotechnical characterization of a thermally cracked marble. *In the 7th International Congress on rock Mechanics* (edited by Wittke, W). Balkema, Rotterdam, 539-544.

Kullmann D.H., Stewart, R.D, and Grodner, M. 1996. A pillar preconditioning experiment an a deep level South African Gold Mine. *2nd North American Rock Mechanics Symposium*. Montreal.

Latjai, E.Z., and Duncan, E.J.S., 1988. The mechanism of deformation and fracture in potash rock. *Canada. Geotech. J., 25*: 262-278.

Lee, J.F., Palandech, R., and Mittra, R., 1992. Modeling 3-dimensional discontinuities in wave-guides using non-orthogonal FDTD algorithm. *IEEE Transactions on Microwave Theory and Techniques.* vol. 40 (2), 346-352.

Lilly, P. and Li, J. 2000. Estimating excavation reliability from displacement modelling. *Int. J. Rock Mech. Min. Sci.* 1261-1265**.**

Linkov, A.M. and Durrheim, R.J., 1998. Velocity amplification considered as a phenomenon of elastic energy release due to softening. *Mechanics of Jointed and Faulted Rock,* Balkema, 243-248.

Liu, E.R., Hudson, J.A., and Pointer, T., 2000. Equivalent medium representation of fractured rock. *J. Geophys. Res.* vol. 105 (B2), 2981-3000.

Lockner, D.A., Walsh, J.B., and Byerlee, J. D., 1977. Changes in seismic velocity and attenuation during deformation of granite. *J. Geophys.* Res., 82, 5374-5378.

Mack, M.G. and Crouch, S.L., 1990. A dynamic boundary element method for modeling rockbursts. *Proceedings of 2nd International Symposium on Rockbursts and Seismicity in Mines,* Balkema*,* 93-99.

Mader, C. 1986. *Explosives and propellants.* CRC Press. Boca Raton.

Malan D.F., 1998. An investigation into the identification and modelling of time-dependant behaviour of deep level excavations in hard rock. *PhD thesis,* University of the Witwatersrand*, Johannesburg.*

Malan, D.F. and Drescher K., 2000. Modelling the post-failure relaxation behaviour of hard rock. *In: Proc. of the fourth North American Rock Mechanics Symposium, edited by J. Girard, M. Liebman, C. Breeds and T. Doe, Balkema, Rotterdam*: 909-917.

Malan, D.F., Drescher, K., and Vogler, U.W., 1998. Shear creep of discontinuities in hard rock surrounding deep excavations. *In: Proc. Mechanics of faulted and jointed rock, MJFR-3,* edited by H.P. ROSSMANITH, Balkema, Rotterdam*:* 473-478.

Marone, C and Kilgore B. 1993. Scaling of the critical slip distance for seismic faulting with shear strain in fault zones. *Nature*. 362. 618-621.

Marti, J. and Cundall, P.A., 1982. Mixed discretization procedure for accurate modelling of plastic collapse. *Int. J. for Num. and Analytical Methods in Geomechanics.* vol. 6, 129-139.

Martin, C.D. 1997. Seventeenth Canadian Geotechnical Colloquium: The effect of cohesion loss and stress path on brittle rock strength. *Can. Geotech. J*. 34: 698-725.

Mazars, J. and Bazant, Z.P. (eds) 1989. *Cracking and Damage: strain localization and size effect* Elsevier. London 391-403.

McGarr, A., 1993. Keynote address: Factors influencing the strong ground motion from mining-induced tremors. *Proceedings of 3rd International Symposium on Rockbursts and Seismicity in Mines, ed.* Young, Balkema, 3-12.

McGarr, A. 1997. A mechanism for high wall-rock velocities in rockbursts. *Pure and Applied Geophysics.* vol. 150, 381-391.

McGarr, A.R., Green, W.E., and Spottiswoode, S.M., 1981. Strong motion of mine tremors: some implications for near source ground motion parameters. *Bull. Seism*. Am, 71.

Milev, A.M., Spottiswoode, S.M., and Stewart, R.D., 1999. Dynamic response of the rock surrounding deep level mining excavations. *Proceedings of 9th ISRM International Congress on Rock Mechanics,* Paris, 1109-1114.

Moon H-K and Kim C-Y, 1993, Scale Effects In The Elastic Moduli And Strength Of Jointed Rock Masses, *Scale Effects in Rock Masses 93*, Pinto da Cunha (ed)

Motosaka, M. and Nagano, M., 1996. Analysis of ground-motion amplification characteristics in Kobe City considering a deep irregular underground structure: interpretation of heavily damaged belt zone during the 1995 Hyogo- ken Nanbu earthquake. *J. Physics of the Earth. v*ol. 44 (5), 577-590.

Moustachi, O., Couvreur, J. F., and Thimus, J. F., 1995. Characterization of failure and dilatacy processes by ultrasonic for isotropic and anisotropy rocks*. In 8th International congress in rock Mechanics* (Edited by Fujii, T.) Balkema, Rotterdam, 169-172.

Muhlhaus, H.B., De Borst, R. Aifantis, E.C. 1991. Constitutive models and numerical analysis for inelastic materials with microstructure. Computer methods and advances in Geomechanics. *Beer, Booker and Carter (eds)*. Balkema. Rotterdam.

Müller, W., 1991. Numerical simulation of rockbursts. *Mining science and technology.* vol. 12, 27-42.

Myer, L.R., Hopkins, D., and Cook, N.G.W., 1985. Effect of contact area of an interface on acoustic wave transmission characteristics. *Proceedings of 26th U.S. Symposium on Rock Mechanics.* Balkema, 565-572.

Napier J.A.L. and Stephansen, S.J., 1987. Analysis of deep level mine design problems using the MINSIM-D boundary element program. *APCOM '87. Proceedings of 20th International Symposium. SAIMM*. 3-19.

Napier, J.A. L., 1990. Modelling of fracturing near deep level mine excavations using a displacement discontinuity approach. *Proceedings of 2nd conference on Mechanics of jointed and faulted rock,* MJFR-2, Vienna, Balkema, 709-715.

Napier, J.A.L. and Malan, D.F., 1997. A viscoplastic discontinuum model of time-dependent fracture and seismicity effects in brittle rock. *Int. J. Rock Mech.,* Vol. 34 (7), 1075-1089.

Napier, J.A.L., 1998. Three dimensional modelling of seismicity in deep level mines. *Proceedings of 3rd conference on Mechanics of jointed and faulted rock.* MJFR-3, Balkema. 285-290.

Napier, J.A.L., Daehnke, A., Dede, T., Hildyard, M.W., Kuijpers, J.S., Malan, D.F., Sellers, E.J., Turner, P.A., 1997. Quantification of stope fracture zone behaviour in deep level gold mines. *J. South African Inst. Min. Metall. v*ol. 97 (3), 119-134.

Napier, J.A.L., Hildyard, M.W., Kuijpers, J.S., Daehnke, A., Sellers, E.J., Malan, D.F., Siebrits, E., Ozbay, M.U., Dede, T. and Turner, P.A., 1995. "Develop a quantitative understanding of rock mass behaviour near excavations in deep mines". Unpublished SIMRAC Final project report (GAP 029).

Napier, J.A.L., Malan, D.F., Sellers, E.J., Daehnke, A., Hildyard, M.W., and Shou, K-J. 1998. "Deep gold mine fracture zone behaviour". Unpublished SIMRAC Final project report (GAP 332).

Nicholls, H.R., Johnson, G.F., and Duvaal, W.J., 1971. Blasting vibration and their effects on structures. *United States Bureau of Mines Bulletin 656.*

Nilson, 1981. R.H. Gas-driven fracture propagation. *J Applied Mech.* 48. 757-762.

O'Connell, R.J. and Budiansky, B., 1974. Seismic velocities in dry and saturated cracked solids. *J. Geophys. Res. v*ol. 79, 5412-5426.

Oprsal, I. and Zahradnik, J., 1999. Elastic finite-difference method for irregular grids. *Geophysics*. vol. 64 (1), 240-250.

Ortlepp, W.D., 1993. High ground displacement velocities associated with rockburst damage. *Proceedings of 3rd International Symposium. on Rockbursts and Seismicity in Mines, ed.* Young, Balkema, 101-106.

Ortlepp, W.D., 1997. Rock Fracture and Rockbursts. *SAIMM.*

Panek, L.A. and Fannon T.A., 1992. Size and Shape Effects In Point Load Tests of Irregular Rock Fragments, *Rock Mechanics and Rock Engineering* 25. 109-140.

Persson, P-A., Holmberg, R. and Lee, J. 1994. *Rock Blasting and explosives engineering.* CRC Press. Boca Raton.

Pinto du Cunha, A., 1993. *Scale Effects in Rock Masses* , Balkema, Rotterdam.

Pitarka, A. and Irikura, K., 1996. Modeling 3D surface topography by finite-difference method: Kobe-JMA station site, Japan, case study. *Geophysical Research Letters*. vol. 23 (20), 2729-2732.

Pitarka, A.; Irikura, K.; Iwata, T.; and Kagawa, T., 1996. Basin structure effects in the Kobe area inferred from the modeling of ground motions from two aftershocks of the January 17, 1995, Hyogo-ken Nanbu earthquake. *J. Physics of the Earth*. vol. 44 (5), 563-576.

Potyondy, D.O., and Cundall P.A., 1998. Modeling Notch-Formation Mechanisms in the URL Mine-by Test Tunnel Using Bonded Assemblies of Circular Particles. Proceedings of NARMS'98, 3rd North American Rock Mechanics Symposium, Cancun, *Int. J. Rock Mechanics & Mining Science, 35(4-5),* Paper No. 067 (1998).

Potyondy, D.O., Cundall, P.A., and Lee, C.A., 1996. Modelling Rock Using Bonded Assemblies Of Circular Particles, *Second North American Rock Mechanics Symposium*, Montreal Quebec, Canada, 19-21 June 1996.

Price, N.J., 1964. A Study of the time-strain behaviour of coal-measure rocks. *Int. J. Rock Mechanics. Mining Science, Pergamon Press*, 1: 277-303.

Pyrak-Nolte, L.J., Myer, L.R., and Cook, N.G.W., 1990a. Transmission of seismic waves across single natural fractures. *J. Geophys. Res.* vol. 95 (B6), 8617-8638.

Pyrak-Nolte, L.J., Myer, L.R., and Cook, N.G.W., 1990b. Anisotropy in seismic velocities and amplitudes from multiple parallel fractures. *J. Geophys. Res.* vol. 95 (B7), 11345-11358.

Rao, M. and Ramana, Y.V., 1992. A study of progressive failure of rock under cyclic loading by ultrasonic and AE monitoring technique. *Rock Mechanics.* Rock Engineering, 25, 237-251.

Robertsson, J.O.A., 1996. A numerical free-surface condition for elastic/viscoelastic finite-difference modeling in the presence of topography. *Geophysics.* vol. 61 (6), 1921-1934.

Rockfield Software Ltd., 1999. *ELFEN user manual v.2.8, University College of Swansea.*

Rorke, A.J. and Brummer, R.K. 1990. The use of explosives in rockburst control techniques. *Rockbursts and Seismicity in Mines.* Fairhurst (ed). Balkema.

Ruina, A., 1983. Slip instability and state variable friction laws. *J. Geophys Res.* vol 88 10359 - 10370.

Rummel, F. and van Heerden, W.L., 1978. Suggested methods for determining sound velocity. In *J. Rock Mechanics. Mining Science & Geomech.* Abstr., 15, 53-58.

Sayers, C.M. and Kachanov, M., 1991. A simple technique for finding effective elastic-constants of cracked solids for arbitrary crack orientation statistics. *Int. J. Solids Structures.* vol. 27 (6), 671-680.

Schoenberg, M., 1980. Elastic wave behaviour across linear slip interfaces. *J. Acoust. Soc. Am.* vol. 68 (5), 1516-1521. 323-329.

Schroeder, W., Martin, K., and Lorensen, B., 1997. The Visualization Toolkit. *An object-oriented approach to 3D graphics*. *Prentice Hall.*

Schwartz, C.W. and Kolluru, S., 1984. The influence of stress level on the creep of unfilled rock joints. *In: Proceedings 25th Symposium Rock Mechanics edited by C. H. Dowding & M. M. Singh*: 333-340.

Sellers, E. A review of models for the propagation of seismic waves in the fractured rockmass around a stope. SIMRA*C Interim Report, GAP029.*

Sellers, E. and Napier, J., 1997. A comparative investigation of micro-flaw models for the simulation of brittle fracture in rock. *Computational Mechanics,* 20, 164-669.

Sellers, E., Berlenbach, J., and Schweitzer, J., 1998. Fracturing around deep level stopes: comparison of numerical simulations with underground observations. *Proceedings of 3rd conference on Mechanics of jointed and faulted rock,* MJFR-3, Vienna, Balkema, 425-430.

Sellers, E.J. and Turner, P.A. 1996. Modelling of blast driven fracture propagation using DIGS. *SIMRAC interim report GAP 332*.

Sellers, E.J., 2001. Modelling of continuum to discontinuum transitions for deep level mining. (Bicanic, Ed.). *4th International conference on the analysis of the deformation of discontinuous media.* University of Glasgow. 63-72.

Siggins, A.F., 1993. Dynamic elastic tests for rock engineering in *Compressive Rock Engineering* (edited by Hudsson, J. A). Pergamon, Oxford vol. 3, 601-618.

Singh, D.P., 1975. A study of creep of rocks. *Int. J. Rock Mechanics Mining Science & Geomech. Abstr., 12*: 271-276.

Siebrits, E., Hildyard, M.W., and Hemp, D.A., 1993. Stability of backfilled stopes under dynamic excitation. *Proceedings of 3rd International Symposium. on Rockbursts and Seismicity in Mines, ed.* Young, Balkema, 117-121.

Spottiswoode, S.M., Durrheim, R.J., Vakalisa, B., and Milev, A.M., 1997. Influence of fracturing and support on the site response in deep tabular stopes. *Proceedings of 1st Southern African Rock Engineering Symposium (SARES*), Johannesburg, South Africa, 62-67.

Squelch, A.P., 1994. The determination of the influence of backfill on rockfalls in South African gold mines. *MSc. dissertation*, University of the Witwatersrand, Johannesburg, South Africa.

Srinivasan, C., Willy, Y.A., and Benady, S., 2001. Rockburst seismic intensity attenuation model for the Kolar Gold Fields hard rock mining region. In *Rockbursts and seismicity in Mines-RaSIM5, South African Institute of Mining and Metallurgy,* Johannesburg.

StatSoft, Inc. 2002. Electronic Statistics Textbook. Tulsa, OK: StatSoft. WEB: http://www.statsoft.com/textbook/stathome.html.

Stewart R.D. and Spottiswoode, S. M. 1993. A technique for determining the seismic risk in deep-level mining. *Proceedings of 3rd International Symposium on Rockbursts and Seismicity in Mines, ed.* Young, Balkema, 123-128.

Swenson D. and Taylor, L. 1983. A finite element model for the analysis of tailored pulse stimulation of boreholes. *Int. J. Numer. Anal. Meth. Geomech*. V7, 469-484.

Tainton, S., 1994. A review of the Witwatersrand basin and trends in exploration. *XV'th CMMI Congress.* SAIMM. Johannesburg. 19-45.

Tang and Kaizer P.K. 1998. Nmerical simulation of cumulative damage and seismic energy release during brittle rock failure. *Int. J. Rock Mech Min Sci*. 113-121.

Tang. C.A., Liu,H. , Lee, P.K.K., Tsui, Y. and Tham, L.G. 2000. Numerical studies of the influence of microstructure on rock failure n uniaxial compression. – Part I: effect of heterogeneity. Int. J. Rock Mech. Min Sci. 555-569.

Tao, G. and King, M. S., 1990. Shear –wave velocity and Q anisotropy in rocks: a laboratory study. Int. *J. Rock Mechanic. Mining Science & Geomech.* Abstr. 27,353-361.

Thimus, J.F., 1993. Contribution of sonic propagation to the study of frost process and thermal degradation of frozen soils. *In Frost in Geochemical Engineering* (edited by Phukan, A) Balkema, Rotterdam, 51-57.

Tinucci, J.P. and Spearing, A.J.S., 1993. Strategies for clamping faults and dykes in high seismicity tabular mining conditions. *Proceedings of 3rd International Symposium. on Rockbursts and Seismicity in Mines, ed.* Young, Balkema, 435-440.

Toksoz, M.N., Johnston, D.H., and Timur, A., 1979. Attenuation of seismic waves in dry and saturated rocks- I Laboratory measurements. *Geophysics* 44, 681-690.

Toper, A.Z., Adams, D.J., Janse van Rensburg, A.L. 1994. Effects of Preconditioning Blasts in Confined Rock. *ISRM Symposium and IV South American Congress on Rock Mechanics.* Santiago. Chile.

Triantafyllidis, N. and Bardenhagen, S., 1996. The Influence of Scale Size On The Stability of Periodic Solids And The Role Of Associated Higher Order Gradient Continuum Models, *J Mechanics Phys Solids* Vol. 44 No 11 1891-1928.

Tse, S.T. and Rice, J.R., 1986 Crustal earthquake instability in relation to the depth variation of frictional properties. *J.Geophys. Res.* v91 B2. 9452-9472.

Turner, P.A. 1995. "Bow wave" fracturing in the walls of tunnels developed in stress: the result of a combination of the ambient field stress and the transient stresses from the blast. *CSIR Internal Report*. SIMRAC project GAP 332.

Uenishi, K., 1997. Rayleigh pulse dynamic triggering of interface slip. *PhD Thesis*, Vienna University of Technology, 1-178.

Van de Steen, B., 2001. Effect of heterogeneities and defects on the fracture pattern in brittle rock. *PhD thesis.* Katholieke Universiteit Leuven, Belgium.

Van de Steen, B., Vervoort, A., Napier, J.A.L., and Durrheim, R.J., 2001. Implementation of a flaw model to the fracturing around a vertical shaft. *Rock Mechanics and Rock Engineering* (submitted for publication).

Van Geet, M., 2001. Optimisation of microfocus x-ray computer tomography for geological research with special emphasis on coal components (macerals) and fractures (cleats) characterisation. *PhD thesis.* Katholieke Universiteit Leuven, Belgium.

Van Gils, M.A.J., Dortmans, L.J.M.G., De With, G., Brekelmans, W.A.M., and De Vree, J.H.P., 1996. Size effect Predictions By Fracture Models For A Refractory Ceramic*, International Journal of Fracture* 75: 273 -283.

Verhelst, F., Vervoort, A., De Bosscher, Ph., and Marchal, G., 1995. X-Ray computerized tomography: determination of heterogeneities in rock samples. *Proceedings of International Congress on Rock Mechanics. (Fujii, T. ed.).* 105-108.

Wagner, H., 1984. Support requirement for rockburst conditions. Proceedings of 1st International Conference. *On Rockbursts and Seismicity in Mines. South African Institute Min. Metall*., Johannesburg.

Wald, D.J., Helmberger, D.V., and Heaton, T.H. 1991. Rupture model of the 1989 Loma Prieta earthquake from the inversion of strong motion and broadband teleseismic data. *Bulletin of the Seismological Society of America*. vol. 81 (5), 1540-1572.

Wawersik, W.R., 1974. Time--dependant behaviour of rock in compression. *In: Proceedings of the third Int. Soc. Rock Mechanics Congress,* Denver: 357-363.

Young, R.P. and Hill, J.J., 1986. Seismic attenuation spectra in rock mass characterization; a case study in open-pit mining. *Geophysics.* vol. 51 (2), 302-323.

Zahradnik, J., Oleary, P., and Sochacki, J., 1994. Finite-difference schemes for elastic-waves based on the integration approach. *Geophysics.* vol. 59 (6), 928-937.

7.0 Supplementary document list

Drescher, K. 2002. An investigation into the mechanisms of time dependent deformation of hard rocks. MSc thesis. University of Pretoria.

Hildyard, M. 2001. Wave Interaction with Underground Openings In Fractured Rock. PhD. Thesis University of Liverpool.

Malan, D.F. 2000. Guidelines for measuring and analysing continuous stope closure behaviour in deep tabular excavations. CSIR Miningtek. The Safety in Mines Research Advisory Committee (SIMRAC)

Sellers E J. 1999. Review of theories of scaling and size effect in rock. CSIR: Mining Technology Project Report No : 99-0258. SIMRAC GAP 601b.

8.0 List of papers written within the scope of GAP 601b.

Bosman, J.D., Malan, D.F. and Drescher, K. (2000), Time-dependent tunnel deformation at Hartebeestfontein Mine. Accepted for publication in : Proc. AITES – ITA 2000 – World Tunnel Congress, Tunnels under Pressure, 13-18 May 2000.

Hildyard, M.W. and Milev, A. (1999), Modelling seismic wave interaction with a tunnel due to an artificial rockburst. In: Hagan, T.O. (ed.) Proceedings of the 2nd Southern African Rock Engineering Proceedings, SARES99, Johannesburg, pp. 273-280.

Hildyard, M.W. and Milev, A.M. (2001a), Simulated rockburst experiment: Development of a numerical model for seismic wave propagation from the blast, and forward analysis. J. South African Inst. Min. Metall., Vol. 101 (5), pp. 235-245.

Hildyard, M.W. and Milev, A.M. (2001b), Simulated rockburst experiment: Numerical back-analysis of seismic wave interaction with the tunnel. J. South African Inst. Min. Metall., Vol. 101 (5), pp. 223-234.

Hildyard, M.W., Napier, J.A.L., and Young, R.P., (2001), The influence of an excavation on ground motion, Proc. 5th Symp. on Rockbursts and Seismicity in Mines (RaSiM 5), Johannesburg, Sept. 2001, S.A. Inst. Min. Metall., pp. 443-452.

Hildyard, M.W. and Young, R.P. (2002), Modelling wave propagation around underground openings in fractured rock. Special issue on induced seismicity, ed. Trifu, Pure and Applied Geophysics, Vol. 159, pp. 247-276.

Malan, D.F. and Napier, J.A.L. (1999), The effect of geotechnical conditions on the time-dependent behaviour of hard rock in deep mines. In:Amadei, B., Kranz, R.L., Scott, G.A. and Smeallie, P.H. (eds) Proc. of the 37th U.S. Rock Mechanics Symposium, Vail Rocks '99, pp. 903-910, Balkema, 1999.

Malan, D.F. (1999), Closure measurements in tabular excavations: Avoiding the pitfalls. In: Hagan, T.O. (ed.) Proceedings of the 2nd Southern African Rock Engineering Proceedings, SARES99, Johannesburg, pp. 238-250.

Malan, D.F. and Drescher, K. (2000), Modeling the post-failure relaxation behaviour of hard rock. Accepted for publication in the 4th North American Rock Mechanics Symposium, Pacific Rocks 2000.

Napier, J.A.L. (1999), Numerical studies of time-dependent failure and implications for the prediction of time to failure. In: Amadei, B., Kranz, R.L., Scott, G.A. and Smeallie, P.H. (eds) Proc. of the 37th U.S. Rock Mechanics Symposium, Vail Rocks '99, pp. 911-917, Balkema.

Napier, J.A.L. (2001), Scale effect in the simulation of time-dependent mine seismic activity. Proc. 38th US Rock Mechanics Symposium. Rock Mechancis in the National interest. Washington D.C. Balkema, Rotterdam.

Sellers, E.J., Vervoort, A., van Cleynenbreugel, J. (2001), Application of CT scanning for three-dimensional visualization of fractures in rock test samples. EUG XI, Strasbourg, April 8th - 12th 2001European Union of Geosciences (Extended abstract and poster).

Sellers, E.J. and Napier, J.A.L. (2001), A point kernel representation of large-scale seismic activity in mining. . RASIM 5. Rockbursts and Seismicity in Mines. van Aswegen, Durrheim, Ortlepp (eds). SAIMM.

Sellers, E.J., Vervoort, A., van Cleynenbreugel, J. (2001), Three-dimensional visualisation of fractures in rock test samples, using x-ray tomography. J. Geological Society, London (submitted)

Sellers E.J. (2001), Modelling of continuum to discontinuum transitions for deep level mining. International conference on analysis of the deformation of discontinua. ICADD-4. University of Glasgow. 63-72.

Sellers E. and Kataka M. (2001), Localization and scaling of acoustic emission sources with mining seismicity. J Geophysical Research (submitted)